Developments in Agricultural Engineering 10

Agricultural Engineering Soil Mechanics

E. McKYES

Macdonald College of McGill University, Department of Agricultural Engineering, P.O. Box 950, Ste. Anne de Bellevue, Qué. H9X 1C0, Canada

ELSEVIER
Amsterdam — Oxford — New York — Tokyo 1989

ELSEVIER SCIENCE PUBLISHERS B.V.
Sara Burgerhartstraat 25
P.O. Box 211, 1000 AE Amsterdam, The Netherlands

Distributors for the United States and Canada:

ELSEVIER SCIENCE PUBLISHING COMPANY INC.
655, Avenue of the Americas
New York, NY 10010, U.S.A.

ISBN 0-444-88080-1

This book is printed on acid-free paper

Printed in The Netherlands

OTHER TITLES IN THIS SERIES

1. Controlled Atmosphere Storage of Grains
   by J. Shejbal (Editor)
   1980 viii + 608 pp.

2. Land and Stream Salinity
   by J.W. Holmes and T. Talsma (Editors)
   1981 vi + 392 pp.

3. Vehicle Traction Mechanics
   by R.N. Yong, E.A. Fattah and N. Skiadas
   1984 xi + 307 pp.

4. Grain Handling and Storage
   by G. Boumans
   1984 xiii + 436 pp.

5. Controlled Atmosphere and Fumigation in Grain Storages
   by B.E. Ripp et al. (Editors)
   1984 xiv + 798 pp.

6. Housing of Animals
   by A. Maton, J. Daelemans and J. Lambrecht
   1985 xii + 458 pp.

7. Soil Cutting and Tillage
   by E. McKyes
   1985 viii + 218 pp.

8. Mechanics of Agricultural Materials
   by G. Sitkei

9. Trickle Irrigation for Crop Production. Design, Operation and Management
   by F.S. Nakayama and D.A. Bucks
   1986 x + 384 pp.

FOREWORD

Since the profession of Agricultural Engineering requires many of the same skills as those used by Chemical, Civil, Electrical and Mechanical Engineers, many courses in Agricultural Engineering degree programs are the same as those in other engineering disciplines, or are indeed taken in those departments of a university. Such a situation does not always work out ideally, and the subject of Soil Mechanics is a case in point. The principles are the same for Agricultural or Civil Engineers, but the applications diverge, especially when it comes to the subjects of agricultural drainage, stability of drain ditchbanks, soil erosion, soil cutting and tillage, compaction of arable soil and the like.

It is for this reason that the effort has been put into writing this book, in the hopes that it may serve as a useful text for students aspiring to enter the profession of Agricultural Engineering. It is hoped also that the text will assist such students and perhaps practising engineers to obtain the foundations of Soil Mechanics theory and its application to typical problems associated with agriculture.

The author would like to thank sincerely certain colleagues who gave generous and helpful advice, comments and suggestions for parts of the work, notably Drs. Suzelle Barrington, Robert Broughton and Chandra Madramootoo.

LIST OF SYMBOLS

α - Blade rake angle
β - Angle of failure plane
γ - Weight density, kN/m^3
δ - Angle of surface friction
ϵ - Angle of a plane
- Engineering strain
η - Porosity
- Negative shear slip line
θ - Angle of a plane
μ - $\pi/4 - \phi/2$
ξ - Positive shear slip line
ρ - Mass density, t/m^3
- Angle
σ - Stress level, kPa
σ_b - Blade stress, kPa
σ_{iw} - Ice-water energy, J/m^2
σ_n - Normal stress, kPa
σ' - Effective stress, kPa
τ - Shear stress, kPa
ψ - c cotϕ
ϕ - Angle of internal friction
a - Length, m
A - Area, m^2
- Soil loss, t/ha
b - Width, m
B - Foundation width, m
c - Cohesion, kPa
c_a - Adhesion, kPa
C - Undrained strength, kPa
- Cropping factor
C_c - Coefficient of compresion
C_v - Coefficient of consolidation, m^2/y
d - Depth, m
D - Grain size, mm
- Overburden depth, m
- Bin diameter, m
e - Void ratio
- Eccentricity, m
F - Force, kN
- Freezing index, ^{0}days
G_s - Solids specific gravity
h - Height, m
H - Height, m
- Horizontal force, kN
k - Stiffness, kPa/m^n
- Permeability, m/s
- Thermal conductivity, J/(ms^0)
K - Erodibilty factor, ton/acre
K_a - Active pressure coefficient
K_c - Cohesion coefficient
K_0 - At rest coefficient
K_p - Passive pressure coefficient
L - Length, m
L_s - Latent heat of fusion, J/kg
LL - Liquid limit, %
m - Slope stability number
m_v - Coefficient of compression, kPa
M - Moment, kNm
n - Exponent
n_d - Number of potential drops
n_f - Number of flow paths
N - Normal force, kN
- Number of passes
$N\gamma$ - Frictional cutting factor
N_c - Cohesional cutting factor
N_{ca} - Adhesion cutting factor
N_q - Overburden cutting factor
p - Pressure, kPa
P - Wall or blade force, kN
P'_a - Effective wall force, kN
P_a - Active wall force, kN
PI - Plasticity index, %
PL - Plastic limit, %
Q - Bearing load, kN
Q_{ult} - Ultimate load, kN
q - Bearing pressure, kPa
- Drainage rate, mm/day
- Heat flow, J/(m^{2}s)
q_0 - Foundation pressure, kPa
r - Radius, m
R - Reaction force, kN
- Hydraulic radius, m
- Erosivity index
R_e - Area reduction factor
s - Shear strength, kPa

s - Field slope, %
- Side width, m
S - Degree of saturation
- Wheelslip, %
SF - Safety factor
t - Time, s
T - Torque, kNm
- Tangential force, kN
- Tensile strength, kN/m
- Temperature, ^{0}C
T_v - Time factor
u - Pore water pressure, kPa
U - Uniformity coefficient
- Degree of consolidation
- Water force, kN/m
v - Water velocity, m/s
- Specific volume, m^3/t
V - Volume, m^3
V_s - Solids volume, m^3
V_v - Voids volume, m^3
V_w - Water volume, m^3
w - Water content, dry basis
- Width, m
W - Weight, kN
W_s - Solids weight, kN
W_w - Water weight, kN
x,X - Horizontal distance, m
Y - Sediment yield, t
- Crop yield, t/ha
z - Settlement, m
z,Z - Vertical depth, m
z_0 - Depth of wall tension, m

Chapter 1. Origins and classification of soils

1.1. ORIGINS OF SOILS

Soils can be defined as masses of mineral particles mixed with varying proportions of water, gases and salts, and often organic matter. Soils are sometimes formed physically and chemically in place from parent rock material, and can occur from this origin in layers up to 25 m deep. Alternatively, they can be removed from rock material by physical and chemical weathering and subsequently be transported and sedimented to a new location.

Sand and gravel, and many silt materials (individual particles larger than 0.002 mm diameter), are generally of the same mineralogical composition as their parent rocks such as quartz, feldspars, calcite, dolomite, micas and others. They are removed from massive rock formations usually by physical agents including wind, water and freezing. Transportation of these granular materials by wind, water, ice or falling down slopes can alter the shape and size of individual particles by abrasion and impact, and can also sort different grain sizes one from another. That is the reason why, for example, many shoreline beaches or desert sand dunes are found to have remarkably uniform sizes of sand particles. Yet, some granular materials such as glacial till comprise a wide mixture of grain sizes, from silt to boulders larger than 300 mm in diameter, because of their mode of transport in ice.

Exceptions to the above case do occur, such as the cryptocrystalline quartz shown in Fig. 1.1. These silt sized quartz particles have been reformed from dissolved constituents in a hot spring in Arkansas, but they have formed into the characteristic rounded shape of quartz crystals found in most sands.

Clay minerals, on the other hand, are formed more usually by chemical changes to produce new minerals such as kaolinite, illite, chlorite, vermiculite, montmorillonite and others. These new minerals tend to break easily into small (less then 0.002 mm) sized particles and have rather chemically active surfaces, as well as a large surface area per unit mass. Fig. 1.2 shows a kaolinite material which has been formed as a residual soil on parent rock in Georgia, U.S.A. The large blocks of clay platelets have not yet been broken up into individual particles due to the lack of sufficient physical and chemical action at this point in their history. Fig. 1.3 shows particles of the same mineral in a finer structure. Fig. 1.4 illustrates a mixed clay soil from the Champlain Sea deposits in Quebec and Ontario. It comprises illite, chlorite and muscovite clay sized particles, as well as silt sized rock grains. Fig. 1.5

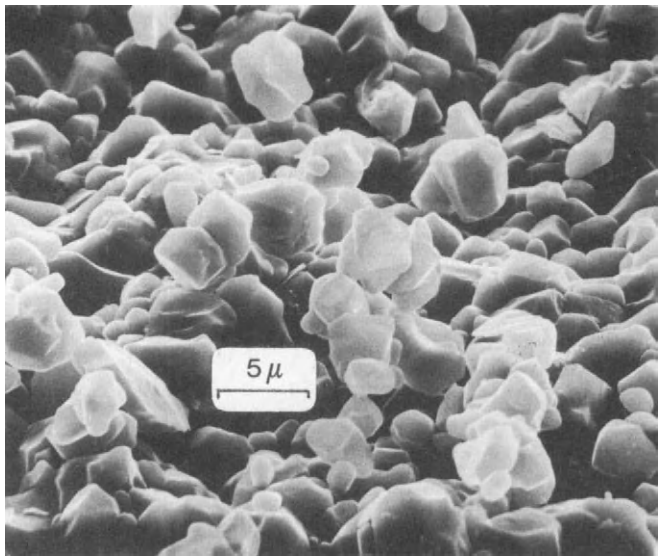

Fig. 1.1. Photomicrograph of cryptocrystalline quartz formed in a hot spring in Arkansas.

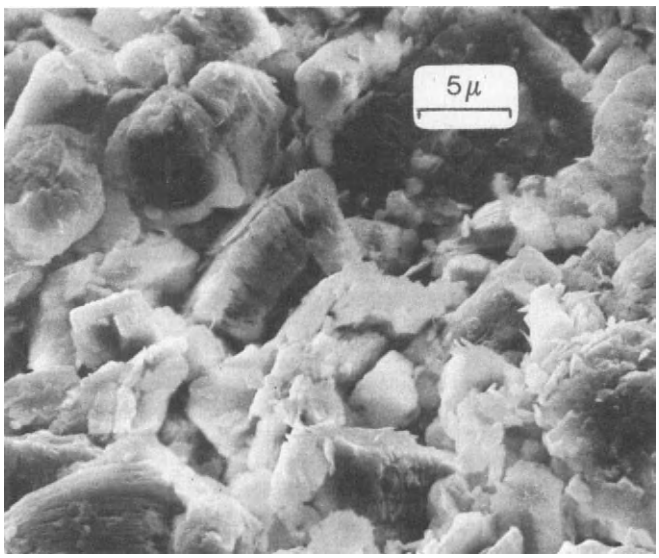

Fig. 1.2. Relatively large blocks of kaolinite MP which have formed mineralogically, but not broken apart.

is a microphotograph of a montmorillonite clay from the North American prairies. This is a mineral which can absorb considerable amounts of water and swell to several times its dry volume.

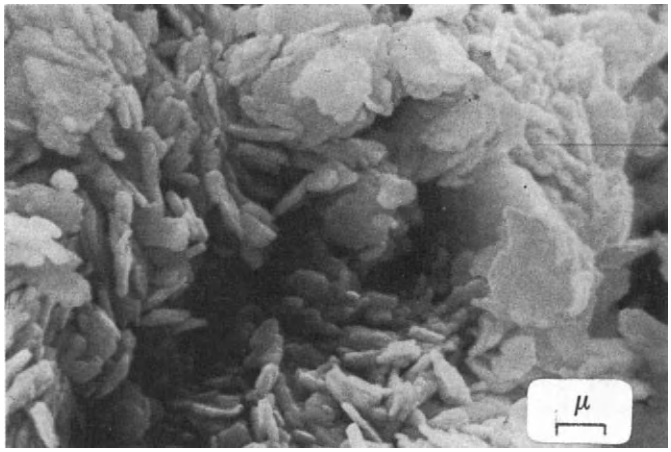

Fig. 1.3. Kaolin clay in individual platelet form.

Clay soils can be formed in situ above parent rock, usually in tropical regions with adequate heat and humidity, or they can be built in solution or formed by the breakdown of other minerals in water suspension and transported to other locations. If transported to a lake or sea, clay particles will slowly sediment to the floor and can build up into layers of 60 m or more in this fashion over hundreds of years. In the case of clay soils, the concentration and types of salts which are contained within the soil water are very influential in controlling their physical behavior. In addition, it is possible for sedimented clays to be leached later in time, and for some salts to be washed out or exchanged for others, causing further alterations in the mechanical nature of the soil.

Besides the natural formation or sedimentation of soils, earthwork construction often involves the filling of soil from another location. Usually it is desirable to compact a fill for reasons of soil strength or impermeability to water flow, depending on the purpose of the structure. But in the case of either a fill or a natural soil deposit, it is necessary to understand the mechanical behavior of the material, and how it can change with time, in order to be confident in designing a safe structure or analyzing the stability of a natural one.

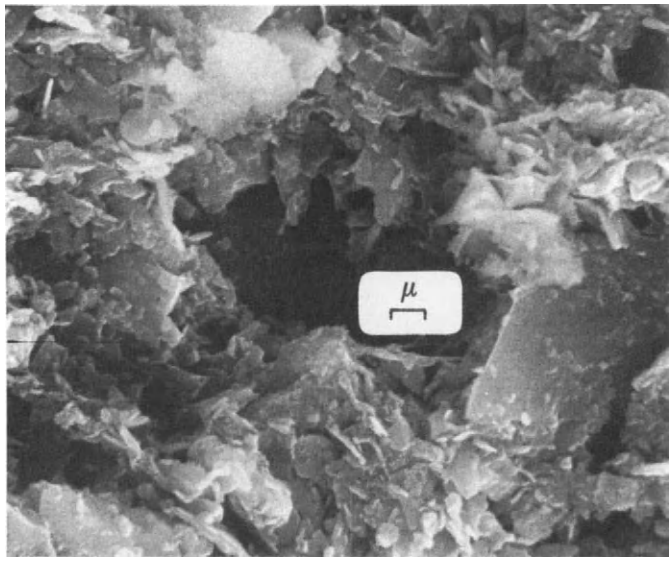

Fig. 1.4. Mixed illite, chlorite and muscvite clay particles with silt sized rock minerals.

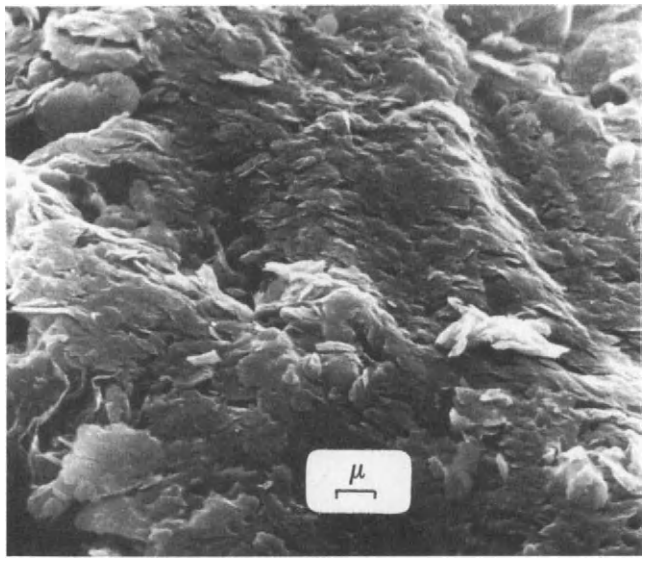

Fig. 1.5. Montmorillonite clay, thin flat particles which can swell a great deal on wetting.

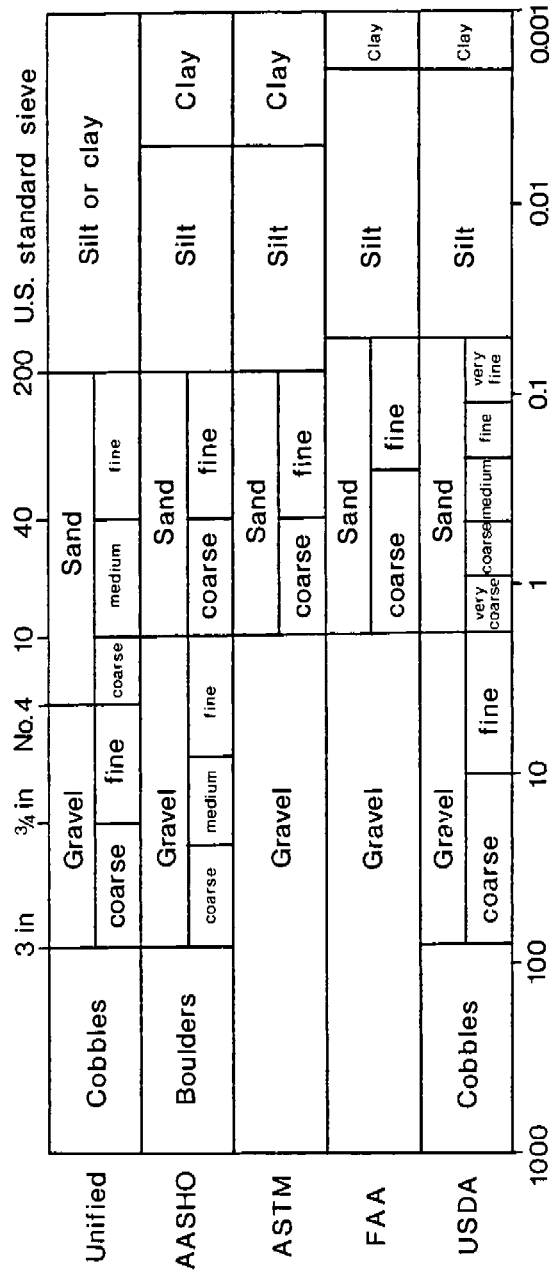

Fig. 1.6. Classification systems of soils by grain sizes.

1.2. CLASSIFICATION OF SOILS

A primary approach to classifying soils is on the basis of the size of individual grains. Fig. 1.6 shows the division of different particle sizes into increasing ranges of clay, silt, sands, gravel and cobbles or boulders. There are several different sets of standards shown in Fig. 1.6, and one must specify the standard system which is referred to when classifying a soil particle size.

Most soils do not fall into only one of the categories in Fig. 1.6, but are mixtures of two or more size classifications. In order to then classify the soils, many soil survey bureaus use the so called textural triangle shown in Fig. 1.7. The particle size analysis of a soil for interpretation on the triangle should be conducted only on that material which is less than 2 mm in size (sand or smaller), and soil should be pulverized or soaked to break down stable aggregates of fine particles. The sand sized particles can be fractionated by

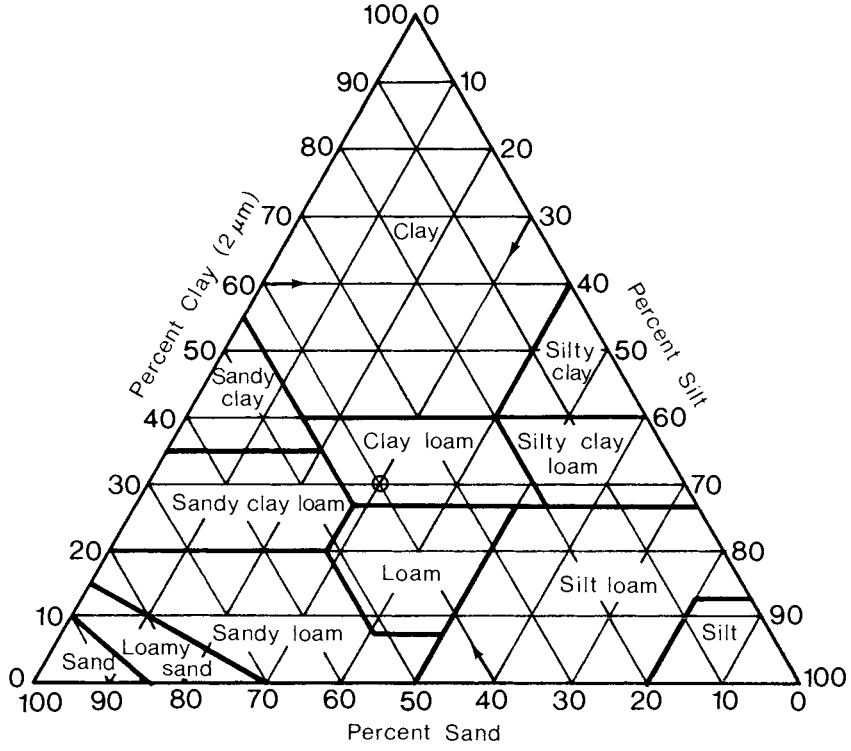

Fig. 1.7. The USDA textural triangle for classification of soil mixtures.

sieves mechanically and the portion of each size fraction weighed. Silt or clay particle fractions must be estimated by a hydrometer or pipette analysis in which the settlement rate of particles suspended in water is measured (Lambe, 1951; A.S.T.M., 1985)

Problem 1.1. A grain size analysis of a soil sample reveals that 100% of the particles by mass are less than 2 mm in diameter, 60% are less than 0.06 mm and 30% finer than 0.002 mm. What is the textural classification of this soil.

The amounts of clay, silt and sand are found as follows.
Clay= 30%
Silt = 60% - 30% = 30%
Sand= 100% - 60% = 40%

On the textural chart, this soil is in the region of clay loam (small circle in Fig. 1.7).

Problem 1.2. A mechanical analysis is performed on approximately 1000 g of a pulverized soil sample, with the following results. What is the textural class of this soil?

U.S. standard sieve	No. 10	No. 40	No. 200	Pan
Mass of soil retained, g	110	482	148	272

Referring to Fig. 1.6, and using the U.S.D.A. classification system for grain sizes, it can be seen that material retained on, and therefore larger than the openings of the No. 10 sieve, is gravel, and it should be subtracted from the total mass for the purposes of the textural triangle. The total mass to be considered, therefore, is that retained on sieves of smaller openings and the pan at the bottom, as follows.

$$482 + 148 + 272 \text{ g} = 902 \text{ g}$$

Sand particles are those retained on the No. 200 and 40 sieves, and these comprise (482 + 148)/902 = 68.5% of the total mass.

Referring now to the textural triangle in Fig. 1.7, the soil is classed either as a sandy loam or a sandy clay loam. If there is less than 20% clay in the 902 g total, the soil is the former, and if there is more than 20% it is the latter. A hydrometer or pipette analysis could then be performed on the material finer than the No. 200 sieve in order to determine this distinction.

Another form of classification is the unified soil classification developed by the U.S. Bureau of Reclamation and Corps of Engineers (Wagner, 1957) which is shown in part in Table 1.1. It is an effort to classify soils on the basis of engineering properties, and has provided useful guidelines in that

respect over the years.

Whether a soil is well graded or poorly graded depends on the variety of different grain sizes contained in the material. One measure of gradation is called the 'uniformity coefficient', U, where;

$$U = D_{60}/D_{10} \tag{1.1}$$

In the expression above, D_{60} and D_{10} are the grain sizes below which 60% and 10%, respectively, of the soil mass is finer. A well graded soil is considered one in which U is greater than 4 for most soils, and 6 for sands.

TABLE 1.1. A summary of the unified soil classification system and the important engineering soil properties.

Name of group	Symbols	Important properties			
		Compacted permeability	Compacted strength	Compressibility	Workability
Well graded gravels.	GW	pervious	excellent	negligible	exec.
Poorly graded gravels.	GP	high	good	negligible	good
Silty gravels.	GM	fair to poor	good	negligible	good
Clayey gravels.	GC	impervious	low	very low	good
Well graded sands.	SW	pervious	excellent	negligible	exec.
Poorly graded sands	SP	pervious	good	very low	fair
Silty sands.	SM	fair to poor	good	low	fair
Clayey sands.	SC	impervious	fair-good	low	good
Inorganic silts.	ML	fair to poor	fair	medium	fair
Inorganic clays of low plasticity.	CL	impervious	fair	medium	fair to good
Organic silts.	OL	fair to poor	poor	medium	fair
Inorganic silts, elastic.	MH	fair to poor	fair-poor	high	poor
Plastic clays.	CH	impervious	poor	high	poor
Organic clays.	OH	impervious	poor	high	poor

The plasticity of soils is another property which can be used as a classification criterion. The plasticity index is defined as the water content range over which a soil is judged to be in a 'plastic' state. The measurement of plasticity index is achieved by two separate tests on a soil, one to measure the lower plastic limit (often called the plastic limit, PL) and the other to measure the upper, or liquid limit, LL. These two water contents are referred to as the Atterberg limits after Atterberg (1911), and were developed further

by Casagrande (1948). The plastic limit is the water content of soil which begins to show cracking when rolled down to a 3 mm diameter cylinder on a glass plate. The liquid limit is measured in a small steel bowl which is dropped repeatedly from a standard height. When a standard width and shape of groove is closed in a layer of soil after 25 blows in the device, the soil is judged to be at the liquid limit. The plasticity index, PI, is then;

$$PI = LL - PL \tag{1.2}$$

While the plastic and liquid limits may appear to have been chosen arbitrarily for soils, they at least comprise tests with repeatable results, and can serve to characterize soils as to their water holding capacity before becoming liquid in behavior. Fine grained soils with high plasticity indices have a relatively larger water holding capacity (such as montmorillonite which, in pure clay form, has a plasticity index of approximately 700%), while those with generally less active surface area, such as kaolinite, have a PI as low as 35%. For the purposes of the unified soil classification system, a fine grained soil is considered highly plastic if the plasticity index is greater than 50%, and of low plasticity if the PI is less than 40%.

1.3. SOIL PHASES

As was noted earlier, soils are mixtures of solid particles, water and solutes and air. There are several definitions which are usually employed to denote the relative volumes of these phases, together with their ratios, densities and the like.

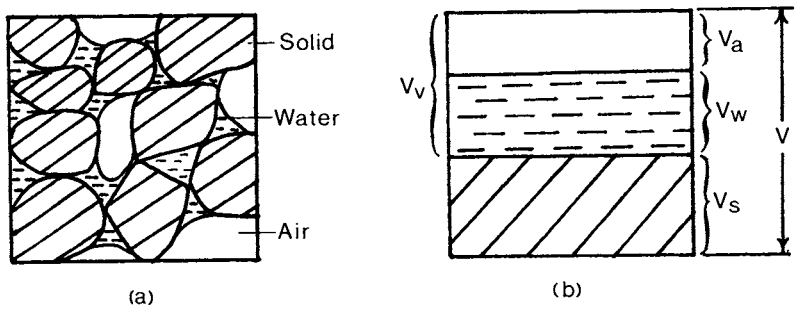

Fig. 1.9. Different phases in soils; (a) schematic of physical soil phases, (b) relative volumes of the soil phases.

In Fig. 1.9, the symbols used are defined as follows.

V = the total volume of soil
V_S = the volume of all solid particles
V_V = the volume of voids, including water and air = $V - V_s = V_a + V_w$
V_W = the volume of water (with solutes)
V_a = the volume of air and other gases

Some of the common definitions of relationships among the soil phases are given below. The various densities, γ, are weight per unit volume.

$$\text{Void ratio } e = V_v/V_s \tag{1.3}$$

$$\text{Porosity } \eta = V_v/V \tag{1.4}$$

$$\text{Degree of saturation } S = (V_w/V_v) \times 100\% \tag{1.5}$$

$$\text{Weight of water } W_w = \gamma_w V_w \tag{1.6}$$

$$\text{Specific gravity of solids } G_s = \gamma_s/\gamma_w \tag{1.7}$$

$$\text{Weight of solids } W_s = \gamma_s V_s = \gamma_w G_s V_s \tag{1.8}$$

$$\text{Total soil weight density } \gamma = (W_s + W_w)/V = (1+w)W_s/V \tag{1.9}$$

$$\text{Water content by weight } w = (W_w/W_s) \times 100\% \tag{1.10}$$

$$\text{Volumetric water content } \theta = (V_w/V) \times 100\% \tag{1.11}$$

$$\text{Soil dry density } \gamma_{dry} = W_s/V = \gamma/(1+w) \tag{1.12}$$

$$\text{Saturated buoyant density } \gamma_{buoy} = \gamma - \gamma_w = \gamma_{dry}(G_s-1)/G_s \tag{1.13}$$

1.4. PROBLEMS

1.3. A mechanical and hydrometer analysis of a soil gives the following masses retained on various sieve sizes. Classify the soil by (a) the textural triangular and (b) the unified system.

U.S. standard sieve size	No. 10	No. 40	No. 200	Pan
Mass retained, g	157	330	351	201 (40% clay)

Answer: (a) Sandy loam (b) SW.

1.4. Plastic and liquid limit determination tests are conducted on five samples each of a clayey soil, with the results shown below. The masses given are of each soil sample in a drying can immediately after each test, the combined mass after drying in an oven at 105C for 24 h and the empty mass of each drying can. Find the plastic limit, liquid limit and plasticity index of the soil, and its classification in the unified system.

Plastic limit test No.	1	2	3	4	5
Mass of can plus wet soil, g	30.96	29.56	30.46	29.19	28.22
Mass of can plus dry soil, g	28.84	27.76	28.37	27.42	26.66
Mass of drying can, g	19.94	20.22	19.78	20.06	20.15
Liquid limit test No.	1	2	3	4	5
Number of blows	21	23	26	28	30
Mass of can plus wet soil, g	85.67	96.79	93.18	83.32	92.27
Mass of can plus dry soil, g	58.30	64.42	61.67	56.20	60.13
Mass of drying can, g	20.34	20.80	19.93	21.02	19.85

Answer: PL = 24.0%, LL = 75.3%, PI = 51.3, CH.

1.5. A soil has a void ratio of 0.90, saturation 50% and specific gravity of solids 2.65. Calculate the total and dry densities.

Answer: $\gamma = 16.0$ kN/m^3, $\gamma_{dry} = 13.6$ kN/m^3.

1.6. A soil has a solids specific gravity of 2.60. Calculate the dry density if the water content of the soil is 35% and the degree of saturation is (a) 100% and (b) 80%.

Answer: (a) $\gamma_{dry} = 18.9$ kN/m^3, (b) $\gamma_{dry} = 17.7$ kN/m^3.

1.7. Given a void ratio of 1.02, a solids specific gravity 2.70 and a water content 30%, find the degree of saturation, total density and dry density of a soil.

Answer: S = 79%, $\gamma = 17.0$ kN/m^3, $\gamma_{dry} = 13.1$ kN/m^3.

Chapter 2. Soil Shear Strength

2.1. COULOMB'S LAW OF FRICTION AND COHESION

For many classes of material, only one value of cutting or shear strength needs to be specified in order to design a structure fabricated of that substance. Metals, for example, are formulated and manufactured to a certain specification of tensile strength or maximum shear stress, and one of these quantities suffices to analyze the strength and safety factor of a structural component. If, as an illustration, a particular grade of carbon steel has a tensile yield strength of 300 MPa (and thus a shear yield strength of 150 Mpa) this value will remain unchanged no matter what level of pressure is placed on the shearing surface within the material.

Soils in general do not fall into this category of material. Being composed of mineral particles which do not interact mechanically as do metallic atoms, a unique value of maximum shear stress (or shear strength) cannot be given. Coulomb (1776) provided the first comprehensive description of soil shear strength. He stated that the limit of shear resistance is composed of two components, namely cohesion and friction. Cohesion is that part of resistance which can be measured by the direct rupture of two parts of a body in tension. In other words, that is the component of shear strength which does not depend on perpendicular pressure on the rupture surface in the material. Coulomb measured values of cohesion by destructive tensile tests on quarry rock from the Bordeaux, France area as depicted in his figure 1 (Fig. 2.1) as well as on bricks of different ages.

Friction, on the other hand, is a process wherein shear resistance depends upon the perpendicular pressure on the sliding surface. Coulomb cited his countryman Amontons for proof that many materials demonstrate a linear frictional behavior, that is to say shear resistance is proportional to normal pressure on a particular plane within a material body. Coulomb used figure 5 in Fig. 2.1 to prove that the angle of the shear failure plane in a frictional material is larger than 45 degrees by half the angle of internal friction, as will be demonstrated in other terminology in Section 2.2, whereas the rupture plane is observed at a 45 degree inclination in purely cohesive materials.

Applying these concepts of soil strength to earthwork mechanics, Coulomb calculated curved failure planes in soil behind retaining walls as shown schematically in his figures 7 and 8. These shapes will be developed in Chapter 4 using a more exact mathematical approach, but yielding much the same results as those of Coulomb over 210 years ago.

In modern strength of materials terminology, Coulomb's law of soil shear strength can be expressed as follows, (see Fig. 2.2).

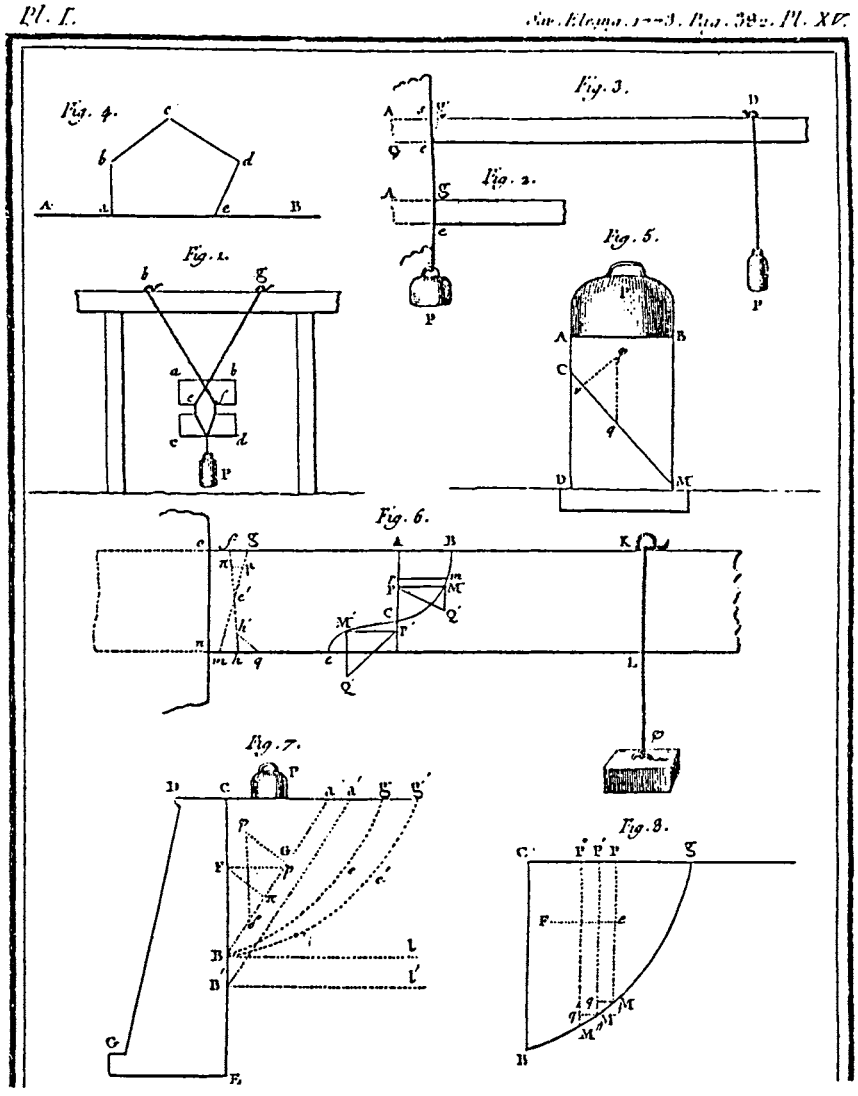

Fig. 2.1. A reproduction of the original illustrations of Coulomb (1776) showing (1) a tensile strength test on white quarry rock, (2 and 3) shear and bending tests on rock beams, (4) the addition of force vectors, (5) a compression test on a masonry pillar and the angle of the failure plane in a frictional material, (6) beam bending stresses and (7 and 8) active soil failure behind a retaining wall with a curved and approximate straight line soil failure surface.

$$s = c + \sigma_n \tan\phi \qquad (2.1)$$

where:

s = soil shear strength (maximum shear stress)
c = cohesion, the part of strength independent of normal pressure
σ_n = normal stress on the sliding plane
ϕ = angle of internal friction of the material.

In Eqn. 2.1, the tangent of the angle of internal friction, $\tan\phi$, is the coefficient of friction commonly used when computing the sliding resistance of one material body over another. In this application, the coefficient is that of frictional strength on an internal surface, and is the constant of proportional increase in shear strength with increasing normal pressure on the surface.

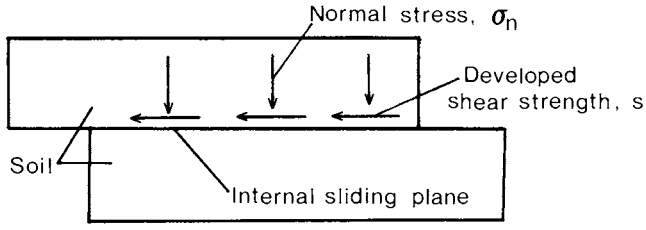

Fig. 2.2. Perpendicular (normal) and parallel (shear) stresses on the internal slip surface of a failing soil block.

In general, soils possess both of these components of shear strength, but there are special cases in which only one or the other is observed. Dry sand, for instance, usually exhibits little or no cohesion, and is designated as a purely frictional material. The angle of internal friction, ϕ, can have a magnitude varying from 18 to 55 degrees (Proctor, 1948), depending on the density of the sand and the properties of its constituent particles. Undrained saturated fine grained soils, on the other hand, demonstrate negligible friction and have a practically constant shear strength regardless of normal total pressure on the failure plane. The shear strength can range from nearly zero, for very wet and loosely consolidated soil, to over 280 kPa for a highly consolidated fine grained soil. Tables 2.1 and 2.2 give typical values of angles

TABLE 2.1. Relative density and angle of internal friction of frictional granular soils (from Teng, 1962).

Compactness	Very loose	Loose	Medium	Dense	Very dense
Relative density, %	0-15	15-35	35-65	65-85	85-100
Standard penetration resistance, blows/ft	0-4	4-10	10-30	30-50	50
Friction angle[1], ϕ^{o}	25-28	28-30	30-36	36-41	41-48
Unit mass, t/m^3					
Moist	1.5	1.8	1.9	2.1	2.1
Submerged	0.9	0.95	1.05	1.2	1.2

[1]Increase five degrees for soils containing less than 5% fines.

TABLE 2.2. Undrained shear strength of cohesive soils (Teng, 1962).

Consistency	Very soft	Soft	Medium	Stiff	Very stiff	Hard
Undrained shear strength, kPa	0-25	25-50	50-100	100-200	200-400	400
Standard penetration resistance, blows/ft	0	2	4	8	16	32
Unit wet mass, t/m^3	1.6	1.7	1.9	2.0	2.1	2.2

of internal friction and undrained shear strength for frictional and cohesional soils, respectively, over a range of density of particle packing.

Other soils which contain mixtures of coarse and fine materials, and which are partially saturated with water, will possess both frictional and cohesive ultimate shear strength properties, and Eqn. 2.1 should be used to calculate total shear resistance to sliding. Appendix 6 presents values of cohesion and friction angle for selected soils at varying moisture contents. Values of strength parameters can be taken from Appendix 6 for a soil which is similar to one of those listed. If, however, there is doubt whether a particular soil can be compared to one of those in the Appendix, then shear strength tests should be conducted on the material in the laboratory or field (Section 2.6 or

2.7).

With the knowledge of the cohesional and frictional strength parameters of a soil, Eqn. 2.1 can be used directly to find the ultimate force on a plane of a given area in a soil, if it is known that that plane is the failure surface. One such simple example is the failure surface beneath a driven lugged tire of a vehicle. At the maximum tire traction force, slip will occur in the soil on a horizontal plane beneath the tire. If the tire lugs have penetrated the soil surface, then the failure plane will be essentially a soil to soil interface, between the material trapped in the spaces between lugs and the soil beneath.

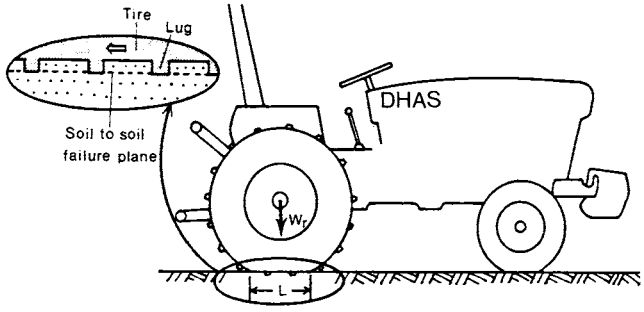

Fig. 2.3. The failure plane in soil under a tractor tire at the maximum traction force application.

Problem 2.1. Fig. 2.3 shows a two wheel drive tractor which has a mass of 4000 kg, of which 75% rests on the rear wheels. The rear driving tires are of size 16.9-28 with a loaded width of 43.2 cm and a contact length, L, of 66 cm on a particular soil. The soil in question has strength properties c=30 kPa and $\phi = 25^{o}$. What is the maximum possible horizontal traction force, H_m of the tractor on this soil, if it assumed that the weight balance between front and rear remains the same, and that complete soil to soil failure is caused by the lugs on the rear tires.

In this example, it is possible to work with normal and shear pressures, but it is perhaps simpler to multiply Eqn. 2.1 by the contact area, A_r, of the rear tires in order to produce an equation of forces. It is assumed that the average normal vertical tire contact pressure, σ_n, multiplied by the total contact area, A_r, of both rear tires, gives the portion of the tractor weight, W_r, which rests on the rear wheels.

$$H_m = sA_r = cA_r + \sigma_n A_r \tan\phi = cA_r + W_r \tan\phi$$

In this case, the cohesion and angle of internal friction of the soil are known, the contact area of the rear tires is the loaded width of each

multiplied by the contact length on the ground, times two tires, and the weight on the rear wheels is 75% of the total tractor weight.

$$H_m = 30 \text{ kPax}0.432 \text{ mx}0.66 \text{ mx}2 + 0.75\text{x}4\text{x}9.8 \tan 25^o \text{ kN}$$

$$= (17.1 + 13.7) \text{ kN} = \underline{30.8 \text{ kN}}$$

At a flat boundary between a soil and another material, such as wood, concrete, steel or rubber, the shear strength is generally less than the internal soil strength, and different parameters must be used. Eqn. 2.2 with its different parameters, adhesion c_a, and boundary surface angle of friction, δ, is then employed to calculate sliding resistance between the two bodies. Adhesion and surface angle of friction play the same roles on an interface as do cohesion and angle of internal friction on planes within the soil material.

$$s = c_a + \sigma_n \tan \delta \qquad (2.2)$$

Appendix 6 gives typical values of these two boundary strength parameters for some of the soils listed therein, which again can be used as rule of thumb estimates when there is a lack of information more specific to a particular design or analysis case.

2.2. THE MOHR CIRCLE OF STRESSES AT A POINT

Eqn. 2.1 of the previous Section allows the calculation of ultimate shear strength on an internal plane of a soil if the normal stress or pressure acting on that plane is known beforehand. However, it is often the case that some stresses are known to be acting on certain surfaces of a soil body which are not coincident with the failure or sliding planes. In such cases it is necessary to be able to calculate stresses on surfaces of different orientations or angles to the horizontal in a soil body. Mohr (1914) showed how this can be accomplished in any solid material so long as equilibrium (no accelerations) can be maintained at all points in the body considered.

One way of developing Mohr's idea is given below. One begins with the two mutually perpendicular planes in a material under mechanical loading which have the highest and lowest normal stresses, respectively. These are known as the 'principal' planes and, as will be demonstrated, they have no shear stress acting on them. In general, all planes at other angles to the principal planes do have some positive or negative shear stress acting on them. In Fig. 2.4, two principal planes are shown with compressive pressures, σ_1 and σ_3 applied to them. The convention for soil mechanics is that compressive normal stresses are considered as algebraically positive, since pressures are nearly always compressive in earthworks. In addition, shear stress is conventionally positive if it acts in a counterclockwise sense on an element

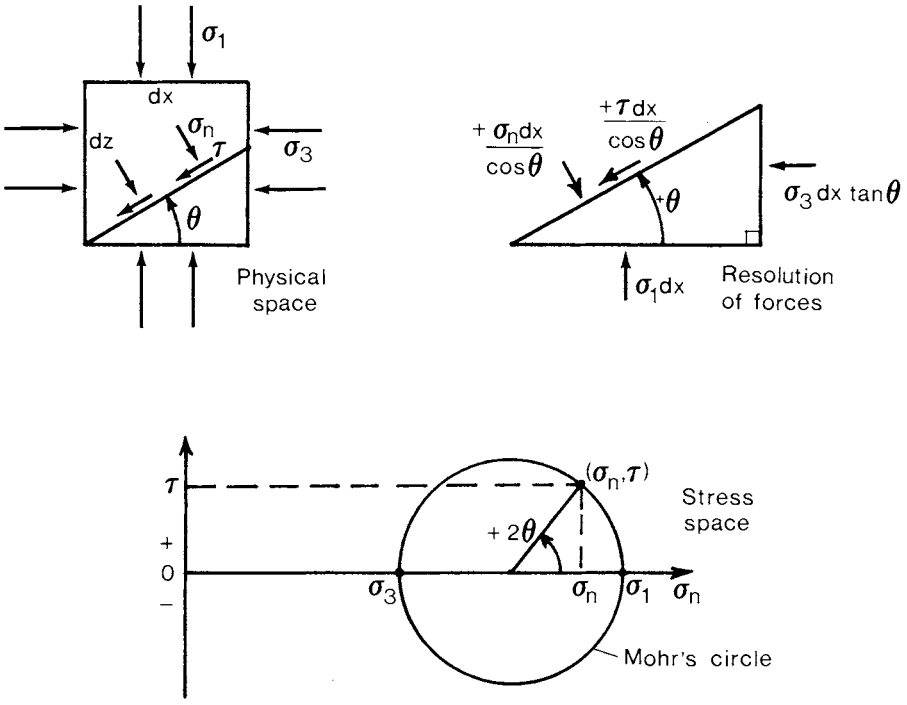

Fig. 2.4. Stresses at a point. Equilibrium of a material element and Mohr's circle of stresses.

of material. This convention is for convenience in rendering the relative angles of different planes in the material the same direction as angles between points for those planes on Mohr's circle of stresses, as will be seen below.

Beginning with the compressive stress levels on the two principal planes, the calculation of normal and shear stresses on any other plane at an angle of θ to the σ_1 plane is carried out by considering a triangular free body of material bounded by the principal planes and the plane at angle θ. The free body has a length of one, and differential width and height, dx and dz. Equilibrium is then imposed on the body which means that the net force on the body in any direction must equal zero. It is convenient to choose directions perpendicular and parallel to the plane of unknown stresses for these force summations, and the results are shown below in Eqn. 2.3 to 2.4.

Perpendicular to the plane at angle θ:

$$\sigma_n dx/\cos\theta - \sigma_3 dx\tan\theta \sin\theta - \sigma_1 dx\cos\theta = 0$$

Parallel to the plane:

$$\tau\, dx/\cos\theta + \sigma_3 dx\tan\theta \cos\theta - \sigma_1 dx\sin\theta = 0$$

$$\sigma_n = \sigma_1\cos^2\theta + \sigma_3\sin^2\theta = \frac{\sigma_1 + \sigma_3}{2} + \left\{\frac{\sigma_1 - \sigma_3}{2}\right\}\cos 2\theta \qquad (2.3)$$

$$\tau = (\sigma_1 - \sigma_3)\sin\theta\cos\theta = \left\{\frac{\sigma_1 - \sigma_3}{2}\right\}\sin 2\theta \qquad (2.4)$$

Eqn. 2.3 and 2.4 together happen to describe the shape of a circle if plotted on a graph of shear stress, τ, versus normal stress, σ_n, to the same scale. Fig. 2.4 shows this circle in τ-σ_n stress space, and indicates that each point on the circle corresponds to the combination of normal and shear stress on a particular plane in the material body. The angle of the point on the circle measured from the major principal stress, σ_1, is twice the angle θ of the actual plane which experiences these two stresses measured from the σ_1 plane in physical space. The two principal planes are not always horizontally and vertically oriented as they are in Fig. 2.4. Furthermore, they are not always the planes upon which stresses are initially known.

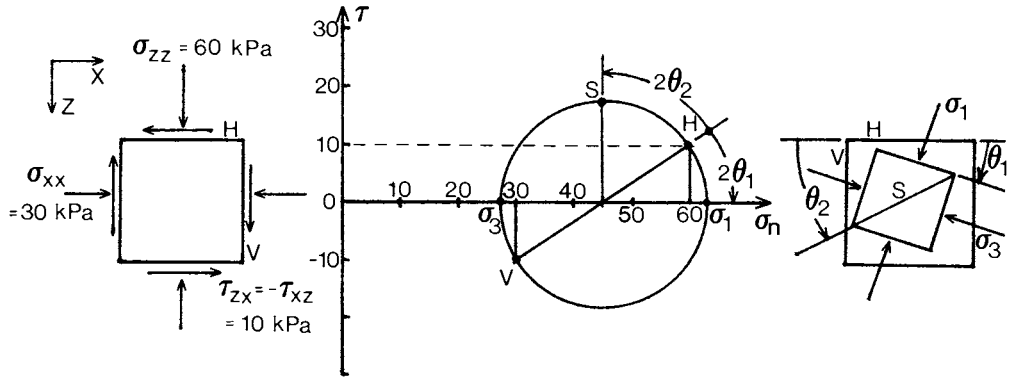

Fig. 2.5. An example of a normal and shear stress combination at a point for Problem 2.2.

Problem 2.2. An example is given in Fig. 2.5 wherein normal stresses σ_{zz} and σ_{xx} are known acting on the H and V planes perpendicular to the z and x directions in space, respectively, as well as the shear stresses $\tau_{zx} = -\tau_{xz}$. The particular Mohr's circle of stresses for this point can be constructed from the stress combinations on these two mutually perpendicular planes as shown in Fig. 2.5. The centre of the circle can be calculated as;

$$(\sigma_{xx} + \sigma_{zz})/2 = (\sigma_1 + \sigma_3)/2 = (60 + 30)/2 \text{ kPa} = 45 \text{ kPa}$$

and the radius as;

$$\sqrt{\left\{(\sigma_{xx} - \sigma_{zz})/2\right\}^2 + \tau_{xz}^2} = \sqrt{\left\{(60 - 30)/2\right\}^2 + 10^2} \text{ kPa} = 18.03 \text{ kPa}$$

Then the principal stresses are equal to the normal stress at the centre of Mohr's circle plus or minus the radius as follows.

$$\begin{Bmatrix}\sigma_1\\ \sigma_3\end{Bmatrix} = 45 \pm 18.03 \text{ kPa} = \begin{Bmatrix}63.03\\ 26.97\end{Bmatrix} \text{ kPa}$$

In addition, the clockwise angle of the major principal plane, θ_1, from the z plane can be found from the geometry of Mohr's circle as:

$$\tan 2\theta_1 = 2\tau_{zx}/(\sigma_{zz} - \sigma_{xx}) = 20/30; \qquad \theta_1 = 16.85^\circ$$

Angles between stress combinations in Mohr's circle diagram do not always have to be measured from the principal stress points. They are relative angles between points on the circle, and are equal to twice the angle between planes in physical space having the corresponding normal and shear stress combinations acting on them. As an example in Fig. 2.5, a point S is identified on Mohr's circle which is the point of maximum positive shear stress (the top of the circle) acting on any plane at any inclination in the material. This point S is located at a relative angle $2\theta_2$ counterclockwise from the horizontal H normal and shear stresses (60,10) kPa. Thus the physical plane S which supports the most positive (counterclockwise) shear stress in the body is located at angle θ_2 from the H plane as shown in Fig. 2.5. The magnitude of this shear stress is the circle radius, 18.03 kPa, and the angle of its plane from the horizontal can be calculated as follows.

$$2\theta_2 = 90^\circ - 2\theta_1; \qquad \theta_2 = 28.15^\circ$$

Note in Fig. 2.5 that the S point in Mohr's circle is 90° from the σ_1 point, and therefore the S plane in the material body is inclined at 45° relative to the major principal (σ_1) plane in the same direction. Further examples of this nature are provided for the purpose of practice at the end of this Chapter.

2.3. THE MOHR-COULOMB CIRCLE OF STRESSES AT FAILURE

The Mohr method of finding stresses on planes at different inclinations in a material body is especially convenient when one is trying to find the stresses on a failure plane within a soil. If, for example, the principal stresses are known on an element of soil that fails, Mohr's circle can be constructed on the shear-normal stress graph as shown in Fig. 2.6. The maximum shear strength which a soil can exhibit is described by Eqn. 2.1, which can also be plotted on the stress graph, and is shown in Fig. 2.6 as the 'failure criterion' straight line. This line of failure shear and normal stress combinations intersects the shear axis (normal stress equals zero) at the value of cohesion, c, and it has a slope angle ϕ to the horizontal axis.

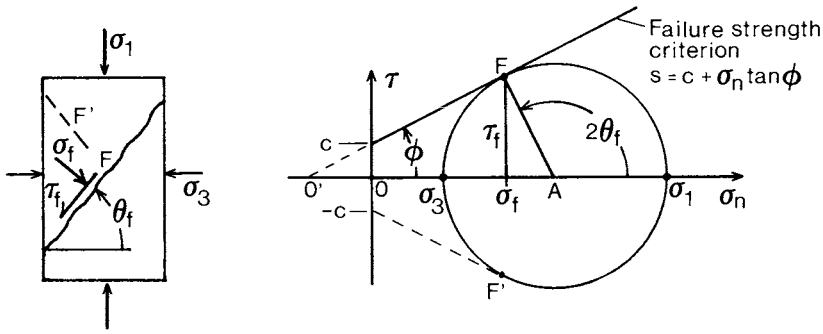

Fig. 2.6. Mohr's circle of stresses at a point in a soil which is failing.

So long as the soil remains in equilibrium while at the same time being in a state of sliding failure, then the stress combination on some plane in the material must meet the failure criterion, and the circle of stresses on all planes must touch the failure criterion line at some point. This point is shown as F in Fig. 2.6, and there is a corresponding second point, identified as F', on the bottom part of the circle. The shear stresses at points F and F' are the same except that one has the negative magnitude of the other. It is not mechanically permitted for each of the internal failure stress lines on the diagram to cut Mohr's circle at more than one point. Otherwise the shear stress on some planes would be greater than the soil strength resisting shear, and extra force would be available to cause mass accelerations in the body. Thus the condition of equilibrium, required for the construction of the Mohr stress diagram, dictates that the circle of stresses be tangent to the failure criterion line at points F and F' when soil failure occurs.

This fact permits the calculation of the shear and normal stresses on the failure plane F, as well as the inclination of the failure plane, and additional information concerning the required ratios of the principal stress values. Because the radius AF to stress point F is perpendicular to the tangent failure criterion line, then triangle FAO' is right angled, and the angle θ_f from the σ_1 plane to the F or F' failure plane can be derived as:

$$2\theta_f = (180^o - \angle FAO) = (90^o + \phi)$$

$$\theta_f = 45^o + \phi/2 \qquad (2.5)$$

It is noteworthy that the angle of the soil internal failure plane is independent of the cohesion portion of strength, and that only the angle of internal friction governs the attitude of the sliding plane. This phenomenon has important consequences for the determination of the shapes of rupture planes behind soil retaining walls, underneath building foundations and the like, as will be seen in following Chapters.

Another consequence of the contact between Mohr's circle of stresses and the failure criterion line in Fig. 2.6 is a prescribed relation between the major and minor principal stresses, σ_1 and σ_3. The radius of Mohr's circle is half of the difference between the principal stresses, and the centre A is located at the average of the magnitudes of the principal stresses, measured from the graph origin, O. The side AO' of the right angled triangle FAO' is the sum of normal stress magnitudes OA and OO'. From these conditions, a relationship between the principal stresses at the failure state can be derived as shown below.

$$OO' = c/\tan\phi = c\ \cot\phi \qquad (2.6)$$

In the right angled triangle AFO';

$$\frac{AF}{AO'} = \sin\phi = \frac{(\sigma_1 - \sigma_3)/2}{(\sigma_1 + \sigma_3)/2 + c\ \cot\phi} \qquad (2.7)$$

$$\sigma_1 - \sigma_3 = (\sigma_1 + \sigma_3)\sin\phi + 2c\ \cos\phi \qquad (2.8)$$

Converting this equation to an explicit expression for the minor principal stress;

$$\sigma_3 = \sigma_1 \left[\frac{1 - \sin\phi}{1 + \sin\phi}\right] - \left[\frac{2c\ \cos\phi}{1 + \sin\phi}\right] = \sigma_1 K_a - 2c\sqrt{K_a} \qquad (2.9)$$

Eqn. 2.9 is known as the Rankine active earthpressure case, and can be applied as is to find the pressure acting on smooth vertical soil retaining walls, as will be seen in Chapter 5. The above derivation shows that it is not

necessary to calculate the actual shear and normal stress on the failure plane in order to know the ratio of the principal stresses for the soil failure condition. In some instances, it is not the principal planes nor the failure plane on which the applied stresses are known, but another set of surfaces having both shear and normal stresses.

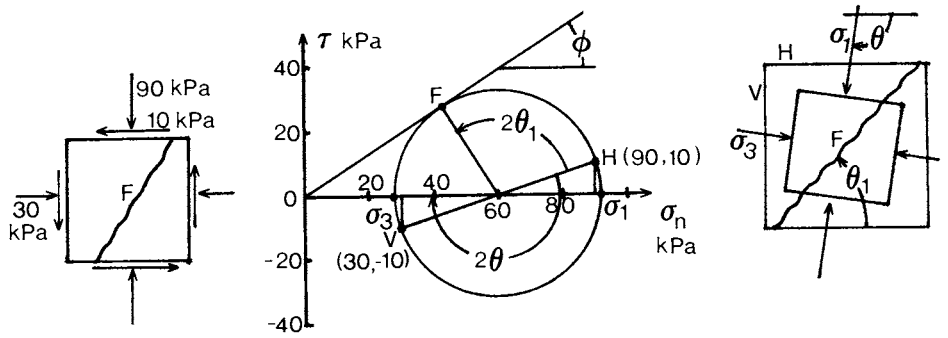

Fig. 2.7. Example 2.3 of the failure condition in a purely frictional soil.

Problem 2.3. The example shown in Fig. 2.7 is such a case in a purely frictional soil. Mohr's circle has been constructed in the figure for the stress condition at this point in the soil, using the known stresses on the H and V planes. From the diagram, the angle of internal friction, ϕ, as well as the inclination of the positive shear failure plane, θ_1, and the attitude, θ, of the major principal stress, σ_1, from the horizontal can be calculated as follows.

$$\begin{Bmatrix}\sigma_1\\ \sigma_3\end{Bmatrix} = \left[(90 + 30)/2 \pm \sqrt{\left\{(90 - 30)/2\right\}^2 + 10^2}\right] \text{kPa} = \begin{Bmatrix}91.6\\ 28.4\end{Bmatrix} \text{kPa}$$

$$\phi = \sin^{-1}\left\{\frac{91.6 - 28.4}{91.6 + 28.4}\right\} = 31.8^\circ$$

$$\theta_1 = \{90^\circ + 31.8^\circ - \tan^{-1}(10/30)\}/2 = 51.7^\circ$$

$$\theta = \{180^\circ + \tan^{-1}(10/30)\}/2 = 99.2^\circ$$

Mohr's circle can be utilized also to find angles and stresses of planes at a boundary between soil and another material. As an illustration, Fig. 2.8 depicts a vertical retaining wall which has a wall to soil friction angle, δ, while the angle of internal friction strength of the soil is ϕ. If the soil fails along the curved line AB shown, sliding will occur simultaneously along the wall surface, W, and on a plane, F, within the soil. In the Mohr diagram of

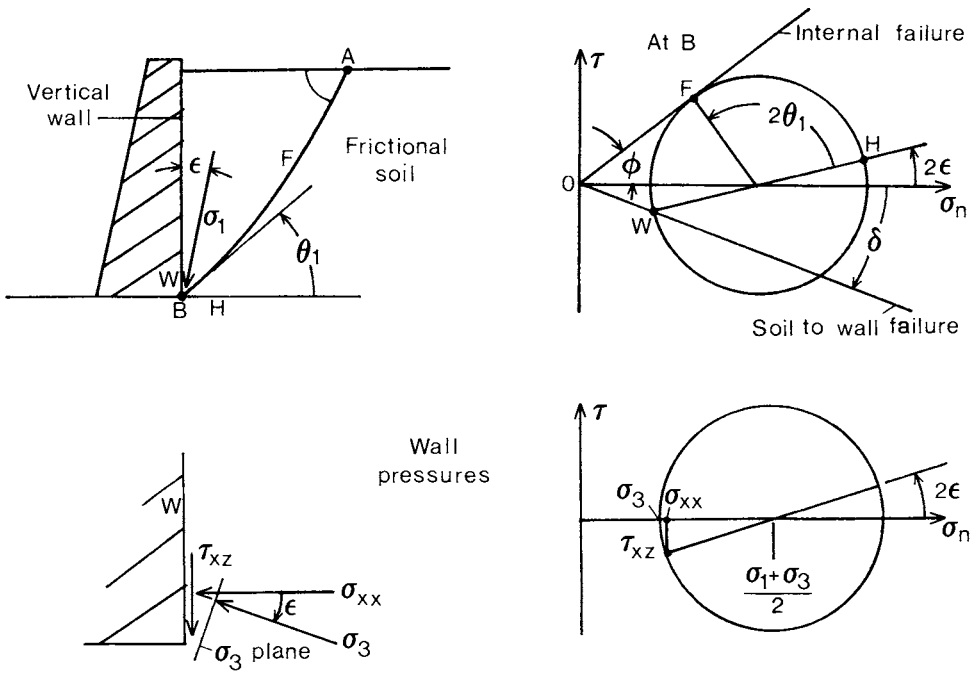

Fig. 2.8. Soil stresses on a retaining wall during active failure.

Fig. 2.8, the stresses on the internal failure surface are indicated as point F, while those on the wall interface are at point W. This latter point is on both the circle of stress combinations acting on all planes in the soil at point B, and the line of wall to soil strength inclined to the normal stress axis at angle $-\delta$. Point W is in the region of negative shear stress because the soil slides downwards along the wall at failure, and the wall exerts a reactive upwards, or clockwise acting shear stress onto the soil. In addition, point W is at the left hand intersection of the wall to soil strength line with the circle of stresses because the soil is presumed to fail downwards in this case, and the smaller normal stress occurs on the vertical plane, with the larger acting on the horizontal plane.

At point B in the soil, the stresses on the horizontal plane are shown as point H on Mohr's circle, which is at an angle 2ϵ from σ_1. When both the

internal and interface strength lines intersect the normal stress axis at the same point, O in Fig. 2.8, the angle ϵ can be calculated as follows from the geometry of the circle.

$$\epsilon = \frac{1}{2}\left[\sin^{-1}\left\{\frac{\sin\delta}{\sin\phi}\right\} - \delta\right] \tag{2.10}$$

And the slope of the soil internal failure plane, as it meets the wall at B can be seen from the stress diagram to be $\theta_1 = 45^o + \phi/2 - \epsilon$. At point A on the soil surface, the major principal stress acts on the horizontal plane because there is no shear there, and the slope of the soil failure plane is $45^o + \phi/2$, as in the Rankine earthpressure case discussed previously. Therefore, when there is a finite angle of wall to soil friction, that is the wall is not perfectly smooth, the above consideration of stresses using the Mohr diagram dictates that the failure line AB behind the wall will be curved, having a smaller slope at the wall bottom than at the top of the soil stratum, as shown in Fig. 2.8.

The actual pressures acting on the wall are only those on the wall plane itself. These are shown in Fig. 2.8 as σ_{xx} and τ_{xz}, perpendicular and parallel, respectively, to the wall surface. σ_3 is shown at the angle ϵ to the wall normal stress, but it does not act on the wall plane, but rather on an internal soil plane at angle ϵ clockwise from the wall surface. The wall pressures can be calculated in the case of soil failure if the centre of Mohr's circle in the stress diagram is known, as shown below. The application of these techniques will be presented in Chapter 5.

$$\sigma_{xx} = \left\{\frac{\sigma_1 + \sigma_3}{2}\right\}\{1 - \sin\phi\cos 2\epsilon\} \tag{2.11}$$

$$\tau_{xz} = \left\{\frac{\sigma_1 + \sigma_3}{2}\right\}\{\sin\phi\sin 2\epsilon\} \tag{2.12}$$

2.4. THE METHOD OF STRESS CHARACTERISTICS

Mohr's stress relationships, combined with the assumption of soil failure, allow the determination of stresses on any desired plane at a point in a soil where some of the stress levels are known. However, in most examples of earthwork design the stress levels vary in the soil body from point to point due to applied loads and gravitational forces. What is needed is a set of relationships which permit the computation of changes in stress levels from place to place within a soil mass. Then Mohr's method can be used at desired points to calculate pressures on different planes.

Fig. 2.9 gives the framework of definitions for the development of equations to determine changes in stresses with distance. Since there are three independent stress variables, σ_{xx}, σ_{zz} and τ_{xz} in the plane stress situation shown, and the equations of plane equilibrium give only two linear equations, in the

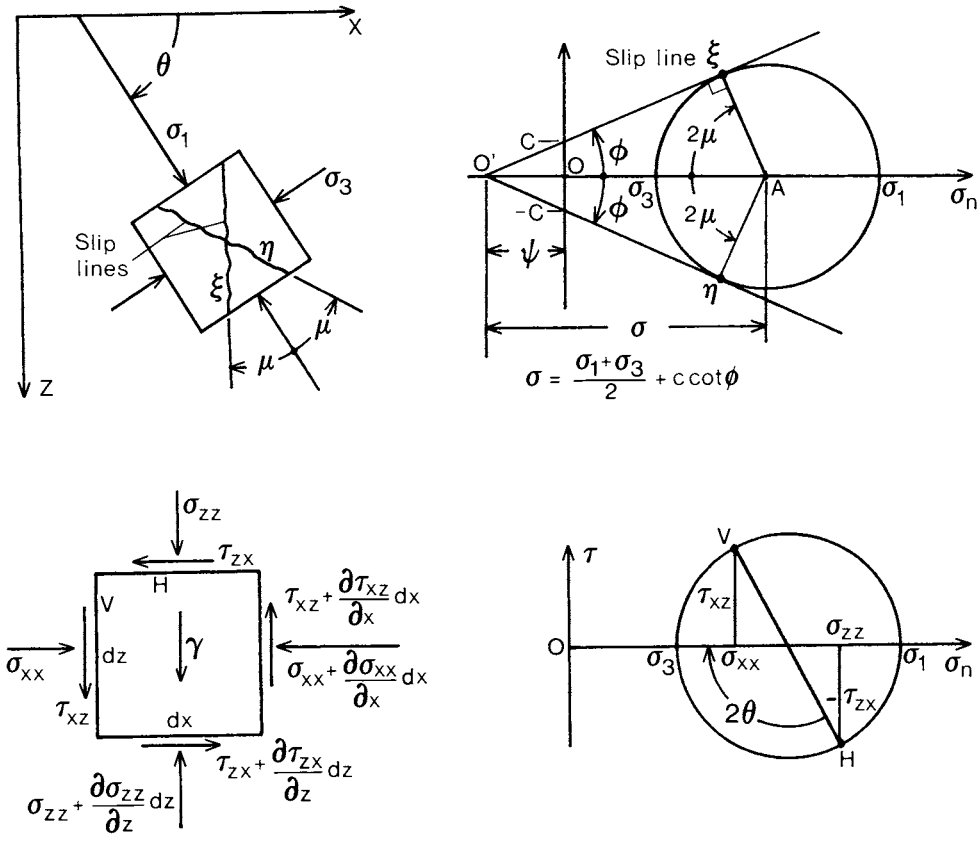

Fig. 2.9. Notation for stress characteristic lines, ξ and η, and the equilibrium of stress gradients at a point.

x and z directions, a third expression is needed to solve for the variations in stresses with position. The assumption for the third equation is that the soil is in a state of shear failure over the soil volume being considered. This state is expressed in terms of stresses by Eqn. 2.1 or 2.9, and also below in Eqn. 2.13 to 2.16 using the newly defined stress variables of Fig. 2.9.

In Fig. 2.9, two new variables are introduced. Stress value σ is the location of the centre of Mohr's circle measured from point O' on the normal stress axis. That is the point where the Coulomb soil failure condition line O'ξ

intersects that axis, and makes σ the hypotenuse of the right angled triangle O'Aξ. The other new variable is angle θ, which is the angle of the major principal stress, σ_1 measured clockwise from the horizontal or x axis. When soil failure has been assumed, these two variables are sufficient to describe completely the stress state at a point, and the principal stresses or stresses on the horizontal and vertical planes in the material can be obtained directly from these variables using the equations below. By employing these two variables, the number of parameters needed to describe the state of stresses at a point has been reduced from three to two, by utilising the assumption of the soil failure condition.

$$\left.\begin{matrix}\sigma_1\\ \sigma_3\end{matrix}\right\} = \sigma(1 \pm \sin\phi) - c\cot\phi = \sigma(1 \pm \sin\phi) - \psi \tag{2.13}$$

$$\sigma_{xx} = \sigma(1 + \sin\phi\cos2\theta) - \psi \tag{2.14}$$

$$\sigma_{zz} = \sigma(1 - \sin\phi\cos2\theta) - \psi \tag{2.15}$$

$$\tau_{xz} = -\tau_{zx} = \sigma\sin\phi\sin2\theta \tag{2.16}$$

Also in Fig. 2.9 is shown an elemental square of soil having sides dx and dz. Applied to this element are the stresses on the vertical and horizontal planes, as well as the possible differential changes which can occur from one side to the other of the element. The changes are shown as partial gradients of the stress levels multiplied by distance, since displacements are considered separately along the x and z directions.

Next, the condition of equilibrium is invoked, as in the Mohr method, along the x and z directions. Forces, not stresses, must be added in each direction to determine the condition of equilibrium, so the stress on each face must be multiplied by the length of the face, and by an assumed unit depth of the elemental volume perpendicular to both the x and z axes.

In the x direction:

$$\sigma_{xx}dz - \sigma_{xx}dz - \frac{\partial\sigma_{xx}}{\partial x}dxdz + \tau_{zx}dx + \frac{\partial\tau_{zx}}{\partial z}dxdz - \tau_{zx}dx = 0$$

$$\frac{\partial\sigma_{xx}}{\partial x} - \frac{\partial\tau_{zx}}{\partial z} = \frac{\partial\sigma_{xx}}{\partial x} + \frac{\partial\tau_{xz}}{\partial z} = 0 \tag{2.17}$$

Similarly, in the z direction:

$$\frac{\partial\sigma_{zz}}{\partial z} + \frac{\partial\tau_{xz}}{\partial x} = \gamma \tag{2.18}$$

These two equilibrium equations are written in terms of the three stress variables acting on vertical and horizontal planes in the soil. At this point, Eqn. 2.14 to 2.16 can be used to substitute the two stress variables, σ and θ, for the three, and result in two partial differential equations in two unknowns.

$$(1+\sin\phi\cos2\theta)\frac{\partial\sigma}{\partial x} + \sin\phi\sin2\theta\frac{\partial\sigma}{\partial z} - 2\sigma\sin\phi(\sin2\theta\frac{\partial\theta}{\partial x}-\cos2\theta\frac{\partial\theta}{\partial z}) = 0 \qquad (2.19)$$

$$\sin\phi\sin2\theta\frac{\partial\sigma}{\partial x} + (1-\sin\phi\cos2\theta)\frac{\partial\sigma}{\partial z} + 2\sigma\sin\phi(\cos2\theta\frac{\partial\theta}{\partial x}+\sin2\theta\frac{\partial\theta}{\partial z}) = \gamma \qquad (2.20)$$

In their present form, Eqn. 2.19 and 2.20 are virtually impossible to integrate over finite x and z displacements because they comprise partial differentials of the stress variables σ and θ. However, Sokolovsky (1956) demonstrated that the two expressions can be rearranged by multiplying them by $\sin(\theta \pm \mu)$ and $-\cos(\theta \pm \mu)$, respectively, with the following result.

$$\frac{\partial\sigma}{\partial x}\cos(\theta\pm\mu) + \frac{\partial\sigma}{\partial z}\sin(\theta\pm\mu) \pm 2\sigma\tan\phi\left[\frac{\partial\theta}{\partial x}\cos(\theta\pm\mu) + \frac{\partial\theta}{\partial z}\sin(\theta\pm\mu)\right]$$

$$= \frac{\gamma}{\cos\phi}\left[\sin\pm\phi\cos(\theta\pm\mu) + \cos\pm\phi\sin(\theta\pm\mu)\right] \qquad (2.21)$$

The two relationships represented by Eqn. 2.21 can now be recognized as expressions of total derivatives of variables σ and θ along certain specific directions in x and z space. The two directions are inclined at angles of $\theta\pm\mu$ to the horizontal x axis. Referring to Fig. 2.9, these directions can be seen to be the same as the soil failure slip lines, ξ and η, respectively. Mathematically, the two directions are known as 'characteristic lines', and in the problem at hand, total differentials of the two stress variables can be defined only along these two orientations in a soil material as follows.

Along ξ slip lines:

$$\frac{dz}{dx} = \tan(\theta + \mu) \qquad (2.22)$$

$$d\sigma + 2\sigma\tan\phi\, d\theta = \gamma(dz + \tan\phi\, dx) \qquad (2.23)$$

Along η slip lines:

$$\frac{dz}{dx} = \tan(\theta - \mu) \qquad (2.24)$$

$$d\sigma - 2\sigma\tan\phi\, d\theta = \gamma(dz - \tan\phi\, dx) \qquad (2.25)$$

In the subsequent chapters, specific applications of the above mathematical technique will be described for the analysis of shallow foundation bearing capacity, lateral pressures on walls, soil cutting and tillage and the like.

2.5. TOTAL AND INTERGRANULAR (EFFECTIVE) STRESSES

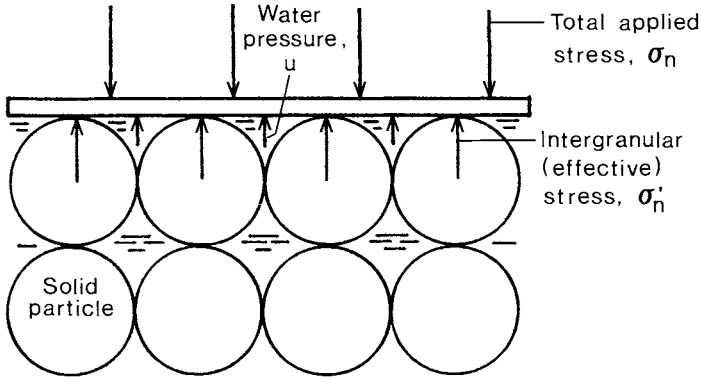

Fig. 2.10. Intergranular (effective) and water pressures in a saturated soil.

When a granular soil has the voids among particles saturated with water, then a pressure can exist in this liquid which, at equilibrium, has an equal magnitude in all directions. For a certain total normal stress level applied to an outside surface of the saturated soil body, the water pressure will support a portion of this total load and will tend to reduce the contact forces among solid soil particles. In such a case, the effective intergranular stress, which is the average sum of individual interparticle forces per unit area, will not equal the total applied stress in the same direction. As shown schematically in Fig. 2.10, the sum of the water pressure within the pore fluid and the effective intergranular stress equals the total stress on a plane surface in the soil, as demonstrated by Terzaghi (1936). The simple mathematical expressions for this result are:

$$\sigma_n = \sigma_n' + u \tag{2.26}$$

or

$$\sigma_n' = \sigma_n - u \tag{2.27}$$

where:

σ_n = total applied normal stress on a plane surface,

σ_n' = effective intergranular stress (average per unit area),

u = pore water pressure, or neutral stress.

If effective normal stresses are used to calculate the soil failure condition, rather than total applied pressure, then the failure parameters, c and ϕ will be different. In fact, if the pore pressure changes in a soil, then the apparent total soil strength will also change, because the forces among, and hence the frictional resistance of soil grains is altered. When water pressure is present in a granular soil, then the effective intergranular stresses should be used if possible, since only then will consistent strength parameters, known as the effective strength constants, c' and ϕ', be observed. Coulomb's soil strength condition can be changed to:

$$s = c' + \sigma_n' \tan \phi' \qquad (2.28)$$

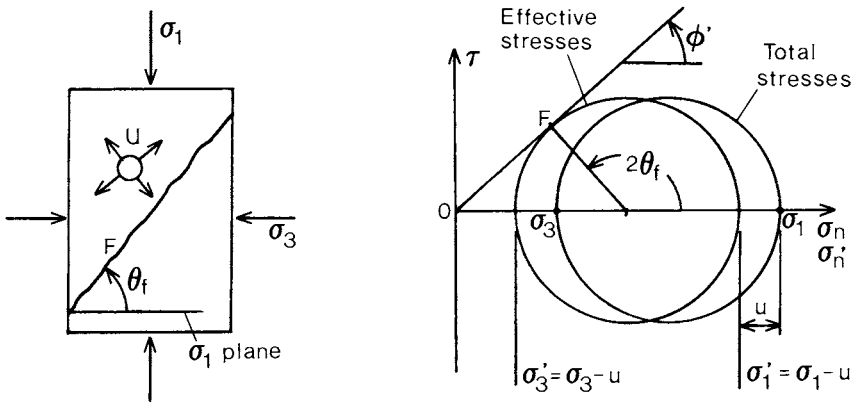

Fig. 2.11. Mohr's circle of stresses for a soil in the failure condition using total and intergranular (effective) stresses.

Fig. 2.11 shows a prism of cohesionless granular soil in a state of failure under applied principal stresses, σ_1 and σ_3, and with pore pressure, u, acting in the pore water. On the accompanying stress diagram, two circles have been drawn, one for the total applied pressures, and the other for calculated effective stresses. When soil cohesion is zero, the effective angle of internal friction, ϕ', is the slope of the tangent from the stress diagram origin to the circle of effective stresses, and the inclination of the failure plane, θ_f, is determined accordingly by substituting ϕ' in Eqn. 2.5.

The situation is not so simple in compressible fine grained soils. So long as such a material is 'normally consolidated', that is compressed from a loose density by the action of the existing normal pressures, then the above effective stress method has been shown to provide predictable results

(Hvorslev, 1937; Bjerrum, 1954; Lambe and Whitman, 1979). However a compressible soil can be in a state of overconsolidation, that is it has been compressed at some time by a larger normal stress than is acting at the present. As water has drained from the soil voids during compression, the soil particles have been forced closer together, and upon release of the pressure to a smaller magnitude, the particles do not rebound to their original density. Because the particles of fine grained soils are very small, the long range electronic forces among them are relatively strong, and they can influence shear strength, as well as can the normal effective stress acting on a plane in the material. Therefore, a compressible soil can have two different strengths even at the same effective confining pressure, depending on whether the soil is 'normally' compressed, or overconsolidated at some previous time.

Hvorslev (1937), as cited in Bjerrum (1954) and Lambe and Whitman (1979), proposed a theory in which fine grained soil strength is a function of both effective normal stress and particle density. For a saturated soil, the particle density is reflected directly by the water content (mass of water in the voids per mass of solids), and the water content can thus be used functionally in place of the particle density. Hvorslev postulated that there can be defined a 'true' effective cohesion and internal friction angle, c'_e and ϕ'_e, which vary with water content, or particle density, for overconsolidated fine grained soils. Fig. 2.12 shows three failure stress criterion lines on a Mohr stress diagram, two of which correspond to overconsolidated soil at water contents w_1 and w_2, and the third of which is used for normally consolidated materials. As the soil particle density increases, and the water content decreases, there are increased interlocking and long range forces among small particles, and the 'true' strength parameters also increase, especially the cohesion term as shown in Fig. 2.12.

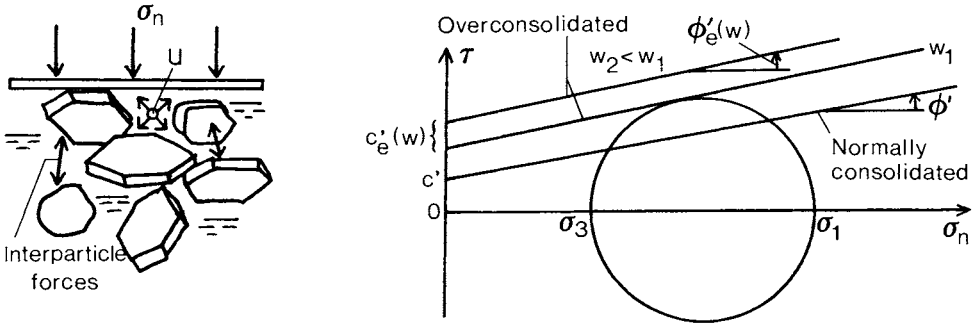

Fig. 2.12. Hvorslev's parameters for soil strength taking into account effective stress and pore water pressure.

The Hvorslev parameters are useful in describing to some extent the role of interparticle forces for compressed fine grained soils, but in soil engineering practice, it is much more practical to use the normal effective strength parameters, c' and ϕ', and to evaluate them for a given soil condition by direct measurement. The applications of pore pressures and effective stresses will be seen in subsequent chapters concerning foundations and wall earthpressures.

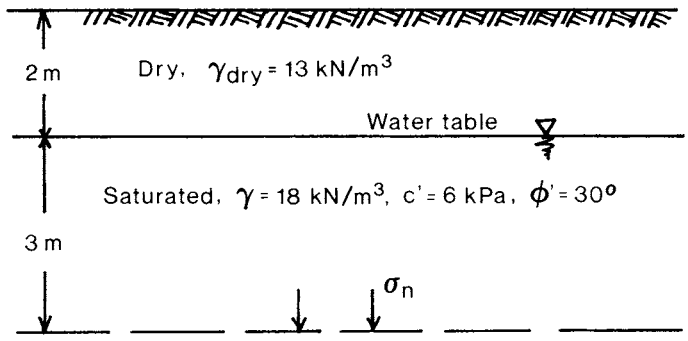

Fig. 2.13. Example of a soil layer with a water table for Problem 2.4.

Problem 2.4. Fig. 2.13 shows a profile of a sandy soil deposit in which the water table is 2 m from the soil surface. What is the shear strength on a horizontal plane at a depth of 5 m?

The effective normal stress must be found on the desired plane by subtracting water pressure, u, from the total stress, following Eqn. 2.27 and 2.28. The total vertical stress is the sum of weight per unit area of soil above the plane in question, or the sum of the total weight densities (mass times gravitational attraction) multiplied by the respective heights of the dry and wet layers. The water pressure is the height of water above the plane times its weight density.

$$\sigma_n = \gamma_{dry} \times 2 \text{ m} + \gamma_{sat} \times 3 \text{ m} = (13 \times 2 + 18 \times 3) \text{ kPa} = 80.0 \text{ kPa}$$

$$u = 9.8 \text{ kN/m}^3 \times 3 \text{ m} = 29.4 \text{ kPa}$$

$$\sigma_n' = \sigma_n - u = (80.0 - 29.4) \text{ kPa} = 50.6 \text{ kPa}$$

Shear strength, $s = c' + \sigma_n' \tan\phi' = (6 + 50.6 \tan 30^\circ) \text{ kPa} = \underline{35.4 \text{ kPa}}$

2.6. LABORATORY METHODS OF SOIL STRENGTH MEASUREMENT

There are rough guidelines for the cohesional and frictional strength properties of typical soils, such as in Table 2.1, 2.2 and Appendix 6. However, there is a great variability among the grain size distributions, mineralogical constitutions, shapes of particles and other compounds in soils, not to mention the change in properties with varying moisture contents. Therefore it is important to measure the mechanical properties of a particular soil if one is to have confidence in any design predictions.

There are two principal classes of soil strength measurement techniques, namely laboratory and field tests. Each of these has its benefits and drawbacks. Laboratory measurements can in general be controlled more carefully, the amount of water draining from the soil is known more precisely and quantities such as forces and deformations can be measured more accurately. From the physical point of view, however, it is difficult to be certain that a soil sample can be removed from its natural location in the field and tested in the laboratory in exactly the same state. Whether the soil is sandy or clayey, there is usually a strong possibility that its density will change, or that some other structural alteration will result from the excavation of a sample and its subsequent transportation to and installation in the laboratory testing device. Thus in many instances, it is impossible to be completely confident that the behavior shown by the laboratory tests measurements will in fact reflect the mechanical performance of the material in reaction to in situ forces.

Added to this is the fact that testing in the laboratory is generally more time consuming and expensive than field mechanical testing. When information is needed quickly, and the level of control and accuracy of a particular test procedure in the field is adequate for the purposes, then the advantages of field tests are evident. If, however, more complete information is needed than can be provided by field devices, then the careful extraction of soil samples and their characterization in laboratory tests are dictated. The details of additional information and control which can be obtained in laboratory devices will be seen within the descriptions of the tests which follow.

2.6.1. The direct shear box.

Schematically represented in Fig. 2.14, the direct shear box is the simplest laboratory device available for the direct measurement of soil cohesive and frictional strength parameters. Soil samples are placed inside two or three concentric round or square rings, which can be moved horizontally relative to each other, and a vertical load, N, is applied. The soil may be allowed to come to a drainage equilibrium under the load N if desired. Then one of the rings is moved relatively to the other(s), usually at a constant speed of one to two mm/s or so, and the required horizontal force, T, measured by mechanical or electronic means.

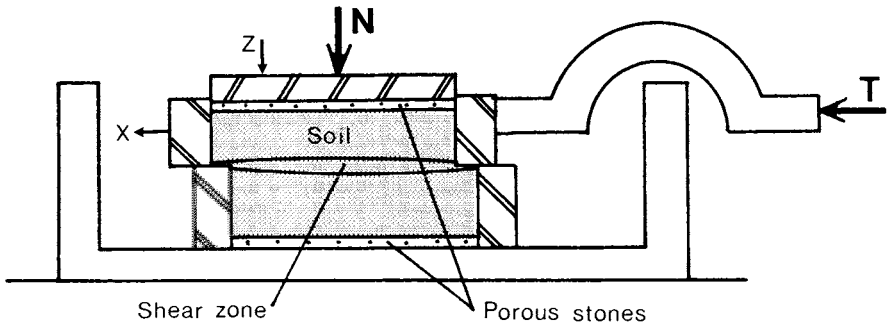

Fig. 2.14. Schematic diagram of a two ring direct shear box for soil strength testing.

As indicated in Fig. 2.14, the entire height of the soil sample does not undergo extensive shearing strain. Rather there is a zone of concentrated deformation of unknown thickness around the separation plane of the rings. During the shear process, the horizontal movement, x, of the ring can be measured and recorded, as well as the vertical movement, z, of the top cap. However, neither of these displacements can be converted to a measurement of strain in the soil because the volume and thickness of the shear zone are not known. Nevertheless, curves of shear force, T, versus increasing shear displacement, x, in the shear zone can be obtained for different vertical loads, N, as illustrated in Fig. 2.15. In fact, these shear force - displacement curves reflect how a soil would behave on a predetermined thin shear zone in the field, such as under a tractor tire as illustrated in Problem 2.1, Section 2.1.

On the force - displacement curve for each vertical load, N, the failure point F is determined, as indicated in Fig. 2.15. This point is the largest shear force, T, or that point where the shear force versus displacement curve increases only slowly along a straight line, depending on the characteristics of the particular direct shear device. In order to estimate the strength parameters of the soil samples tested, the failure shear force values, T, are plotted against the normal loads, N, as shown in Fig. 2.16. The best fit straight line through the points corresponding to individual shear tests has the slope ϕ and intercept cA on the shear force axis, where A is the horizontal cross section area of the shear box rings. The best fit line can be drawn by eye, or the shear and normal force pairs can be summed on a calculator to obtain cA and $\tan\phi$ directly by a least squares linear regression.

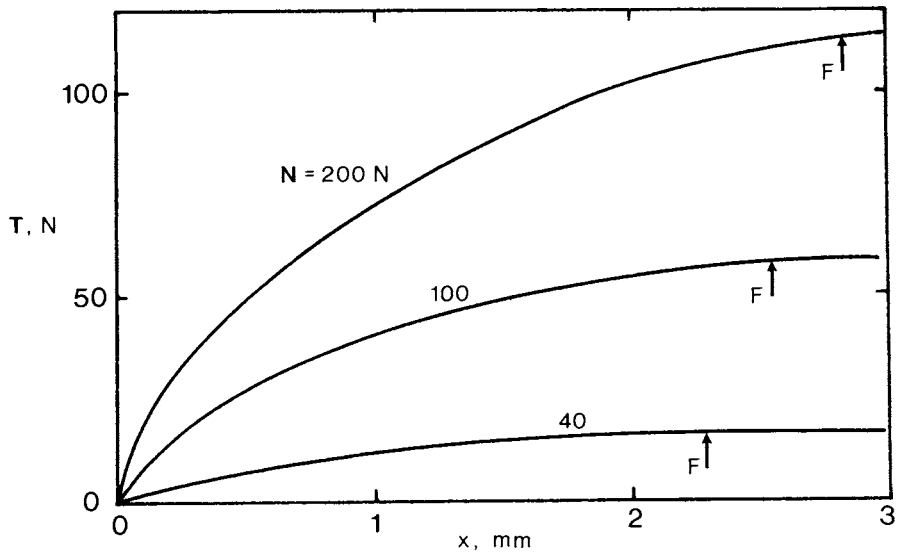

Fig. 2.15. Results of shear force versus horizontal deformation measurements for a sandy soil in a direct shear box.

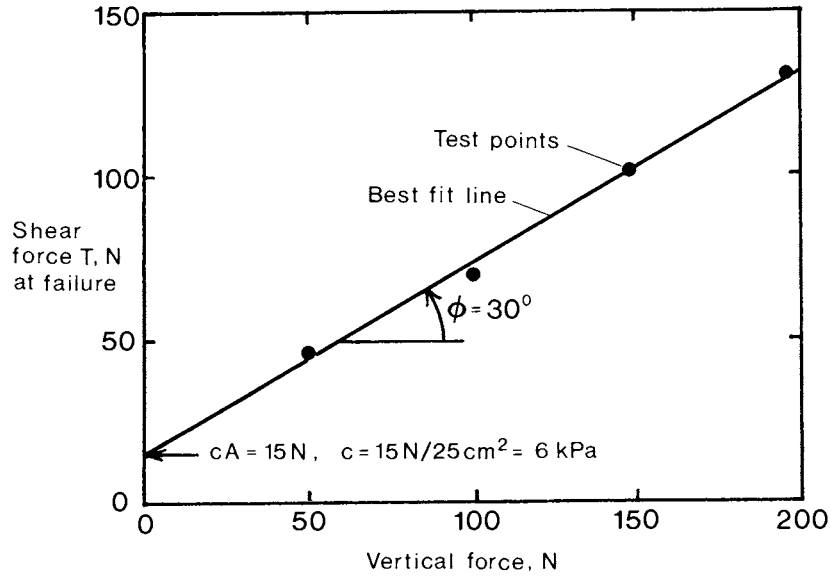

Fig. 2.16 Plotting of soil failure shear force measurements versus vertical loads to find soil cohesion and friction angle parameters.

Either drained or undrained shear strength measurements are possible with this device. If drained tests are desired on a fine grained soil, however, the shearing must be performed at a sufficiently slow speed to allow drainage of excess water pressure from the center of a sample by the time that the failure shear stress is achieved. Depending on the hydraulic conductivity of the soil, this could take up to several days for a fine clay soil, whereas a few seconds of time can often suffice in the case of a coarse sand. When undrained tests are required, the porous stones at the top and bottom of the soil samples can be replaced by impermeable plates, and the shear tests performed quite quickly. There is really no effective way of measuring the pore water pressure, nor its variation with location in the soil sample, so a total stress analysis must be employed in undrained tests.

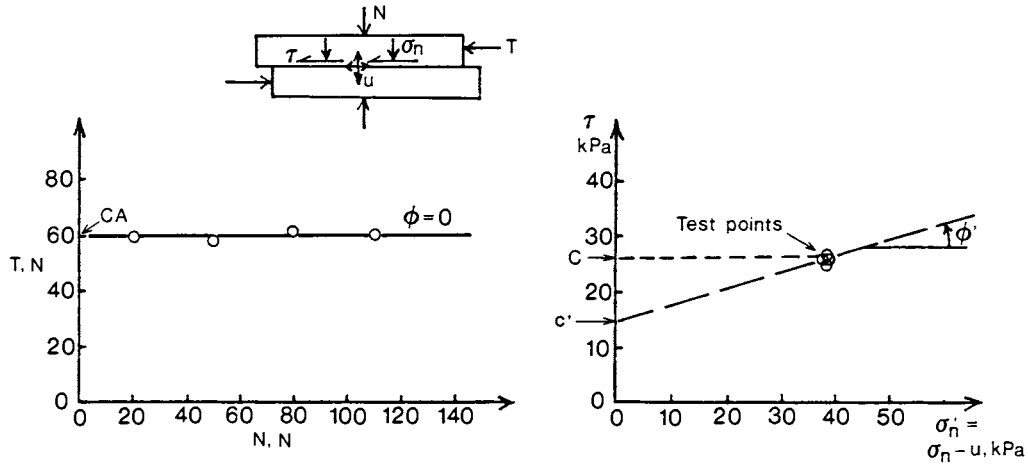

Fig. 2.17. Results of a direct shear test for a saturated undrained soil.

Fig. 2.17 shows typical failure shear force versus varying normal force values for an undrained shear box test series on samples of a saturated clay soil. The force quantities in this plot reflect the total applied stresses on the soil, and the result indicates an apparent zero angle of internal friction. If the pore pressure in each test could be known, it would show that the increase in normal force is balanced by a larger pore water pressure in the soil, and the actual effective normal stress on the soil failure plane is essentially the same in each test. Thus the shear strength is equal for all normal force levels, and is defined as the undrained shear strength, C. This

result can be applied to design cases where the clay soil is at the same effective confining pressure as the test samples, and when it is not allowed to drain significantly during the time period of interest.

The installation of granular soils into the direct shear box is effected simply by pouring them in and vibrating or tamping them to a certain packing density if so desired. Cohesive soils, on the other hand, must first be cut to dimensions very close to those of the inside of the shear box circular or square rings. For most commercially available shear box devices, properly dimesioned cutting rings with sharpened edges are provided for this purpose. Care must be taken, however, to reduce the disturbance to the internal structure of each cohesive soil sample to a minimum during the cutting process. Otherwise, the results of soil strength measurement in the shear tests may not reflect the natural structure of the soil accurately.

2.6.2. The triaxial test.

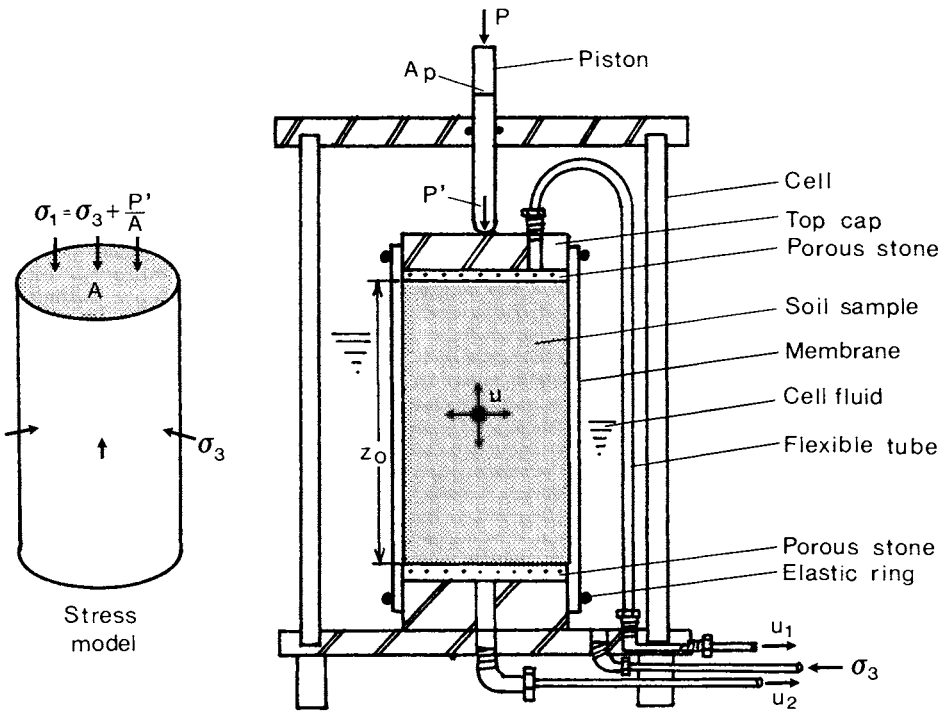

Fig. 2.18. Schematic diagram of the triaxial soil strength testing device.

The triaxial test, illustrated schematically in Fig. 2.18, is considerably more versatile than the direct shear box test in its ability to control soil strains, stress combinations and the drainage or measurement of pore water pressure. Cylindrical samples of any soil type are surrounded by a membrane and confined by the pressure, σ_3, in the cell fluid. The source of this cell pressure can be a liquid column, pressurized gas, mechanical pump or other device. Additional stress (compressive or tensile) is applied to the top of the soil cylinder by a movable piston, and the difference between pressures on the top and side surfaces of the soil cylinder generate shear stresses on different planes as shown in Fig. 2.4 to 2.6. Because the cell pressure acts on the piston from the inside of the cell, the force, P', applied to the top cap is less than P applied externally to the piston, as follows.

$$P' = P - \sigma_3 A_p \tag{2.29}$$

where A_p is the cross sectional area of the piston opening in the cell.

The net force P' is added to the cell confining pressure, and this sum is divided by the cross section area of the soil cylinder in order to calculate the average vertical stress applied to the sample. The area, however, changes during a compression test owing to the shortening and widening of the soil cylinder. If the test is undrained and the soil almost saturated, then the volume change during axial compression will be practically nil, and the area at any point during the test may be calculated by the following formula.

$$A = A_0/(1 - \epsilon_{zz}) \tag{2.30}$$

where

A = the soil cylinder cross section area at any time,
A_0 = the initial area,
ϵ_{zz} = the vertical strain of the soil sample = $\Delta z/z_0$ (compression).

If the soil changes volume during a triaxial test, and the amount of volume change is measured, then the following formula can be applied.

$$A = V/z = (V_0 + \Delta V)/\{z_0(1 - \epsilon_{zz})\} \tag{2.31}$$

where

V = the soil sample volume at failure,
z = the sample height at failure,
V_0 = the initial soil cylinder volume,
ΔV = the change in soil volume from the initial value (expansion),
z_0 = the initial soil cylinder height.

The applied force P may be increased in steps by weights, or the top piston can be displaced at a desired constant speed by a mechanical device. In any event, the force, P, the vertical movement, Δz, of the piston and the change in soil volume, ΔV, can all be monitored during a soil shear test. The porous stone at the bottom of the soil sample, and one possibly at the top as well, allow access to the pore water at the ends of the sample. This access permits either the control of the drainage of pore water before and during shear testing, or the measurement of saturated soil pore water pressure in the undrained case, by a gauge or transducer which allows almost no volume change.

As a result of the flexibility permitted by the triaxial test fixtures, three principal types of stress-strain and strength tests are possible, namely the;

1. Consolidated Drained test (CD), in which the soil sample is allowed to drain completely and come to equilibrium zero pore water pressure before shear testing under the cell confining pressure. Also, pore water is allowed to drain during a slow increase of applied force P. The volume of water exiting can be measured to indicate the soil volume change both before and during shear testing.

2. Consolidated Undrained test (CU), in which the sample is drained to equilibrium under σ_3 before P is applied, but water is not permitted to exit the system when P and shear stresses are imposed in the soil. However, during shear tests, the pore pressure can be measured in saturated soils as mentioned previously. The rate of application of P or vertical strain must be slow enough to allow the pore pressure to be transmitted from the sample center to the external pressure monitoring device at each stage of the shear process.

3. Unconsolidated Undrained test (UU), in which pore water is never allowed to flow from the soil either when the cell pressure or the additional vertical stress is applied. Here again, pore pressure can always be measured.

Fig. 2.18 shows also the stress model which is assumed for the triaxial test configuration. The cell fluid pressure comprises a principal stress on the side of the soil cylinder, and it is assumed that the top and bottom caps also apply normal stress only. From measurements during shear tests, information concerning the vertical compressive or tensile strains and the volume changes of saturated soils as a function of principal stress difference can be obtained. In addition, the principal stresses can be recorded when the sample fails, either with an accompanying visible rupture surface, or by more uniform bulging at the maximum shear stress.

Fig. 2.19 gives an example set of vertical strain ($\epsilon_{zz}=\Delta z/z_o$) versus principal stress difference curves, at different cell confining pressure levels, measured on samples of a particular unsaturated soil. Also, Mohr's circles are

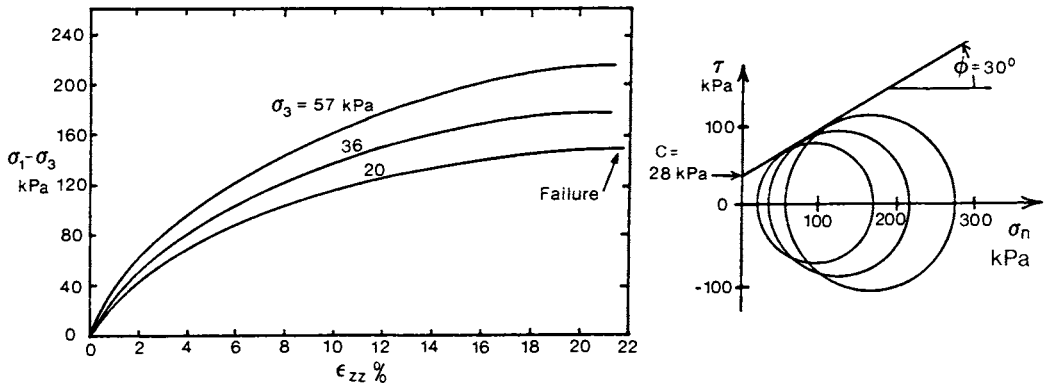

Fig. 2.19. Curves of principal stress difference versus vertical soil strain in a triaxial test for different cell confining pressures, and Mohr's circles of failure stress combinations.

constructed in shear-normal stress space at the point of failure for each test, from which the soil cohesion and angle of internal friction can be estimated. For instance, at the point of failure during the test at 57 kPa confining pressure, the principal stress difference,

$$\sigma_1 - \sigma_3 = 218 \text{ kPa}, \quad \text{and} \quad \sigma_1 = (218 + 57) \text{ kPa} = 275 \text{ kPa}$$

In the analysis of strength from triaxial test results, both consolidated undrained tests and those performed on unsaturated soils can be handled simply by total stress analyses as in Fig. 2.19. When, however, pore pressures are involved and have been measured, then an effective stress treatment should be applied as demonstrated in the example problem below.

Problem 2.5. The table below gives the measured principal stresses and pore pressures for the undrained failure of similar specimens of a saturated clay soil consolidated to different confining pressures (CU tests). Find the effective soil cohesion and angle of internal friction.

Test No.	σ_3, kPa	σ_1, kPa	u, kPa
1	13	78	3
2	70	157	15
3	120	238	28
4	155	302	35

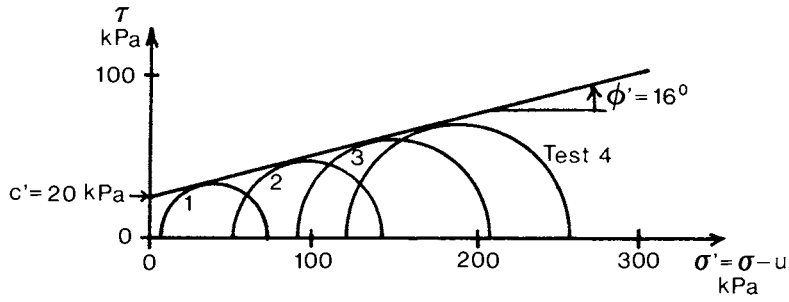

Fig. 2.20. Problem 2.5 construction of Mohr's circles of effective failure stresses to obtain effective cohesion and friction angle.

The pore pressure, u, is subtracted from both principal stresses for each test, and Mohr's circles constructed using these effective or intergranular principal stresses, as illustrated in Fig. 2.20. For example, in test No. 1, σ'_1 = 78 - 3 kPa = 75 kPa and σ'_3 = 13 - 3 kPa = 10 kPa, from which the first circle is drawn in Fig. 2.20. The resulting effective strength parameters are c' = 20 kPa and $\phi' = 16^\circ$.

The estimation of strength parameters from sets of Mohr's circles at soil failure, such as in Fig. 2.20, can be accomplished by graphical means on a large scale graph, and the values of cohesion and friction angle measured. Alternatively, Eqn. 2.32 below, from Eqn. 2.9, can be adapted to an analytical estimation of c and ϕ, or c' and ϕ' for effective stresses, using the total or effective principal stresses at soil failure.

$$\sigma_3 = \sigma_1 K_a - 2c\sqrt{K_a} \tag{2.32}$$

Sets of σ_1 and σ_3 value pairs at soil failure for individual triaxial tests can be used as x and y values, respectively, in a linear regression. The resulting slope is the best fit K_a, either total or effective, from which the friction angle, ϕ or ϕ', can be calculated as shown below, and the regression intercept is $-2c\sqrt{K_a}$ or $-2c'\sqrt{K_a}$.

$$\phi = \sin^{-1}\left[\frac{1 - K_a}{1 + K_a}\right] \tag{2.33}$$

The preparation of soil samples for triaxial tests must be executed carefully for reliable results. Except for granular materials, the same sample cannot really be used for repeated strength tests owing to the irreversible structural damage which can occur to the soil fabric by shearing and failure. This is especially true in sensitive clay soils which suffer reduced shear strength when their structure is disturbed. The only recourse for multiple trixial tests is to obtain several samples of such a soil which are as similar as possible, and as little disturbed from their in situ condition as is feasible.

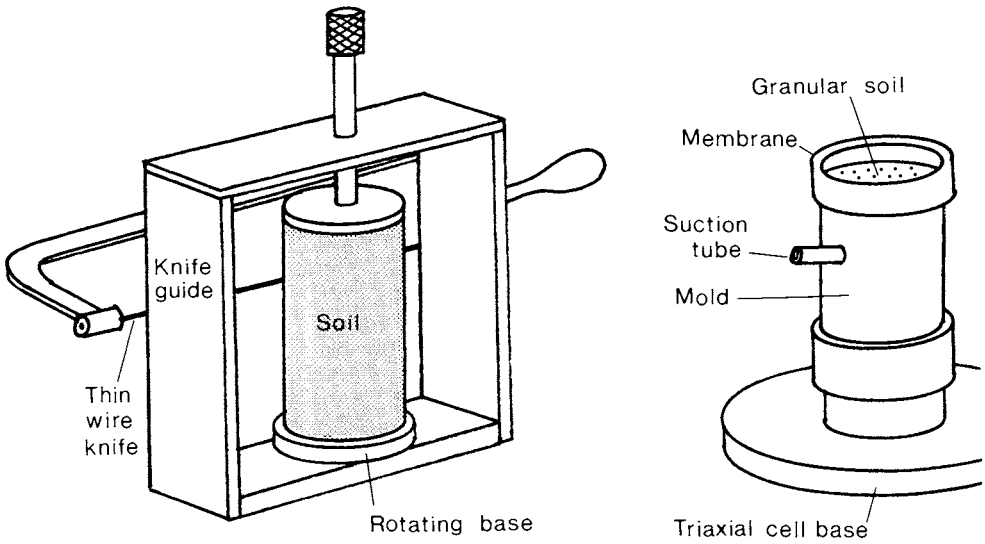

Fig. 2.21. Soil lathe for shaping cylindrical samples of cohesive soil for the triaxial test, and a mold for holding cohesionless samples before a vacuum can be applied internally.

For cohesive soils, the cylindrical test samples can be prepared by cutting their shape on a soil lathe with a thin wire knife, Fig. 2.21, and they will retain their shape during installation in the test machine. Cohesionless soils, however, will not stand up in the cylindrical shape by themselves and require support before the cell confining pressure can be applied. For this purpose, metal molds are available as depicted in Fig. 2.21. The sample's rubber membrane is first placed inside the mold and drawn to the inside surface by means of a small amount of vacuum through the suction tube (mouth power

suffices here). After the mold with membrane is placed on the triaxial cell base, the granular material is deposited in the mold, either loosely or tamped and vibrated to a desired density. The top cap and elastic membrane retaining rings are installed next, and a small vacuum applied to the interior of the soil through one of the pore water access ports of the device. This vacuum will provide sufficient positive effective stress in the granular soil for it to retain its shape until the remainder of the cell components are in place, and the required cell confining pressure has been established.

If so desired at this point, water can be introduced from the bottom pore water access inlet, and the air within the soil expelled through the top access, while still maintaining a small cell confining pressure to support the sample. Subsequently, the cell pressure can be brought to the desired level for a particular test, and shear testing can proceed normally under either drained or undrained conditions with the application of vertical force P.

Problem 2.6. Three consolidated drained triaxial tests are performed on similar saturated clay soil samples from the same site. The initial volume of all samples was 76 cm^3 and the original height was 7.6 cm. The cross sectional area of the piston where it passes through the top of the triaxial cell is 1.25 cm^2. From the measured results below at the point of failure of each sample, find both the total and the effective cohesion and friction angle.

Test No.	1	2	3
σ_3, kPa	200	300	400
P, N	460	655	845
Δz, cm	1.40	1.45	1.40
u, kPa	35	49	65
P', N	435	618	793
A_f, cm^2	12.3	12.4	12.3
$\sigma_1-\sigma_3$, kPa	354	498	645
σ_1, kPa	554	798	1045
σ_1', kPa	519	749	980
σ_3', kPa	165	251	335

c = 19.9 kPa, ϕ = 24.9°, c' = 21.4 kPa, ϕ' = 27.5°

Eqn. 2.29 has been used to find the net force, P', applied to the top cap at soil failure for each of the tests. Then Eqn. 2.30 was used to calculate the average cross section area in each case. Dividing the cylinder area into the net force gives the average principal stress difference at failure. The table above shows these calculations, together with the derivation of effective stresses. Also, the estimation of total and effective strength parameters is done, using linear regressions in the form of Eqn. 2.32.

2.6.3. The consolidation test.

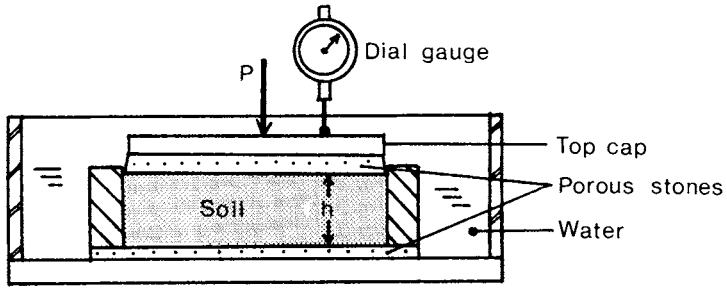

Fig. 2.22. Fixed base consolidation test apparatus, or oedometer.

The theory of consolidation of fine grained soils will be described in Chapter 4. It involves the movement of water in soil as increases in vertical confining pressure cause soil particles to compress closer together. Fig. 2.22 provides a schematic illustration of a typical consolidation test apparatus. A soil cylinder is compressed by force P, and is confined in the horizontal direction in a rigid ring. Measurements are made of the settlement of the top cap, usually by a mechanical dial gauge to an accuracy of 0.002 mm. The settlement measurements fulfil two purposes, firstly to calculate the change in soil volume as force P is increased, and secondly to estimate the time required for the soil to come to an equilibrium volume under each load level.

For the estimation of time to 100% consolidation under each constant load, the settlement readings must be plotted on a semilogarithmic graph versus time during the test. On this plot, of which an example is shown in Fig. 2.23, the primary consolidation appears as a straight line. Near the end of primary consolidation, when the pore water pressures in the soil are decreasing close to zero, the line curves to a smaller rate of settlement until finally it reaches a new straight line slope. This latter period corresponds to secondary consolidation, or creep. At this time the pore water is essentially at zero pressure, but there is still slow movement of soil particles relative to one another.

It is primary consolidation which is the principal process to be quantified in the apparatus. During each of the first constant loads in the test, settlement readings are taken with time and plotted versus the logarithm of time as in Fig. 2.23. Casagrande (1936) described how the intersection of the slopes of the primary and secondary curves on this graph intersect at a point which may be considered the time of 100% primary consolidation. This time is shown as t_{100} in Fig. 2.23 as about 1500 min or 25 h in this example. When

t_{100} has been established during a few trials with increasing loads, P, the plotting of settlement versus time does not need to be repeated for all other loads, because the time remains relatively constant.

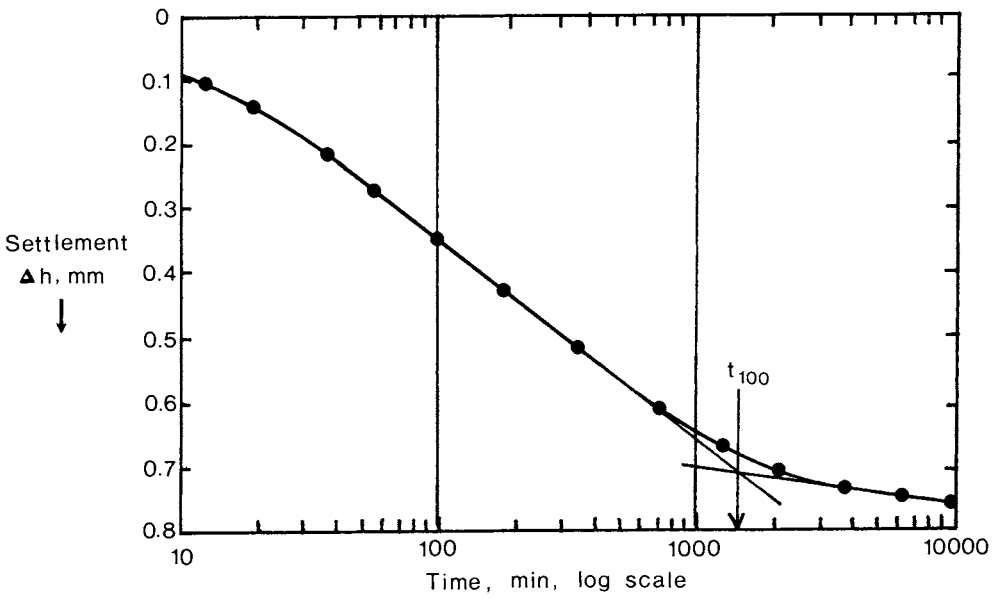

Fig. 2.23. Results of change of soil height in a consolidation test plotted against time on a logarithmic scale.

Conventionally, the volume measurement used for consolidation predictions is the void ratio, e = volume of voids divided by volume of solids. For each new load, P, the average vertical pressure is found by dividing P by the circular soil area. The change in void ratio after 100% consolidation for each load is the net change in sample height divided by one plus the void ratio at the beginning of application of that load. A graph of final void ratio versus the logarithm of pressure is then plotted, as shown in Fig. 2.24. The significance of the slope of the curve will be described in Chapter 4.

It is difficult to know the void ratio of the soil sample at the beginning of the consolidation test, because loading must begin after the sample has come to equilibrium under a very small initial load. The procedure for determining void ratios at the various loads is to quickly remove the sample after the last load, and determine its moisture content by oven drying and weighing. Then, knowing the specific gravity of the solid particles, the final void ratio, e_f, is calculated as follows.

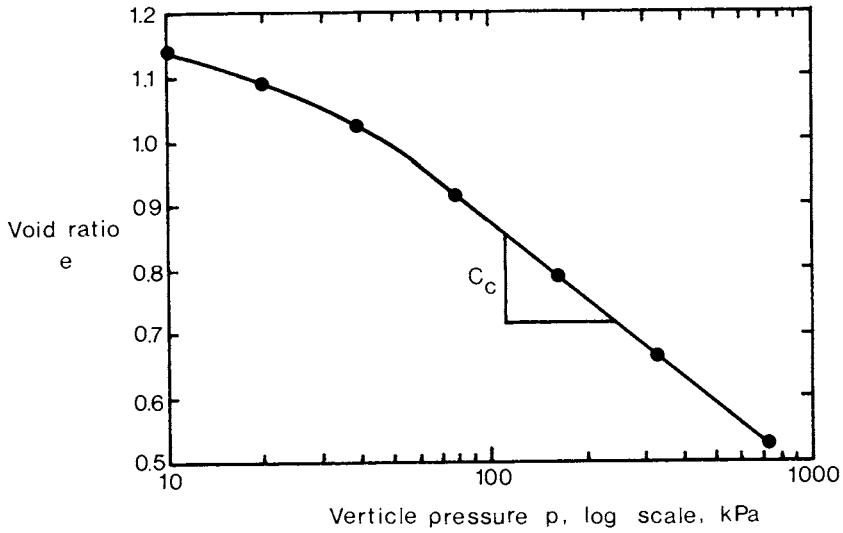

Fig. 2.24. Final consolidated soil void ratio values plotted against vertical pressure on a logarithmic scale.

$$e_f = wG_s \tag{2.34}$$

where e_f = the final void ratio of the soil,
w = the moisture content on a dry weight basis,
G_s = the specific gravity of the solid particles.

Void ratio values for each height, h, of soil sample are then back calculated from the final void ratio, e_f, and final measured height, h_f.

$$e = e_f + \frac{h - h_f}{h_f(1 + e_f)} \tag{2.35}$$

2.6.4. Compaction tests.

In Chapter 10 the theory and practice of soil compaction will be discussed, but compaction tests are included here together with the other soil property measurement techniques. Generally, a compaction test is used either to simulate the field compaction of a soil in earthwork construction, or to characterize a particular soil with respect to its in situ compaction behavior.

In both cases volume change response of an unsaturated soil to loading as a function of varying moisture content is very important. This information is needed to predict the range of soil moisture appropriate for compaction of

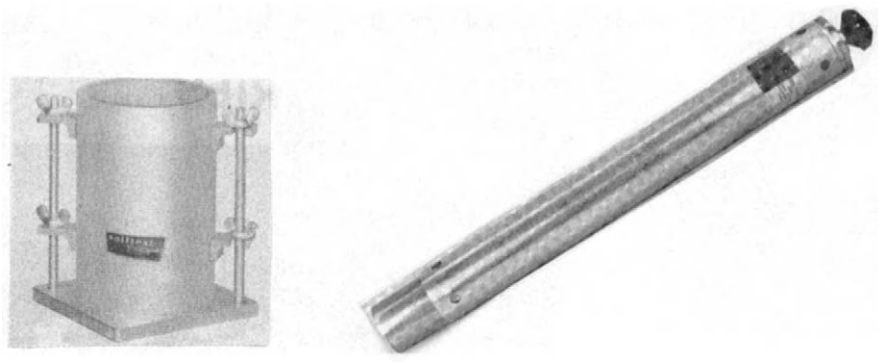

Fig. 2.25. Standard Proctor compaction mold and hammer (Soiltest Inc.).

roads, earthdams, foundation sub-bases and the like, or to recommend suitable field moisture ranges for machinery traffic in agricultural operations.

The most popular compaction test device in North America is the Proctor test in either its standard or modified form (Proctor, 1933; ASTM, 1985). As shown in Fig. 2.25, the Proctor apparatus comprises a compaction mold and a hammer. The mold, when a sample is trimmed to its final dimensions, has a diameter of 4 inches (101.6 mm) and height 4.584 inches (116.4 mm), giving a volume of 1/30 ft^3 or 1/1060 m^3. The hammer for the Standard Proctor test has a mass of 5.5 lb (2.49 kg) and a drop of 12 in (304.8 mm), while the Modified hammer has a mass of 10 lb (4.54 kg) and a drop of 18 in (457.2 mm).

The procedure for this test is to fill the mold, with a collar attached to the top, to approximately one third full, using granulated soil at about the desired moisture content. Then the soil surface is impacted uniformly 25 times by allowing the hammer to fall from its full drop height each time. The mold is then filled two thirds full with loose soil, impacted again 25 times and finally filled and compacted a third time. After the top collar is removed, the top of the compacted soil volume is trimmed with a wire knife to the final dimensions of the mold. The outside of the mold is cleaned and the mold and compacted soil therein weighed. Three samples of the compacted soil of about 50 g are removed from the top, middle and bottom regions of the sample in the mold, and are weighed, dried and reweighed in order to determine the average moisture content of the soil. The test is continued by thoroughly mixing more water with the soil removed from the mold and loosened, and repetitions of the compaction, weighing and moisture determination procedures.

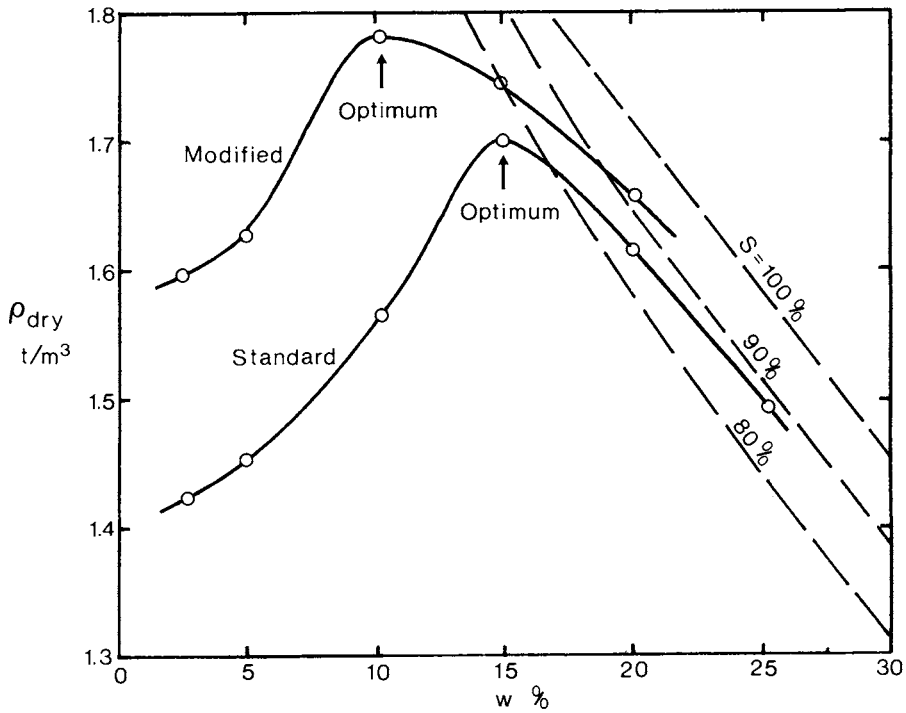

Fig. 2.26. Results of dry density versus molding water content for the standard and modified Proctor compaction tests, together with calculated lines of dry densities at different degrees of saturation.

The usual representation of the test results is a plot of soil dry density versus moisture content, such as the ones depicted in Fig. 2.26 for both the Standard and Modified Proctor tests. The dry density is calculated for each test repetition by subtracting the water mass from the total mass density, or by the formula,

$$\rho_{dry} = \frac{\rho}{1 + w} \tag{2.36}$$

where w = mass of water divided by mass of solids.

If the specific gravity of the solid particles, G_S, is known, lines of theoretical dry density for the soil at saturation levels of 100%, 90%, 80% and so on can be plotted on the same graph, as in Fig. 2.26. Then the

approximate saturation of the compacted soil can be estimated at any point by its location on the graph in relation to the relative saturation lines. The theoretical dry mass density at different moisture contents and degrees of saturation, S (= volume of water divided by volume of voids), is given by the following formula.

$$\rho_{dry} = \frac{\rho_w}{w/S + 1/G_s} \tag{237}$$

In Fig. 2.26, the optimum moisture contents for compaction of the example soil, at the energy levels of these two particular tests, are 15% and 10%, for the Standard and Modified tests, respectively. The maximum densities (100% relative density) for the two tests are 1.7 and 1.79 t/m^3. Maximum density, and relative densities less than 100% of the maximum, always must be referred to the precise test which has been employed to determine them.

The Standard Proctor test, developed in the 1930's, was designed to simulate the field input energy of an average kneading compaction machine used at that time in road or earthdam construction. Later, with the advent of larger construction machines, the Modified test was proposed to give compaction results more appropriate to the larger input energies of the bigger and heavier equipment. Other similar tests are used with different masses of hammer and number of blows per soil layer. For example, the standard AASHO test uses the same size of mold, but specifies 12 blows for each of five layers in the mold, with a hammer having 4.54 kg mass and a 457 mm drop. The modified AASHO test uses 55 blows per each of five layers with the same hammer. In general, both of these tests will produce a maximum density higher than that of the Standard Proctor procedure.

Static tests can also be performed on unsaturated soils in order to characterize their behavior under more steady loads in the field. The consolidometer (Section 2.6.3) or a similar apparatus may be used for this purpose. The volume change under repeated increases in vertical pressure can be monitored by measuring the vertical movement of the top piston, as is done in the consolidation test. Alternatively, various single quantities of pressure can be applied to loose unsaturated soil samples, and the weight, density and moisture content of each specimen determined subsequently. Static tests of this nature are more suitably matched to the conditions undergone by topsoil due to the actions of steady surface loads or slowly moving vehicles and the like.

It will be noted in Chapter 10 that both compressive stresses and shear strain govern the degree of compaction sufferred by an unsaturated soil. This has been demonstrated in field experiments and in specially fabricated laboratory devices. However, commercial test devices are not available for the measurement of the shear strain during the compaction process, and the experience gained by others must be used for predictive purposes, as will be discussed in the appropriate Section of Chapter 6.

2.7. FIELD STRENGTH TESTS

As mentioned in the previous Section, tests performed to measure soil strength parameters in the field may not yield the same degree of control or accuracy as laboratory tests. However, they do offer the advantages of generally speedier results, and the possibility of measuring mechanical properties without removing soil from its original environment. Some field strength tests are suitable for all types of soil, while others are useful only in the case of wet cohesive soils.

Some of the most popular field testing devices are shown in Fig. 2.27.

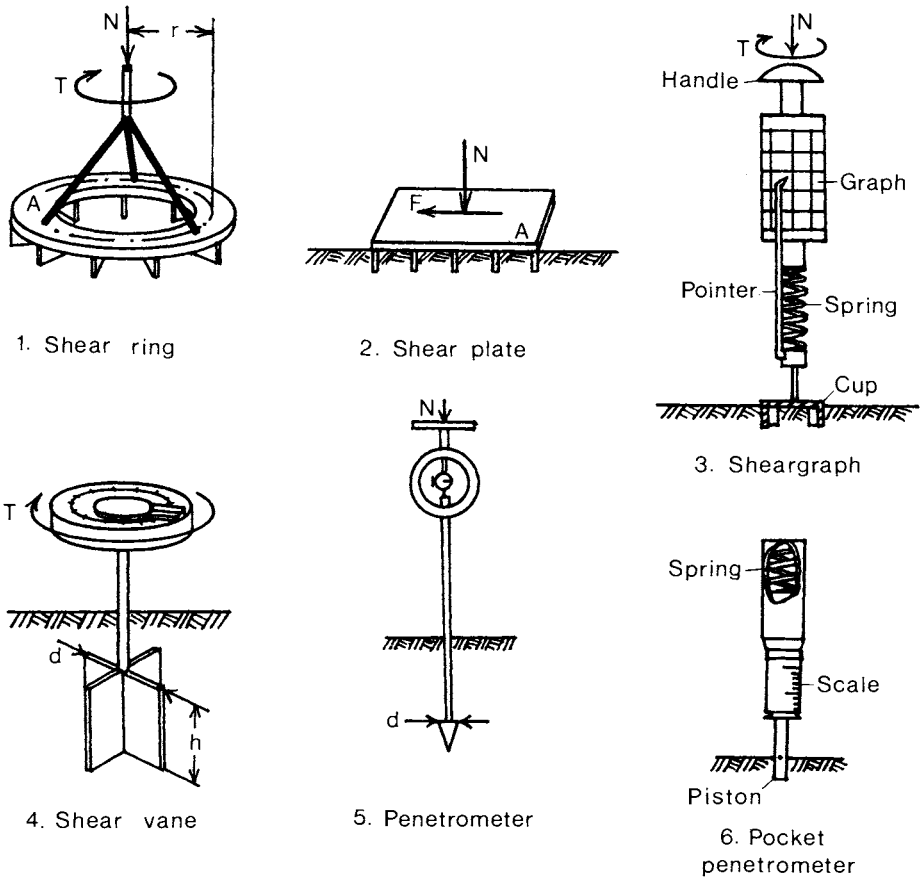

Fig. 2.27. Six common field soil strength testing devices.

The first three devices identified are similar in their principle of operation, namely they measure the maximum shear force on an internal horizontal plane near the soil surface. In this respect, these three tests simulate the mode of soil failure produced in the direct shear box laboratory apparatus (Section 2.6.1). The shear ring and shear plate are constructed so as to attempt to produce relatively uniform levels of normal and shear stress on the soil potential failure plane, which occurs at the bottom of the vertical lugs which penetrate the soil surface. Torque, T, is applied to the shear ring, and horizontal force, F, to the plate until the maximum magnitude is achieved when the soil fails on a horizontal slip plane under a particular vertical load, N. The maximum torque, T_m, applied to the ring is related to the Coulomb soil strength parameters by the following relation.

$$T_m = (cA + N\tan\phi)r \tag{2.38}$$

where A is the ring plan area, and r is the average ring radius. The maximum shear plate horizontal force, F_m, is;

$$F_m = cA + N\tan\phi \tag{2.39}$$

in which A is the horizontal plate area.

In practice, the shear ring is more convenient to operate in the field because it is both manually or mechanically easier to provide a forcing torque to the device, than to find the anchorage and strength needed to apply large horizontal forces to the plate. Although neither the shear ring nor plate are readily available for purchase, many models have been built over the years by researchers and soil testing teams. They have ranged from simple manual devices, in which the vertical force is provided by dead weights, and the torque or horizontal force applied by handles, to automated and electronically monitored hydraulic or electric powered machines mounted on vehicles. The type of device required depends on the resources available, and the number of measurements to be made. Large research institutes with sufficient funding often opt for an automated vehicle-mounted model, while typically postgraduate researchers with limited resources are forced to build and manually operate their own apparatus. In the latter case, the applied torque is generally measured by some sort of spring gauge device. This does not imply that the accuracy of measurements must be compromised in either case, provided that care is taken to insert and operate the shear testing devices properly.

Problem 2.7. A shear ring is operated on the surface of a moist clay loam field. The device has a ring outside diameter of 250 mm and inside diameter 200 mm. Normal loads of 100, 200 and 300 N are placed on the shear ring, and the resulting maximum levels of torque for these loads are 45.0, 50.2 and 55.5 Nm, respectively. Estimate the soil cohesion and angle of internal friction on the plane of failure immediately below the shear ring lugs.

The effective radius of the shear ring is the average diameter divided by two, or;

$$r = (250 + 200)mm/4 = 112.5\ mm = 0.1125\ m$$

and the area of the ring is;

$$A = (250^2 - 200^2)/4\ mm^2 = 17{,}700\ mm^2 = 0.0177\ m^2$$

Eqn. 2.38 can be divided by the average ring radius, r, which shows that at soil failure;

$$T_m/r = cA + N\tan\phi$$

The three torque values divided by r are 400, 446 and 493 N, respectively. If these three quantities are used as values of x, and the vertical forces as y in a linear regression, the resulting intercept and slope are cA and $\tan\phi$. Thus;

$$cA = 353.3\ N, \quad \underline{c = 20.0\ kPa}$$
$$\tan\phi = 0.465, \quad \underline{\phi = 24.9^o}$$

The third test device in Fig. 2.27, the Cohron sheargraph (Soiltest, 1976) also ultimately fails the soil on a horizontal plane with relatively uniform shear stress, if the soil is failed to a sufficient deformation. But the radius to each point of shear stress cannot be approximated as a constant as is assumed for the shear ring. The shear stress times radius is integrated over the circular area of the soil contacting cup of overall radius, r, in order to arrive at the torque required for a particular shear stress applied to the soil, as shown in the formula below.

$$T = \int_0^r \tau r dA = \int_0^r 2\tau\pi r^2 dr = \frac{2}{3}\tau\pi r^3 \qquad (2.40)$$

It is not necessary, by virtue of the design of the sheargraph, to perform the calculations of shear stress as a function of applied torque. Together, the applied torque and vertical force cause simultaneous rotary and vertical deformations in the sheargraph spring, which are calibrated to the average applied vertical pressure and shear stress. The pointer, which is fixed to the soil contacting cup, then moves vertically and rotationally with respect to the upper barrel of the device. And on this cylindrical barrel is affixed a sheet of pressure sensitive graph paper, already calibrated to give readings of shear stress on the soil (on the horizontal axis) versus normal stress (on the vertical axis as viewed in Fig. 2.27).

The preferred procedure for the sheargraph test is to first insert the soil circular cup with internal lugs firmly into the soil in order to ensure complete

contact between cup and soil. Then hand pressure is applied vertically on the handle until the pointer moves to the desired vertical stress indication on the graph. Next, while attempting to maintain constant vertical force, the handle is rotated, thus increasing the torque applied to the soil. Once the maximum torque has been reached, the pointer no longer moves along the shear stress direction with respect to the graph on the upper barrel. Rather, it either remains at a fixed spot in the case of a soil with a constant plastic failure

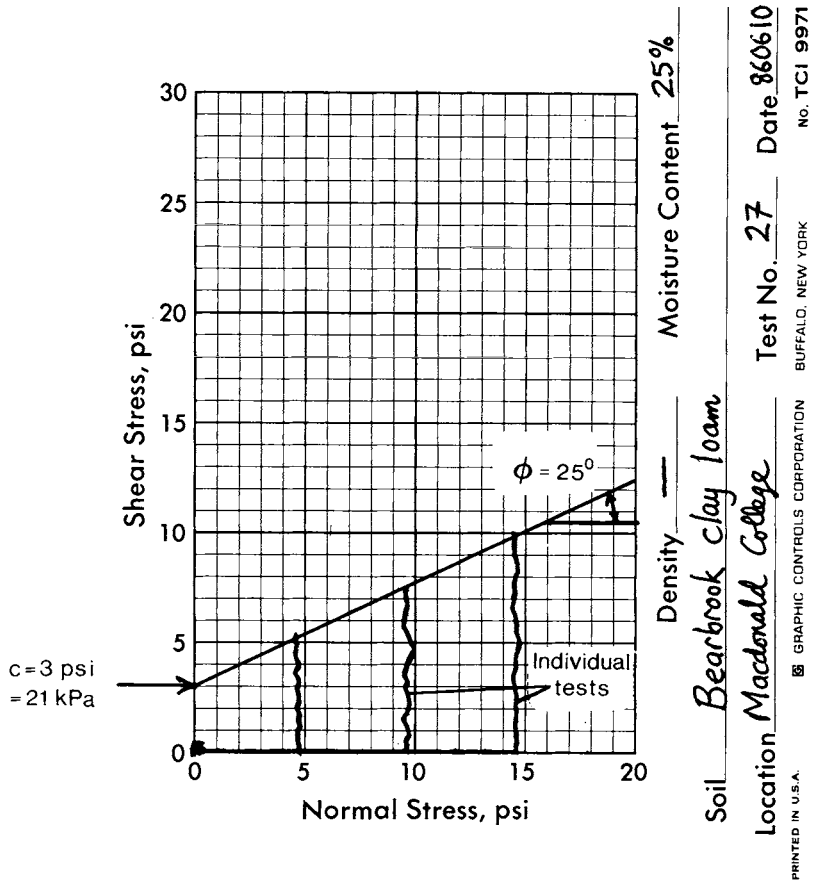

Fig. 2.28. Results of a series of sheargraph tests on a clay loam soil.

strength, or declines somewhat in shear stress for a sensitive soil which loses strength with considerable shear deformation. In either event, the highest point on the shear versus normal stress graph identifies the point of maximum shear strength of the soil, for a particular normal load.

The test is then repeated at different normal pressure levels, at the same spot for a soil with strength insensitive to deformation, or at nearby locations for a sensitive soil. Then directly on the graph sheet laid flat, a line can be drawn through the points of maximum shear stress. This line will be at the slope ϕ to the normal stress axis, and will have intercept c on the shear stress axis, as demonstrated in Fig. 2.28. This result is similar to that of the direct shear box (Fig. 2.16).

As well as measuring the internal soil strength, the sheargraph can be adapted to measure the strength properties of different materials in contact with a soil surface. The Soiltest sheargraph, for instance, comes equipped with two inserts for the soil contacting cup. One of these is faced with smooth steel, and can be used together with the calibrated spring and graph sheet to find the adhesion and angle of surface friction of steel on soil, just as c and ϕ are found as described above. Also, an insert with a medium hard rubber facing is provided for the same purpose with respect to rubber on soil strength parameters. These attachments are useful for estimating the strength coefficients of metal tools or smooth metal wheels or tracks in contact with soil, or a smooth rubber tire or track.

The sheargraph is designed primarily to measure soil strength at the ground surface. However, it can be adapted to estimate properties at moderate depths if a careful excavation is made with minimal disturbance to the soil structure. Also, strength measurements can be made on a vertical plane in the soil by applying the sheargraph to vertical sides of an excavated hole in the ground. All three of the shear ring, shear plate and sheargraph devices must be operated in an accessible and visible location, because it must be ensured for each test that the soil contacting plates or cup are in fact in good continuous contact with a flat soil surface.

The fourth popular field strength testing device shown in Fig. 2.27 is the shear vane. This apparatus fails soil in shear mostly on a vertical plane, and there is no way in which to control the normal stress on this plane. It is conceived for almost saturated cohesive soils which act in a frictionless fashion when undrained, and is operated with the standard handle at depths of 0 to 30 cm. The shear stress on the failure planes is then the undrained shear strength, C. If it is assumed that the soil is not significantly disturbed when the shear vane is inserted to a particular depth, then the shear strength measured is principally at the vertical edges of the vanes, and on the bottom surface. For vanes of height, h, and overall diameter, d, this shear strength C requires a turning torque T for complete soil failure, as follows.

$$T = \pi c d^2 h/2 + \pi c d^3/12 \qquad (2.41)$$

If the height h of the vanes is more than twice the overall vane diameter, d, then the second term in the formula above, which is derived from the shear stress on the bottom of the vane, is less than 8% of the total torque, and can be neglected to provide a simpler formula. Several commercially available models of shear vane have calibrated torque sensing springs, and a scale which indicates the undrained shear strength, C, of a wet clay directly.

Extensions rods are also available, or can be fabricated fairly easily for shear vanes, in order to measure the undrained shear strength at greater depths in the soil. Without further preparation, a shear vane can be pressed into the soil surface, and undrained shear strength measured at desired depths up to 45 cm or so. If measurements are required deeper than that, a clearance hole should be excavated in order to remove the adhesion of soil on the extension rod, which would artificially increase the indicated shear strength of the vane. This hole can be made with a 5 cm or so diameter auger, and the shear vane subsequently inserted a few centimetres below the bottom of the hole to avoid the volume of soil which was disturbed by the excavation process (Fig. 2.29). Such deep shear strength tests are particularly useful for the design of wide footings which have a large depth of influence, such as for heavy silos and the like. They can be utilized also to determine the internal undrained strength of a slope formed of wet cohesive soil for the purpose of future slope stability calculations.

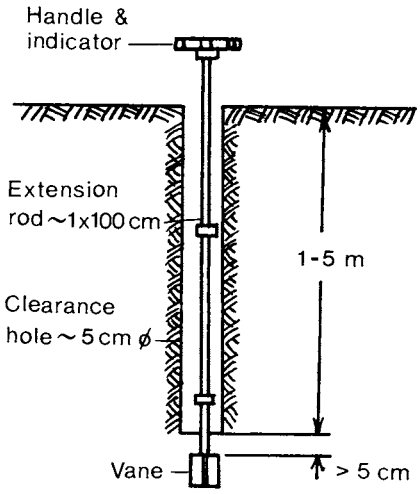

Fig. 2.29. The use of an auger hole and extension rods for deep undrained shear strength measurements with a shear vane.

Field device number 5 in Fig. 2.27 is a penetrometer. Unlike the aforementioned tests, the information received from the penetrometer does not relate to the Coulomb soil strength parameters, c and ϕ. Instead, a single quantity is measured, namely the force required to move the penetrometer at a selected constant speed and a particular depth in the soil. This force is often normalized by dividing by the the base area of the penetrometer tip, to arrive at the average applied vertical pressure, known as the cone index. While either the penetration force or the cone index by itself does not allow the estimation of soil cohesion or friction angle, it has been used often to give an indication of the relative soil strength, density, root penetration, trafficability by vehicles or other design application. These uses of the penetrometer require extensive testing and calibration of the cone index measurements with respect to the application desired, but many examples of this procedure are available in the soil mechanics literature.

The pocket penetrometer is designed for an application different from the general penetrometer test. A circular flat tipped rod is pressed into a soil surface up to an indicated depth. By the theory of bearing capacity of footings on cohesive soils (Chapter 3) the required force is converted to the undrained shear strength, C, and this is indicated on the calibrated spring scale on the instrument. This device is useful for a rapid and approximate determination of the undrained shear strength and bearing capacity of shallow cohesive undrained soils.

Comparing the applicability of all the tests illustrated in Fig. 2.27, only the shear vane and pocket penetrometer are always restricted to use in saturated cohesive soils. Both of these devices give an indication of the undrained shear strength, C, with the assumption that total stress angle of friction is zero. The shear ring, shear plate and sheargraph can give drained strength parameters, provided that the soil in question has adequate hydraulic conductivity to release developed pore water pressures over the time period of each test. Even for the few centimetres of distance between the soil under one of these shearing devices, it can take more than one hour for the pore water to move and reduce the pore pressure, if the soil hydraulic conductivity is less than 10^{-4} cm/sec. Because this is not a practical time delay for the conduction of these tests, only undrained strength properties will be measured in such soils, which comprise many clays and fine silty materials.

If the saturated hydraulic conductivity of a soil is greater than 10^{-1} cm/sec, then only a few seconds are required for nearly all of the pore water pressure caused by added normal stress and shear strain to move a couple of centimetres from the soil interior to the surface, and drained or effective cohesion and friction angle can be estimated.

2.8. PROBLEMS

2.8 At a point in a frictional soil which is undergoing failure, the normal compressive stress on the horizontal plane is 140 kPa and that on the vertical plane 40 kPa. Also on the horizontal plane is a counterclockwise acting shear stress of 15 kPa. Find the angle of internal friction of this soil, and the angle θ_f of the two potential rupture planes from the horizontal.

Answer: $\phi = 35.5^o$, $\theta_f = 54.4^o$ (ccw), 71.1^o (cw).

2.9 A series of direct shear box tests is performed on a moist silty soil. The shear box is a square single ring device with a sample length and width of 5.08 x 5.08 cm. At soil failure, the following shear forces, T, were recorded for different vertical forces, N. Find the cohesion and angle of internal friction of the soil.

N (N)	20	40	80	160	320
T (N)	31	40	59	100	175

Answer: c = 8.2 kPa, $\phi = 25.8^o$.

2.10 A series of consolidated drained triaxial tests is performed on four essentially identical samples of a wet silty clay soil. All samples are initially trimmed to cylinders of diameter 38.1 mm and length 76.2 mm. The top loading piston has a diameter of 10.16 mm where it passes through the top of the cell. The results below indicate the external piston force, P, at the points of soil failure, and the total changes in height and volume of each sample during both the consolidation and shear testing phases. Find the cohesion and angle of internal friction of this soil.

Test No.	σ_3, kPa	P, N	Δz, mm	ΔV, cm^3
1	70	203	-1.37	1.5
2	105	300	-1.40	-1.6
3	210	530	-1.42	-2.7
4	315	780	-1.46	-3.3

Answer: c = 10.2 kPa, $\phi = 30.2^o$.

2.11 A consolidation test is conducted on a saturated clay soil. The measurements below are the total change in height of the sample at various elapsed times after the application of a pressure increase. Estimate the time to 100% consolidation of this soil.

Time, h	0.1	0.2	0.5	1	2	5	10	20	50	100
Δh, mm	0.05	0.10	0.29	0.39	0.54	0.60	0.68	0.72	0.76	0.78

Answer: t_{100} = 4 hours.

2.12 A modified Proctor compaction test is conducted on a clay soil. The mass of the mold without top collar is 3.650 kg, and the mold has an inside diameter 101.6 mm and height 116.4 mm. From the recorded results below of combined mass of compacted soil and mold versus soil water content on a dry mass basis, find (a) the optimum moisture content of this soil, and (b) its 100% relative dry mass density.

w, %	5	10	15	20	25	30
Total mass, kg	4.84	5.00	5.22	5.41	5.42	5.37

Answer: (a) w = 20%, (b) 100% dry density = 1.55 t/m^3.

2.13 An annular shear ring is employed to estimate the strength parameters of the surface of a clay field. The shear ring has an outside diameter of 30 cm, inside diameter 20 cm and is fitted with 20 vertical lugs of length 2 cm. From the results given below of shear ring applied torque at soil failure versus vertical force placed on the ring, estimate the cohesion and friction angle of this soil. What can be said about the drainage conditions in the soil during the tests?

Applied force, N	100	200	400	800
Torque, Nm	103.1	103.2	103.9	104.8

Answer: c = 20.9 kPa, ϕ = 1.2^o. Soil is essentially undrained.

Chapter 3. Shallow Foundations

3.1. BEARING CAPACITY

A foundation is a structural element which distributes a vertical load over a certain soil contact area, and a shallow foundation is defined generally as one which is not located deeper below the soil surface than two or three times its own width. The approach to the design of foundations is usually to compute the maximum allowable average contact pressure, or bearing pressure, over the contact area, and then to reduce this pressure to a design level. The maximum bearing pressure, or maximum bearing capacity, is divided by the 'safety factor' in order to arrive at the design pressure. In this application, the safety factor has two principal functions. Firstly, it protects the design from experimental error in the measurement of soil strength properties, unexpected loadings on the foundation and the like. Secondly, by providing lower shear stresses in the soil than the maximum strength, the accompanying strains hopefully are reduced to a magnitude which will not result in an unacceptable sinkage of the total structure. In general, a safety factor of 3.0 has been found to accomplish both of these functions satisfactorily, and is a good rule of thumb to follow in the absence of more specific criteria.

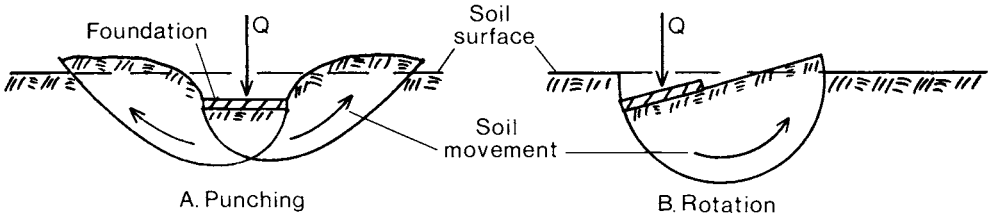

Fig. 3.1. Modes of soil failure under a surface footing.

Fig. 3.1 shows two common modes of foundation failure under a vertical force, Q. If the foundation is constrained to descend in a level attitude, for example by a rigid connection to a vertical column, then the foundation punches into the soil as shown in case A. A free standing load usually causes a foundation to rotate as in case B, since the soil tends to move to one side of the foundation before the other. In fact the analysis for the force which causes incipient failure is practically identical for both cases.

3.1.1. Soil with small angle of friction

Fig. 3.2 provides a simplified method of analysis for the ultimate bearing capacity of a soil which is assumed to have a small angle of internal friction.

This case is not an accurate representation of the general situation in which a soil possesses a considerable friction angle, but it serves to illustrate the general trends of stress transfer beneath a rigid foundation, and prepares one for an understanding of the more complex analytical cases.

It is assumed in the model of Fig. 3.2 that the foundation is much longer than its width, B, that the bearing pressure, q_o, is distributed evenly over the

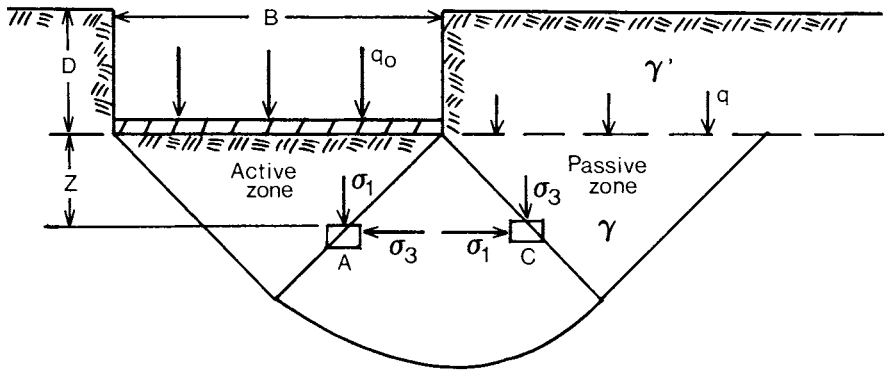

Fig. 3.2. A simplified analysis of soil failure at the ultimate bearing capacity on a material with a small angle of internal friction.

smooth contact area with the soil, and that the depth of the active zone (soil moving downwards) is the same as that of the passive zone (soil moving up). To the sides of the foundation base and at the same elevation, there is a vertical pressure acting in the soil arising from a depth D of overburden. The magnitude of this pressure is:

$$q = \gamma' D \tag{3.1}$$

where γ' is the effective weight density of the soil above the foundation.

When the soil fails beneath the foundation, slip lines are generated as shown through points A and C. At any depth z, the vertical pressure at a point beneath the foundation, such as A, is the major principal stress with a magnitude;

$$\sigma_1 = q_o + \gamma z$$

where γ = the effective weight density below the foundation
= the total density of a dry or moist soil,
= the buoyant density of a saturated soil (Section 2.4).

At soil failure, the principal stresses at point A obey the Mohr-Coulomb strength criterion of Eqn. 2.8.

$$\sigma_3 = \sigma_1 K_a - 2c\sqrt{K_a}$$

where $$K_a = \frac{1 - \sin\phi}{1 + \sin\phi}$$

If it is assumed that there is practically no stress change between points A and C, then σ_3 at point A equals σ_1 at point C, since the major principal stress changes direction between the two points. At point C, the vertical stress is;

$$\sigma_3 = \gamma z + q = \gamma z + \gamma' D$$

Relating σ_3 to σ_1 at point C by Eqn. 2.8, and equating σ_1 at point C to σ_3 at point A, the result is;

$$q_o = \gamma z(K_p^2 - 1) + qK_p^2 + 2c\sqrt{K_p}(1 + K_p)$$

where $K_p = 1/K_a = \frac{1 + \sin\phi}{1 - \sin\phi}$ (3.2)

Taking the average effective depth of soil failure below the foundation base as B/2, the average stress, q_o, can be formulated as;

$$q_o = (K_p^2 - 1)\gamma B/2 + 2c\sqrt{K_p}(1 + K_p) + qK_p^2$$
$$= (\gamma B/2)N_\gamma + cN_c + qN_q \qquad (3.3)$$

The latter form of Eqn. 3.3 is Terzaghi's bearing capacity equation (Terzaghi, 1943). Fig. 3.3 shows the values of the N factors of Eqn. 3.3, together with the results of more accurate computations taking friction angle into account by Meyerhof (1955) for $N\gamma$ and Prandtl (1921) for N_q, which will be described in the following Sections. It can be seen that the simple approach above compares well to the more comprehensive methods up to angles of internal friction of approximately 10^o for N_q and 20^o for $N\gamma$. For cases of soils with larger friction angles, this simplified approach to bearing capacity computations cannot be justified, and a more comprehensive approach must be taken.

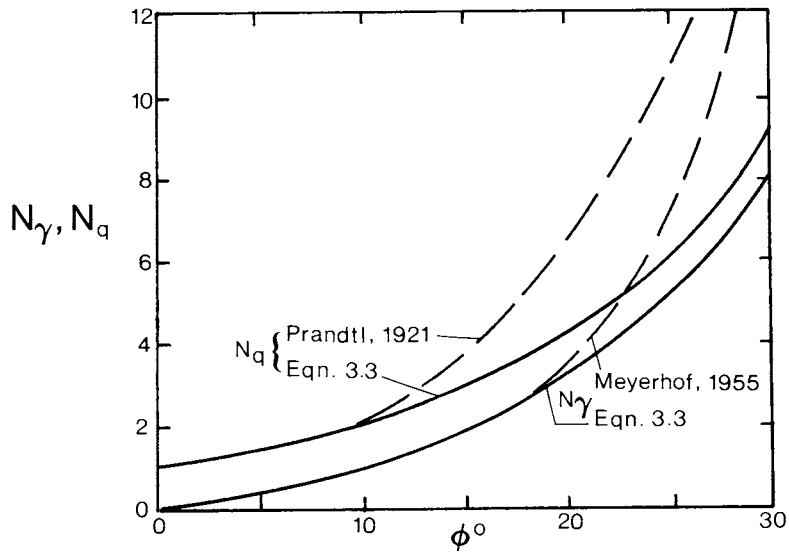

Fig. 3.3. Values of the N_γ and N_q bearing capacity factors from two sources.

3.1.2. Prandtl's solution for smooth shallow footings

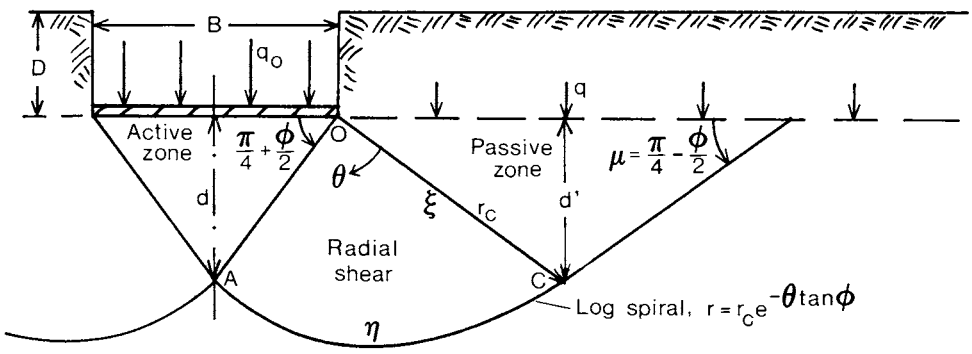

Fig. 3.4. The model of Prandtl (1921) for failure of a frictional but weightless material under a plate loading.

As shown in Fig. 3.3, the assumption of a small angle of internal soil friction is not valid for the general case of frictional soils. Prandtl (1921) showed how a different simplifying assumption can be used to solve the bearing capacity problem for general friction angles, and the model is represented in Fig. 3.4 for a continuous smooth footing i.e. a long narrow footing having no shear stress on the base. There is an active Rankine soil failure zone beneath the foundation which moves downwards, and passive zones to the sides which move up against the surcharge pressure, q, arising from the depth D of soil above the foundation base. Between these zones is another called the radial shear zone in which the soil rotates during failure. Lines OA and OC which form the side boundaries of this radial shear zone are ξ slip lines (Fig. 2.8) having positive shear stress, while the lower boundary formed by the curved line AC is an η slip line.

Prandtl (1921) showed that if the soil weight in the radial shear zone is not important compared to the soil cohesion force along line AC, then the shape of the boundary is a log spiral as shown in Fig. 3.4. In addition, the assumption of negligible soil density times the depth of the zone, compared to cohesion strength, allows a straightforward integration of Eqn. 2.23 along line AC, and thus the determination of the stress parameter, σ, at point A as shown below. The angle, θ, of the major principal stress is 0 at point C and $\pi/2$ at point A.

$$d\sigma - 2\sigma \tan\phi \, d\theta = \gamma(dz - \tan\phi \, dx) = 0 \tag{3.4}$$

$$\int_{\sigma_C}^{\sigma_A} \frac{d\sigma}{\sigma} = \int_0^{\pi/2} 2\tan\phi \, d\theta \tag{3.5}$$

$$\sigma_A = \sigma_c \, e^{\pi \tan\phi} \tag{3.6}$$

At point C, stress parameter, σ_C, is found using Eqn. 2.11 in terms of the principal stress, σ_3, which is the vertical stress at that point. Then σ_A is calculated by Eqn. 3.6 above, and σ_1 derived using Eqn. 2.11 again to convert to the major principal stress at point A.

$$\sigma_c = \frac{\sigma_3 + c\cot\phi}{1 - \sin\phi} = \frac{\gamma d' + q + c\cot\phi}{1 - \sin\phi} \tag{3.7}$$

$$\sigma_A = \frac{q + \gamma d + c\cot\phi}{1 + \sin\phi} = \sigma_c e^{\pi\tan\phi} = \left\{\frac{\gamma d' + q + c\cot\phi}{1 - \sin\phi}\right\} e^{\pi\tan\phi}$$

In the expression above, d and d' are the maximum depths of soil failure below the midpoints of the active zone beneath the footing and the passive zone, respectively. They are found as described below, using the assumed log spiral radial shear zone boundary.

$$r = r_c e^{-\theta \tan\phi}$$

$$\frac{d}{\cos\mu} = \frac{d'}{\sin\mu}\left\{e^{-\frac{\pi}{2}\tan\phi}\right\}$$

$$d' = d\ \tan\mu\ e^{\frac{\pi}{2}\tan\phi}$$

The depth of soil in the active and passive failure zones is not constant across the footing width, and varies linearly from the maximum values of d and d' to zero at the foundation outer edges. Thus the average soil depths are one half of these maximum values, and the average footing bearing capacity is:

$$q_o = \gamma\frac{B}{2}\left[\left\{\frac{1+\sin\phi}{1-\sin\phi}\right\}e^{\frac{3}{2}\pi\tan\phi} - \cot\mu\right] + c\cot\phi\left[\left\{\frac{1+\sin\phi}{1-\sin\phi}\right\}e^{\pi\tan\phi} - 1\right] + q\left\{\frac{1+\sin\phi}{1-\sin\phi}\right\}e^{\pi\tan\phi}$$

$$= (\gamma B/2)N\gamma + cN_c + qN_q \qquad (3.8)$$

As Eqn. 3.8 indicates, this analysis results in an equation of the same form as Terzaghi's bearing capacity formula, Eqn. 3.3, and the N factors are;

$$N\gamma = \left\{\frac{1 + \sin\phi}{1 - \sin\phi}\right\}e^{\frac{3}{2}\pi\tan\phi} - \cot\mu \qquad (3.9)$$

$$N_c = \cot\phi\left[\left\{\frac{1 + \sin\phi}{1 - \sin\phi}\right\}e^{\pi\tan\phi} - 1\right] \qquad (3.10)$$

$$N_q = \left\{\frac{1 + \sin\phi}{1 - \sin\phi}\right\}e^{\pi\tan\phi} \qquad (3.11)$$

The values given for N_c and N_q in Eqn. 3.10 and 3.11 above are those accepted in engineering practice today, and given in most textbooks on soil mechanics and foundations. They are provided graphically in Appendix 1 of this book. The $N\gamma$ magnitudes predicted by Eqn. 3.9, however, are too large in comparison to other theoretical models which include the effects of shear forces on a foundation base. These latter models, developed by Terzaghi (1943), Meyerhof (1955) and Sokolovsky (1956) are described in the next Section. Fig. 3.5 shows that the smooth base prediction of the $N\gamma$ bearing capacity factor (Eqn. 3.9) yields values which are about two to four times higher than the models which include base shear effects. It can thus be concluded that the smooth base $N\gamma$ factors are not sufficiently conservative in that they indicate a larger bearing capacity. The computed values of Meyerhof and Sokolovsky are the accepted design quantities, and have subsequently proved to be reasonably accurate for practical predictions.

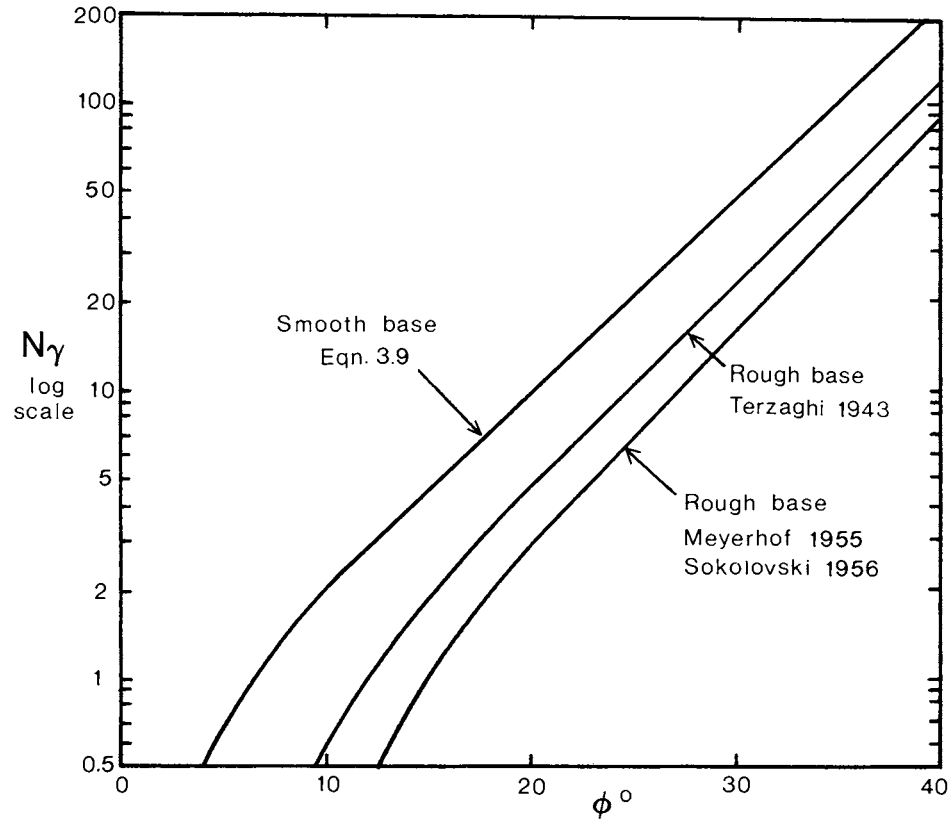

Fig. 3.5. Comparison of $N\gamma$ bearing factors for a smooth footing and a rough surfaced footing as calculated by Terzaghi, Meyerhof and Sokolovski.

3.1.3. Rough footing on frictional soil

A real situation of a shallow foundation resting on a frictional soil with weight is more complex than the previous models. Firstly, soil density cannot be set to zero in the characteristic equations 2.21 and 2.23. In addition, there is no justification for the assumption that no shear stress exists on the footing base. In fact, the equations of stress distribution under the footing, Eqn. 2.20 to 2.23, cannot be solved explicitly in these conditions. However, repetitive numerical computations can be made by putting the characteristic equations into a finite difference form, and solving for values of stress magnitudes and orientations through a net of characteristic lines. Such a result is depicted in Fig. 3.6(a), and results for footing bearing capacity have been obtained in this way by Lundgren and Mortensen (1953), Meyerhof (1955), Sokolovsky (1956), Harr (1966) and others.

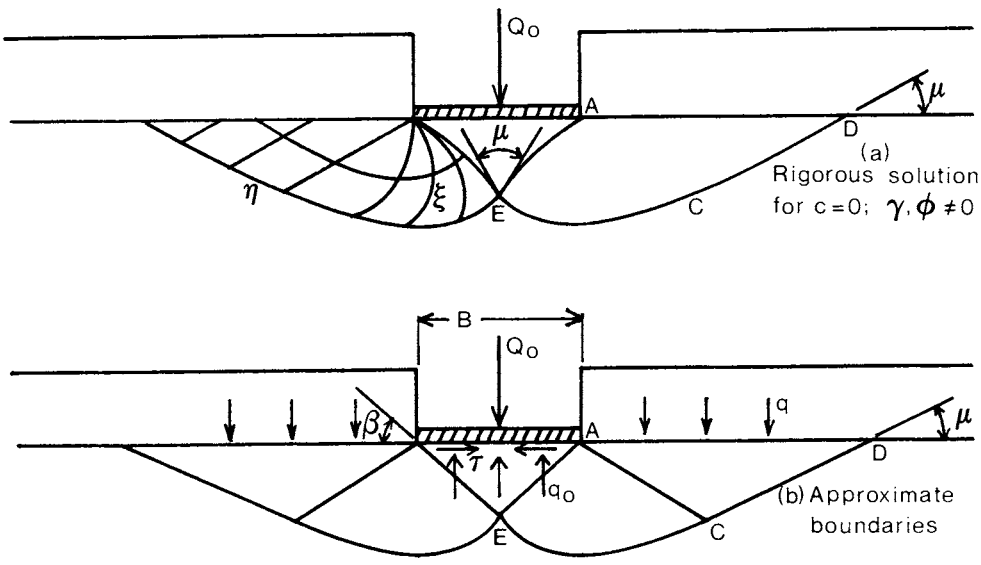

Fig. 3.6. The pattern of soil failure as predicted (a) by stress characteristics and (b) the approximate solution of Terzaghi (1943).

Terzaghi (1943) showed how an approximation to these numerical solutions can be accomplished. Straight lines are used to bound the active soil failure zone under the footing, such as AE in Fig. 3.6(b), and the passive zone ACD. The principal stresses are determined along line AE just as in the log spiral method of Section 3.1.2, and resolved into vertical normal and horizontal shear stresses acting on the footing base. The average vertical stress for this assumed soil failure configuration is the ultimate bearing capacity, q_o, and the values of the corresponding bearing capacity factor, $N\gamma$, are given in Fig. 3.5. This simplified model still yields factors higher than the Meyerhof-Sokolovsky magnitudes, but much closer than the smooth base model of the previous Section.

Meyerhof (1955) and Sokolovsky (1956) have obtained the approximate values of the various bearing capacity equation N factors which are accepted in practice today. The N_C and N_q factors are calculated as Prandtl (1921) did assuming a weightless soil. The values of $N\gamma$ were computed assuming a cohesionless soil, as in Fig. 3.6(a). It was demonstrated by Sokolovsky (1956) that the superposition of the effects of soil weight, cohesion and overburden in the bearing capacity equation, Eqn. 3.3, yields conservative results for

ultimate bearing capacity. Thus the use of the N factors, as given by Appendix 1, in Eqn. 3.3 for vertical bearing capacity determinations, will give design results for strip footing widths which are on the safe side. It should be remembered always to apply the appropriate safety factor (usually 3.0) to reduce the design pressure on a footing from the ultimate bearing capacity, as mentioned previously in Section 3.1.

Problem 3.1. Consider a long narrow rigid strip footing to be installed at a depth of 1 m in a clay loam soil having a moist density of 17.6 kN/m^3, c=15 kPa and ϕ=30^o. If the strip footing is to be designed to carry a load of 500 kN per metre length safely, what should be the width of the footing?

The ultimate bearing strength of the footing must be the design pressure (load per unit length divided by the footing width) multiplied by the safety factor, 3.0.

$$q_o = 3x500 \text{ kN/m/B}$$

From Appendix 1, the bearing capacity factors are N_γ=16, N_c=30 and N_q=18. Using Eqn. 3.3, the ultimate bearing capacity is given as;

$$q_o = (\gamma B/2)N_\gamma + cN_c + qN_q = (17.6x16B/2 + 15x30 + 1x17.6x18) \text{ kPa}$$

$$= 1500 \text{ kN/m/B}$$

Thus 1500 kN/m = (141B^2 + 774B) kN/m
and B = 1.52 m is the required footing width.

3.1.4. Footings with finite length and inclined loads

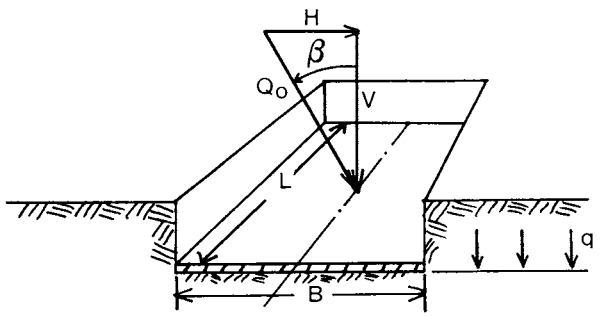

Fig. 3.7. The more general case of a shallow footing with finite length and an inclined load.

Fig. 3.7 shows a shallow footing case where the length, L, is not semi-infinite compared to the width, B, but is larger than B. Also, the total loading force, Q_o, is not acting perpendicular to the footing but is inclined at an angle β to the vertical. The components of the load can be considered as H in the horizontal direction, and V in the vertical. The fact that the footing length is finite has the effect of increasing the ultimate bearing capacity of the footing on cohesive soil, since there is additional shear resistance to footing settlement in the soil below the two ends. In a frictional soil, there is the opposite effect, since the footing bearing pressure is spread out in two dimensions at depth in the soil, and frictional shear resistance is reduced compared to the long strip footing case.

In addition, an inclination of the footing load from the vertical reduces its maximum possible value, since it changes the shear stress condition on the footing base, and reorients stress directions in the subsoil. This results in shorter and weaker slip planes at soil failure, as shown in Fig. 3.8.

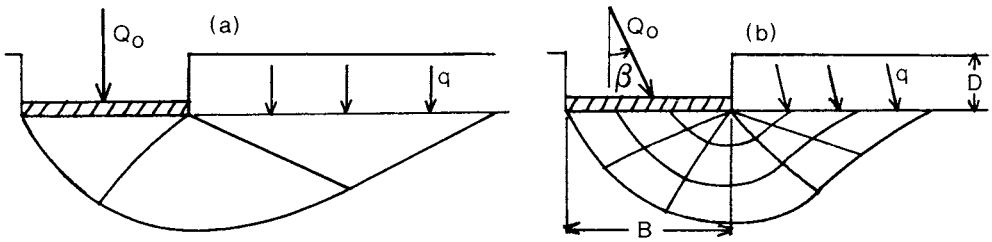

Fig. 3.8. The failure of soil beneath footings with (a) a vertical load and (b) an inclined load.

Hansen (1957) reported research conducted on both of these complications in the calculation of bearing capacity. He summarized the resulting recommendations for ultimate bearing capacity estimations as follows.

For granular soils (c = 0):

$$q_o = \frac{1}{2}\gamma B N_\gamma \left[1-0.3\,\frac{B}{L}\right]\left[1-1.5\,\frac{H}{V}\right]^2 + \gamma' D N_q \left[1+0.2\frac{B}{L}\right]\left[1+0.1\,\frac{D}{B}\right]\left[1-1.5\,\frac{H}{V}\right] \quad (3.12)$$

Limitations: $B \leq L$, $D < 15B$, $H < V\tan\phi$

For cohesive soils ($\phi = 0$):

$$q_o = 5c\left[1 + 0.2\,\frac{B}{L}\right]\left[1 + 0.2\,\frac{D}{B}\right]\left[1 - 1.3\,\frac{H}{V}\right] + \gamma D \qquad (3.13)$$

Limitations: $B \leq L$, $D < 2.5B$, $H < 0.4V$ ($\beta < 22^o$)

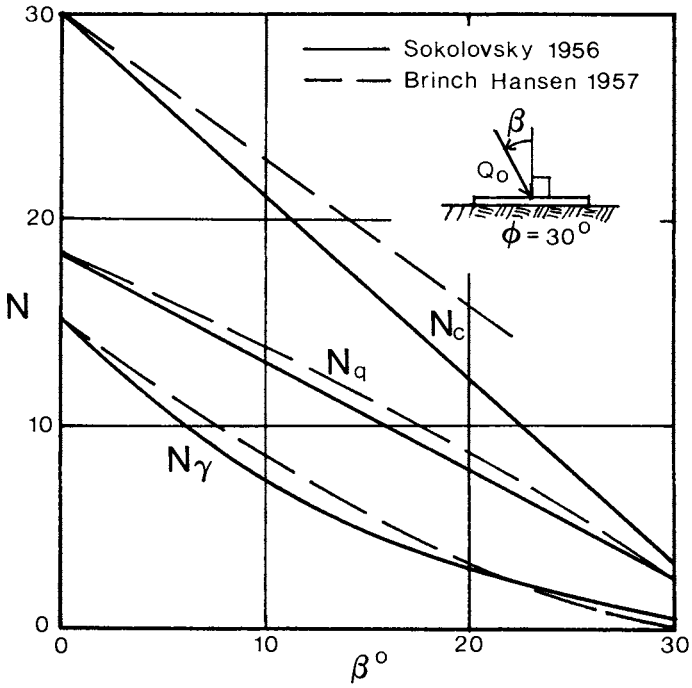

Fig. 3.9. Bearing capacity formula N factors under inclined loads as estimated by Sokolovski (1956) and Brinch Hansen (1957).

The terms in Eqn. 3.12 and 3.13 are those illustrated in Fig. 3.7 and 3.8. Sokolovsky (1956) also examined the question of inclination of footing loads, and analyzed the problem by approximate solutions of the form shown in Fig. 3.8(b). A comparison is made of these calculations with those formulae proposed by Hansen (Eqn. 3.12 and 3.13) in Fig. 3.9 for a soil friction angle of 30°. Both methods have the same starting values for zero angle of load inclination in Fig. 3.9, and they can be seen to produce very similar results for the $N\gamma$ and N_q terms over the range of inclinations. The N_c term of Hansen is generally higher than Sokolovsky's, and there is evidently a difference in philosophy here. In fact, the two methods would also yield

comparable results if the H/V term in Eqn. 3.13 were multiplied by 1.64 instead of 1.30.

For the case of a square footing, Eqn. 3.12 and 3.13 are similar to the ideas proposed by Terzaghi (1943) in which the cohesional bearing capacity is increased by 20% over the long strip footing, and the soil self weight term decreased by 20%. For a circular foundation of radius r, Terzaghi (1943) proposed the following formula.

$$q_o = 0.6\gamma rN\gamma + 1.2cN_c + qN_q \qquad (3.14)$$

The first term involving soil self weight contains the factor 0.6r = 0.3B, where B is the circular footing diameter. This is a smaller factor than 0.4B proposed for a square footing, since the circular footing has a smaller width towards the ends than at the center, and thus a variable depth of influence in the soil. As a result, the depth of influence and corresponding soil weight pressure are less near the edges than under the footing centre.

3.1.5. Effect of soil water

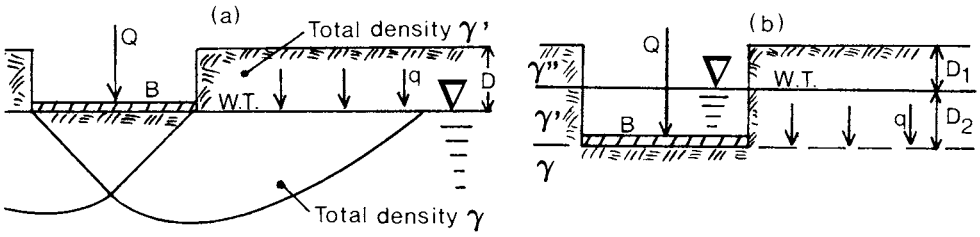

Fig. 3.10. Shallow footings on a soil with a water table (a) at the footing depth and (b) above the footing base.

If a soil is saturated below a shallow footing and the water is not moving, then static water pressure acts within the soil and one must consider effective intergranular stresses in calculating frictional shear resistance, as discussed in Chapter 2. Fig. 3.10 demonstrates two possible cases involving water in the subsoil. In case (a) the water table is at the base of the footing. In a granular soil, the water pressure will be nearly zero at that level, and the full amount of the surcharge pressure, $q = \gamma' D$, will apply there vertically. However, the effective soil density below the water table is reduced by water pressure (the buoyancy effect) and normal stresses on the soil failure surfaces reduced. For this case, the ultimate bearing capacity expression, Eqn. 3.3, can be rewritten as:

$$q_o = \gamma_{buoy}(B/2)N\gamma + cN_c + qN_q \tag{3.15}$$

where $\gamma_{buoy} = \gamma - \gamma_w$ (3.16)

and γ_w = the weight density of water = 9.8 kN/m^3

In case (b), the water table is higher than the foundation base, and is partway into the surcharge material. Here some of the surcharge pressure is reduced by water pressure, and there are at least three possible total material densities corresponding to the soil beneath the footing, and to those portions of the surcharge mass which are saturated or not. An effective surcharge pressure, q', can be used in this case in Eqn. 3.15, where:

$$q' = \gamma''D_1 + (\gamma' - \gamma_w)D_2 \tag{3.17}$$

The densities γ'' and γ' are the total densities, comprising the weights of solids plus water per unit volume, of the surcharge material at the expected moist and saturated water contents.

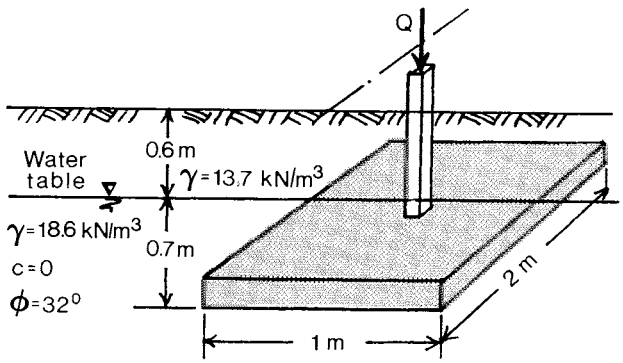

Fig. 3.11. Shallow footing example for Problem 3.2.

Problem 3.2. Fig. 3.11 shows a rectangular footing of width 1 m and length 2 m to be constructed at a depth of 1.3 m in a sandy soil. If the water table is at a depth of 0.6 m, and the soil densities and strength properties are as shown, what will be the ultimate central bearing capacity force, Q_{ult}? (It must be remembered that the design force should be less by the safety factor 3.0.)

For a granular soil, the bearing capacity Eqn. 3.12 can be modified to account for buoyancy effects both below and above the footing base. It will take account of the rectangular shape (B/L=0.5) as well. From Appendix 1, the appropriate bearing capacity factors are $N\gamma$=22.5 and N_q=23. The soil buoyant

density below the footing should be used in the first term of Eqn. 3.12 instead of γ.

$$\gamma_{buoy} = (18.6\text{-}9.8)\ kN/m^3 = 8.8\ kN/m^3$$

For the second term in Eqn. 3.12, which represents the effect of the depth of footing placement, the net pressure on the soil beside the footing base (Eqn. 3.17) should be used in place of the quantity γD.

$$q' = [13.7x0.6 + 8.8x0.7]\ kPa = 14.4\ kPa$$

The ultimate bearing capacity pressure and force are thus;

$$q_o = [8.8x0.5x22.5(1\text{-}0.3x0.5) + 14.4x23(1\text{-}0.2x0.5)]\ kPa = 382\ kPa$$

$$Q_{ult} = 382\ kPa x 1m x 2m = \underline{764\ kN}$$

3.1.6. Layered soils

Soils in real field situations are often not uniform with depth. If discrete layers having widely differing strength properties are found, it is not always simple to find representative soil strength and density parameters to plug into the bearing capacity equation. Button (1953) showed how an estimation of bearing capacity can be made for a cohesive soil having two layers of different strength. He proposed a modification to the N_C factor for bearing, depending on both the relative magnitudes of cohesional strength, and the relative depth of the boundary between the two layers. His analysis was based on a simplified circular soil failure shape beneath a strip footing, which has been shown to provide reasonable accuracy for cohesive soils (Skempton, 1948).

As Fig. 3.12 shows, the top horizontal cohesive soil layer is considered to have cohesion c_1, and the lower c_2. By a consideration of the equilibrium of moments tending to rotate the soil and footing, Button (1953) calculated the effective bearing capacity factor, N'_C by which the upper layer cohesion should be multiplied in order to estimate the ultimate bearing capacity pressure as follows.

$$q_o = c_1 N'_C \qquad (3.18)$$

The above procedure is equivalent to calculating a weighted average of the upper and lower layer values of cohesion, in the proportion of length of slip semi-circle over which each one acts. Fig. 3.12 gives the appropriate values of N'_C for various ratios of layer depth to footing width, D/B, and lower to upper layer cohesion magnitudes, c_2/c_1.

In the case of a layered soil with considerable frictional strength, the analysis is not as simple. However, a rough estimate can be made of weighted average strength parameter values which could be used in the standard bearing

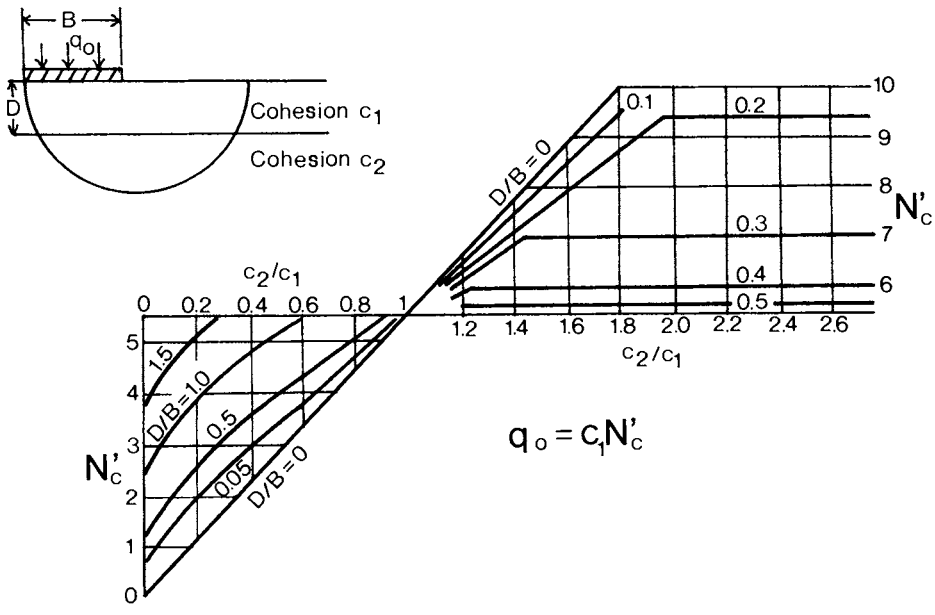

Fig. 3.12. The N'_c bearing capacity factor on a layered cohesional soil (Button, 1953)

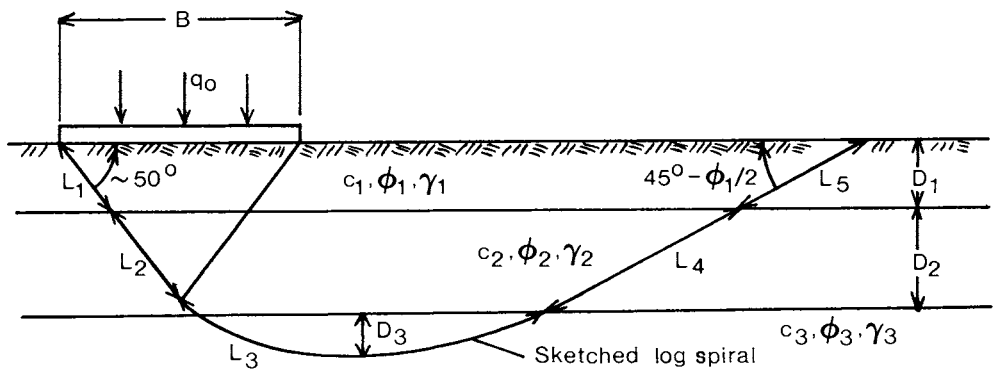

Fig. 3.13. Approximate analysis of bearing capacity in a layered soil having both frictional and cohesional strength components.

capacity equation. As Fig. 3.13 indicates, the slip surface in the soil can be divided into lengths contained within each soil layer. In the example shown, three distinct layers are present, and the weighted average soil properties which could be used are:

$$\gamma = (\gamma_1 D_1 + \gamma_2 D_2 + \gamma_3 D_3)/(D_1 + D_2 + D_3) \tag{3.19}$$

$$c = [c_1(L_1 + L_5) + c_2(L_2 + L_4) + c_3 L_3]/[L_1+L_2+L_3+L_4+L_5] \tag{3.20}$$

$$\phi = [\phi_1(L_1 + L_5) + \phi_2(L_2 + L_4) + \phi_3 L_3]/[L_1+L_2+L_3+L_4+L_5] \tag{3.21}$$

The same principle could be used for two or four layers if so desired, and at least a crude estimate of ultimate pressure can be obtained using these average parameters in the bearing capacity equation.

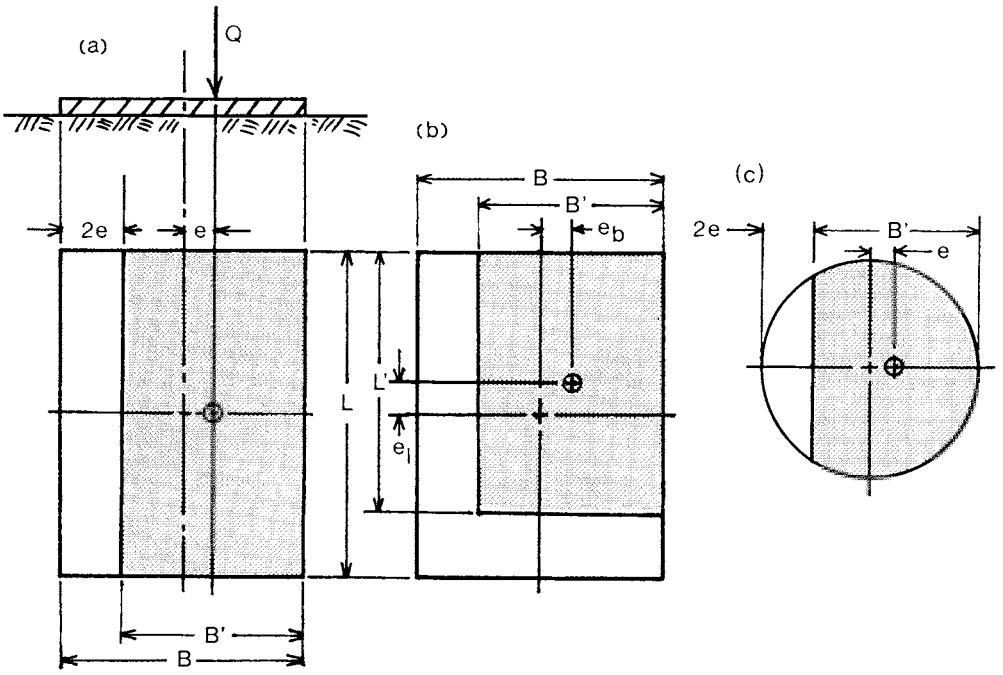

Fig. 3.14. The effective bearing areas of footings having eccentric loading for the cases of (a) eccentricity in one direction, (b) eccentricity in two directions and (c) a circular footing.

3.1.7. Eccentric loading

If the center of applied load is not at the centroid of a rectangular or circular foundation, then the pressure distribution on the subsoil cannot be expected to be symmetrical. Meyerhof (1953) showed that on a cohesive soil, it is appropriate to identify a useful portion of the footing surface which is symmetric about the load center. The remaining area of the footing is assumed simply to be superfluous. In Fig. 3.14(a), a single eccentricity, e, is considered, the load Q being centered on a point at distance e sideways from the footing centerline. Taking, then, the effective useful footing to extend equal distances, B/2-e, on each side of the load point, a new effective width, B', is found. The shaded area of the footing in Fig. 3.14(a) is considered to be the useful bearing area, and the bearing capacity computed accordingly. The effective width and bearing area are calculated as follows.

Effective width $B' = B - 2e$ (3.22)

Effective bearing area $A' = B'L$ (3.23)

In the case of double eccentricity, as shown in Fig. 3.14(b), the same principle can be used to find reductions in both the useful or effective width

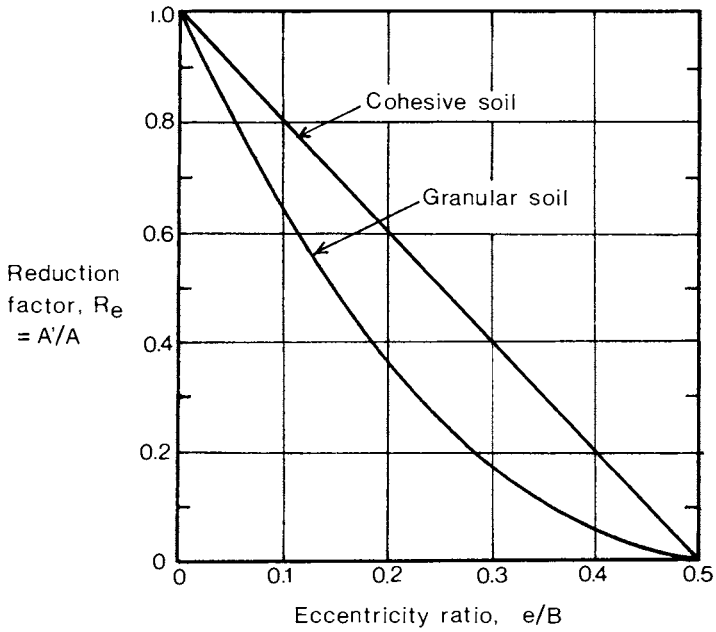

Fig. 3.15. The bearing capacity reduction factor for eccentric loading in the cases of cohesive and granular soils (Meyerhof, 1953).

and length, as in Eqn. 3.22, and the useful bearing area found as;

$$\text{Effective bearing area} \quad A' = B'L' = (B - 2e_b)(L - 2e_l) \tag{3.24}$$

When a footing is circular, as depicted in Fig. 3.14(c), the useful width, B', is calculated in the same manner as for the rectangular case with single eccentricity, Eqn. 3.22. This useful width, or the useful radius, r'=B'/2, is used in the bearing capacity expression for circular foundations, Eqn. 3.14, with conservative results.

For all of the above foundation configurations, the reduction factor, R_e, is the ratio of the useful bearing area to total footing area for a certain loading eccentricity, and is calculated as follows.

$$\text{Reduction factor} \quad R_e = A'/A \tag{3.25}$$

Meyerhof (1953) found that the proportional reduction in bearing area described above does not function well in granular, frictional soils, but only in cohesive soils. He determined that the effective bearing area reduction factor is more a parabolic function of eccentricity in granular soil than a linear one, and proposed the relationship given in Fig. 3.15. In the latter case, the granular soil reduction factor should be utilized to multiply the total footing area in order to estimate the useful bearing surface.

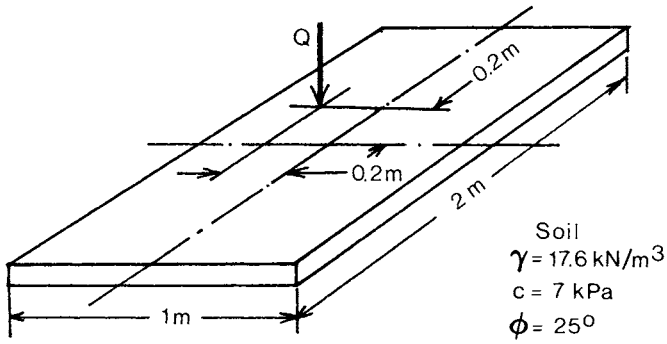

Fig. 3.16. A footing with eccentric loading for Problem 3.3.

Problem 3.3. A rectangular footing on the soil surface is illustrated in Fig. 3.16. The point of action of the load, Q, is off the centre of the footing by 0.2 m in both directions as shown. What design load could be applied to the footing on the unsaturated soil described?

The effective width and length of the footing can be estimated as;

$B' = B - 2e = (1.0 - 0.4)m = 0.6$ m, and $L' = (2.0 - 0.4)m = 1.6$ m

Since the footing is rectangular and rests on a soil having both cohesion and internal friction, the expressions of Hansen (Eqn. 3.12 and 3.13) can be added with the substitution of the foundation width reduced due to load eccentricity. For an angle of internal friction, $\phi=25^{o}$, the bearing capacity factors from Appendix 1 are $N\gamma=6.3$ and $N_c=21$, and the width to length ratio, $B'/L'=0.375$.

$$q_o = 0.5\gamma B'N\gamma(1 - 0.3B'/L') + cN_c(1 + 0.2B'/L')$$

$$= [17.6x0.5x0.6x6.3(1 - 0.113) + 7x21(1 + 0.075)]kPa$$

$$= 188 \text{ kPa}$$

The design footing load is then the ultimate bearing capacity, q_o, multiplied by the useful or effective bearing area, B'L', and divided by the usual safety factor of 3.0.

$$Q_{design} = q_o B'L'/SF = 188 \text{ kPa} \times 0.6m \times 1.6m/3 = \underline{60 \text{ kN}}$$

3.2. FOUNDATION SETTLEMENT

3.2.1. Traditional prediction methods

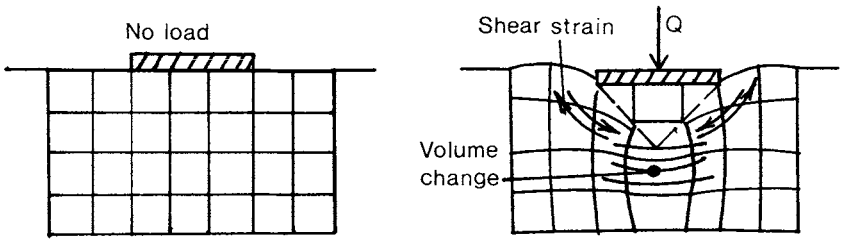

Fig. 3.17. The settlement of footings in soil generally involves both shear strain and volume changes.

When soils are subjected to loading stresses, they respond by deforming, as indicated by the stress-strain behavior examples given in Sections 2.4 previously. Underneath a foundation, these soil strains translate into a subsidence of the soil surface, and sinkage of the structure. Both changes in specific volume of the soil material and shear strains can contribute to foundation settlement, as shown in Fig. 3.17. In the case of coarse-grained materials (sand and gravel), most of the soil deformation takes place within a few minutes of time. In a wet fine-grained material, such as silty or clayey soil, there is some initial settlement upon loading of a foundation, and there is also slow settlement arising from shear "creep" of the material, and consolidation accompanied by slow water movement within the soil. These latter phenomena will be discussed subsequently in Chapter 4, and only the short term soil deformations leading to "initial" foundation settlement will be treated in this Section.

Taylor (1948) suggested different settlement versus loading behaviors for cohesive as opposed to cohesionless soils. When settlements are small, he reasoned that coefficients of settlement can be calculated for each particular soil, assuming that deformations are approximately proportional to applied load Q. In the case of cohesionless soils, the settlement coefficient appears in practice to be dependent upon the size of the footing, and the relation below was proposed.

$$z = qBC_2 \tag{3.26}$$

where z = foundation settlement,
q = average foundation bearing pressure
C_2 = a soil settlement constant (in units of pressure^{-1})

In the case of a cohesionless soil, absolute settlements seem to be almost independent of footing width, B, for the same loading pressure, and Taylor (1948) proposed;

$$z = qC_1 \tag{3.27}$$

where C_1 = a constant coefficient (settlement per unit pressure)

Terzaghi and Peck (1967) added some sophistication to the formula for settlement on cohesionless soil by noting some effect of footing width. They proposed that a test footing can be loaded vertically to a certain pressure level and the settlement measured. Then the settlement of a proposed foundation (usually larger than the test model) can be estimated for the same loading pressure as shown below.

$$\frac{z}{z_o} = \frac{4}{(1 + B_o/B)^2} \tag{3.28}$$

where z = the settlement of a proposed footing
z_o = the settlement of the test footing
B = the width of the proposed footing
B_o = the width of the test footing

Field tests have shown the above formula to be approximately correct, although actual results of full scale footing settlement measurements show considerable scatter about the predicted values, (Bjerrum and Eggestad, 1963; Lambe and Whitman, 1979). The predictions of Eqn. 3.28 must be based on loading a test footing to the same pressure as the proposed foundation, and do not give an indication of the shape of the load-settlement curve.

3.2.2. Pressure-settlement curves - Bekker's formula

Bernstein (1913) and Goriatchkin (1937) had proposed a curved relationship for applied pressure versus the settlement of rigid plates on the soil surface, following a power law as shown below.

$$q = kz^n \tag{3.29}$$

where k = a soil stiffness constant (units of pressure/sinkage^n)
z = total plate settlement
n = a constant exponent for a soil

This relationship is useful for approximating the shape of a pressure-sinkage curve in a real soil quite well in most cases, but it cannot take account of the size dependency for different scales of footing width. In 1956, Bekker presented a synthesis of the power function for sinkage curves, together with a size factor similar to that of Taylor (1948) and proposed a general sinkage formula which could be used for both cohesional and cohesionless soil types, as follows.

$$q = (k_c/B + k_\phi)z^n = kz^n \tag{3.30}$$

where k_c and k_ϕ = soil stiffness constants, independent of width B.

In SI or Imperial units, the dimensions of these constants are;

k_c: kPa/m^{n-1} or psi/in^{n-1}, k_ϕ: kPa/m^n or psi/in^n

Bekker (1960) did find that for circular plates resting on soil, B should be the radius of the footing, whereas B is the width (smaller than or equal to the length) of a rectangular or square footing. This concept is similar to the reduction of circular footing effective width for bearing capacity estimations, as proposed by Terzaghi (1943) in Eqn. 3.14 above.

In order to calculate the three soil constants of Eqn. 3.30, at least two sinkage tests must be performed on test footings of differing width, with

settlement measurements taken for progressive levels of vertical load. Then by graphical or analytical means, the exponent, n, and the stiffness constant, k, can be found for each footing size. An example of the technique is shown in Fig. 3.18, wherein average loading pressures are plotted versus observed total sinkage values for two footings on log-log scales. The theoretical curve shape on log-log paper is a straight line with the equation:

$$\log(p) = \log(k) + n \log(z) \qquad (3.31)$$

Then n is the slope of the line, and k can be found as the intercept with the vertical axis through log(z)=0, or z=1 (either 1 m or 1 in), as indicated in Fig. 3.18. Rather than relying on graphical methods and "eyeballing" of the best fit straight line to a set of experimental points, it is simple nowadays to perform a linear regression on the logarithms of pressure and sinkage values measured in sinkage tests, by using an electronic calculator (or a

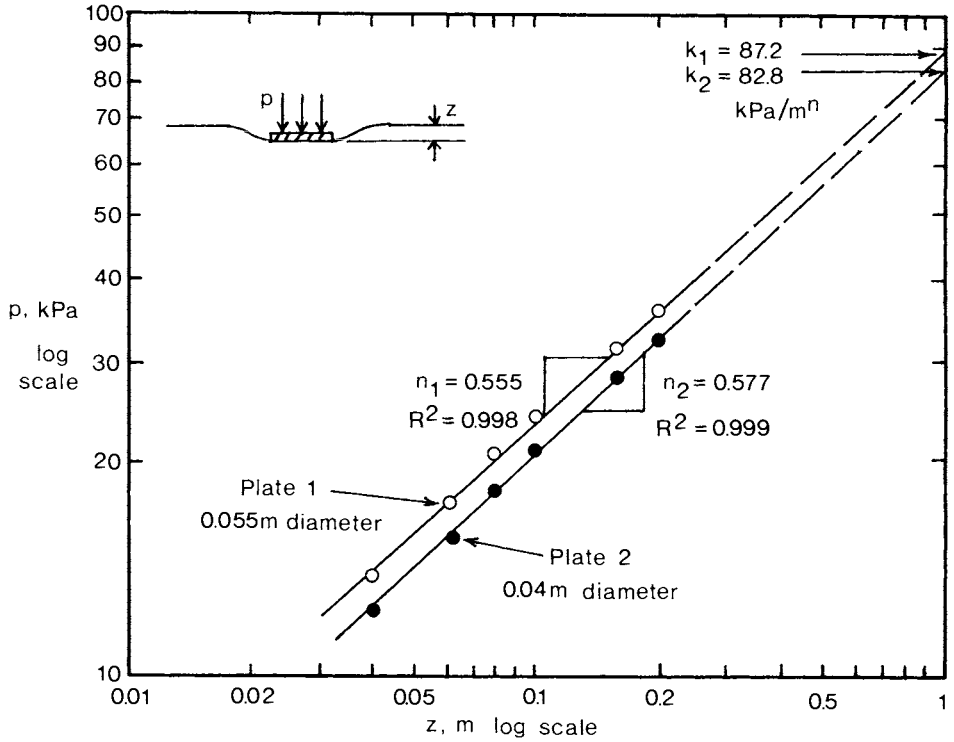

Fig. 3.18. Graphical determination of sinkage parameters n and k using plate sinkage measurements (data from Fan, 1985).

computer). The slope and intercept resulting from the regression for a particular sinkage test will be the exponent, n, and log(k), respectively. Having two values for k corresponding to two plate widths, B, one can solve for the three constants k_c, k_ϕ and n as shown below, using the the example values from Fig. 3.18.

$$k_c = B_1B_2(k_1 - k_2)/(B_2 - B_1) = -0.323 \text{ kPa/m}^{n-1} \quad (3.32)$$

$$k_\phi = (k_2B_2 - k_1B_1)/(B_2 - B_1) = 71.1 \text{ kPa/m}^n \quad (3.33)$$

$$n = (n_1 + n_2)/2 = 0.566 \quad (3.34)$$

Considering the variability of soil mechanical properties, even within a small volume of the material, it is a risky proposition to estimate the above settlement constants from the results of only two plate sinkage tests. Fan (1985) and McKyes and Fan (1985) have shown that the statistical errors involved can be reduced substantially by employing a series of three, four or five settlement tests with plates of different sizes. Measurements were conducted in a uniformly prepared sand using five circular plates having diameters ranging from 3.5 to 5.5 cm. When each pair of tests is compared, values for sinkage constants k_c, k_ϕ and n can be obtained by Eqn. 3.32 to 3.34 above. Thus for five plate sizes, ten combinations of two plates each are possible, and ten different magnitudes of the sinkage constants can be calculated. After conducting 20 such test series of five plates each, Fan (1985) found that the coefficient of variation (standard deviation divided by the mean value) can range between 50% and 125% for k_c, and from 18% to 35% for k_ϕ, using pairs of plates as described above. The variation in the values of n were considerably smaller, averaging 1.5%.

If more than two individual settlement tests are used to find the sinkage constants, the linear Eqn. 3.32 and 3.33 cannot be used, since there are three or more different values of k and B to compare. What is required is a best fit procedure using variables k from each test and the reciprocal of width, 1/B, as indicated in Eqn. 3.30. The slope and intercept of such a linear regression will be k_c and k_ϕ, respectively. An example graphical representation of this procedure is given in Fig. 3.19, while the values of slope, k_c, and intercept, k_ϕ, are more accurately computed using a calculator linear regression.

Fan (1985) demonstrated that the confidence in sinkage contants increases markedly if sets of three or four plates having different sizes are used for settlement tests. Table 3.1 gives the average coefficients of variation in the constants for four series of sinkage tests, using increasing numbers of plates. It is evident that in the type of soil tested, improvements in the confidence of the k values can be improved by more than five times if four plates of different widths are used instead of two.

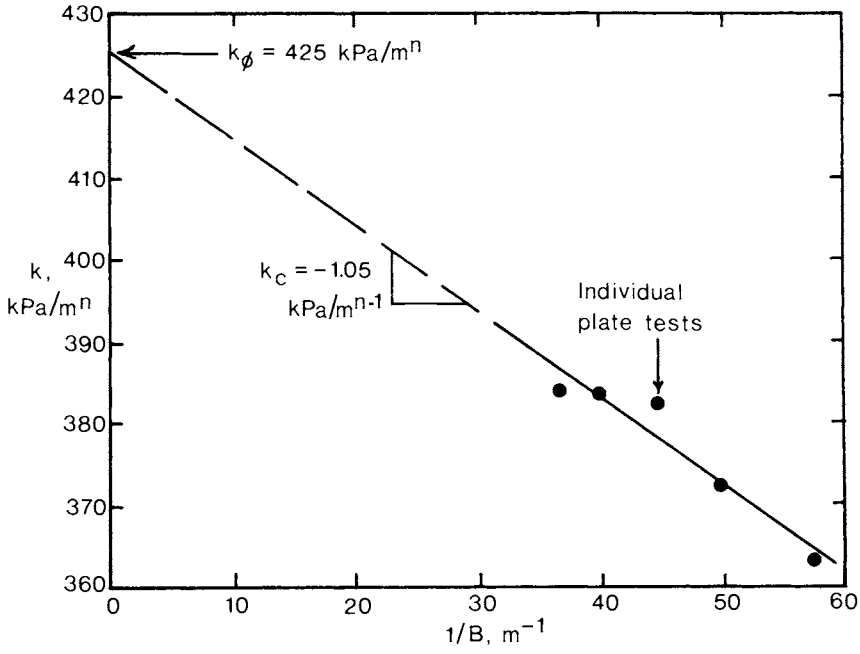

Fig. 3.19. Graphical determination of k_c and k_ϕ parameters.

TABLE 3.1. Average coefficients of variation of sinkage constants when different numbers of plates are used (McKyes and Fan, 1985).

No. plates used	Average coefficient of variation, %		
	k_c	k_ϕ	n
2	81.6	26.3	1.5
3	27.0	7.2	1.1
4	15.6	4.6	0.7

Fan (1985) also demonstrated that the sinkage constants computed using a series of four or five different plates can be used successfully to describe the settlement behavior of a larger footing. Having tested five circular plates of diameters ranging from 4.5 to 6.5 cm, he calculated the sinkage constants and employed them to predict the pressure versus sinkage values of a 15 cm diameter plate. These predicted values of pressure were all within 10% of actual measured magnitudes for the various sinkages of a 15 cm plate on the same soil, (McKyes and Fan, 1985).

However, one cannot expect that the extrapolation of sinkage constants obtained from small plate tests can be extended to very large footings, which are several orders of magnitude wider. The experience cited above shows that such a procedure is feasible to a scale multiplication of at least three, and perhaps it is possible for a factor up to ten. But without substantiating evidence, one would be wiser to use model plate settlement tests with widths not less than one quarter or so of the design foundation dimension. Sinkage tests are more economical when smaller model footings are used because less load needs to be carried to the field. Nevertheless, the closer that one can approach the actual design foundation width using model footings, the more accurate the predicted settlement behavior is likely to be.

Problem 3.4. A series of sinkage tests is performed on a bare sandy loam soil using three circular plates having diameters, d, of 5, 7.5 and 10 cm. If the measurements of cumulative sinkage depths versus applied vertical pressure are those shown below, what are the sinkage constants in Eqn. 3.30 for this soil?

d_1, cm	p, kPa	z, cm	d_2, cm	p, kPa	z, cm	d_3, cm	p, kPa	z, cm
5	50	0.4	7.5	50	0.6	10	50	0.8
	100	1.0		100	1.6		100	1.9
	200	2.7		200	4.4		200	5.3
	300	4.8		300	7.9		300	9.8

For each of the three plates, the sinkage measurements are changed to units of metres, and these together with the applied pressures are converted to logarithmic values to fit Eqn. 3.31. Then a least squares linear regression can be performed to find the best fit values of log(k) and exponent n for each plate. These results are shown below.

d, cm	5	7.5	10
k, kPa/m^n	2683	1751	1602
n	0.719	0.694	0.711

The effective exponent, n, for this site can be estimated as the average of the three calculated values.

$$n = (n_1 + n_2 + n_3)/3 = 0.71$$

Since the test plates are circular, then each radius, r=d/2, is used instead of plate width, B, in Eqn. 3.30. The values of k_c and k_ϕ are best estimated by performing another linear regression with the variables 1/r and k as x and y. Following the form of k in Eqn. 3.30, k_c will be the slope of this linear regression, and k_ϕ the intercept.

$$k = (\tfrac{1}{r})k_c + k_\phi$$

$$k_c = 56.3 \text{ kPa/m}^{n-1} \text{ and } k_\phi = 385 \text{ kPa/m}^n$$

(Correlation coefficient R = 0.98)

3.3. PRESSURE DISTRIBUTION UNDER FOUNDATIONS

The theory of elastic materials can be used to calculate the distribution of pressure underneath a rigid footing, but the results often do not match what occurs in practical experience. Terzaghi and Peck (1948) and Scott (1963), among others, have shown that the stress patterns under rigid footings have different characteristics depending on the soil type. On a cohesive soil, for example, vertical pressure distributions closely resemble those predicted by elastic theory. An example is given in Fig. 3.20(a) together with approximate magnitudes of the pressures under a long strip foundation having a vertical loading along the centreline.

On a cohesionless soil, however, the pattern changes, with greater pressure being observed near the footing centreline, as shown in Fig. 3.20(b). This discrepancy does not make a great difference to the internal forces within the footing itself. The shear force diagrams for both cases are given in Fig. 3.20, and despite a slightly different shape, both soils will result in the same maximum shear force at the foundation centreline. (The convention used is that positive shear force is counterclockwise acting.) There is more variation in the magnitude of bending moments of the two cases. As shown in the figure, the cohesive soil footing has about 50% more bending moment at the centre than that on the frictional soil (downwards bending action positive). With these results, structural design techniques can be used to design the foundation slab to be safely strong for the expected loading and soil reaction.

There are other types of foundation loadings, and an example is given in Fig. 3.21. This is a wide raft type of footing which acts both as the building floor and as the foundation supporting the wall and roof weights. Since the footing is wide, it can be assumed that the pressure distribution in the soil is nearly uniform as shown. The pressure diagram is the same as that of a simply supported, uniformly loaded beam turned upside down, and the shear force and

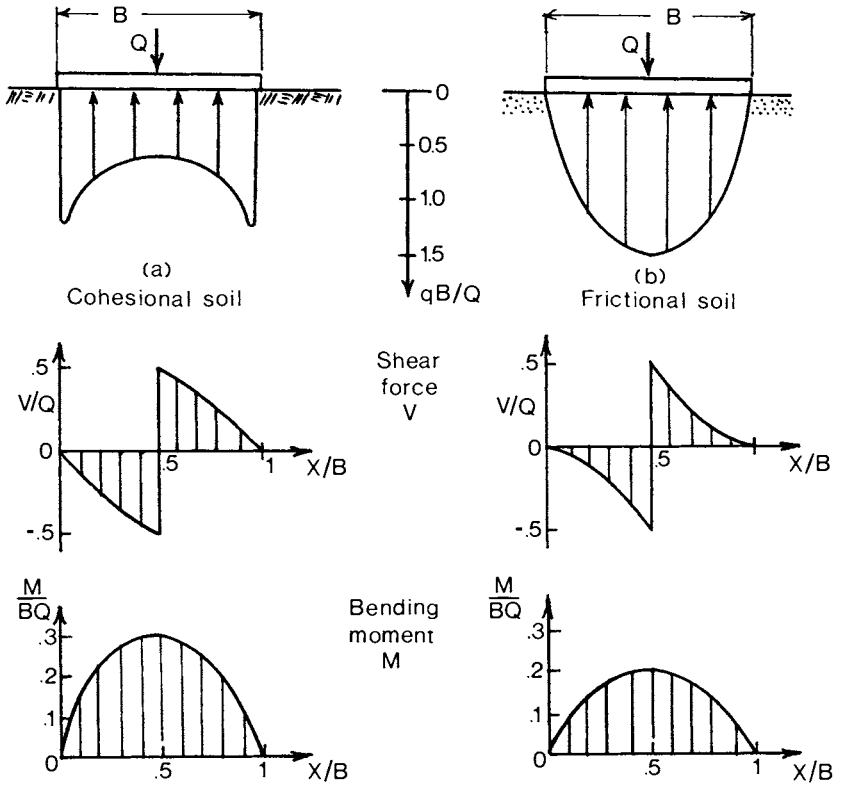

Fig. 3.20. Groundpressure distributions, shear forces and bending moments in footings on (a) cohesional and (b) frictional soils.

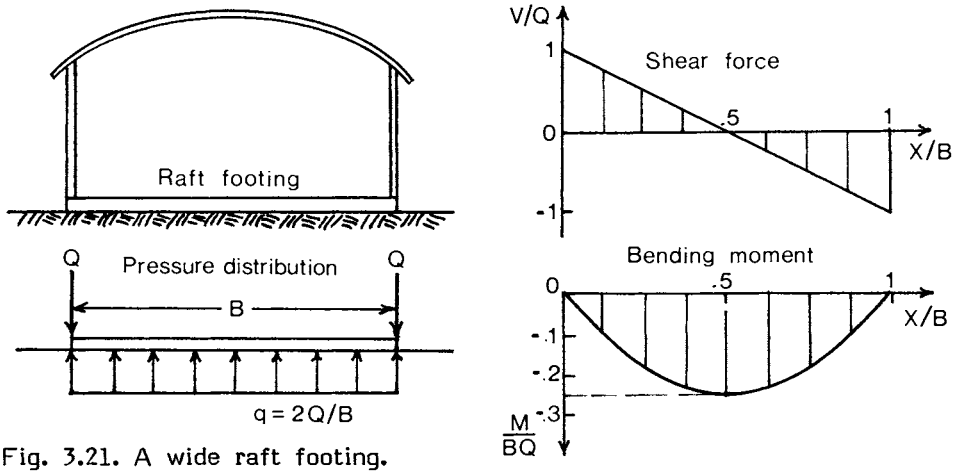

Fig. 3.21. A wide raft footing.

bending moment diagrams are similar to such a case. If the footing is considered to be rigid, then considerable bending moments can be generated along the centreline due to the relatively large size of width, B.

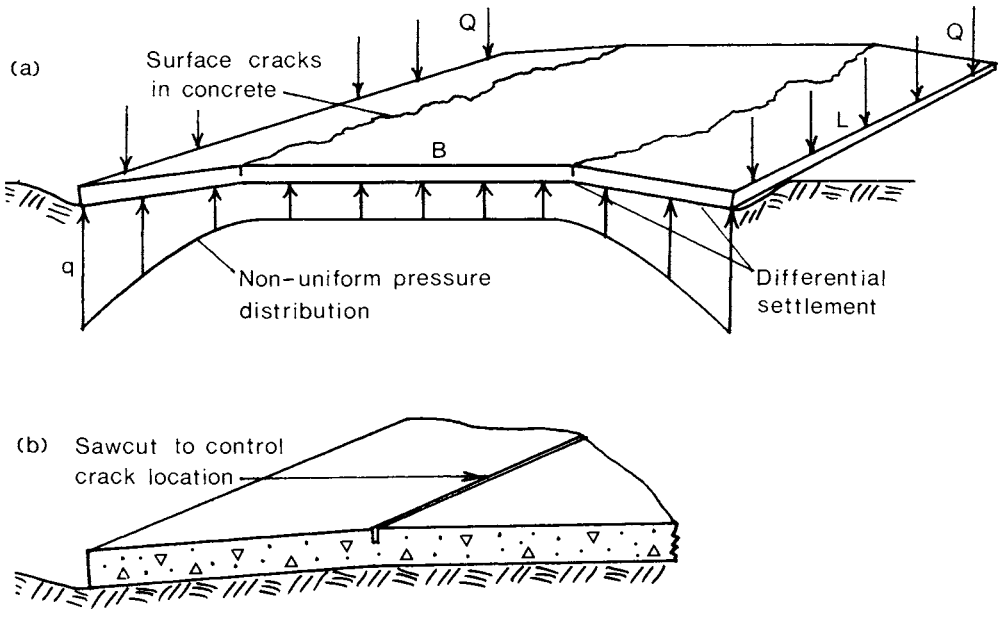

Fig. 3.22. The control of surface cracking in a wide raft footing.

What often happens in practice is that the sinkage of the soil is not uniform because the raft foundation is not perfectly rigid. In such a case, the bearing pressures tend to be larger near the ends of the footing than at the centre, as shown in Fig. 3.22(a). Increased soil settlement towards the outside edges of the floor develops higher soil reaction pressures. However, the differential settlements are usually too great for brittle concrete foundations to suffer without local material failure, and surface cracks are often observed in the floor.

A practice which is common in the construction of such wide "floor" foundations is to make shallow sawcuts in the top of the footing where cracking would be expected. The philosophy is that the floor cannot be expected to remain perfectly rigid on soil which exhibits differential settlement, but the sawcuts encourage local floor cracking to occur at their locations, thus permitting cracks in a more aesthetic straight line, Fig. 3.22(b).

3.4. TOWER SILO FOUNDATIONS

3.4.1. Bearing capacity

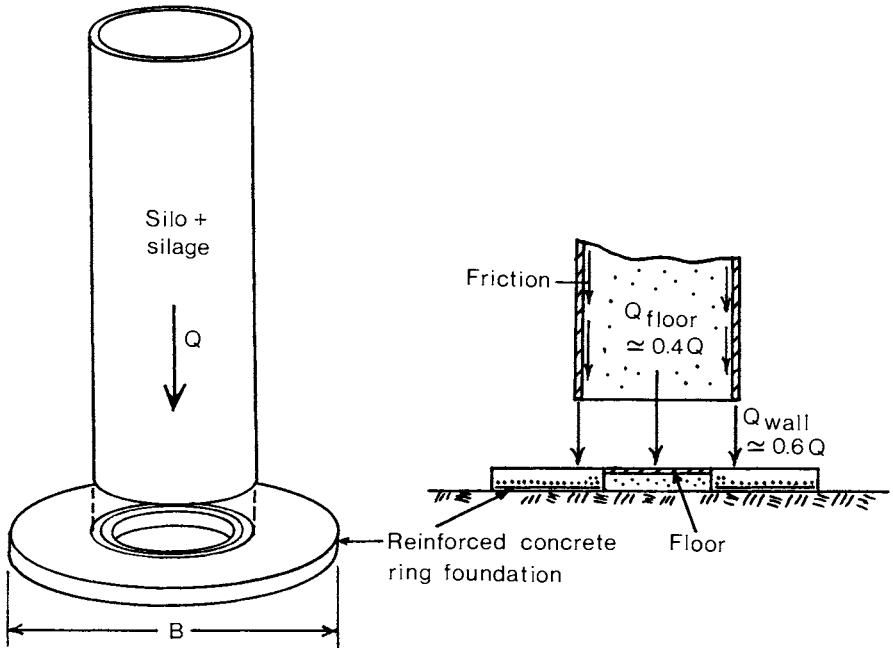

Fig. 3.23. Wall and floor force partition in a tower silo.

Foundations for tower silos present some unique problems owing both to the circular shape of silos, and to the large masses concentrated over small surface areas. Modern tower silos are commonly built with diameters of 7 to 9 m and heights of over 24 m, (Fig. 3.23). A silo of these dimensions can contain between 800 and 1300 t of corn or grass silage, and yet the base area is only 36 to 64 m^2. The average pressure over the base of the silo itself is thus in the order of 210 kPa (which is about 30 psi or 4400 psf).

The actual silage pressure on the floor is considerably less than the above figure since much of the silage weight is transferred to the wall by frictional force. For a silo with a three to one height to diameter ratio, approximately half of the total silage weight is supported by wall friction (Negi et al., 1977; Turnbull et al., 1979). Therefore, the vertical force at the wall base comprises about half of the total weight of contents, in addition to the weight of the structure itself and any attachments above ground, such as top unloaders and the like. A 7.3 m diameter by 24.4 m height concrete silo with 15 cm thick walls, for example, has a mass of over 200 t, bringing the total full silo mass

to about 1120 t. Of this, approximately 40% rests on the silo floor, while the remainder is supported at the wall base as shown in Fig. 3.23.

The design of a tower silo foundation must be approached from several viewpoints. Firstly, the overall average bearing pressure under the footing must be within the allowable range. For this purpose, the bearing capacity Eqn. 3.12 to 3.14 can be utilized to find the maximum possible bearing pressure on the particular soil in question. In order to find the allowable design bearing pressure, this maximum pressure, q_o, is divided by the appropriate factor of safety. (Subsequent discussion will suggest that this factor be 3.0.) The required overall width or diameter, B, of the ring foundation can then be found from the following expression. It calculates average bearing pressure, q, as the total weight of all the silo components, including the foundation itself, divided by the overall surface area within the bounds of the foundation.

$$q = q_o/SF = Q/A = (Q_{silage} + Q_{silo} + Q_{footing})/(\frac{\pi}{4}B^2) \qquad (3.35)$$

where Q_{silage}, Q_{silo} and $Q_{footing}$ = total component weights.

Problem 3.5. A steel silo is planned to have a diameter of 7.3 m, a height of 24.4 m and a net mass of 30 t including the roof. The expected content of the silo is 820 t. What would be the necessary outside diameter of a 60 cm thick circular footing for this structure on the surface of a soft clay soil having c=25 kPa and a very small friction angle?

Although the total weight of the footing itself cannot be known before the diameter is found, its bearing pressure can be calculated as the unit weight of concrete (about 23.6 kN/m^3) times footing thickness, if the foundation is assumed to be a complete disc.

$$Q_{footing}/A = 23.6\ kN/m^3 \times 0.6\ m = 14.2\ kPa$$

Then Eqn. 3.35 can be rearranged by subtracting the footing bearing pressure from both sides, as follows.

$$q - 14.2\ kPa = q_o/SF - 14.2\ kPa = (Q_{silage} + Q_{silo})/A$$

The ultimate bearing capacity is calculated by Eqn. 3.14 for a circular footing, using the N_c factor from Appendix 1.

$$q_o = 1.2cN_c = 1.2 \times 25\ kPa \times 5.14 = 154.2\ kPa$$

The bearing capacity equation can then be evaluated as;

$$q - 14.2\ kPa = (154.2/3 - 14.2)\ kPa = (8036 + 294)kN/(\frac{\pi}{4}B^2)$$

from which B = 16.9 m is the required footing diameter.

3.4.2. Settlement and safety factor

A further consideration is the settlement of the structure, which should be a maximum of 2.5 cm for a successful design, (see Table 3.2). There are at least two ways in which to assess this aspect of the foundation. Model footing settlement tests could be performed at the selected site, and their results used to estimate the sinkage constants of Eqn 3.30 above. However, this can be a time consuming and costly practice, especially since large loads must be carried to the site in order to create plate bearing pressures in the order of those expected in the actual design.

TABLE 3.2. Performance criteria for tower silos (Ontario Silo Association, 1980).

Rating	Performance	Vertical settlement, mm	Tilt	
			Degrees	% height
A	Excellent.	Below 25	Below 0.2	Below 0.3
B	Good with slight problems.	25 - 75	0.2-0.5	0.3-0.8
C	Important problems.	75 - 150	0.5-1.0	0.8-1.7
D	Serious problems.	150 - 300	1.0-1.5	1.7-2.5
E	Very serious problems.	Over 300	Over 1.5	Over 2.5

Another way in which to reduce silo settlements to acceptable levels is to make the bearing safety factor sufficiently high that soil strains will be limited below the footing. For example, Morin and Bozozuk (1983) conducted a performance survey of 108 concrete tower silos sited on weak, compressible marine clay soils in the southern Quebec region. They based the performance ratings of the silos upon the amount of total settlement and tilt from the vertical. In 28 cases, footing settlement and tilt were measured for four years, and soil shear strength measurements taken at depths up to 12 m using a Nilcon shear vane.

From the soil strength measurements, the maximum bearing capacity of each of the silo foundations was estimated using Eqn. 3.13. The actual bearing pressure was calculated in each case, and divided into the maximum bearing capacity in order to estimate the safety factor. Individual safety factors are compared to the settlement and tilt measurements for the first loading cycle of each of the silos in Fig. 3.24.

Few of the silos tilted more than 0.3%, and none of those had an estimated safety factor greater than 2.5. Also, most of the silos with a safety

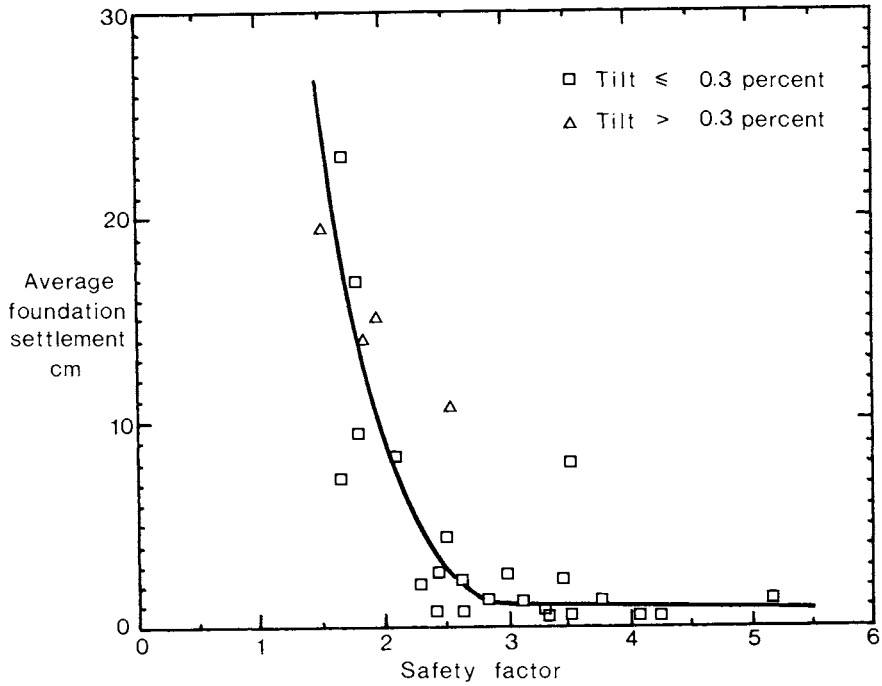

Fig. 3.24. A comparison of observations of average concrete tower silo settlements versus caculated safety factors (from Morin and Bozozuk, 1983).

factor less than 2.1 or so exhibited settlements of more than 8 cm, which is very likely to cause problems with operation and attached structures. On the other hand, those silos with calculated safety factors greater than 2.5 showed less than 3 cm settlement after the first loading, with only one exception.

Morin and Bozozuk (1983) gave a breakdown of the performance ratings of these silos in comparison to their calculated safety factors, as shown in Table 3.3.

Table 3.3 demonstrates that when a tower silo is sited on a weak compressible soil, it is preferable to employ a safety factor of 3.0 in order to ensure a successful foundation design. Such a safety factor makes it more likely that problems of excessive settlement or tilting will not occur.

TABLE 3.3. Performance ratings on concrete tower silo foundations on clay soil (Morin and Bozozuk, 1983).

Calculated Safety Factor	Performance Rating
≥ 3.0	Excellent
2.5	Very good
2.0	Tolerable, important problems could be expected
< 2.0	Generally unsatisfactory, serious problems could be expected

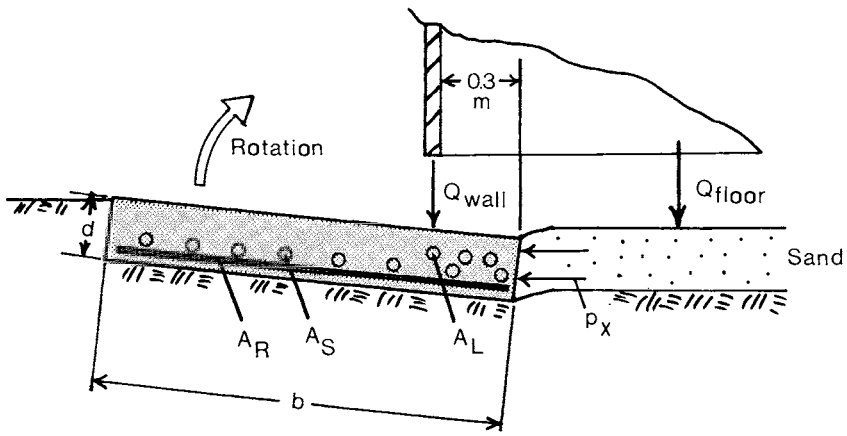

Fig. 3.25. A section through a tower silo extended ring foundation showing the tendency for rotation, and the location of internal reinforcing steel (from Turnbull et al., 1983).

3.4.3. Silo foundation design

The design of a ring foundation itself is a complex affair, and is closely linked to the related soil mechanics. Fig. 3.25 shows a section through part of a ring foundation, together with the load applied by the silo walls. There is an additional pressure, p_x, on the inside vertical face of the ring which is transferred through the underfloor sand from the floor loading. Canada Plan Service (1977) and Turnbull et al. (1979) described how the following elements should be included in the design of the ring footing.

A_R, radial reinforcing bars to resist bending

A_S, spiral reinforcing bars to prevent rotation of the ring

A_L, additional reinforcing to resist lateral pressure, p_x

b, the ring width to provide the necessary safe soil bearing area

d, the ring thickness sufficient for bending resistance

Turnbull et al. (1979) estimated the total loads of various sizes of concrete cast-in-place and stave silos, and calculated the required magnitudes of the design elements listed above. They found that the radial reinforcing bars specified in previous designs were not necessary provided that sufficient spiral reinforcing is installed. This spiral reinforcing can resist the tendencies of the ring footing both to rotate and to bend under the wall load, and the spiral reinforcing should be placed 10 cm from the bottom of the concrete footing. The results of their computations are given in Appendix 2 as a function of silo size and the safe soil bearing pressure. This safe bearing pressure is the ultimate bearing capacity, q_o, divided by the safety factor (preferably 3.0). Once the soil shear strength is known, (see Chapter 2), the ultimate bearing capacity can be found from Eqn. 3.13 and, in the case of cohesive soils, it is fortunately independent of overall footing diameter, B.

3.5. PILE FOUNDATIONS

3.5.1. Pile capacity

Piles are long slender structural units used to transfer loads to soil or rock. They can be made of wood, concrete or metal materials, and can have cross sectional shapes which are circular, square or H-shaped. Piles are utilized most commonly in structures associated with agriculture for the following specific purposes, as illustrated in Fig. 3.26.

(a) To carry weight through soft, weak soil layers to stronger strata.
(b) To distribute loads in weak soils along the pile length by means of shear stress or 'skin friction'.
(c) To resist an uplift or tension force as an anchor.

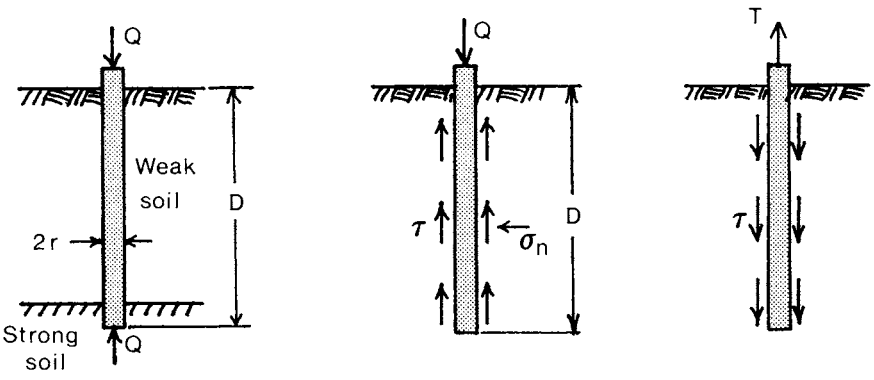

(a) End or point-bearing pile (b) Friction pile (c) Tension pile

Fig. 3.26. Three types of load bearing piles.

In the case of the end or point-bearing pile, it is assumed that the shear force along the pile length contributes a negligible amount to the load bearing resistance. The tip of the pile therefore serves as the bearing point, of which the ultimate capacity can be estimated like a foundation with an adaptation of Eqn. 3.14 below (Teng, 1962). As in foundation design, the ultimate bearing capacity of a single pile or group of piles should be divided by a safety factor (preferably 3.0) to arrive at the estimated design load.

$$Q_{ult} = \pi r^2(0.6\gamma r N_\gamma + 1.3cN_c + \gamma D N_q) \tag{3.36}$$

where r = the radius of a circular pile.

In the case of friction piles, practically the entire bearing capacity is considered to arise from the shear strength along the pile length, as follows.

$$Q_{ult} = 2\pi r \tau D \tag{3.37}$$

The nature of the pile to soil shear stress, τ, will depend on the type of soil and the deformations which the soil has undergone either during the pile installation or thereafter. In general, the interface adhesion-friction shear strength concept can be used.

$$\tau = s = c_a + \sigma_n \tan\delta \tag{3.38}$$

The difficulty with the above formula is the determination of the magnitude of the normal stress, σ_n, at different depths in the soil. The coefficient of lateral earthpressure at rest, K_o, relates the horizontal stress on the pile, σ_n, to the vertical pressure, σ_{zz}, at a particular depth.

$$\sigma_n = \sigma_{zz} K_o = \gamma z K_o \tag{3.39}$$

For straight smooth pile sides, the coefficient of earthpressure at rest suggested by Terzaghi (1943), K_o=0.5, can be used. Higher coefficients may be allowed for different shapes of pile. Ireland (1957) has suggested that K_o can be as high as 1.75 for step-tapered concrete piles, which become smaller in diameter with depth. The same Eqn. 3.37 can be used to find the tension load capacity, T, for uniform diameter tension piles as well, since the configuration of shear stress along the pile length is the same, only reversed in direction.

3.5.2. Pile groups

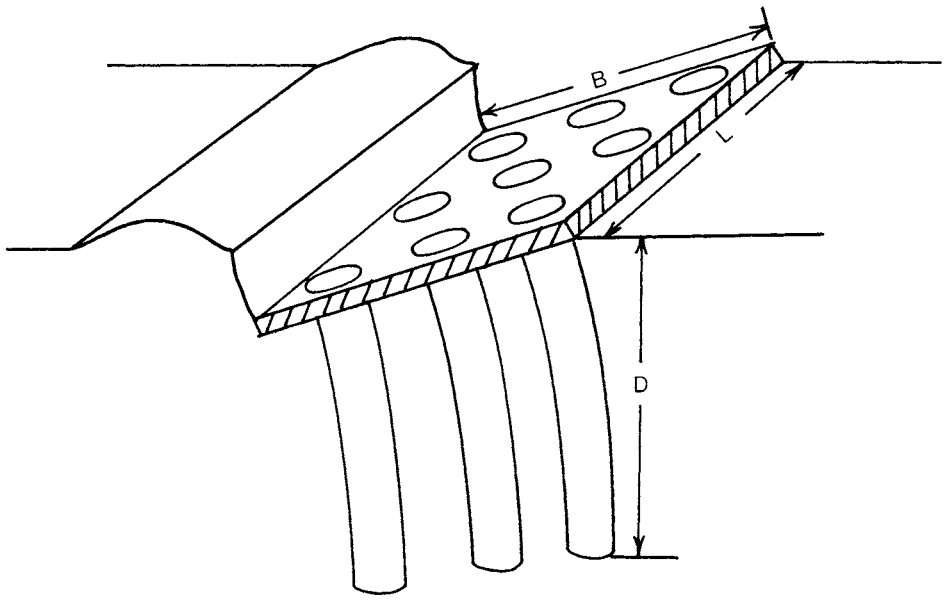

Fig. 3.27. Settlement of the end cap of a pile group.

It has been shown by Terzaghi and Peck (1967) that a connected group of friction piles in a silt or soft clay soil can settle together like a single foundation (Fig. 3.27). The formula below was proposed to describe the ultimate pile group bearing capacity, Q_g, for this case. B and L are the width and length of the pile cap, and q_{ult} is the ultimate bearing pressure of a rectangular foundation having the same length and width as the pile cap and a depth D. Soil internal shear strength s is the average value calculated over the range of depth, D.

$$Q_g = q_{ult}BL + D(2B + 2L)s \qquad (3.40)$$

Terzaghi and Peck (1967) noted further that such a pile group as illustrated in Fig. 3.27 can be considered safe if the total design load on the group is less than $Q_g/3$.

3.5.3. Negative skin friction

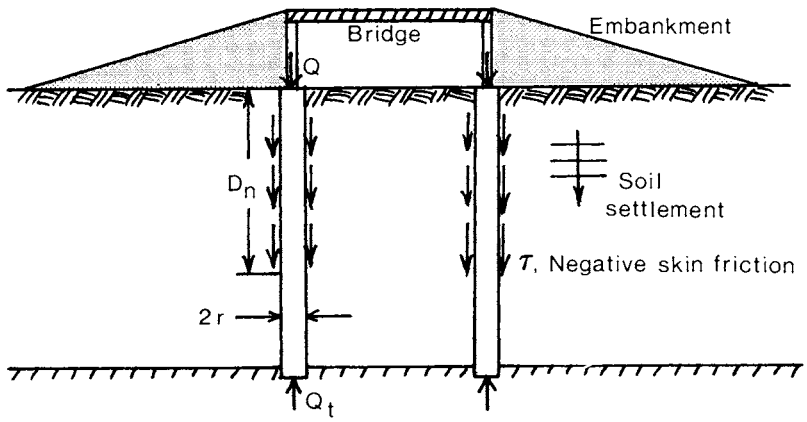

Fig. 3.28. Negative skin friction on deep end bearing piles due to soil settlement.

There are cases in which a load is carried by a pile, and additional downward force is applied by the drag of soil which is settling. Such an example is illustrated in Fig. 3.28 for the case of a highway bridge supported on piles, and adjoining an earth fill embankment on the soil surface. With time, the weight of the embankment causes consolidation and settlement of the subsoil surrounding the piles. In turn, the soil settlement results in a downward drag on the pile surface, which adds to the total vertical load which the piles must carry.

The amount of soil settlement may not be enough over the entire soil depth in order to cause appreciable downward drag, or negative skin friction, along the whole length of the piles. In Fig. 3.28, an effective depth, D_n, has been identified over which effective negative skin friction is considered to act. There is no exact rule for determining the effective depth, D_n. However, experience with shear testing of compressible soils would indicate that at least two or more mm of soil settlement relative to the pile movement is required to develop a major fraction of the soil to pile shear strength. Thus, by using the techniques described in Chapter 4.1.2 for estimating the consolidation settlement of a compressible soil at different depths, one could locate the depth at which, say 2 mm of soil settlement occurs in time, and identify that depth as D_n.

Having the depth D_n thus defined, the total load to be supported by the pile near the bottom can be estimated as the sum of the load carried at the top, and the downward drag of the surrounding soil. The negative skin friction shear stress, τ, cannot be greater than the ultimate shear strength of the soil to pile interface, $c_a + \sigma_n \tan\delta$. At any depth within D_n, the downward drag force per unit depth is;

$$dQ_t/dz = 2\pi r(c_a + \sigma_n \tan\delta) = 2\pi r(c_a + \gamma z K_o \tan\delta)$$

Thus
$$Q_t = Q + 2\pi r(c_a D_n + \tfrac{1}{2}\gamma D_n^2 K_o \tan\delta) \qquad (3.41)$$

where r is the pile cross-sectional radius, K_o is the coefficient of earthpressure at rest and z is the soil depth.

For smooth surfaced piles, the coefficient of lateral earthpressure at rest, K_o, can be estimated as 0.5. In cases where D_n is large, the second part of the total pile load, arising from negative skin friction, can be many times the load Q supported by the top of the pile. This can have important consequences for the design of the strength of the pile, as well as the required bearing capacity at the lower pile tip.

Problem 3.6. As illustrated in Fig. 3.29, a reinforced concrete pile carries a load on the top of 2000 t mass through a clay layer which is 45 m thick. Measurements of the soil properties have shown that the clay to concrete adhesion is 5 kPa and the angle of surface friction is 10^o. Also, the effective depth of negative skin friction is 25 m under the relevant conditions of soil settlement. If the pile can be designed to have a safe compressive strength of 35 MPa, what is the required pile diameter?

The force capacity of the pile is the design strength multiplied by the cross sectional area. Therefore, Eqn. 3.41 can be changed to;

$$Q_t = 35{,}000\,\pi r^2 \text{ kPa} = Q + 2\pi r(c_a D_n + \gamma D_n^2 K_o \tan\delta/2)$$

$$= 19{,}600 \text{ kN} + 1{,}220\,\pi r \text{ kN/m}$$

From which the required pile diameter $D = 2r = 0.88$ m.

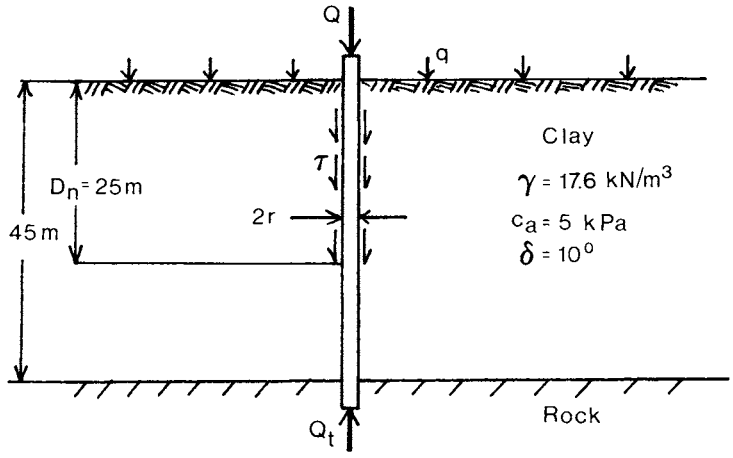

Fig. 3.29. A deep end bearing pile for Problem 3.6.

3.6. PROBLEMS

3.7. A long footing of width 1 m rests on the surface of an unsaturated silty sand which has a density of 17.6 kN/m^3, cohesion 15 kPa and internal friction angle 25^o. If the load on the footing is 120 kN/m, what is the safety factor of the design?

Answer: S.F. = 3.1.

3.8. A rectangular footing of length 1.5 m and width 1 m is constructed at a depth of 1 m in a silty soil. The soil has a dry density of 13.7 kN/m^3, a saturated density of 18.6 kN/m^3, cohesion 10 kPa and angle of internal friction 30^o. For the case of a water table situated at the footing base, and the soil above it relatively dry, find the safe load which can be carried by this footing.

Answer: Q = 339 kN.

3.9. A building column carries 200 kN vertically. It is desired to design a square footing for the column 1 m deep in a wet clay soil having C = 20 kPa and density 16.7 kN/m^3. What are the dimensions of the square footing for a safety factor of 3.0?

Answer: B = L = 2.1 m.

3.10. A clay field is measured to have k_c = 100 kPa/m^{n-1}, k_ϕ = 700 kPa/m^n and n = 0.5. A 1000 N load is placed on two plates, (a) 3x4 cm and (b) 4x4 cm, on the surface of the field. What are the expected settlements of plates (a) and (b) under this load? Are the settlements of the plates proportional to the pressures acting on them?

Answer: (a) z = 4.3 cm, (b) z = 3.8 cm. The settlements are not proportional to the pressures. Plate (a) has 33% more pressure on it but settles only 13% more than plate (b).

3.11. A tractor has rear tires with a ground contact length of 965 mm and a wheel load of 13.2 kN on each. On a soil with k_c = 30 kPa/m^{n-1}, k_ϕ = 100 kPa/m^n and n = 0.5, what width of tire, b, would be required in order to limit the rear tire sinkage to 50 mm?

Answer: b = 312 mm.

3.12. A farmer wishes to construct a grain storage silo of 4.9 m diameter by 9.1 m height to have a full mass of 200 t excluding the foundation. The proposed site is on a rather soft wet clay having an undrained shear strength of 17 kPa. What outside of diameter of a 45 cm thick circular foundation would be needed for a safety factor of 3.0?

Answer: B = 8.8 m.

Chapter 4. Water flow in soils

4.1. CONSOLIDATION AND SETTLEMENT RATES

Consolidation is defined as the gradual expelling of water from a nearly saturated soil and concurrent reduction in the total soil volume. The final amount of consolidation which will occur in a given soil depends upon the stiffness of the solid matrix of the soil, that is the increase of interparticle forces accompanying the bringing of particles closer together. The rate at which compression of a saturated fine grained soil will take place is a function also of the hydraulic conductivity (speed of water flow under a certain pressure gradient) and the distance which water must flow to escape the soil mass.

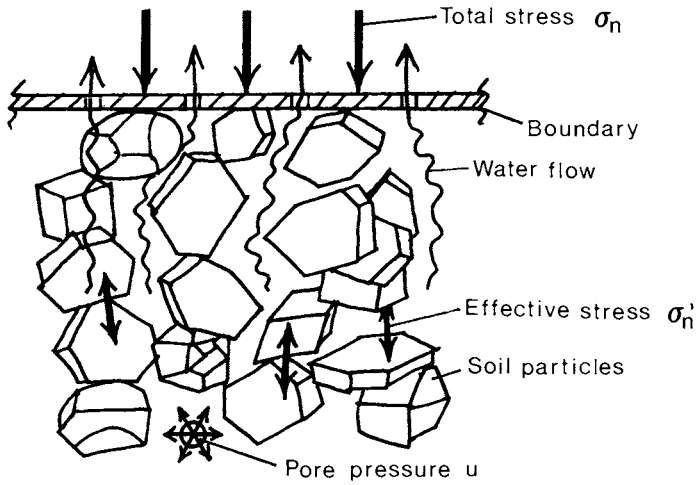

Fig. 4.1. Schematic diagram of soil consolidation.

Fig. 4.1 shows schematically what takes place during consolidation of a saturated fine grained soil. When the total stress, σ_n, is increased from the original equilibrium value, initially the pore water remains at its original volume within the soil, and supports virtually all of the pressure increase through an increase in pore water pressure, u. The excess pore pressure gives rise to a pressure gradient between the centre of the soil mass and the boundary, and water begins to flow to the outside. As the volume of water is decreased gradually the total soil volume decreases, allowing a closer

proximity of soil particles. The approaching of particles in turn causes their interacting repulsive forces to increase, thus decreasing the pressure in the water. When all of the additional total boundary stress is supported by the interparticle stress, then water flow ceases and the primary consolidation process is complete.

4.1.1. One dimensional consolidation

Terzaghi (1943) developed a theoretical analysis for the rate of consolidation for one dimensional flow of water in a uniform saturated fine grained soil, based on the following assumptions.

- Water flow velocity is proportional to hydraulic pressure gradient (Darcy, 1856).
- Water is incompressible compared to the soil particle matrix structure.
- Over a certain limit of volume change, the increase in effective or intergranular stress is proportional to the decrease in soil volume.

From the first assumption, the apparent velocity of water flow, v, that is the total volume of water passing through a unit cross sectional soil area per unit time, can be expressed as by Darcy's equation (1856) as follows.

$$v = ki = -k\frac{\partial h'}{\partial z} = -\frac{k}{\gamma_w}\frac{\partial u}{\partial z} \qquad (4.1)$$

Here, k is the hydraulic conductivity of the soil (in units of length per unit time) and h' is the excess hydraulic head, above the static head caused by water unit weight and depth. Here, pore pressure u signifies excess pressure above the static water head also, and is expressed in units of pressure. The second underlying assumption dictates that an increase in effective intergranular stress in the soil cannot occur before the soil particles approach each other through water movement and soil volume change. Before volume change occurs, the pore water supports all additions in total stress supported by the soil. Thus, for a constant total boundary stress, the sum of effective stress and pore pressure will remain constant, and changes in one must equally offset those in the other. Conventionally, the symbol p is used to represent effective normal stress in consolidation.

$$\frac{\partial p}{\partial t} = -\frac{\partial u}{\partial t} \qquad (4.2)$$

The third assumption leads to a relationship between soil volume and effective stress over a limited range, which can be stated as follows for constant total pressure.

$$\frac{\Delta V}{V} = -m_v \Delta p = m_v \Delta u \qquad (4.3)$$

where m_v is the coefficient of volume compressibility, which is assumed to be practically a constant over a limited range of soil volume change, and

p is the effective vertical soil stress. The basic equation for rate of soil consolidation comes from the principle of conservation of matter. It is stated as the rate of change of water velocity over distance equals the rate of change of volume at a point per unit time, or in terms of the above symbols;

$$\frac{\partial v}{\partial z} = -\frac{1}{V}\frac{\partial V}{\partial t} = m_v \frac{\partial p}{\partial t} = -m_v \frac{\partial u}{\partial t} \tag{4.4}$$

From Eqn. 4.1, the water velocity above can be replaced by a function of pore pressure, with the following equation having u as the only dependent variable.

$$\frac{\partial u}{\partial t} = \frac{k}{\gamma_w m_v}\frac{\partial^2 u}{\partial z^2} \tag{4.5}$$

Although Eqn. 4.5 describes variations in pore pressure u, this can be converted easily to volume change of the soil by Eqn. 4.3 above. At any point in the soil, therefore, a reduction in pore pressure is assumed to be proportional to the decrease in soil volume, and the degree of consolidation from initial conditions to the final equilibrium state can be defined by the relative magnitude of either pressure or volume.

For the one dimensional water flow case, an added vertical total stress is assumed to be constant at all points in a soil layer. The initial pore pressure, at time t=0, is assumed to be equal to this additional total stress, and then to decrease with time. These assumed initial conditions do not lend themselves to a simple solution of the differential equation 4.5, because the natural solution to the equation is a sinusoidal function of depth, z, multiplied by an exponential function of time, t. However, a Fourier series can be used to combine many terms of the natural solution form to yield the appropriate initial conditions, and yield the degree of consolidation, U.

$$U = \frac{u}{u_o} = \sum_{n=1}^{\infty} \frac{4}{n\pi}(1-\cos n\pi)\sin\left[\frac{n\pi z}{2H}\right] e^{-\left[\frac{kn^2\pi^2 t}{4\gamma_w m_v H^2}\right]} \tag{4.6}$$

A nondimensional time factor, T_v, can be found in Eqn. 4.6 as follows.

$$T_v = \frac{C_v t}{H^2} = \frac{kt}{\gamma_w m_v H^2} \tag{4.7}$$

C_v is called the coefficient of consolidation, and is in units of length squared per unit time. The one dimensional consolidation rate of any layer of uniform soil can be determined by substituting the appropriate coefficient of consolidation and layer drainage length, H, into Eqn. 4.7, and then finding the degree of settlement at a particular time from Eqn. 4.6, or its graphical representation in Fig. 4.2.

The drainage length, H, depends on whether water can escape from both the top and bottom boundaries of the compressible soil layer. If water can move in only one direction, as in Fig. 4.2(a), then the situation is termed "single drainage", and H is the total layer thickness. If, on the other hand, water can move practically without resistance from both the top and bottom surfaces, then "double drainage" is the appropriate term, and H is one half of the layer height, as shown in Fig. 4.2(b).

For large changes in soil volume, it is the proportionality between vertical effective pressure and settlement assumption in the development above which becomes the most inaccurate. In fact, a loose saturated compressible soil changes volume proportionally to the logarithm of applied pressure, rather than linearly. Traditionally, the change in volume is expressed as variations in void ratio (volume of soil voids divided by volume of solid particles) as shown in Fig. 4.3 plotted against vertical pressure, p, on a logarithmic scale. The void ratios on this diagram are the final quantities, after enough time has passed for primamry consolidation to be practically completed, and for excess pore water pressure to be essentially zero. On this kind of diagram, most compressible soils exhibit nearly a straight line void ratio versus logarithm of

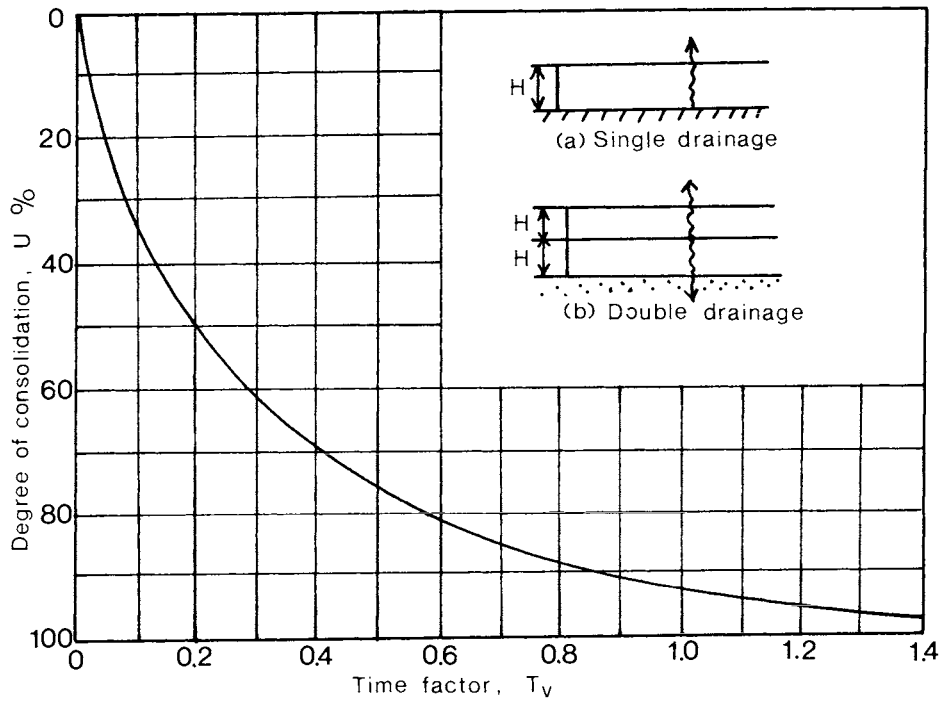

Fig. 4.2. Degree of conslidation versus time factor for the one dimensional uniform pressure case (Terzaghi, 1943).

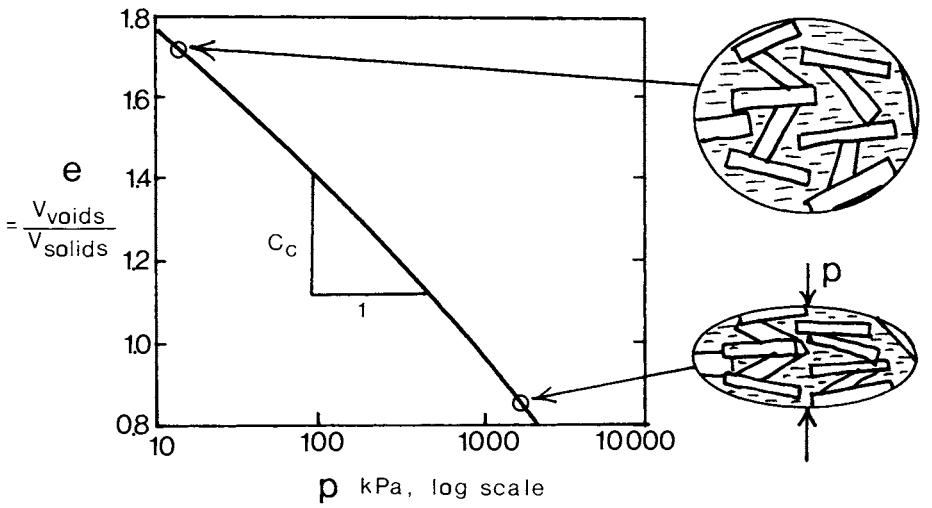

Fig. 4.3. Final consolidated void ratio versus the logarithm of pressure.

pressure behavior The slope of this line is called the coefficient of compression, and is defined as follows.

$$-C_c = \frac{\Delta e}{\Delta \log p} = \frac{e_2 - e_0}{\log(p_2/p_0)} \tag{4.8}$$

To convert the variation in void ratio to the change in soil volume, or settlement in the one dimensional case, the following equation can be used, in which V_0, h_0 and e_0 represent the initial conditions and Δh is the observed settlement of a soil layer. Here, h refers to the total height of the compressible layer, and is not always equal to the maximum drainage length, H, above.

$$-\frac{\Delta V}{V_0} = \frac{\Delta h}{h_0} = \frac{\Delta e}{1 + e_0} \tag{4.9}$$

To calculate the settlement of a soil which has been normally consolidated (that is has not suffered a larger pressure at some time in the past), the change in pressure, Δp, can be used in the following expression.

$$\Delta h = h_0 \left[\frac{C_c}{1 + e_0}\right] \log\left[\frac{p_0 + \Delta p}{p_0}\right] \tag{4.10}$$

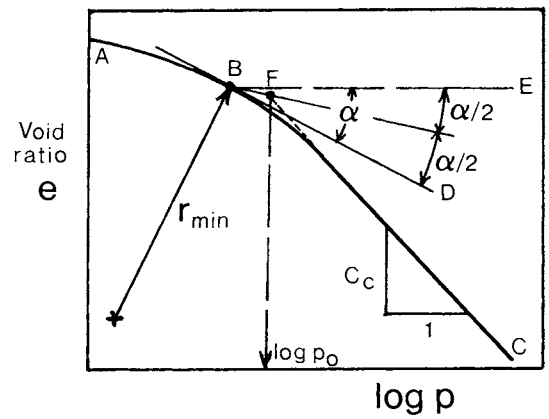

Fig. 4.4. Consolidation curve for a preconsolidated compressible soil, and the method of estimation of the preconsolidation pressure, p_o, of Casagrande (1936).

For a soil which has been preconsolidated to a higher pressure than the ambient one, then the p_o used in Eqn. 4.10 should not be the initial pressure exerted vertically on the soil, but should be the preconsolidation pressure to which the soil was formerly exposed. Fig. 4.4 shows the typical void ratio versus pressure behavior of a compressible soil when it is subjected to pressure which begins below the historical preconsolidation pressure, and then increases beyond it. At low pressure, such as point A in Fig. 4.4, the ratio of change in void ratio to increase in logarithm of applied pressure, p, is much smaller than at higher pressures above p_o. This is because the soil particles "remember" the higher preconsolidation stress, p_o, to which they were previously consolidated, and will not begin to compress at the normal coefficient of compression, C_c, until this preconsolidation stress has been exceeded.

A commonly used method for estimating the preconsolidation pressure from the results of a consolidation test was proposed by Casagrande (1936) and is shown in Fig. 4.4. The point B where the minimum radius of curvature occurs is located, and a tangent BD and horizontal line BE drawn through this point. Point F above the estimated preconsolidation pressure, p_o, is found at the intersection of the bisector of angle DBE and the slope C_c of the higher pressure straight line portion of the consolidation curve. Having found the estimated value of p_o, one can then calculate the expected settlement of a thin, wide soil layer by inserting this p_o value in Eqn. 4.10. Δp in the equation

is the increase in vertical pressure above p_o, or;

$$\Delta p = p_2 - p_o \tag{4.11}$$

where p_2 is the final applied pressure.

As discussed in Chapter 2, the coefficient of consolidation, C_v, can be estimated also from the results of a consolidation test if measurements of settlement are made at different times, and the nondimensional time factor T_v is read from Fig. 4.2. Furthermore, the saturated hydraulic conductivity, k, can be approximated from Eqn. 4.7, and the linear coefficient of volume compressibility, m_v, estimated.

$$m_v = \frac{\Delta V}{V_o \Delta p} = \frac{\Delta h}{h_o \Delta p} \tag{4.12}$$

In summary, the final one dimensional settlement of a soil layer can be calculated from Eqn. 4.10 as a result of a vertical pressure increase over the presonsolidation stress. And the progress of that settlement with time is most easily estimated by computing the time factor, T_v, at different times, and reading the percentage of the final consolidation amount from Fig. 4.2.

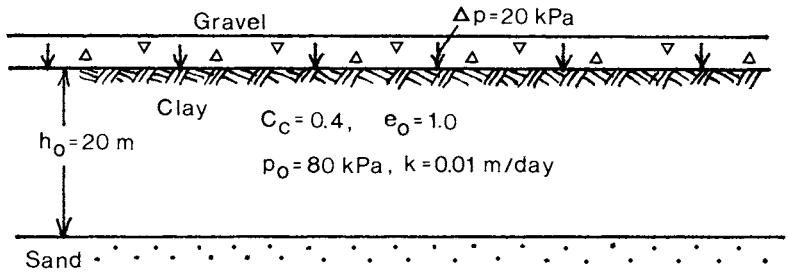

Fig. 4.5. A uniform clay layer in Problem 4.1.

Problem 4.1. Fig. 4.5 shows a uniform clay layer of depth 20 m sitting on sand. An overburden of 20 kPa pressure is placed on the clay surface at time zero. What will be the final settlement of the surface due to consolidation, and how long will it take for 50% of this subsidence to occur?

In this example, the coefficient of consolidation, C_v, is not provided, but it can be worked out from the hydraulic conductivity, k, and the coefficient of compressibility, m_v, by Eqn. 4.7. m_v will be estimated using Eqn. 4.3 after the final settlement has been calculated by Eqn. 4.10.

$$h = h_o\left[\frac{C_c}{1 + e_o}\right]\log\left[\frac{p_o + \Delta p}{p_o}\right] = 20m\left[\frac{0.4}{2.0}\right]\log\left[\frac{80+20}{80}\right] = 0.388\ m$$

$$m_v = \frac{\Delta h}{h_o \Delta p} = \frac{0.388m}{20m \times 20kPa} = 9.69 \times 10^{-4}\ (kPa)^{-1}$$

For the calculation of C_v, the hydraulic conductivity, k, must be converted to units of velocity per unit pressure gradient in force per unit area per length, rather than the pressure unit, head of water, as it is given.

$$k = 0.01\ (m/day)/(1\ m\ head/1\ m\ length)$$
$$= 0.01\ (m/day)/(9.8\ kPa/m) = 1.02 \times 10^{-3} m^2/(kPa\ day)$$

$$C_v = 1.02 \times 10^{-3} m^2 kPa/(9.69 \times 10^{-4}\ kPa\ day) = 1.05\ m^2/day$$

For 50% consolidation, Fig. 4.2 indicates that the time factor, T_v, is 0.20. The time for 50% consolidation can then be found using Eqn. 4.7 with H = 20m/2 due to drainage at both the top and bottom of the clay layer.

$$T_v = C_v t/H^2 = 1.05t\ (m^2/day)/100\ m^2 = 0.20$$

$$\underline{t = 19\ days}\ \text{for 50\% settlement}$$

4.1.2. Three dimensional cases

In Terzaghi's (1943) development of consolidation theory outlined above, there was also some consideration of special cases which did not exhibit uniform confining pressure with depth. One, shown schematically in Fig. 4.6(a) was the case of a hydraulically placed landfill. Initially, the fill is essentially a fluid and the effective granular stress is zero at the top, and increases more or less linearly with increasing depth due to the self weight of soil particles. This situation can be approximated by a linear increase in pore water pressure with depth initially, as shown. The variation in initial pressure with depth requires a different Fourier series of sinusoidal terms as a function of soil depth, and the decrease in pressure with time is given in Appendix 4 as curve C.

Another case is rather the reverse, namely a decrease in initial excess pore pressure with depth. This is the case when the surcharge causing consolidation is of finite width compared to the soil layer thickness. The additional applied pressure from the load, Q, shown in Fig. 4.6(b), spreads out with depth over an increasingly large horizontal area, and thus decreases at greater depths. The simplest model, assuming that the excess vertical pressure and initial pore pressure is nearly zero at the soil layer base, is shown in Fig. 4.6(b). The corresponding settlement behavior with time is given by curve B in Appendix 4.

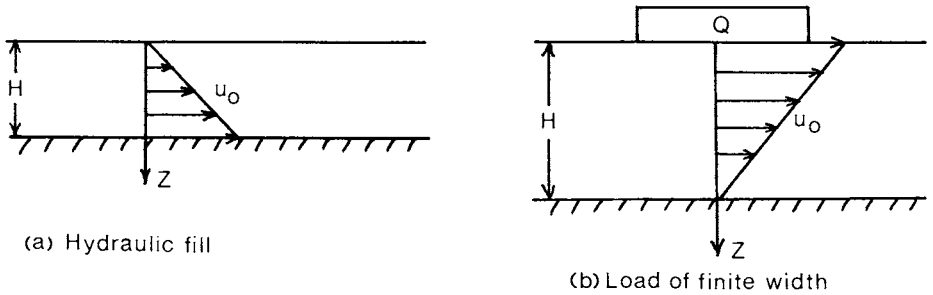

Fig. 4.6. Cases of consolidation pressures which are not uniform with depth: (a) hydraulic fill and (b) a load of finite width.

In fact, it is very difficult to estimate the actual time for a certain fraction of settlement to take place in a three dimensional case. Curve B in Appendix 4 has been calculated based on the assumption that water flow is only vertical. And yet an examination of Fig. 4.6(b) would indicate that excess pore water pressure could easily cause water to flow to the sides of the pressure zone beneath the surcharge load, Q, as well as vertically. It must be concluded, therefore, that curve B in Appendix 4 gives a rather conservative estimate of the time required for a particular percentage of settlement to occur, and that actual times will probably be smaller, even in a uniform isotropic soil.

A further consequence of a finite width load on a compressible soil is that the additional pressure and settlement are not constant with depth. Fig. 4.7 shows both a long and a rectangular load on a soil layer. A traditional rule has been that the pressure spreads out with depth within a zone of influence of which the boundary has a slope of 1:2 to the horizontal as shown. For a load of width B, the area influenced at a depth Z is then B+Z. Assuming a uniform pressure distribution on each horizontal plane for simplicity's sake, the pressure at depth Z is less than the surface pressure, p_1. It can be found for the strip and rectangular loads using Eqn. 4.13 and 4.14, respectively. In addition, a circular load can be treated like the rectangular load by putting both B and L equal to the diameter in Eqn. 4.14.

$$\Delta p = p_1 \left[\frac{B}{B + Z} \right] \tag{4.13}$$

$$\Delta p = p_1 \left[\frac{BL}{(B + Z)(L + Z)} \right] \tag{4.14}$$

Because the added pressure changes with depth, as well as the initial pressure and very possibly the soil properties, Eqn. 4.10 cannot be used to find the total soil settlement. However, a finite element model can be used for an approximation as shown in Fig. 4.7. The soil layer is cut into horizontal slices, with the upper slices being thinner than the lower ones. This is because

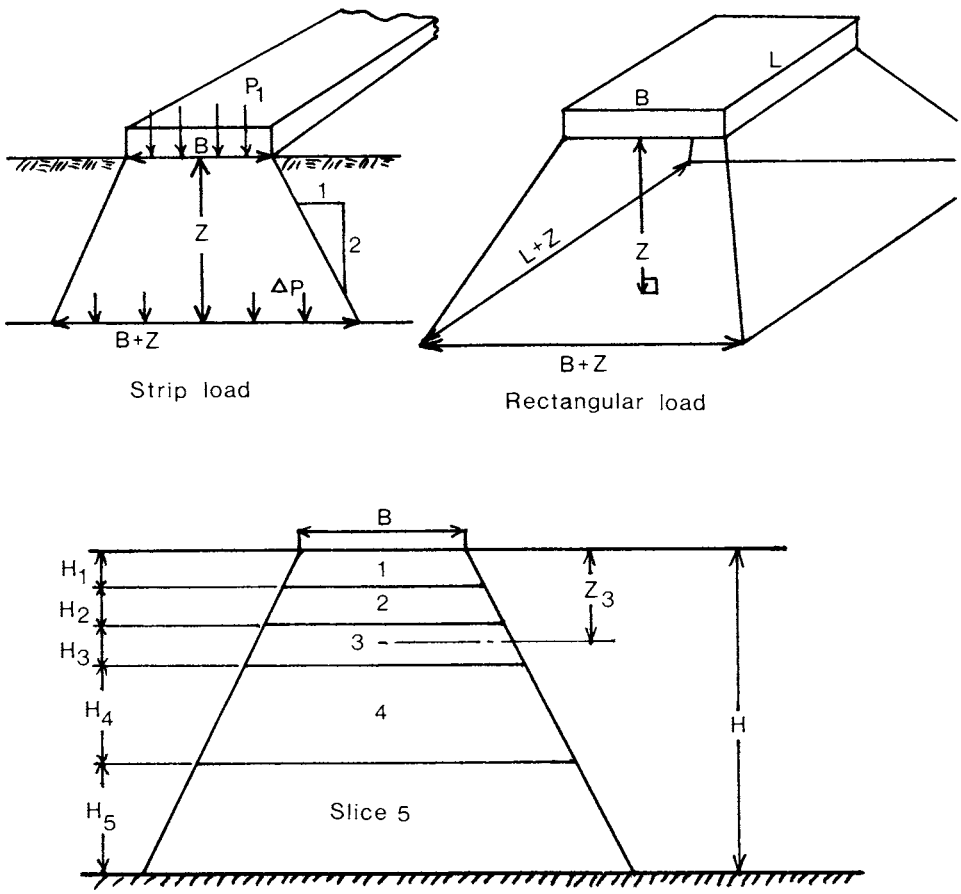

Fig. 4.7. An estimation of the areas affected by consolidation pressure at depth for a finite load width or rectangle, and the method of slices to be used in such a case for settlement calculations.

the surcharge pressure is larger near the top, and the initial pressure lower, causing most of the settlement to occur in the upper part of the layer. The average width of each slice is calculated at the slice centre, such as Z_3 in Fig. 4.7, and the pressure estimated from Eqn. 4.13 or 4.14 as the case dictates. For a normally consolidated soil, the initial pressure, p_o, can be estimated as the soil buoyant density times the average depth of each slice. In the case of a presonsolidated soil, the values of p_o must be determined from consolidation tests on soil samples from different depths in the total layer. Eqn. 4.10 can then be applied to each slice to find its eventual change in height, and all of the settlements are added to estimate the total settlement of the soil surface.

Problem 4.2. An example of the above procedure is given in Table 4.1 for a situation which resembles that in Fig. 4.7.

TABLE 4.1. Example calculations of the settlement of a saturated clay soil under a strip load. C_c = 0.2, γ = 19.6 kN/m^3, p_1 = 50 kPa, B = 10m, average e_o = 1.0 and H = 30 m. Eqn. 4.10 is used for each horizontal slice.

Slice	H_i, m	z_i, m	Width, m	Δp, kPa	p_o, kPa	ΔH, mm
1	4	2	12	42	39	127
2	4	6	16	31	118	41
3	4	10	20	25	196	21
4	8	16	26	19	314	20
5	10	25	35	14	490	12
Total	30					221

It can be seen in Table 4.1 that more than half of the total soil profile settlement takes place in the first 4 m thick layer, while only about five percent occurs in the bottom layer. These proportions are even more disparate under a rectangular or circular load where the applied pressure decreases even more with increasing soil depth.

4.2. WATER FLOW IN SATURATED SOIL

Eqn. 4.1 described the apparent speed of water flow in response to a pressure gradient (that is the speed at which a certain volume of water moves through the soil total volume). If water movement is not one dimensional, then the speed of water flow can change from place to place. Fig. 4.8 illustrates such a case. Flow lines can be described parallel to the direction of water

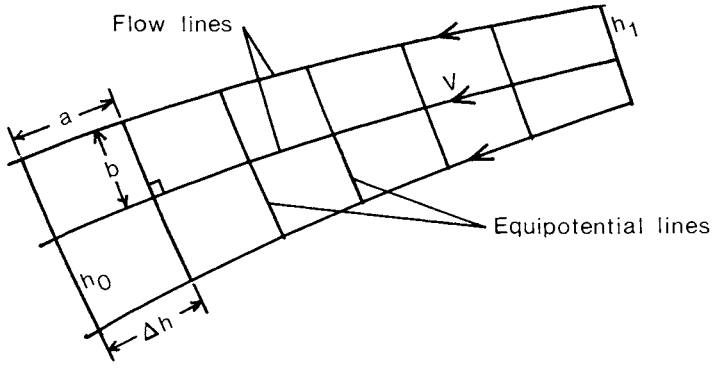

Fig. 4.8. Water flow lines and lines of equal potential.

movement, and in an isotropic soil, these flow lines are perpendicular to equipotential lines along each of which the dynamic hydraulic pressure is the same. In Fig. 4.8, the distance between successive equipotential lines is labelled a, and the separation of flow lines as b. The total rate of water flow through each flow channel, bounded by a pair of flow lines, can thus be calculated as follows, for a unit depth of soil.

$$q = \frac{dV}{dt} = vb = k\Delta h \frac{b}{a} \tag{4.15}$$

If the flow and potential lines are drawn as 'squares' with equal distances between them at any point, the Eqn. 4.15 becomes even more simple because b/a becomes unity. When this is done, then the difference in hydraulic potential, or potential drop, is the same between any two adjacent equipotential lines, and can be calculated as the total potential difference across the entire soil mass under consideration, divided by the number of drops or potential lines, n_d. Also, the total water flow in the soil mass is the equal quantity of flow in each flow channel multiplied by the number of channels, n_f. In that case, if the total hydraulic potential on the upstream and downstream ends of the water flow region are h_1 and h_o, respectively, the total volume of water flow per unit time for a unit soil depth is;

$$\frac{dV}{dt} = k (h_1 - h_o) \frac{n_f}{n_d} \tag{4.16}$$

4.2.1 Flow nets in soil structures

The application of the above technique for the calculation of rates of water flow can be applied to most configurations of soil structures, provided that the hydraulic conductivity is the same in all directions.

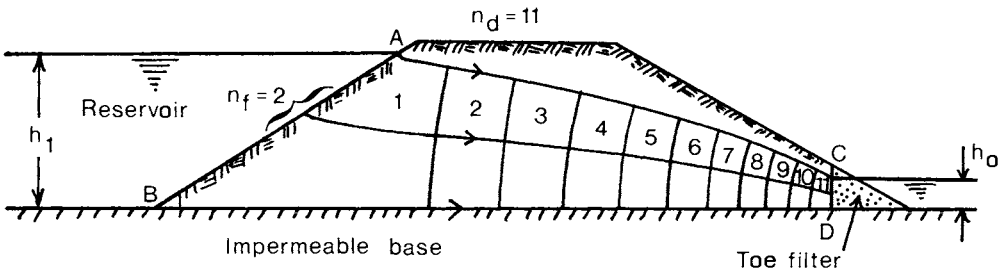

Fig. 4.9. Construction of a flow net through an earthdam for Problem 4.3.

Problem 4.3. In Fig. 4.9 an example is given of a small uniform earth dam on a relatively impermeable base. (If the subbase is more permeable than the dam soil material, then more water would flow below the dam than through it.) The technique which has been used in Fig. 4.9 is to draw flow lines, such as AC and BD, normal to equipotential lines such as AB. The equipotential lines are drawn in also between AB and CD, such that approximate squares are formed by the intersecting lines. Near the upstream dam slope, AB, it is difficult to make exact squares because the flow lines curve considerably, but an effort is made to make the distance between equal head lines about the same as the width of the flow path.

The uppermost line, AC, is called the phreatic line or surface, as it is at zero gauge pressure. The potential of this line at any point is therefore only its height above the reference elevation, line BD. In drawing equipotential lines intersecting line AC, the difference in height of AC should be the same between potential drops. Thus the phreatic line curves downwards with increasing negative slope as the equipotential lines become closer together, and the flow paths become narrower near CD.

In the example shown, the numbers of flow paths and head drops in the structure are $n_f=2$ and $n_d=11$. These numbers are then substituted into Eqn. 4.16, together with the soil permeability, in order to calculate the volume of water leakage through the dam per unit time and per unit length of the dam. For instance, if in the example $h_1=10$ m, $h_o=1$ m and $k=3$ m/year, then the total volume of water flow through the soil in the dam would be;

$$q = \frac{dV}{dt} = 3\frac{m}{y}(10m - 1m)\frac{2}{11} = \underline{4.9\ m^3/year/m\ length}$$

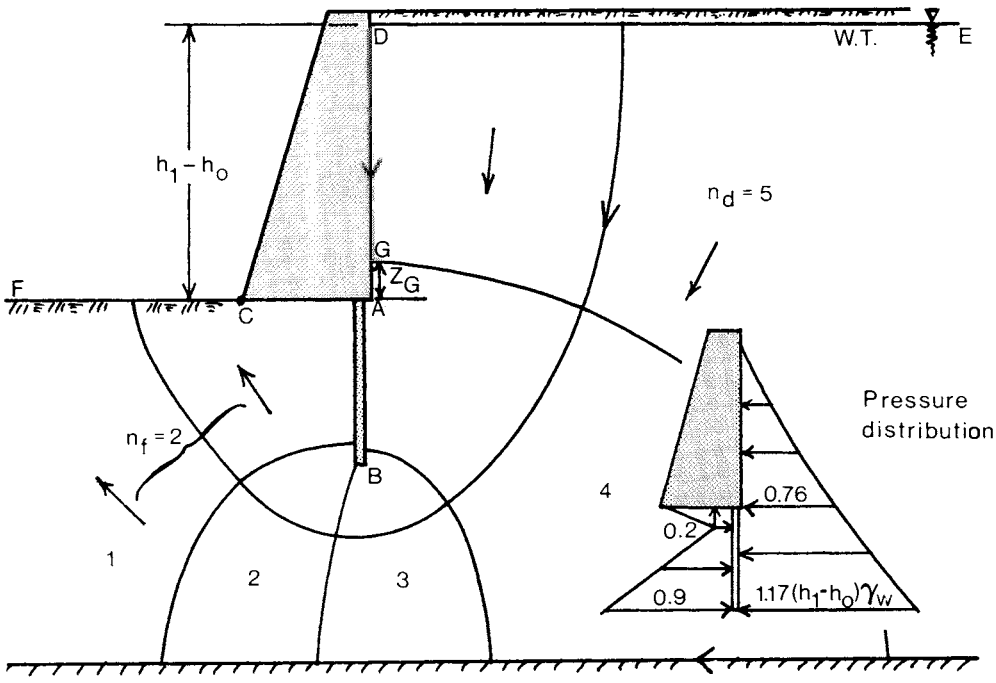

Fig. 4.10. Flow beneath a retaining wall for Problem 4.4.

Problem 4.4. Another example of water flow in a soil structure is given in Fig. 4.10. It is a retaining wall supporting soil with a water table near the top, and a water cutoff wall, AB, designed to lengthen the water flow paths, and to reduce the hydraulic pressure near the wall edge C. An attempt is made to draw square shapes contained among intersecting equipotential and flow lines, although the endmost 'squares' are not very exact square shapes. Here, DE is the first potential line with the reference potential h_1-h_o, and there are three flow lines shown; one along the wall following path DABC, the centre one and one along the horizontal bedrock. The last potential line, with the lowest potential, is CF (AC being part of the uppermost flow line).

The number of potential drops in this case is five, and there are two flow paths. These numbers are then inserted into Eqn. 4.16 to estimate the rate of water flow per unit time per unit wall length.

In both the cases of the earth dam and wall shown above, the drawing of water flow nets gives information not only concerning the rate of water flow, but also of the hydraulic pressures acting within the earthworks. Because potential, h, has been defined as the 'excess' hydraulic head above that due to static head, it may be defined also as the sum of total water pressure (expressed as a height unit) plus the relative height of a point of water. This concept is fairly clear in the case of the dam, Fig. 4.9, wherein all of the water in the reservoir behind the dam is considered to have the same potential, h_1, regardless of height above the base. At all points in the reservoir, the water has the same sum of elevation and pressure, ($z+u=h_1$), both expressed in height units. At the top surface, for example, the gauge pressure is zero, but the elevation is h_1, while at the bottom, the height is zero relative to elevation BD, but the pressure is h_1 m of water.

The same is true for the water in the soil around the wall in Fig. 4.10. Since 'square' potential and flow lines have been drawn, then all of the potential lines represent equal potential drops. At point G, for example in Fig. 4.10, the potential drop is one fifth of the total head loss along the flow path, and the potential at that point is $0.8(h_1-h_0)$. The elevation of point G is Z_G above the reference h_0 of line CF. Therefore, the actual static water pressure at this point is the total potential minus the elevation, or;

$$u = h - z_G = 0.8(h_1 - h_0) - z_G \qquad (4.17)$$

The water pressure will be in units of water height in Eqn. 4.17, and requires multiplication by the density of water (γ_w = 9.8 kN/m^3) in order to convert it to a specific force pressure (kPa). The pressure distribution is shown in Fig. 4.10 with the values noted representing a proportion of the water height (h_1-h_0) multiplied by the weight density of water. It can be seen that the installation of the cutoff wall has reduced the pressures on the bottom of the wall considerably.

Problem 4.5. Another example of this technique is shown in Fig. 4.11, for the case of a small impermeable concrete dam on an isotropic permeable soil layer. The flow lines and equipotential lines are drawn for the water flow through the soil beneath the dam, making squares as much as possible. The calculation of static water pressure is simpler in this case, since the base of the concrete dam is all at the same elevation. Taking this elevation to be the reference zero potential, then the water pressure values along the dam base are equal to the potential quantities at each point.

In Fig. 4.11(a), the potential lines with whole numbers have been labelled (h=4 m, etc.), and the head associated with each potential line is the static pressure acting on the dam base at the point where that line meets the base surface (such as point A for the 4 m head). The water pressure at point A is thus 4 m x 9.8 kN/m^3 = 39 kPa, and the pressures at other potential lines are calculated in the same manner. In Fig. 4.11(b), the water pressure diagram is shown below the flow net figure, and this diagram can now be of assistance

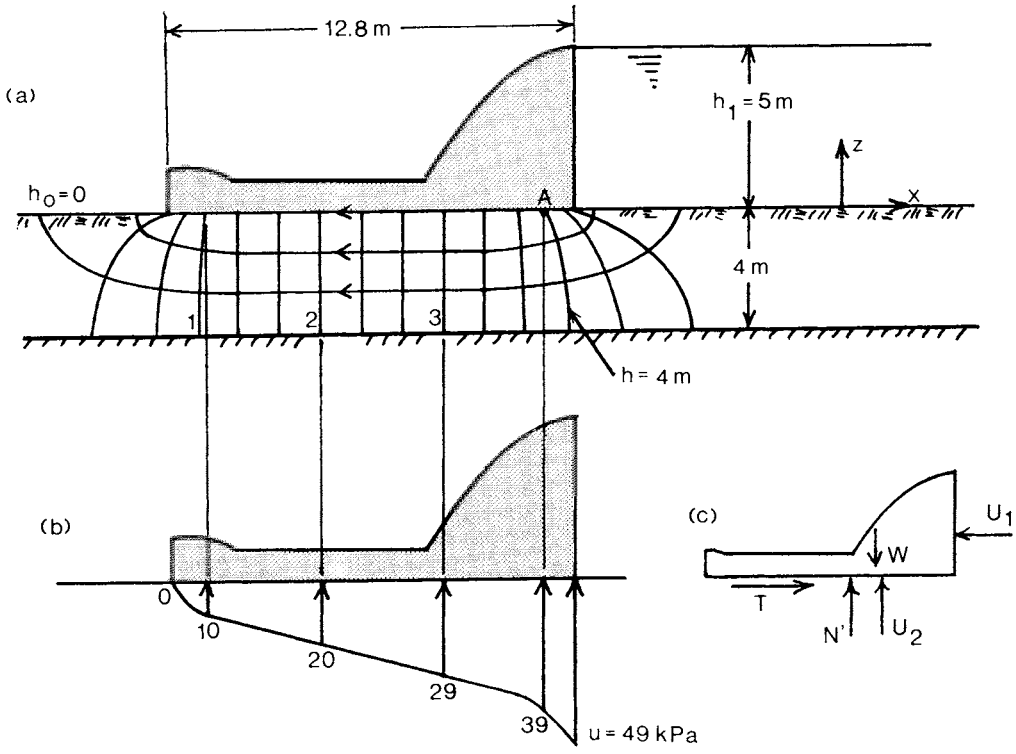

Fig. 4.11. Water flow through soil under a concrete dam, and the water pressure distribution on the dam.

in determining all of the forces acting on the dam (Fig. 4.11c), and its stability. The vertical water force on the dam bottom, U_2, is found by integrating the water pressure distribution of Fig. 4.11(b). In the example shown, this force is approximately U_2=300 kN/m length.

In Fig. 4.11(c), the forces on the dam, per unit length in the y direction, are indicated as U_1, the hydrostatic force from the water in the reservoir behind the dam; U_2, the force from the pore water pressure illustrated in Fig. 4.11(b); N', the effective soil particle to dam base force; W, the weight of the dam itself; and T, the sliding resistance force. The stability of the concrete dam in sliding is assessed using the formulae below. Example quantities which have been used are W=600 kN/m length, c_a'=3 kPa and δ'=25°.

$$U_1 = \frac{1}{2}\gamma_w h_1^2 = 122.5 \text{ kN/m} \tag{4.18}$$

$$N' = W - U_2 = 300 \text{ kN/m} \tag{4.19}$$

$$T = U_1 = 122.5 \text{ kN/m} \tag{4.20}$$

$$T_{max} = c_a'(12.8 \text{ m}) + N'\tan\delta' = 178 \text{ kN/m} \tag{4.21}$$

$$\text{Safety Factor} = \frac{T_{max}}{T} = \underline{1.46} \tag{4.22}$$

Further examples of dynamic pressures in earth structures will be seen in Chapter 5, Slope Stability.

4.2.2. Flow to subsurface drains

Another structure in which the flow of water is important is a subsurface drain system. Such a system is used in humid areas in order to remove excess soil water during and just after periods of rain, and to remove excess salts in saline soils or under irrigation with brackish water. A typical subsurface drain configuration which is used to lower or maintain the depth of a water table is shown on a cross section in Fig. 4.12(a). Fig. 4.12(b) illustrates the actual flow net pattern for this case. Unfortunately, this pattern involves complicated equations for an analysis of the drainage rate, q, (the volume of water removed per unit area and time) of such a system. In 1940, Hooghoudt developed a transformation of the subsurface drain flow net to a simpler vertical and horizontal flow situation. His method of analysis is explained by van Schilfgaarde (1957), Luthin (1973) and Smedema and Rycroft (1983), and it is the simplest and most often used analytical method today.

Hooghoudt reasoned that the flow of water to buried drain pipes above an impermeable level barrier at depth, D, below the drainpipes, resembles that to parallel open ditches. The principal difference between the two cases is the radial flow pattern close to the drainpipe itself, as can be seen in Fig. 4.12(b). Hooghoudt transformed this radial flow into a horizontal flow, as illustrated in Fig. 4.12(c), but through a reduced depth, d, to the impermeable barrier. The following formulae give the equivalent depth, d, in the cases of relatively deep and shallow impermeable barriers, for a pipe radius, r.

For $D > L/4$;

$$d = \frac{D}{\frac{8D}{\pi L}\ln\left[\frac{D}{\pi r}\right] + 1} \tag{4.23}$$

For $D < L/4$;

$$d = \frac{L}{8\ln\left[\frac{L}{\pi r}\right]} \tag{4.24}$$

Since the pattern of water flow has been transformed to vertical flow mostly above the drain elevation, and horizontal flow below that, it was simple to modify the prediction of drainage rate for the situation in which

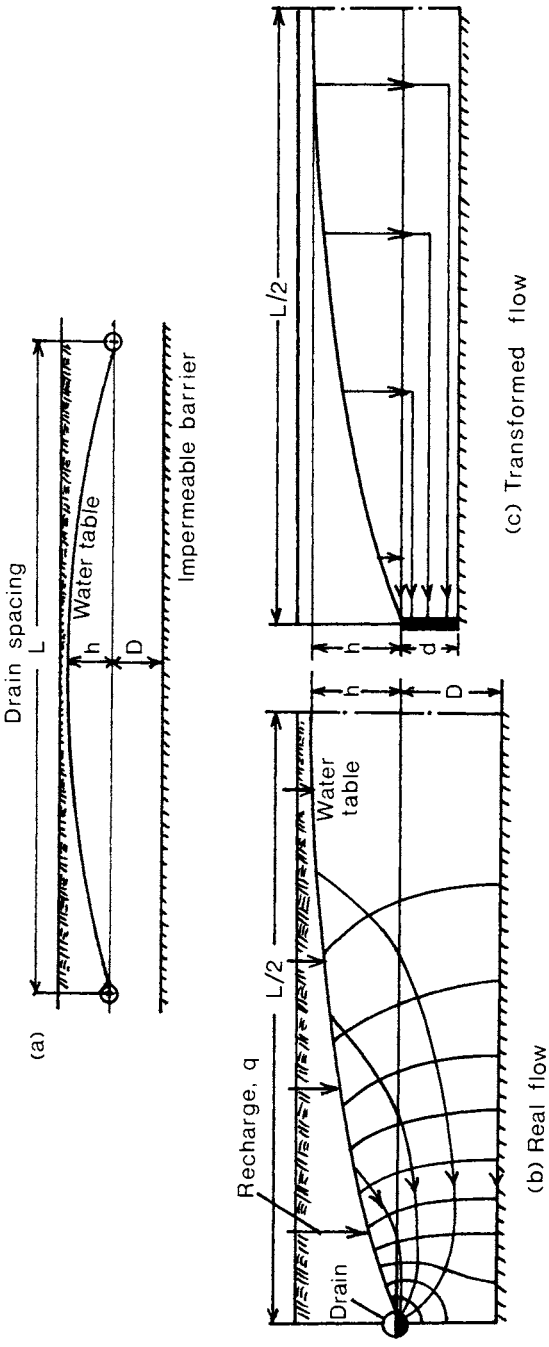

Fig. 4.12. The transformed flow net to parallel subsurface drain tiles (Hooghoudt, 1940).

there are different hydraulic conductivities, k_1 and k_2, above and below the drain level, respectively. Hooghoudt's equation for the drainage rate in this case is thus;

$$q = \frac{8k_2dh}{L^2} + \frac{4k_1h^2}{L^2} \qquad (4.25)$$

Eqn. 4.25 allows the prediction of drainage rate from a specific system in a particular soil of known properties. Alternatively, the drainage system may be designed in terms of drainpipe spacing and depth in order to maintain a desired drainage rate and water table height. The reader is directed towards Luthin (1957, 1973), Schwab et al. (1981) or Smedema and Rycroft (1983) for further information on drainage theory and techniques.

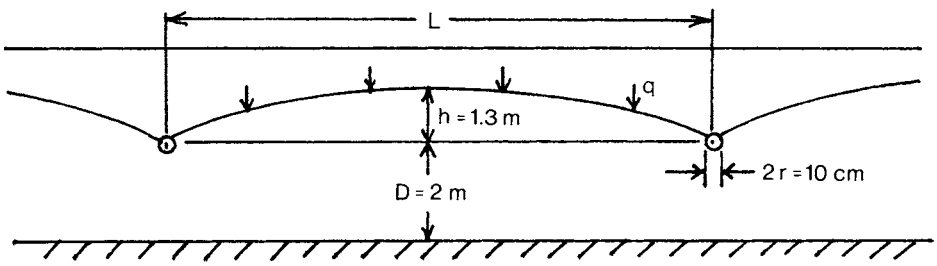

Fig. 4.13. Subsurface drains in Problem 4.6.

Problem 4.6. It is desired to drain a clay field with parallel drains of diameter 10 cm placed at a depth of 1.3 m below the water table, as shown in Fig. 4.13. The saturated conductivity has been measured to be an average of 0.1 m/day above the drain depth, and 0.01 m/day below the drain depth to an impermeable layer 2 m below the drains. What drain spacing, L, should be used to provide removal of 10 mm/day of rainfall?

Assuming that the depth from the drains to the impermeable layer is less than one quarter of the drain spacing, Eqn. 4.24 is used to find the reduced depth, d.

$$d = \pi L/[8\ln(L/\pi r)]$$

$$q = 8k_2\pi Lh/[8L^2\ln(L/\pi r)] + 4k_1h^2/L^2$$

$$= 0.048(m^2/day)/[L\ \ln(L/.05\ m)] + 0.676(m^2/day)/L$$

By trial and error, the required drain spacing L = 8.75 m.

4.3. PROBLEMS.

4.7. A layer of wet clay soil 5 m thick has more permeable layers both above and below it. A vertical pressure of 20 kPa is added uniformly to the layer, and it is observed that the settlement of the layer is 25 cm after a long time, and that it took two years for one half of this settlement to occur. Estimate the permeability of the soil.

Answer: $k = 0.015$ m/y $= 4.9 \times 10^{-8}$ cm/s.

4.8. A uniform wet layer of compressible soil is 10 m deep and rests on relatively impermeable rock. The soil is found to have $C_C = 0.20$, $C_V = 10$ m^2/y, $e_0 = 1.05$ and $p_0 = 50$ kPa. If a pressure of 10 kPa is applied across the surface of this soil, (a) what will be the final settlement of the layer, and (b) how long will it take for 90% of the settlement to occur?

Answer: (a) $\Delta h = 7.7$ cm, (b) $t_{90} = 8.5$ y.

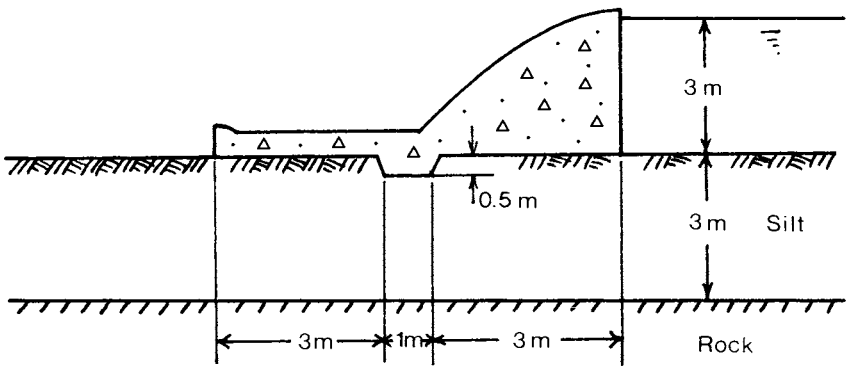

Fig. 4.14. Concrete dam in Problem 4.9.

4.9. Fig. 4.14 shows a small concrete dam constructed on a layer of silt soil which has a saturated hydraulic conductivity of 10 m/y. Find (a) the volume of water which will seep under the dam per metre length per year, and (b) the water pressure uplift force on the dam per metre length.

Answer: (a) Flow $= 6.9$ m^3/m/y, (b) $U = 150$ kN/m.

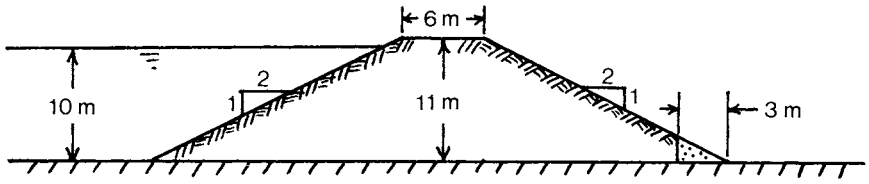

Fig. 4.15. Earthdam in Problem 4.10.

4.10. In Fig. 4.15 an earthdam is illustrated. If the saturated permeability of the soil is 5 m/y, what annual water loss will occur through the dam per metre length?

Answer: Flow = 7.7 m^3/m/y.

4.11. An agricultural field has a deposit of fine sand 3.3 m deep situated on relatively impermeable rock. Perforated tile drains of 10 cm diameter are placed in the field at a spacing of 15 m and an average depth 1.3 m. The saturated hydraulic conductivity of the soil has been measured to be a fairly consistent 0.05 m/day at all depths down to the rock. If it is desired to maintain the water table no higher than 30 cm from the surface, what precipitation rate can this drainage system handle?

Answer: q = 3.2 mm/day.

4.12. A loam soil is 3.5 m deep above a relatively impermeable layer, and it is desired to drain the field with a water table no higher than 30 cm deep. The hydraulic conductivity of the soil has been measured to be an average 0.1 m/day at all depths. If the specification is for a drainage rate of 10 mm/day of input precipitation, what would the required spacing of 10 cm diameter perforated drain tiles be at depths below the soil surface of (a) 1.3 m and (b) 2.3 m?

Answer: (a) L = 8.5 m, (b) L = 16 m.

Chapter 5. Slope Stability

5.1. SLOPE STABILITY DETERMINATION

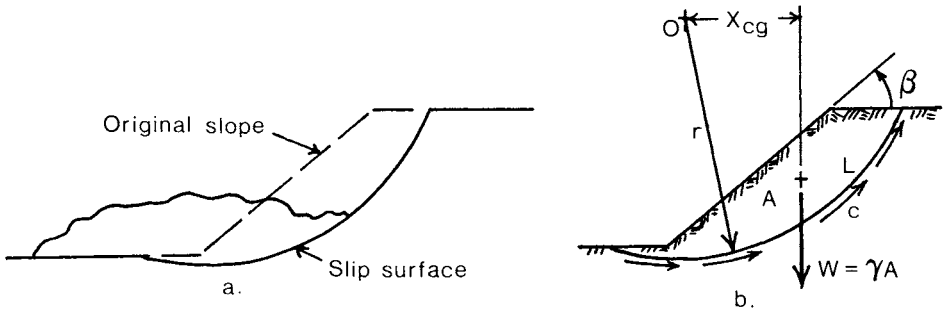

Fig. 5.1. Slump failure of a simple slope on a circular slip surface.

5.1.1. Uniform soils

Fig. 5.1(a) shows a simple plane slope, and the way in which such an earth structure usually fails when it is not stable. The slip surface is very close to a circular shape, and such an assumption is very helpful in the mechanical analysis of slope stability. In Fig. 5.1(b) are shown the forces and stresses acting on the section of cohesive soil which slips. Here, O is the center of the circular slip shape, r is the circle radius, A is the cross sectional area of the soil section, L is the length of the slip surface, W is the weight of the soil section (equal to weight density times area for a uniform soil) and c is the cohesional shear resistance along the slip circle.

In this case, the safety factor of the structure can most simply be defined as the resisting moment of force about center O, divided by the moment tending to cause the soil section to move downwards, as follows.

$$S.F. = \frac{cLr}{WX_{cg}} = \frac{cLr}{\gamma AX_{cg}} \tag{5.1}$$

As shown in Eqn. 5.1, the factor of safety depends on the cohesion and density of the soil, as well as on the geometric factors of circle radius, slip line length, area of sliding soil section and the horizontal distance of the center of gravity of the section from the circle center. For a particular slope angle, β, these geometric quantities are not known beforehand. However, Taylor (1937, 1948) demonstrated that trial slip circles could be drawn, the factor of safety calculated for each and the circle with the smallest

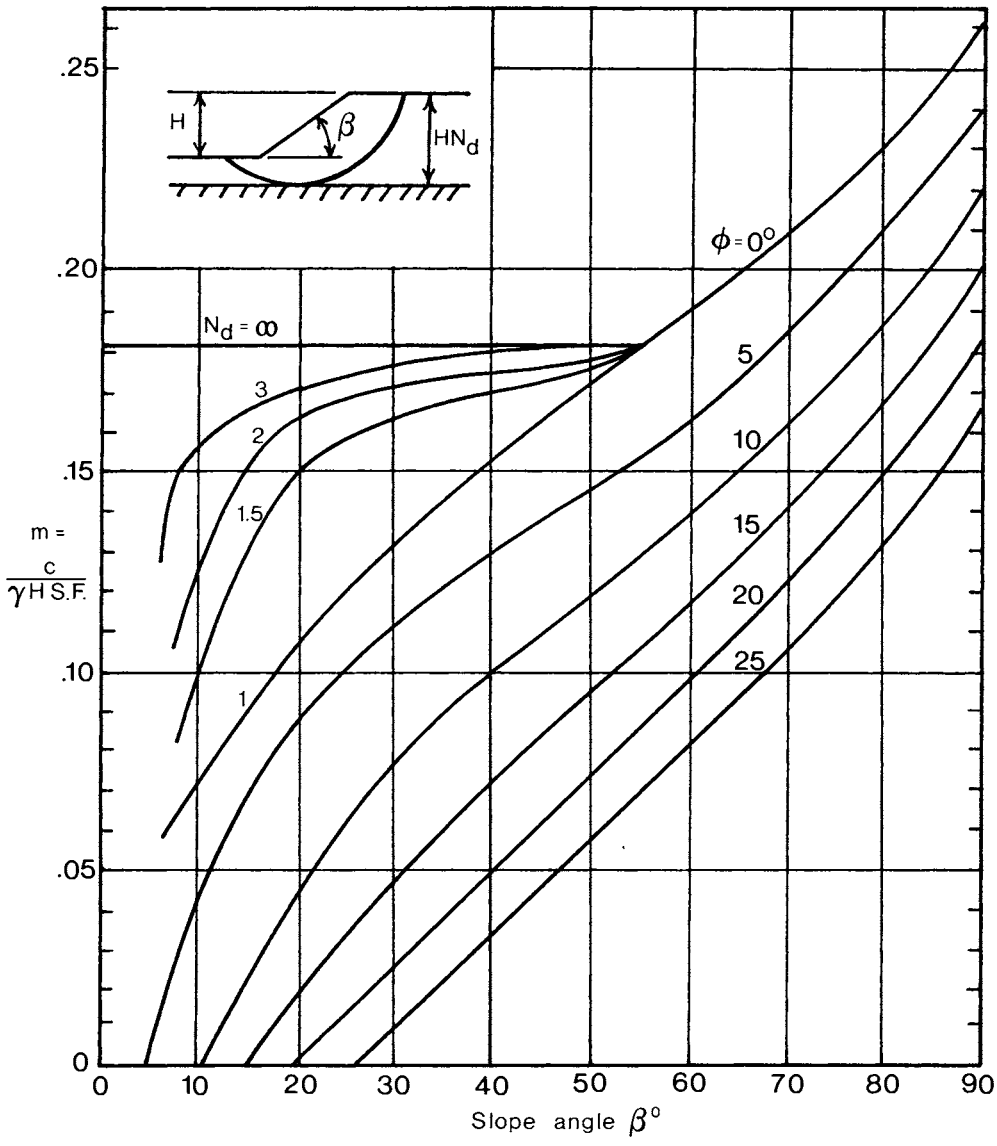

Fig. 5.2. Simple slope stability numbers, m (after Taylor, 1937).

estimated safety factor can be considered as the "critical" and most likely failure circle.

For different slope angles and soil internal friction angles, Taylor rearranged Eqn. 5.1 into the form below. Term m is called the "stability number" of the slope. It is a dimensionless quantity which can be measured or calculated from the critical circle geometric parameters.

$$m = \frac{c}{H(S.F.)\gamma} = \frac{AXcg}{LrH} \qquad (5.2)$$

Fig. 5.2 gives the stability numbers which Taylor (1937, 1948) found for different slope angles, β, and angles of internal friction, ϕ. The numbers can be used in various ways. For instance, the maximum height of a slope structure can be found for a certain slope angle and desired safety factor using Eqn. 5.2. Alternatively, the required slope angle can be determined for a fixed height of slope and desired safety factor, or the safety factor of a given soil strength, slope angle and height can be assessed.

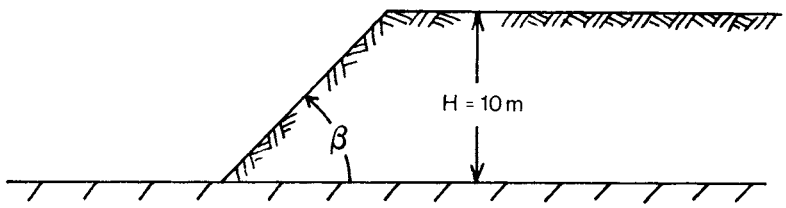

Fig. 5.3. A simple slope in Problem 5.1.

Problem 5.1. The 10 m high slope illustrated in Fig. 5.3 rests on a stronger soil deposit. The soil in the slope is frictionless with a cohesive strength of 23.5 kPa and a density 16 kN/m^3. What is the highest permissible slope angle?

From Eqn. 5.2, $m = c/(\gamma H) = 0.15$
Fig. 5.2 shows that the maximum slope angle for ϕ=0 and n_d=1 is 38^0.

Problem 5.2. If the slope in Fig. 5.3 had an angle β=45^0, density 18 kN/m^3, cohesion 13 kPa and friction angle 25^0, what would be the estimated safety factor?

Fig. 5.2 gives m = 0.042 for β = 45^0 and ϕ = 25^0. Thus the safety factor, $S.F. = c/(m\gamma H)$ = 1.72.

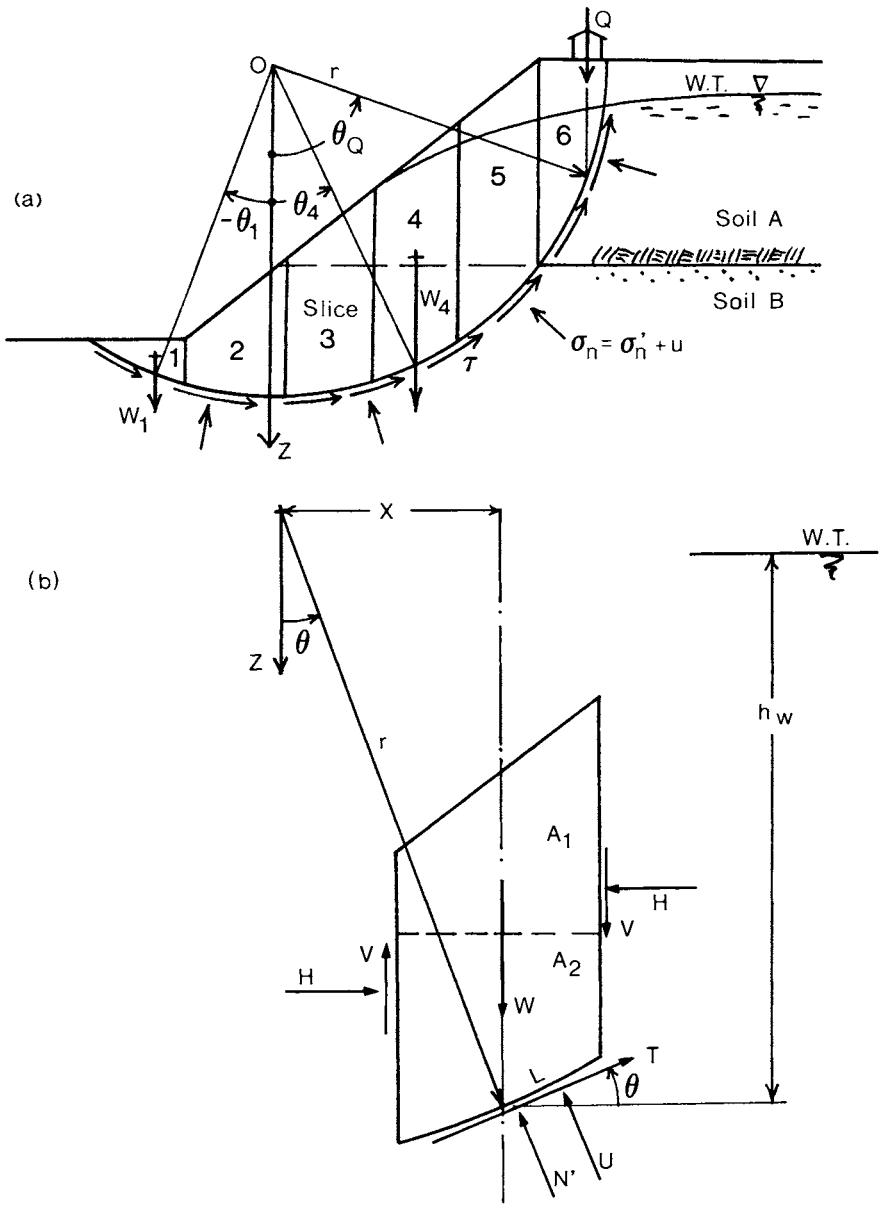

Fig. 5.4. (a) The method of slices for analyzing slope stability. (b) Forces on one slice, (Taylor, 1948)

5.1.2. The Method of Slices

As usual in soil mechanics, a great many real situations are more complex than the straight slope composed of uniform soil shown in Fig. 5.1. Layered soils, the presence of a water table, irregularly shaped slopes, surface loads and other factors cannot be handled by the stability numbers of Fig. 5.2. In complicated cases, the method of slices can be used, as described by Taylor (1948). Fig. 5.4(a) depicts a slope in a soil having two layers, a water table and a surface load, Q. The analysis method of slices involves the drawing of a trial soil slip circle with a center chosen at O and radius r, as shown. The potential sliding soil sector is then split into slices with vertical sides. The creation of six slices has been shown in Fig. 5.4(a) as an example, with the objective being to have the bottom boundary of each slice not far away from a straight line with constant inclination (such as L in Fig. 5.4(b)). This will allow the resolution of forces on each slice in singular directions.

The slope of the bottom of each slice is measured at a point vertically below the center of gravity. In slices with two vertical sides, such as slices 2, 3, 4 and 5 in Fig. 5.4, the center of gravity lies essentially along the vertical centerline, such as the line of W_4. In slices with more triangular shapes, as numbers 1 and 6 in the example of Fig. 5.4, an attempt should be made to estimate the location of the center of gravity, and measure the bottom boundary slope below it, like $-\theta_1$. In the case of a surcharge load, Q, angle θ_Q is measured on the slip circle directly below the center of Q as shown.

Each slice can now be analyzed as pictured in Fig. 5.4(b). W is the weight of the slice which has cross sectional area A. In uniform soils, the slice weight is simply the weight density times the area. If the slice comprises more than one soil type or degree of saturation, the area can be divided into appropriate parts, such as A_1 and A_2, and the weights of the parts summed to yield the total wet weight. On the bottom surface there act normal and tangential forces, N and T. For the purpose of an effective stress analysis, the normal force should be divided into the effective intergranular force, N', plus the water force, U. The water force is found by determining the water pressure, u, at the bottom midpoint and multiplying by length, L. Water pressure, u, in the absence of significant dynamic water pressure, is the height of the water table, above the slice bottom midpoint h_w times the unit weight of water. Thus the water force U is:

$$U = \gamma_w h_w L \tag{5.3}$$

In the case that the flow of water in the slope causes dynamic shifts of the static pressure regime, then flow nets should be drawn as shown in Chapter 4. Fig. 5.5 gives an example of a slope having a water table at height h_1 above the toe, and an impermeable underlying base. The flow net is drawn as described in Chapter 4, with squares being made among intersecting equipotential and flow lines. After the possible failure slip circle has been drawn, the water pressure can be evaluated at all points along this surface.

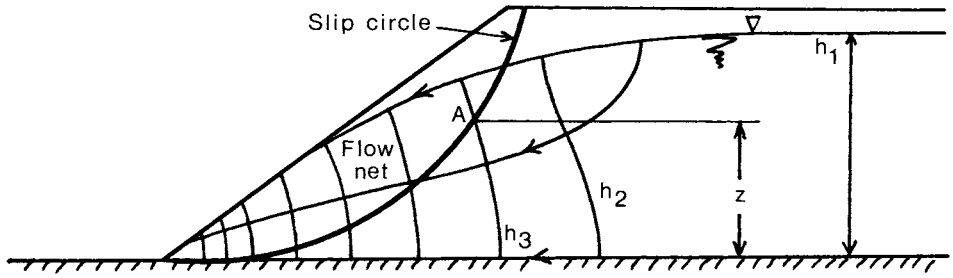

Fig. 5.5. A waterflow net in a slope, and the measurement of height, z, and potential, h, at a slice bottom midpoint, A.

At point A, for instance, the total water potential (static pressure plus elevation) is h_3, which is two equal potential drops less than h_1. The height of point A is z above the reference elevation, and thus the pore pressure, u, at that point can be found as;

$$u = (h_3 - z)\,\gamma_w \tag{5.4}$$

In the simplified method of slices, it is assumed that the forces on the slice sides, horizontal, H, and vertical, V, are equal on both sides. Then for equilibrium, the sum of force components normal to the base equals zero, as follows.

$$N = N' + U = W\cos\theta \tag{5.5}$$

Force T parallel to the slice base is the actual force required to maintain equilibrium. Its maximum possible value, T_{max}, can be found from Coulomb's soil strength law, modified for effective stresses.

$$T_{max} = N'\tan\phi' + c'L = (W\cos\theta - U)\tan\phi' + c'L \tag{5.6}$$

At this stage, one can consider the moments which are tending to rotate each slice along the assumed circular slip line, as compared to those moments which can potentially resist this rotation. Such a concept is used commonly in soil mechanics to assess the safety factor of a structure, and such a factor can be defined for the entire slope by summing the potential resisting and active rotating moments of all the slices and the surface load. It should be noted that load Q contributes both to the total rotating moment, and to the resisting moment by virtue of the additional frictional strength it can produce on the slip circle below it. However, there is no additional cohesive shear strength along the circle associated with Q.

$$S.F. = \frac{\sum \text{Resisting moments}}{\sum \text{Rotating moments}} = \frac{\sum[\gamma A\cos\theta - uL + Q\cos\theta_Q]\tan\phi' + c'L]}{\sum[\gamma A\sin\theta + Q\sin\theta_Q]} \quad (5.7)$$

Eqn. 5.7 now gives an estimation of the safety factor for the trial circle which was originally drawn. However, this does not guarantee that the 'critical' or most likely failure surface has been found. The above procedure should be repeated for some other circular slip surfaces having different radii and centers. Fig. 5.6 gives an example of a thorough analysis of a slope in this fashion. If a sufficient number of trial circles are drawn and analyzed for their estimated safety factors, loci of slip circle centers yielding equal factors of safety can be found. The slip circle and its center which gives the smallest safety factor is deemed to be the critical circle, and its safety factor the likely one for the structure. In usual practice, not that many circles need to be constructed and analyzed, because experience in this method generally allows the critical failure circle to be chosen quickly.

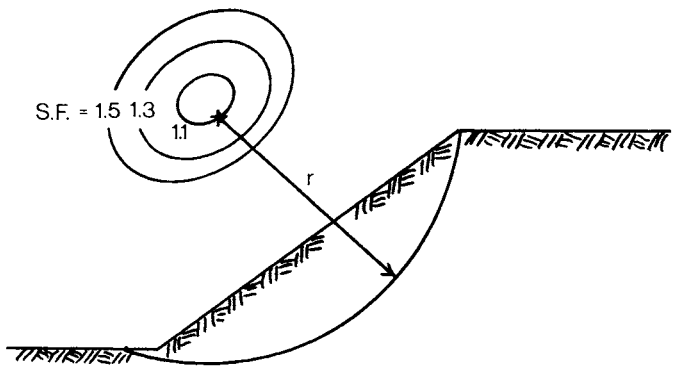

Fig. 5.6. The loci of centres of slip circles which give equal estimations of slope stability safety factors.

Problem 5.3. Fig. 5.7 shows an example of a fairly steep slope comprised of uniform cohesive and frictional soil, and having a surface load, Q. Load Q is 3 m wide and is 200 kn/m of length. Because the slope is fairly steep, the slip circle is likely to pass through the toe at point B. And since there is a considerable surcharge load Q, with a defined width of effect, 3 m, the slip circle most probably intersects the edge of the surcharge at point C. In this example, four circles have been drawn through points B and C, along with a fifth circular section, DE, not passing through B and C. Table 5.1 is constructed to record the areas, angles and weights of the individual slices systematically, in order to fit them conveniently into Eqn. 5.7.

TABLE 5.1. Measurements and calculations for the slope slices of Fig. 5.7 to use in Eqn. 5.7 for the safety factor determination.

r m	Slice	θ^0	A m^2	W kN/m	W$\cos\theta\tan\phi$ kN/m	L m	cL kN/m	W$\sin\theta$ kN/m
12	1	3	3.0	52.9	24.6	2.5		2.8
	2	12	8.7	153.5	70.0	2.6		31.9
	3	24	12.5	220.5	93.9	2.9		89.7
	4	37	15.0	264.6	98.5	3.2		159.2
	5	56	12.0	211.7	55.2	6.8		175.5
	Q	60	-	200.0	46.6	-		173.2
					388.8	18.0	324.0	632.3
S.F. = (388.8 + 324.0)/632.3 = 1.13								
14	1	9	2.5	44.1	20.3	2.5		6.9
	2	13	7.5	132.3	60.1	2.6		29.8
	3	28	11.3	199.3	82.1	2.8		93.6
	4	42	13.0	229.3	79.5	3.1		153.4
	5	56	9.0	158.8	41.4	6.6		131.7
	Q	59	-	200.0	48.0	-		171.4
					331.4	17.6	316.8	586.8
S.F. = (331.4 + 316.8)/586.8 = 1.10								
16	1	12	2.4	42.3	19.3	2.6		8.8
	2	21	7.2	127.0	55.3	2.7		45.5
	3	30	10.0	176.4	71.2	2.8		88.2
	4	41	11.8	208.2	73.3	3.0		136.6
	5	54	8.3	146.4	40.1	5.9		118.4
	Q	57	-	200.0	50.8	-		167.7
					310.0	17.0	306.0	565.2
S.F. = (310.0 + 306.0)/565.2 = 1.09								
20	1	13	2.0	35.3	16.0	2.6		7.9
	2	24	6.6	116.4	49.6	2.7		47.3
	3	32	8.8	155.2	61.4	3.0		88.2
	4	42	10.0	176.4	61.1	3.0		118.0
	5	51	7.5	132.2	38.8	5.9		102.8
	Q	54	-	200.0	54.8	-		161.8
					281.7	17.1	307.8	520.0
S.F. = (281.7 + 307.8)/520.0 = 1.13								
12	1	-5	5.9	104.1	48.3	5.5		-9.1
(DE)	2	9	11.8	208.2	95.9	2.5		32.6
	3	21	16.3	287.5	125.2	2.6		103.0
	4	35	20.0	352.8	134.8	2.8		202.4
	5	51	22.0	388.1	113.9	9.8		301.5
	Q	53	-	200.0	56.1	-		159.7
					574.2	23.2	417.6	790.1
S.F. = (574.2 + 417.6)/790.1 = 1.26								

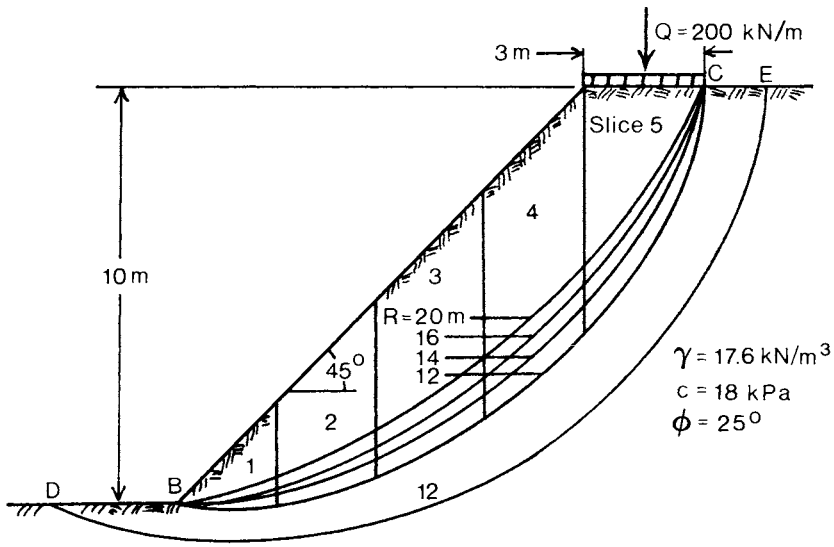

Fig. 5.7. Analysis of slope in Problem 5.3 by the method of slices.

In Table 5.1, the 16 m radius circular section has the smallest safety factor of 1.09, thus making the critical circle very close to this radius. As suspected, section DE, which does not intersect the slope toe or the edge of the surcharge, has a considerably higher safety factor of 1.26.

5.2 STABILITY OF WATERCOURSE BANKS

The construction of watercourses, especially drainage waterways, poses serious problems of bank stability in many soil types. The difficulty is generally most serious at specific times of each year when a large amount of water is present in the soil beside a watercourse, either due to high rainfalls, or spring melting in colder climates. Fig. 5.8(a) shows the case of a high water table adjacent to a watercourse. As water flows from the soil towards the ditchbanks, a flow net is established similar to the one illustrated in the figure.

At any point on the potential circular soil slip surface shown, the water pressure can be calculated as the potential value of the equipotential line intersecting that point, less the elevation of the point above the zero

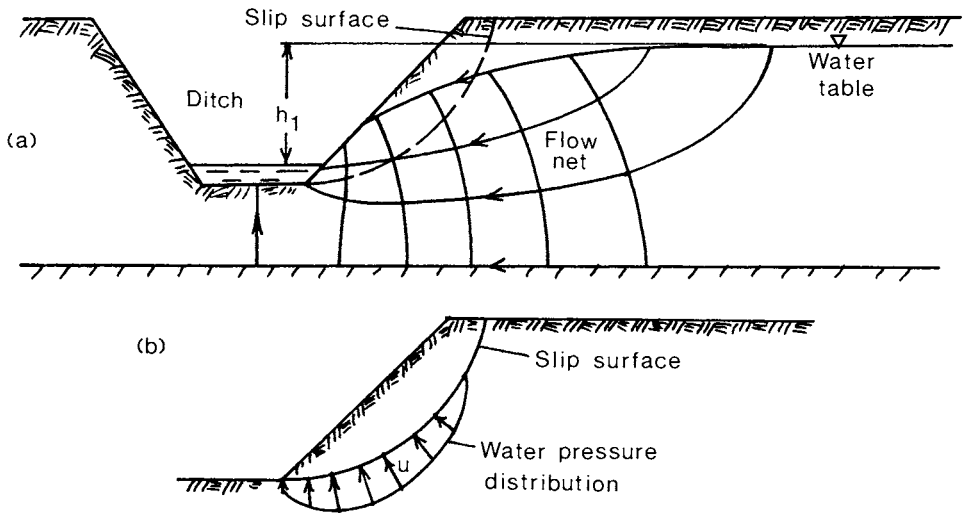

Fig. 5.8. (a) Water flow in a ditchbank with a high water table in the adjacent field. (b) Water pressure distribution on the potential slip surface.

reference potential (the level of the water in the ditch bottom in this case), as described in Section 4.2.1. In Fig. 5.8(b), a typical water pressure distribution diagram has been constructed for the relevant case.

When the stability of the bank is estimated, using the method of slices of Section 5.1.2, the water pressure acting on the slip surface will have a considerable effect in reducing the effective normal stress on the slip surface, and hence the soil shear strength. This explains the fact that watercourse banks very often are seen to fail at times when there is much water in the adjacent soil above the level of the ditch bottom.

Even if the presence of water does not cause the entire bank to slip at one moment, the high pressure gradient near the bank toe can cause 'quick' conditions there (practically zero effective normal stress and shear strength) particularly in granular soils. This phenomenon gives rise to the conditions illustrated in Fig. 5.9(a), (b) and (c). Following the slaking of soil from the toe region, a new effective slope angle is given to the entire bank. This new configuration is less stable than the original, and with the aid of the water in the adjacent soil, the entire bank slumps into a new shape. The new shape may well be stable for some time, but the bottom of the watercourse has been raised by the fallen soil material, and thus the effective ditch depth is less. In addition, if water is moving quickly in the watercourse, the loose failed soil material is washed easily downstream to cause even greater concentrations of sediment at some settling location down the way.

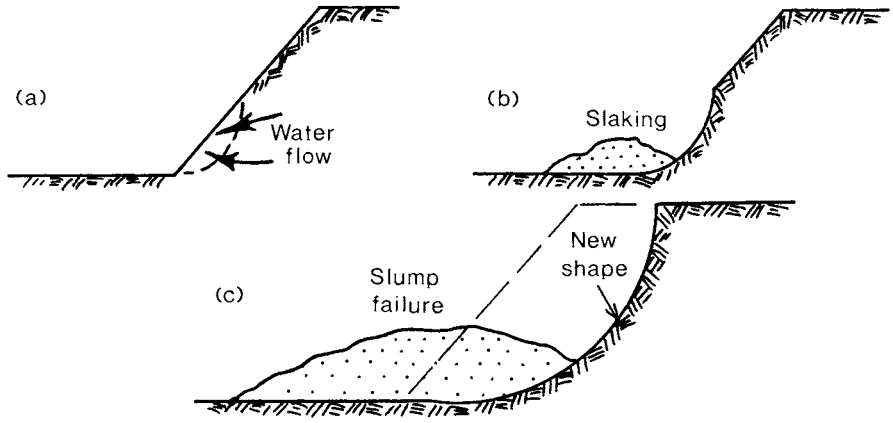

Fig. 5.9. (a) Water flow from the toe region of a watercourse bank causing (b) slaking of the toe, and possibly (c) total slope instability.

The lowering of the bank slope angle will increase the overall stability of the bank, but by itself cannot guarantee the prevention of the local slaking and subsequent failure shown in Fig. 5.9. One method which may be costly, but promises to be effective in preventing bank failure due to seepage pressures, is the installation of an interceptor subsurface perforated drain tile parallel to the watercourse, and at a depth equal to or greater than the ditch bottom. As shown in Fig. 5.10(a), the drain effectively lowers the water table near the watercourse bank, and reduces the hydraulic pressures acting within the slope and at its face. The drain tile can have a smaller longitudinal slope than the watercourse bed, and thus have an outlet in the ditch itself at some point downstream, as shown in Fig. 5.10(b).

5.3. EROSION OF BANKS

Not only can water inside the soil cause instability in sloped watercourse banks, as shown in the previous Section, but the water moving in the waterway, or into it, can also give rise to structural damage. If the water is moving too fast at the bottom of the watercourse, erosion can take place at the toe of each side of the ditch and produce a shape similar to that pictured in Fig. 5.9(b) above. Theoretically, a certain water velocity is required to move soil particles, as described by the equation of Mavis (1935) below.

$$v = 0.152D^{4/9}(G_S - 1)^{1/2} \qquad (5.8)$$

where v = the minimum water velocity for movement (m/s)
D = average soil particle diameter (mm)
G_s = specific gravity of particles (usually 2.6 - 2.7)

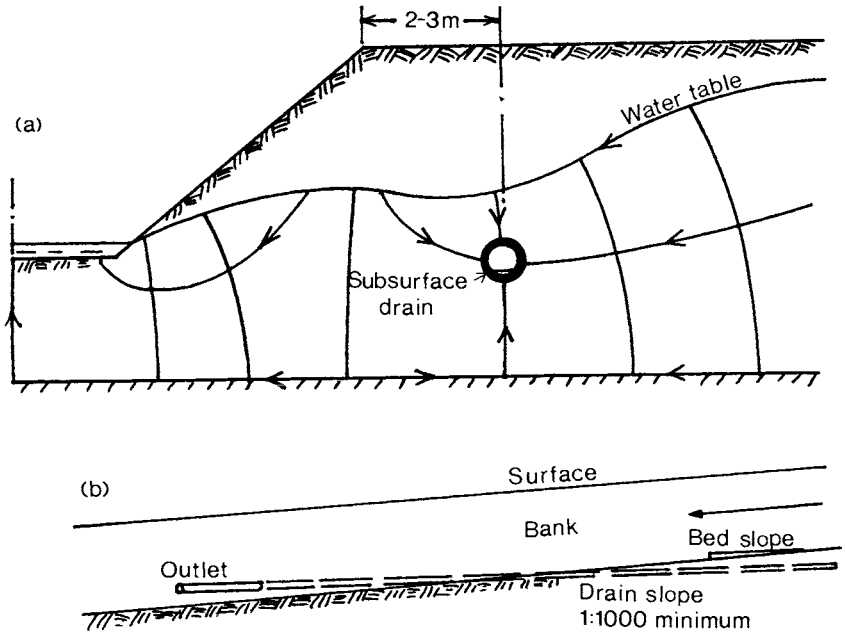

Fig. 5.10. (a) The action of a subsurface drain in a watercourse bank in lowering the water table near the bank. (b) The downstream outlet of the drain.

For soil mixtures, Table 5.2 developed by Fortier and Scobey (1926) gives the maximum permissible average flow velocities in unprotected straight waterways with small grades.

TABLE 5.2. Maximum permissible flow velocities in unprotected ditches, (Fortier and Scobey, 1926).

Soil material	Maximum water velocity, m/s	
	Clear water	Water with suspension
Fine sand	0.45	0.75
Silty loam and silt	0.50-0.60	0.75-1.00
Loam	0.70-0.80	1.00-1.10
Clay	1.10-1.20	1.50
Fine gravel	0.75	1.50
Coarse gravel	1.20	1.80

Smedema and Rycroft (1983) have also interpreted some recommended watercourse design guidelines employed in the Netherlands, both for maximum permissible water velocity and side slopes, as shown in Table 5.3. The lower velocities and slopes apply to unprotected watercourse banks, while the larger quantities on each line refer to vegetated canals.

TABLE 5.3. Limitations on flow velocity and on side slope in drainage canals (Smedema and Rycroft, 1983, adapted from ILRI, 1964).

Soil type	Permissible mean flow velocity (m/s)	Maximum side slope
Fine sand	0.15-0.30	1:3-1:2
Coarse sand	0.20-0.50	1:3-1:1.5
Loam	0.30-0.60	1:2-1:1.5
Heavy clay	0.60-0.80	1:2-1:1

In order to limit the mean flow velocity in waterways, the grade of the bed must be controlled, or well designed drop structures are required along the waterway length. Readers are referred to the books by Luthin (1973), Schwab et al. (1981) or Smedema and Rycroft (1983) for further details on the appropriate design practices for watercourse profiles.

Erosion and deformation of ditch banks can arise also from water flowing down into a watercourse from the sides during periods of heavy runoff from adjacent lands. The description of such erosion will be found in Chapter 7. In general, the best method for combatting such erosion on watercourse banks seems to be the establishment of a vigorous growth of grassy vegetation, by whatever technique is appropriate to the local climate. Table 5.3 indicates that a good cover of vegetation on canal sides allows a doubling of the interior water flow velocity, without serious erosion on most soils. This would indicate also a similar improvement in resistance to rill and gully erosion arising from water running down the banks.

5.4. STABILITY OF SMALL EARTHDAMS

Fig. 4.9 illustrated a waterflow net through a small earthdam in the case where the reservoir behind the dam is full. The analysis of stability of this slope is carried out in the same manner as those described in Section 5.1.2. Fig. 5.11 shows the kind of water pressure distribution which occurs on a potential slip circle for the same type of dam as shown in Fig. 4.9. The water pressure acting on each slice bottom center is mutliplied by the slice length, L, to give the water force U for insertion in Eqn. 5.7, in order to estimate the slope stability safety factor.

One instance in which hydraulic gradients and internal pore water pressures can become critically large in an earthdam is the condition of drawdown. This occurs when the reservoir behind the dam has been emptied quickly, and there still remains most of the water inside the soil, as shown in Fig. 5.12. This figure also shows the kind of water pressure distribution which can arise in such a case, both on the former upstream and downstream sides of the earth structure. The method of slices, as explained in Section 5.1.2 should be employed to verify the stability safety factor of both sides of the dam in this instance.

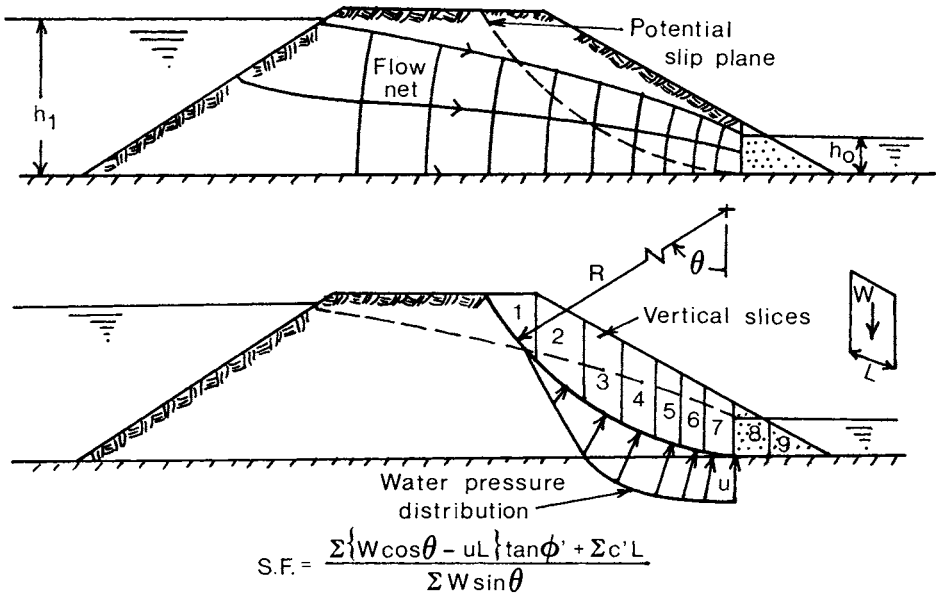

Fig. 5.11. Water flow net in an earthdam and the water pressure distribution on the potential slip circle when the reservoir is full.

The illustrated drawdown case is not a permanent state, since after a time the phreatic line will be lowered as water drains from within the dam. Nevertheless, the situation does remain much as pictured in Fig. 5.12 for some time, and the structure could be in danger of failing during that period. As with the steady state case of leakage as shown in Fig. 5.11, the water pressure distribution, calculated from the potential of water along the slip circle minus the elevation at each point, is used in Eqn. 5.7 to determine the safety factor of both slopes involved.

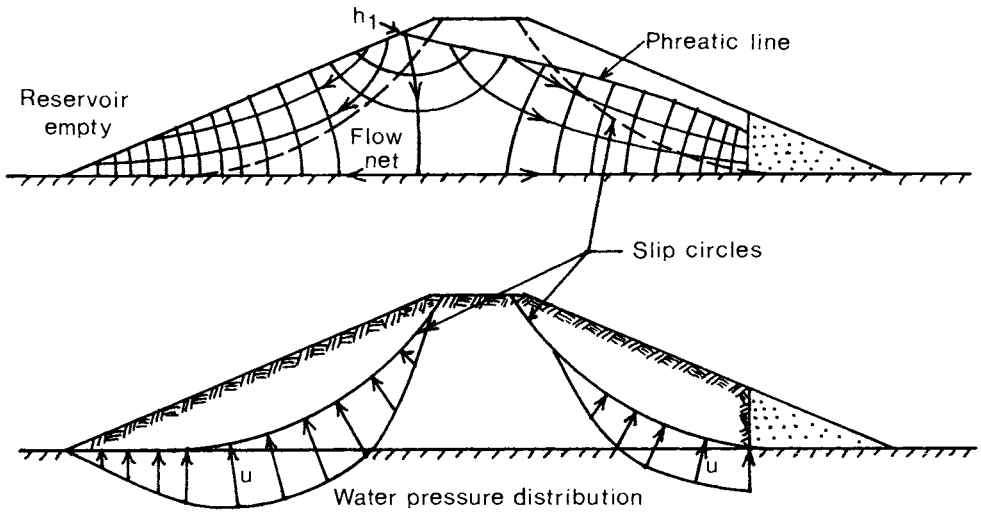

Fig. 5.12. Water flow nets and water pressure distribution on potential slip circles during drawdown of the water in an earthdam.

5.5. PROBLEMS

5.4. It is desired to cut a slope 10 m high in a frictionless soil having a cohesion of 20 kPa and a density 17 kN/m^3. What is the maximum possible angle of the slope?

Answer: $\beta = 23^0$.

5.5. A 9 m high slope has a slope angle of 40^0 and the soil is a clay loam having a density of 17.6 kN/m^3, cohesion 10 kPa and angle of friction 20^0. What is the safety factor of the slope?

Answer: S.F. = 1.26.

5.6. The slope shown in Fig. 5.13 is a composite being formed of layers of sand and clay soils, with the properties shown. Using the method of vertical slices, estimate the safety factor of this slope.

Answer: S.F. = 1.75.

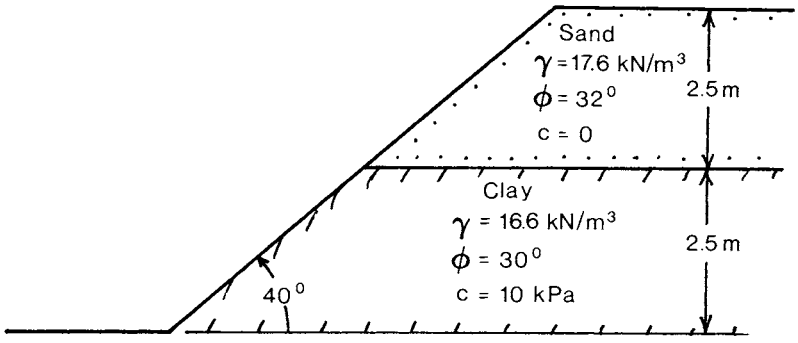

Fig. 5.13. Layered slope in Problem 5.6.

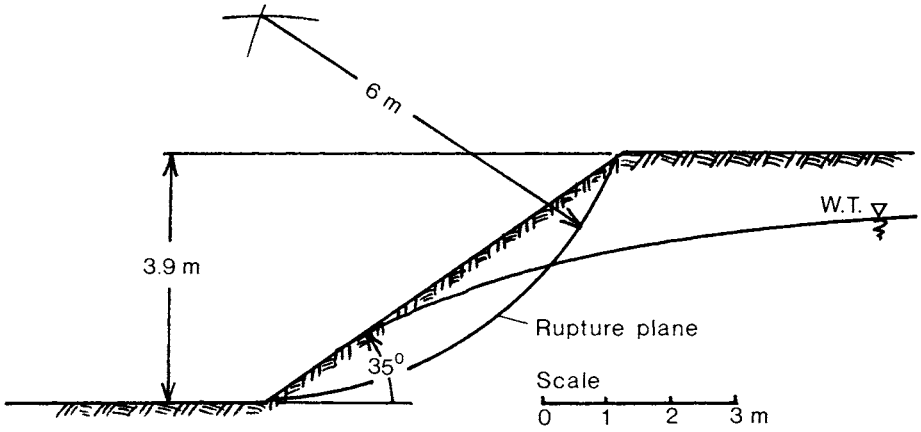

Fig. 5.14. Slope with a water table in Problem 5.7.

5.7. The slope of Fig. 5.14 is composed of a sandy loam soil having a density of 16.7 kN/m^3, effective friction angle 30^0 and cohesion 2.25 kPa. In the spring after snowmelt and rains, the water table in the slope is as shown to scale in Fig. 5.14. If the slope potential failure circle has a radius of 6 m as shown, find the slope safety factor (a) with the water table as shown, and (b) with the water table removed by time or subsurface drainage. (Assume that the soil effective strength and density remain approximately the same in both cases).

Answer: (a) S.F. = 0.90, (b) S.F. = 1.4.

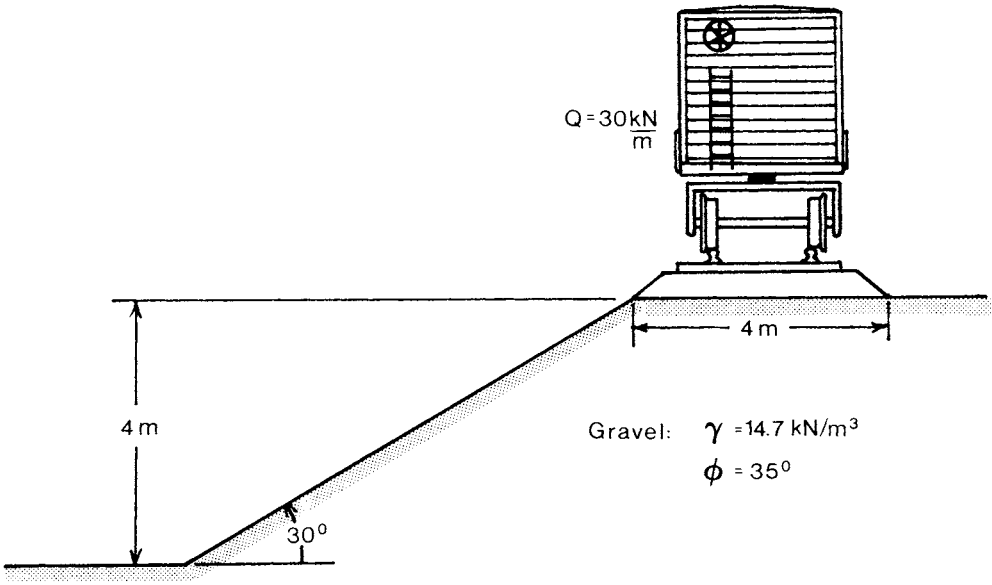

Fig. 5.15. Gravel slope of Problem 5.8.

5.8. The gravel slope shown in Fig. 5.15 is used to support a railway embankment. Estimate the safety factor of the slope using the given weight of train per unit length.

Answer: S.F. = 1.9.

Chapter 6. Lateral Earth Pressures

6.1. ACTIVE AND PASSIVE WALL PRESSURES

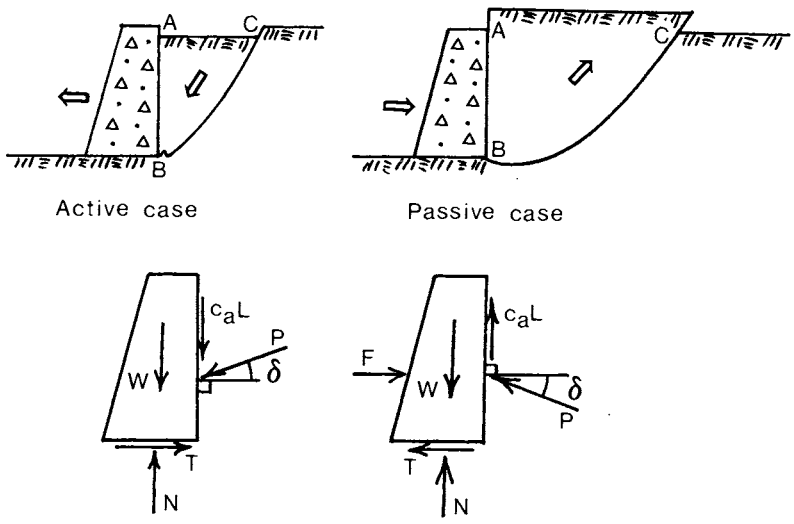

Fig. 6.1. Active and passive lateral earthpressure cases and wall forces.

Lateral, or wall pressures are those acting more or less in the horizontal direction from soil onto retaining structures or soil cutting tools. The term 'active' soil pressure is used in cases where the soil is moving downwards with gravity, and is actively moving a wall away from its original position. 'Passive' soil pressure occurs when soil is being forced upwards against gravity by a moving structure or soil cutting tool, as depicted in Fig. 6.1. Both of these cases represent the limit equilibrium state, and the soil is considered to be failing, both on internal rupture surfaces, such as lines BC in Fig. 6.1, as well as at the interface with the contacting object along lines AB. Fig. 6.1 shows also the basic systems of forces acting on a wall or other object in the active and passive soil failure cases.

In Fig. 6.1, the force from the soil perpendicular to the wall has been combined with the frictional shear resistance force parallel to the wall to form a single resultant, P, inclined at angle δ to the perpendicular. It should be noticed that the wall adhesion force, c_aL, the frictional component of soil force P, and the base shear resistance force, T, all act in directions opposite to the relative motion of the soil with respect to the wall.

There are further possibilities for the directions of interface shear forces in the case that the wall or tool is not moved horizontally, but these are situations rarely met in practice. Fig. 6.2 shows the conditions of shear and normal stresses on the wall face, AB, for four possible cases of active and passive soil failure, using the Mohr stress diagram and the same conventions as shown in Chapter 2. Situations number 1 and 2 are those represented in Fig. 6.1 for the normal active and passive soil failure cases, respectively, while situations number 3 and 4 are rarely seen.

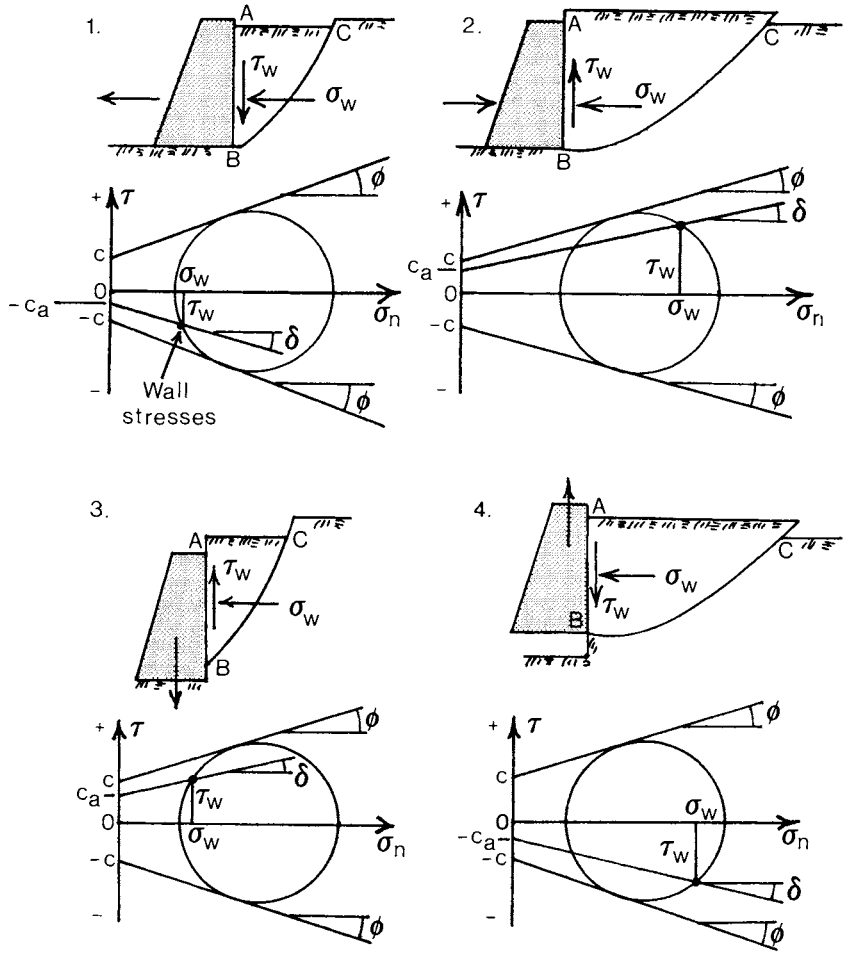

Fig. 6.2. Four possible soil to wall failure configurations. Cases 1 and 2 are the normal active and passive conditions.

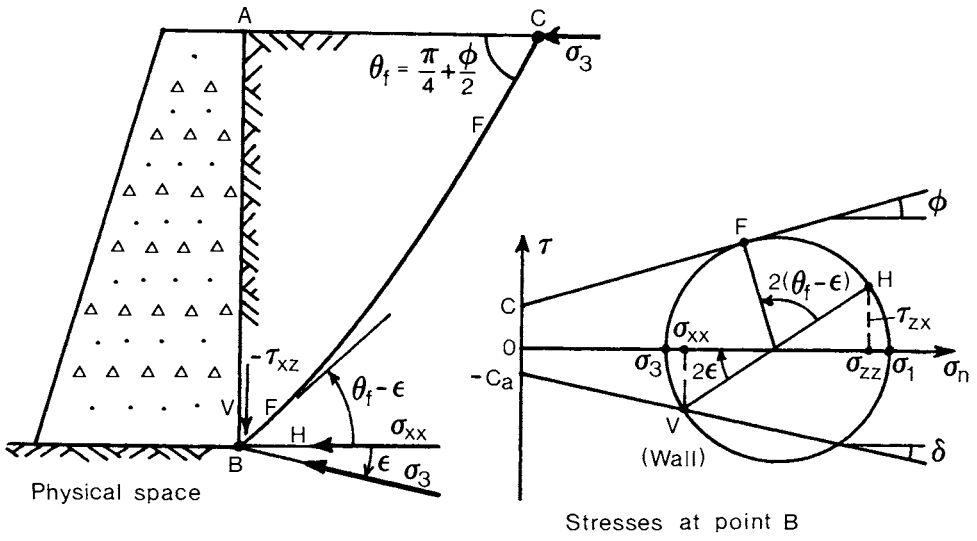

Fig. 6.3. Stress conditions on a wall during active soil failure.

In Fig. 6.1 and 6.2, the soil internal failure surfaces, BC, are shown as curved. This results when there is frictional shear resistance along a vertical wall face, as depicted in Fig. 6.3. At point C on the soil surface, there is no shear on the horizontal plane, and thus the vertical and horizontal pressures are principal stresses, the latter being σ_3. The inclination of the soil failure plane at point C is $\theta_f = (\pi/2 + \phi)/2$, as in Fig. 2.6. In general, however, there is shear stress along the soil to wall interface, and for the vertical wall face shown in Fig. 6.3, the normal pressure on the wall cannot be a principal stress. Instead, the wall surface is a soil to wall failure plane of which the strength is governed by the soil to wall coefficient of friction and adhesion (Eqn. 2.2), and the principal stresses together with the soil rupture plane are rotated to a different inclination than that at point C.

In Fig. 6.3, the wall normal and shear stresses are identified on the Mohr diagram as point V, the shear being negative. This stress combination lies also on the line of soil to wall strength which has intercept $-c_a$ on the shear axis, and slope $-\delta$. The minor principal stress, σ_3, is located at a clockwise angle of 2ϵ in the Mohr diagram from the wall stresses. Therefore, σ_3 is inclined clockwise at angle ϵ from σ_{xx} which is perpendicular to the vertical wall. The major principal stress, σ_1, as well as the soil failure plane are rotated also at that same angle compared to their attitudes at point C on the soil surface.

In the cases where soil weight density times depth is significant compared to internal cohesion, it is impossible to analyze the exact stress variations from point C to point B behind a retaining wall. This is because stress

characteristic equations 2.21 and 2.22 cannot be integrated exactly between those two points in x-z space. Some simplifications or numerical mathematical techniques must be employed in order to arrive at a solution to the forces acting on soil retaining walls in the general case.

6.1.1. Coulomb's method

In 1776, Coulomb did not have the techniques of Mohr's circle of stresses at his disposal, nor the method of stress characteristics. Nevertheless, he managed to analyze the forces on a certain class of retaining walls, locate the approximate soil internal failure plane and find the necessary constraining force from a wall for the active soil failure case.

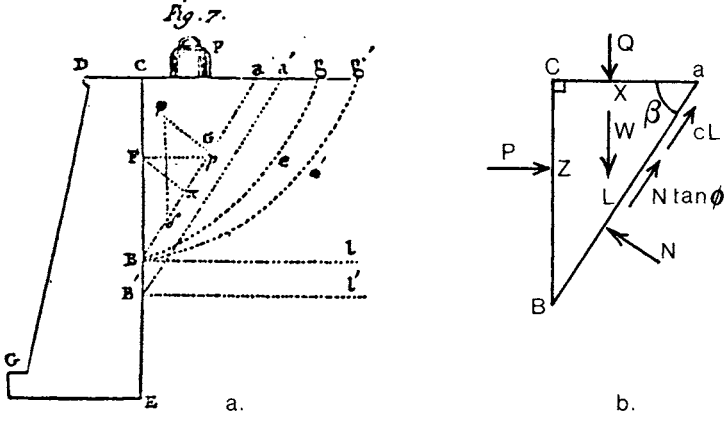

Fig. 6.4. (a) Coulomb's (1776) drawing of active soil failure behind a smooth retaining wall (lines gB and g'B') and approximate straight line failure planes aB and a'B'. (b) Contemporary notation for the forces.

Fig. 6.4(a) is reproduced from Coulomb's original paper (1776), and it shows some observed curved soil rupture surfaces, such as Beg and Be'g', similar to Fig. 6.1, 6.2 and 6.3. Coulomb noted that to find the soil failure plane, it is necessary to locate that path in the soil which will result in the largest pressure on the wall during active soil failure. In other words, the weakest plane in the soil, taking account of internal friction, cohesion strength and soil weight, is the likely rupture surface.

However, Coulomb stated also that the appropriate theoretical straight line soil rupture plane, such as Ba in Fig. 6.4(a), will yield a wall retaining force which "does not differ except by a very small quantity" from that of the curved failure line, Beg. He proceeded to establish the force system on the soil mass bounded by a horizontal surface, the straight internal failure plane and a smooth vertical wall. Fig. 6.4(b) shows the force system, using present day terminology for the force vectors.

Here, P is the required wall retaining force to just prevent movement, N is the soil reaction normal to the internal failure plane and $N\tan\phi$ and cL are the frictional and cohesional components, respectively, of soil shear strength along the rupture surface Ba. Resolving all of these forces in directions perpendicular and parallel to the failure plane, Ba, and invoking equilibrium for the condition of the limiting forces when soil failure is imminent, the following expression results for the wall force P in terms of the soil strength parameters and the geometry of soil failure.

$$P = \frac{\frac{1}{2}\gamma x(z - x\tan\phi) - c(x^2 + z^2)}{x + z\tan\phi} \tag{6.1}$$

where γ is the soil specific weight.

In Eqn. 6.1, the dimension x of the soil wedge has not yet been determined since the inclination, β, of the soil failure surface is not known. Coulomb applied the calculus principle of maximization to find the rupture attitude which gives the largest wall force, as follows.

$$\frac{dP}{dx} = \frac{(\gamma z\tan\phi + c)(z^2 - 2xz\tan\phi - x^2)}{(x + z\tan\phi)^2} = 0 \tag{6.2}$$

$$x = z(\sqrt{1 + \tan^2\phi} - \tan\phi) \tag{6.3}$$

$$z/x = \tan\beta = (\sqrt{1 + \tan^2\phi} - \tan\phi)^{-1} = \tan(\pi/4 + \phi/2) \tag{6.4}$$

$$P = \frac{1}{2}\gamma z^2\left[\frac{1 - \sin\phi}{1 + \sin\phi}\right] - 2cz\sqrt{\frac{1 - \sin\phi}{1 + \sin\phi}} \tag{6.5}$$

This is the well known Coulomb solution for the active force on a smooth vertical earth retaining wall. It can also be expressed in terms of the active earthpressure coefficients, K_a and K_c.

$$P = \frac{1}{2}\gamma z^2 K_a - 2czK_c \tag{6.6}$$

where in the case of the smooth vertical wall,

$$K_c^2 = K_a = \frac{1 - \sin\phi}{1 + \sin\phi} \tag{6.7}$$

6.1.2. Tension cracks

A problem with the Coulomb solution above for wall pressures is that the wall force, P, can have a negative magnitude. This occurs when the second term of Eqn. 6.5 or 6.6 is larger than the first, in cases of walls with small height and soils of large cohesional strength. The physical meaning of such a

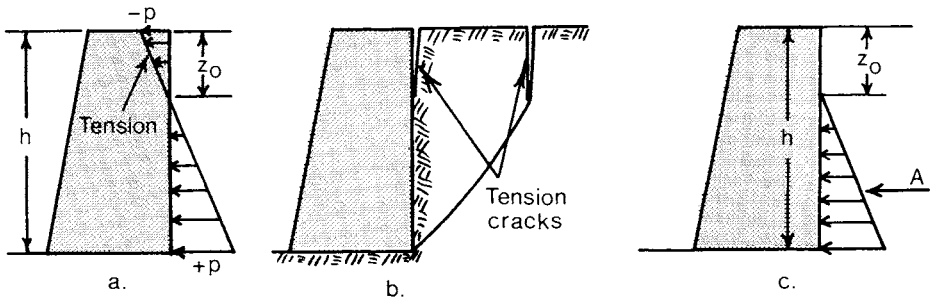

Fig. 6.5. (a) Apparent tension from soil at the top of a wall predicted by the Coulomb method. (b) Actual tension cracks which form. (c) A more realistic picture of stress on the wall.

situation is that a tensile force must be applied on the soil to wall interface in order to cause active failure. Even if the net force is in positive compression, the upper section of the wall is theoretically under tension from the soil according to Coulomb's theory, as shown in Fig. 6.5(a). Such a state is not practical over a finite length of time, because air would enter between the soil and the wall, causing a tension crack at that interface, Fig. 6.5(b). In addition, Fig. 6.5(b) illustrates that tension cracks can appear from the ground surface behind the wall to a depth similar to that at the wall surface. From Eqn. 6.6, the depth of apparent tension can be calculated as;

$$z_o = \frac{cK_c}{\gamma K_a} \tag{6.8}$$

Therefore, the pressure distribution shown in Fig. 6.5(c) is the one which should be used for design purposes. It will result in a net estimation of active force on a wall of height h which is shown below, and which is evidently larger and more conservative than that of Eqn. 6.6.

$$P = \int_{z_o}^{h} p\,dz = \left[\tfrac{1}{2}\gamma z^2 K_a - czK_c\right]_{z_o}^{h} = \tfrac{1}{2}\gamma(h^2 - z_o^2)K_a - c(h - z_o)K_c$$

$$= \tfrac{1}{2}\gamma h^2 K_a - chK_c + \frac{c^2 K_c^2}{2\gamma K_a} \tag{6.9}$$

6.1.3. The general wedge theory

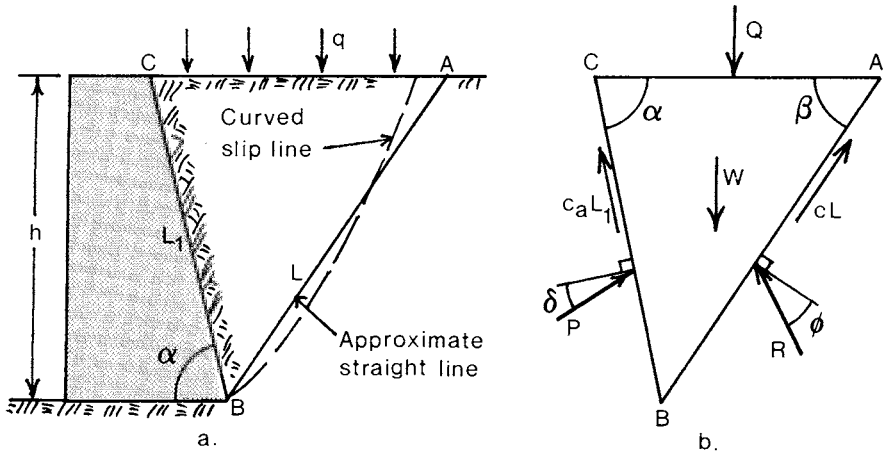

Fig. 6.6. (a) A wedge of sliding soil bounded by an assumed straight line slip plane, and (b) the forces acting on the wedge.

In the general case, retaining walls are not smooth nor are they necessarily vertical. They exhibit a coefficient of friction, $\tan\delta$, in contact with the soil, as well a possible adhesion strength, c_a. These complexities, as well as a possible surcharge, q, on the soil surface are shown in Fig. 6.6(a). Fig. 6.6(b) depicts the forces acting on an assumed soil failure wedge. On the inclined wall face, BC, a resultant force P is composed of a normal force and the frictional component of shear resistance, and thus P is inclined to the perpendicular at the friction angle, δ. In addition, there is the adhesive resistance force component, c_aL_1, acting contrary to the direction of motion of the soil mass relative to the wall. The inclination angle of the wall face to the horizontal is α.

In the same manner as Coulomb employed, these forces can be resolved parallel and perpendicular to force N, and equilibrium required, with the following expression resulting for force P.

$$P = \frac{[W+Q]\sin(\beta-\phi) - cL\cos\phi - c_aL_1[\cos(\alpha+\beta) + \sin(\alpha+\beta)]\cos\phi}{\sin(\alpha+\beta-\delta-\phi)} \qquad (6.10)$$

Substituting the geometrical details for W, Q, L and L_1, and putting the above expression in the form of the active earthpressure coefficients, the formulae below result.

$$P = \tfrac{1}{2}\gamma h^2 K_a - chK_c - c_a hK_{ca} + qhK_a \tag{6.11}$$

$$K_a = \frac{(\cot\alpha + \cot\beta)\sin(\beta - \phi)}{\sin(\alpha + \beta - \delta - \phi)} \tag{6.12}$$

$$K_c = \frac{\cos\phi}{\sin\beta \sin(\alpha + \beta - \delta - \phi)} \tag{6.13}$$

$$K_{ca} = \frac{\cos\phi \sin(\alpha + \beta) + \cos(\alpha + \beta)}{\sin(\alpha + \beta - \delta - \phi)} \tag{6.14}$$

In order to find the angle, β, of the soil failure plane, the K_a term is maximized with respect to this angle with the following result.

$$dK_a/d\beta = 0$$

$$\cot\beta = \frac{\sqrt{\frac{\sin(\alpha - \delta)\sin(\delta + \phi)}{\sin\alpha \sin\phi}} - \cos(\alpha - \delta - \phi)}{\sin(\alpha - \delta - \phi)} \tag{6.15}$$

The value of failure angle β calculated from Eqn. 6.15 can then be substituted into Eqn. 6.12 to 6.14 to find the earthpressure coefficients. The K_a factors thus calculated are the same as those computed by Terzaghi in 1943. Appendix 3 gives the values of the coefficients for a variety of soil and wall friction angles and wall inclination angles.

As in the case of the smooth vertical wall, Section 6.1.2, the theoretical model above can predict negative, or tensile pressures on the upper portion of any wall, which is not practical in real life. In the general case, the depth to which such negative wall pressure is predicted can be found by Eqn. 6.16 below. Only positive values of depth z_0 should be used. If z_0 is calculated in Eqn. 6.16 to be zero or negative, then it should be ignored, and Eqn. 6.11 used to compute wall forces. If z_0 is predicted to be positive, then Eqn. 6.17 should be employed.

$$z_0 = (cK_c + c_a K_{ca} - qK_a)/\gamma K_a \tag{6.16}$$

And the integration of only the positive pressures acting on a wall face will yield the force as formulated below.

$$P = \frac{\gamma}{2} K_a(h^2 - z_0^2) - cK_c(h - z_0) - c_a K_{ca}(h - z_0) + qK_a(h - z_0) \tag{6.17}$$

In the event that the soil behind a wall is saturated with water up to a

certain depth, then the effective stress method should be used. The soil slip angle and the active earthpressure K factors should be calculated using the effective soil friction angle, and the wall pressure evaluated at each depth. This pressure is then integrated to give the effective or intergranular force on the wall, and then the force arising from water pressure is added to give the total. An example of such a calculation is shown in Fig. 6.7. As is often the case, the water force is much larger than the intergranular soil force on the wall.

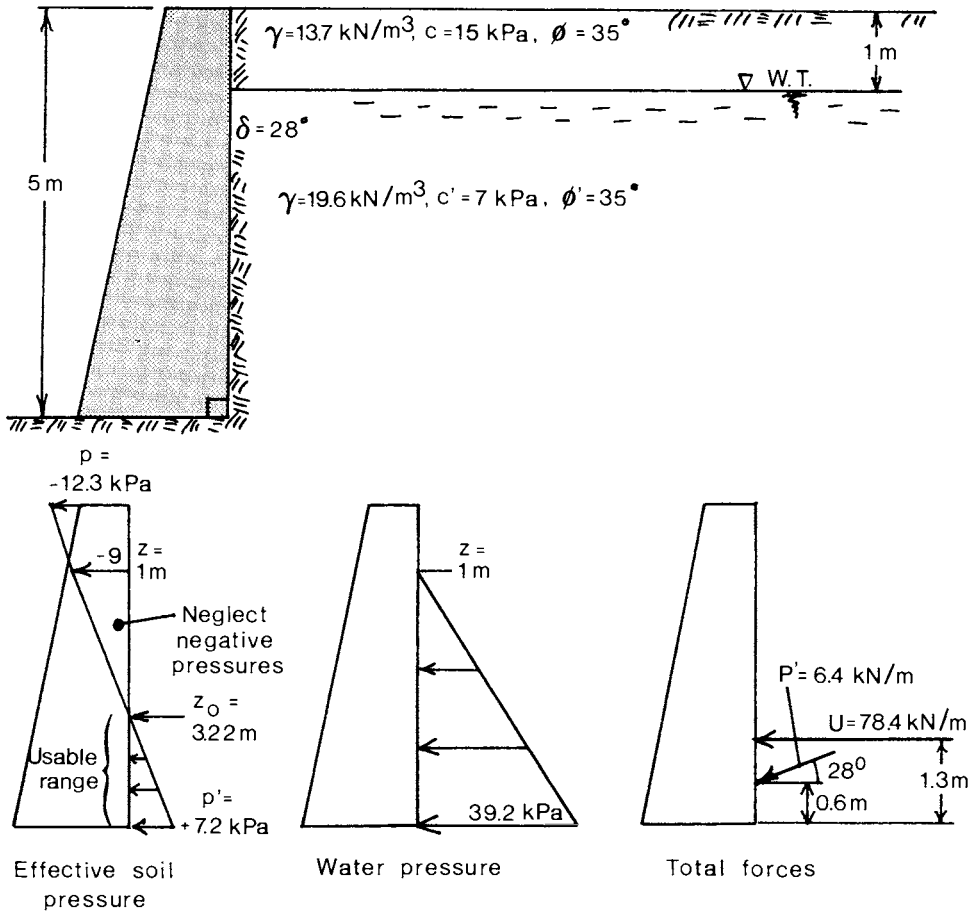

Fig. 6.7. (a) A level water table in soil behind a retaining wall. (b) The calculation of total wall pressures for the active failure case.

The general wedge theory described above may not be as exact as some more complex methods using Sokolovski's (1956) characteristic equations given in Chapter 2, although the error in the active soil failure case does not total more than a few percent of the wall forces. However, the wedge theory can be extended fairly easily to handle nonhomogeneous soils, layered backfills, water tables, point surface loads and other complications which more rigorous analytical techniques cannot. It may not be as easy to find the angle, β, of the approximate soil slip line directly as was accomplished by Eqn. 6.4 or 6.15, but a trial and error procedure can be used. Always using the philosophy that internal and soil to wall friction properties determine the shape of the soil failure surface, then only the terms involving soil weight, water pressures and surcharge loads should be maximized to find the likely straight failure line approximation, and terms involving cohesion and adhesion should be omitted from this procedure.

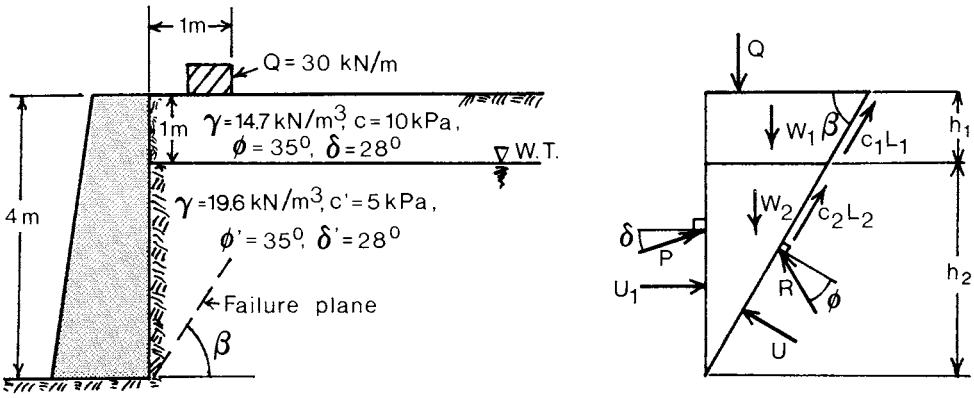

Fig. 6.8. A layered soil behind a retaining wall in Problem 6.1.

Problem 6.1. Fig. 6.8 shows an example of a vertical wall behind which there are two layers of soil having different densities and cohesions, separated by the water table surface. Find the effective soil particle to wall force P. (The water force U_1 must be added to this effective force to estimate the total force on the wall.) Soil to wall adhesion is assumed to be zero here.

All the forces acting on the soil failure wedge are added as shown in Fig. 6.8, and the following expression is obtained for the effective force, P. It can be separated into two components, P_a and P_c, of which the first will be used to determine the likely critical straight line failure plane angle in the soil.

$$P = \frac{W_1 + W_2 + Q - U(\cot\beta) - (c_1h_1 + c_2h_2)(1 + \cot\beta\cot[\beta-\phi])}{\sin\delta + \cos\delta\cot(\beta-\phi)}$$

$$= \left[\frac{30 + 110.25\cot\beta}{\sin\delta + \cos\delta\cot(\beta-\phi)} - \frac{25(1 + \cot\beta\cot[\beta-\phi])}{\sin\delta + \cos\delta\cot(\beta-\phi)}\right] kN/m = P_a - P_c$$

Table 6.1 shows the values of P_a which result from different trial values of the slip angle, β. This Table can be produced in only a few minutes using a programmable hand calculator to perform repeated evaluations of P_a. In this case, the failure line inclination of 67^0 gives the prediction of the largest wall force component P_a due to the soil weight, surcharge load and water pressure, and thus a net force $P = P_a - P_c$ of 18.49 kN/m. The critical failure angle is influenced somewhat by the surface load, Q. If the surcharge did not exist, a smaller failure line angle of 58^0 would result in the maximum P_a force. There are, of course, innumerable possible examples of retaining walls with slopes, sloped backfills, layered soils, irregularly distributed surface loads and the like. But in each case, by using common sense, a mechanical model equation for P, similar to that above, should be possible, with a subsequent trial and error solution for angle β which gives the maximum, and most likely wall force component due to effective soil and surcharge weights, including water pressure influences.

TABLE 6.1. Trial and error solutions for different failure plane inclinations, β, for the maximum wall force component P_a in the example of Fig. 6.8.

β^0	P_a, kN/m	$P=P_a-P_c$, kN/m
65	40.73	18.12
66	40.79	18.34
67	40.80	18.49
68	40.75	18.58

Problem 6.2. Fig. 6.9 shows an excavating machine situated near the edge of a braced sheet steel retaining wall. The machine has a weight of 88 kN/m of length parallel to the wall. Estimate the active wall force.

Fig. 6.9 illustrates that there are two possible failure mode cases in this instance. In Case a, the failure surface is too steep to allow both supporting tracks of the excavator to apply surcharge force to the soil failure wedge, and only one of the tracks, or half the weight of the machine, comes into play. Only the left hand track would descend with the soil in this pattern, and the machine would tilt. In Case b, the failure plane occurs at a sufficiently small slope ($\leq 45^0$) to permit all of the machine weight to act on

the soil wedge. For both cases, the formula for P is the same, as determined by equilibrium of the soil wedge, but the value of surcharge load, Q, is 44 or 88 kN/m, respectively.

$$P = \frac{(W + Q) - ch(1 + \cot\beta \cot[\beta - \phi])}{\sin\delta + \cos\delta \cot(\beta - \phi)} = P_a - P_c$$

where $W = \frac{1}{2}\gamma h^2 \cot\beta = 141.1 \cot\beta$ kN/m

In Case a, surcharge load Q is set at 44 kN/m. Maximization of the P_a term above results in a critical failure angle of 66^0, P_a of 64.4 kN/m and P = 49.0 kN/m. The failure angle is within the allowable limits of the force diagram of Case a.

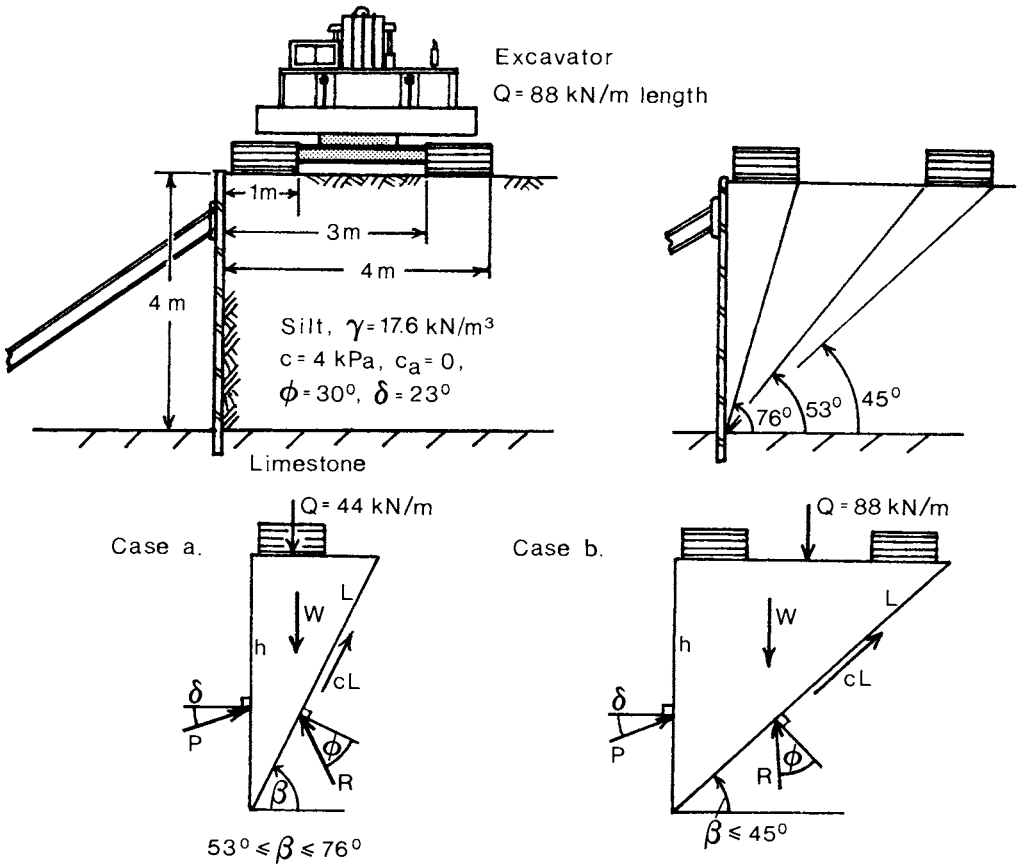

Fig. 6.9. Computation of wall forces with a surcharge in Problem 6.2.

In Case b, a maximization of P_a indicates that β should be 82^0. This failure angle, however, is not compatible with the condition that all of the excavator weight is located on the top of the soil failure wedge. Setting the failure angle at the maximum possible angle, 45^0, for physical reality yields a value for P_a of 59.9 kN/m, which is less than the result of Case a. It can be concluded for this particular example that Case a is the likely failure mode of the soil under the combined effects of soil and machine weights, and that P = 49 kN/m is the wall active force.

If the weight of the excavator were larger in comparison to that of the soil wedge, Case b might well have been the more critical failure mode giving a larger quantity of P_a acting on the wall. Each design example must be approached with common sense in this way.

6.1.4. Strip loading surcharge

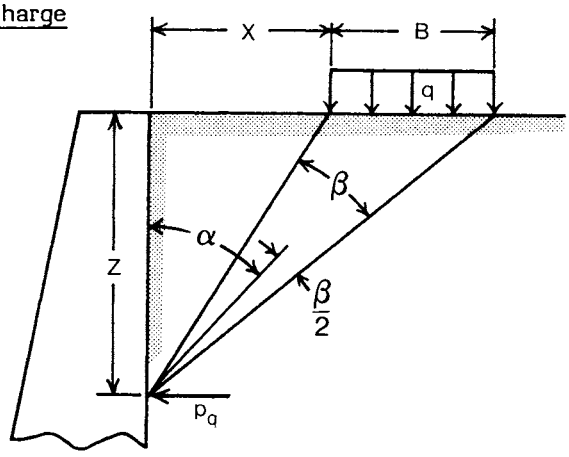

Fig. 6.10. Terzaghi's (1954) calculation of wall pressure from a surcharge.

For uniform strip loads on the soil surface behind a vertical retaining wall, it is possible to use the theory of elastic materials to predict the horizontal pressure resulting from this load. Terzaghi (1954) performed some experiments which demonstrated that the elastic theory does not work exactly for soil material, but that measured pressures on a rigid vertical wall were consistently twice those predicted by the theory of elasticity. He proposed that the following expression gives a reasonable estimate, using the parameters shown in Fig. 6.10, for the wall pressure p_q.

$$p_q = 2q(\beta - \sin\beta \cos 2\alpha)/\pi \qquad (6.18)$$

where angles α and β in Fig, 6.10 are measured in radians.

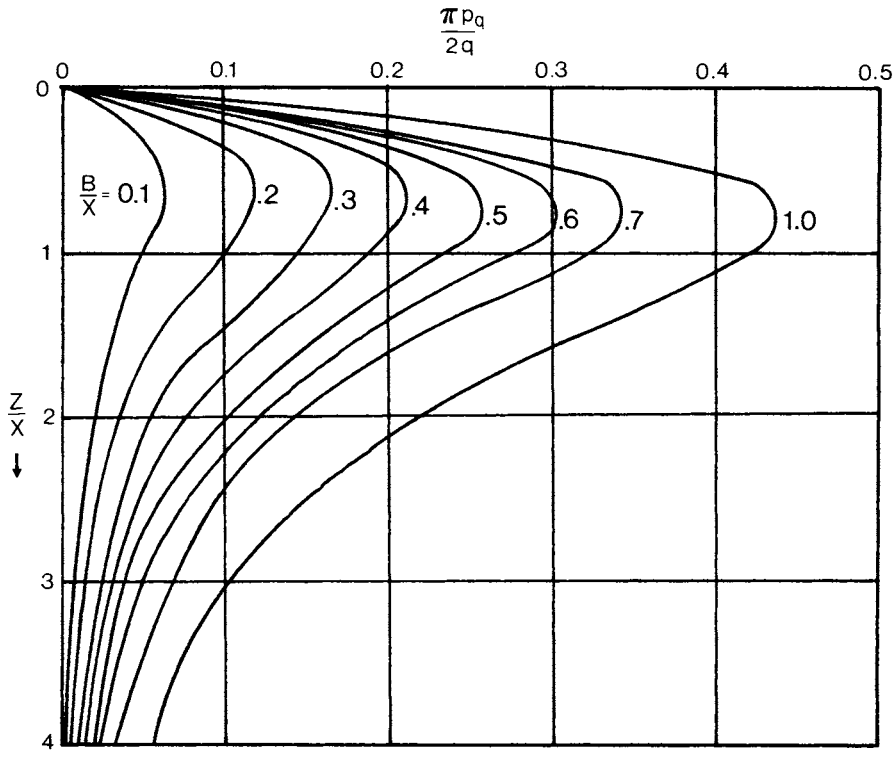

Fig. 6.11. Dimensionless wall pressure factors versus depth, resulting from a surcharge pressure as a function of surcharge width and distance.

In terms of the depth, z, the distance, x, from the wall to the edge of the strip load and the width, B, of the load, Fig. 6.11 gives nondimensional values of the wall pressure divided by the strip surcharge pressure, versus depth divided by x, for various values of strip load width divided by x. The curves in Fig. 6.11 reflect the actual shapes of pressure distributions which are expected on a vertical wall due to a strip load. Such a pressure distribution must be added to the active earthpressures in order to arrive at the total pressures to be supported by the wall.

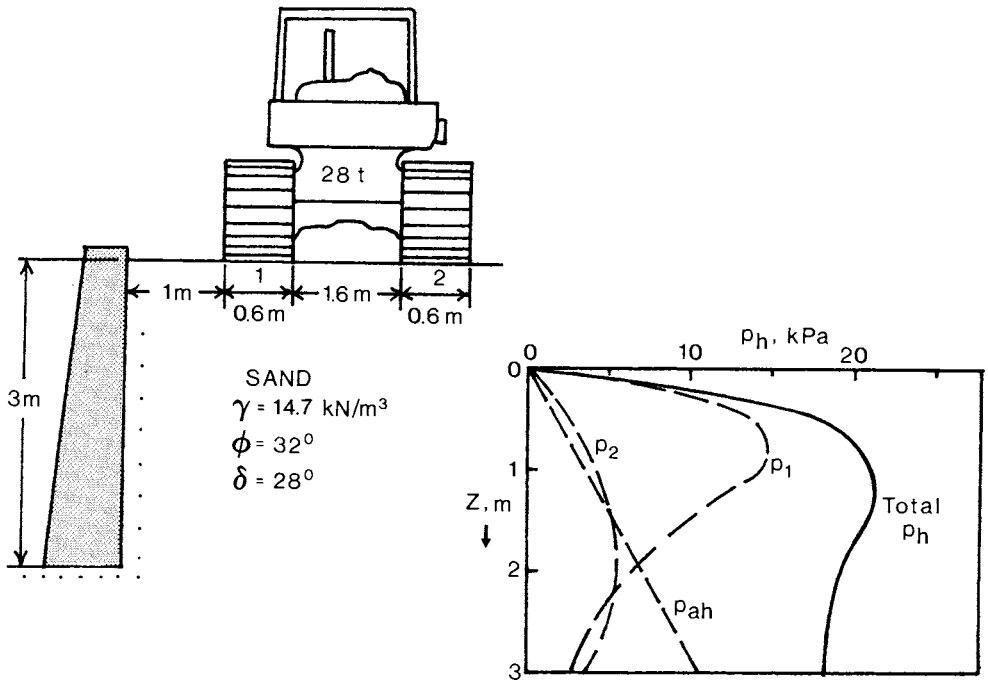

Fig. 6.12. Surcharge load for Problem 6.3 and the resulting pressure distribution on the retaining wall.

Problem 6.3. An example situation which can be approximated as a strip surcharge load beside a retaining wall is shown in Fig. 6.12. A 28 t tracked tractor with the dimensions noted rests on sand at a distance of 1 m from a retaining wall of 3 m height. The tractor tracks are 2.90 m long on the ground. What is the pressure distribution with depth on the wall?

Each track will be approximated as a strip load. The average surcharge pressure is the weight on each track divided by the track ground contact area as follows.

$$q = (28t \times 9.8kN/t)/(2 \times 0.6m \times 2.9m) = 78.9 \text{ kPa}$$

Labelling the left track as No. 1 and the right No. 2, the following are the respective widths, B, divided by the distances, X, from the wall.

$$B_1/X_1 = 0.60/1.00 = 0.60, \quad B_2/X_2 = 0.60/3.20 = 0.19$$

There is also pressure on the wall due to the active effect of the soil. The coefficient of active horizontal earthpressure is obtained from Appendix 3 as 0.243 for this soil and a vertical wall, and the pressure due to the soil is calculated as;

$$p_{ah} = \gamma K_{ah} z = 14.7 \times 0.243 z \text{ kN/m}^3 = 3.57 \text{ z kN/m}^3$$

The table below presents the calculations of the pressures arising from tracks 1 and 2, calculated from Eqn. 6.18 or Fig. 6.11, as well as that from the soil weight. The individual pressure distributions and the total are also shown graphically in Fig. 6.12.

z, m	z/x_1	$p_1/2q$	z/x_2	$p_2/2q$	p_1	p_2	p_{ah}	Total p_h, kPa
0.5	0.5	0.28	0.16	0.05	14.1	2.5	1.8	18.4
1.0	1.0	0.28	0.31	0.08	14.1	4.0	3.6	21.7
1.5	1.5	0.20	0.47	0.11	10.0	5.5	5.4	20.9
2.0	2.0	0.12	0.63	0.12	6.2	5.6	7.1	18.9
2.5	2.5	0.08	0.78	0.11	4.0	5.5	8.9	18.4
3.0	3.0	0.05	0.94	0.10	2.5	4.9	10.7	18.1

6.2. DESIGN OF RETAINING WALLS

Fig. 6.13 shows the forces acting on two types of self supporting retaining walls, (a) a gravity wall and (b) a cantilever wall. P and cL_1 are the effective soil forces acting on the wall, while U is the water force in the case of saturated soil backfills. W is the weight of the gravity wall, or that of the cantilever wall plus the soil entrapped in the zone BCD. The surface of this soil wedge, BC, is considered like a wall surface, but it has the shear strength properties internal to the soil (i.e. $\delta = \phi$ and $c_a = c$).

The safe design of such walls against active soil failure and wall displacement must take account of the two possible modes of wall movement, namely sliding and tipping. The sliding mechanism is simpler to analyze and will be considered first.

The horizontal components of forces P and U tend to move the wall horizontally, while force T, along the wall base, resists this motion. The maximum possible value of force T is the shear strength force at the soil to wall base interface, and depends upon the normal force N as well as the frictional and adhesive strength properties between the soil and wall material (usually concrete). For equilibrium to exist, the following equations must hold for forces in the horizontal and vertical directions.

$$T = P\sin(\alpha - \delta) + U\sin\alpha - c_a h\cot\alpha = H + U\sin\alpha - c_a h\cot\alpha \qquad (6.19)$$

$$N = P\cos(\alpha - \delta) + U\cos\alpha + c_a h + W = V + U\cos\alpha + c_a h + W \qquad (6.20)$$

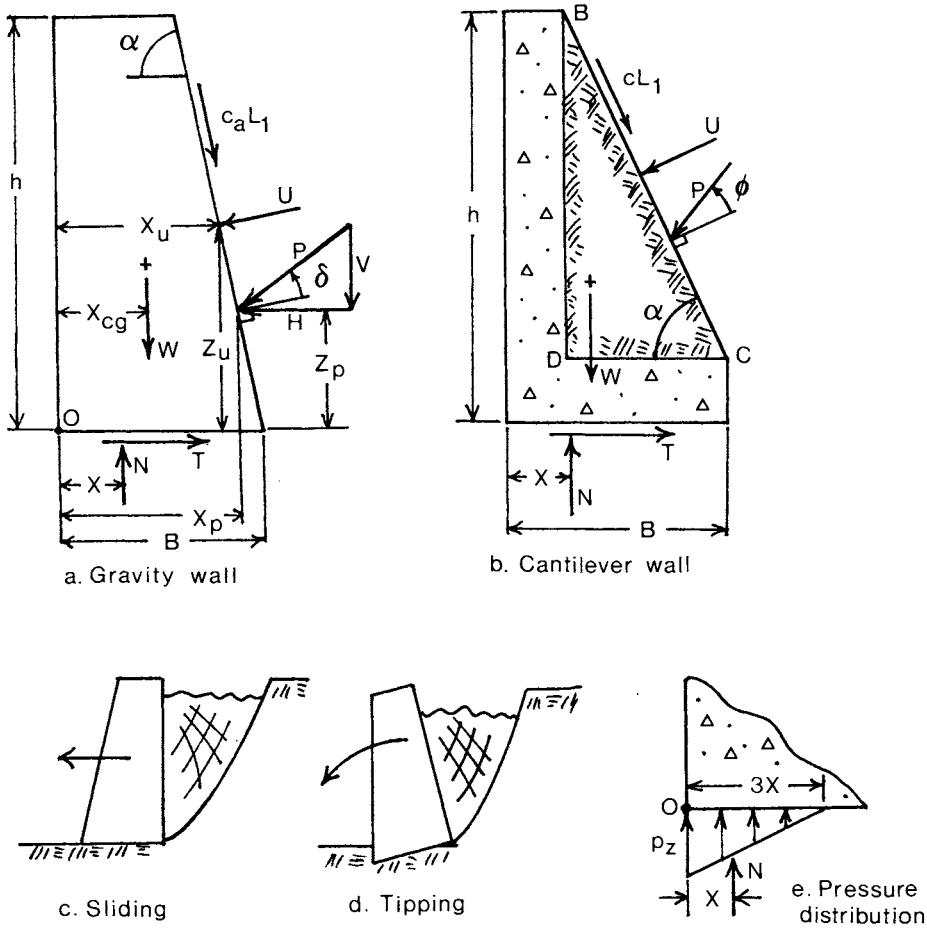

Fig. 6.13. Forces on (a) a gravity retaining wall and (b) a cantilever wall, plus for your added entertainment (c) the sliding wall failure condition, (d) wall tipping and (e) the pressure distribution under the walls.

The safety factor, S.F., of a particular wall design depends on the ultimate shear strength at the wall base, compared to the actual horizontal shear force required for equilibrium, and can be expressed as shown below. B is the width of the wall base in contact with the soil, and forces N and T are in units of force per unit wall length.

$$S.F. = (N\tan\delta + c_a B)/T \tag{6.21}$$

The expected forces N and T are governed by the geometry of the wall design, especially the wall inclination angle, α, as well as by the total mass of the wall. If a design is analyzed and found to have a small safety factor, less than or just larger than one, then the size of the wall must be increased in order to alter the force quantities in Eqn. 6.21.

The tipping scenario is more complex to analyze. The sum of the moments attempting to rotate the wall structure both clockwise and counterclockwise must be in equilibrium. In addition, the bearing capacity of the soil under the wall must be sufficient to sustain the vertical force N with a suitable safety factor. In Fig. 6.13, the vertical force N on the wall base is shown concentrated at a point positioned a distance X from the left hand wall edge. This distance X can be determined from the equilibrium of wall rotation by taking the moments of all forces about point O, as follows.

$$M_o = Hz_p - Vx_p + U\sin\alpha\, z_u - U\cos\alpha\, x_u - c_a hB - Wx_{cg} + NX = 0 \tag{6.22}$$

$$X = [Vx_p - Hz_p + U\cos\alpha\, x_u - U\sin\alpha\, z_u + c_a hB + Wx_{cg}]/N \tag{6.23}$$

Assuming a triangular distribution of the pressure, p_z, on the wall base, as shown in Fig. 6.13(e), the effective width of the bearing surface can be considered as 3X, and the average design bearing pressure as $q = N/3X$. Recalling Eqn. 3.3, the ultimate bearing capacity of this area of the wall base can be calculated, as illustrated below.

$$q_{ult} = \tfrac{1}{2}\gamma 3XN\gamma + cN_c \tag{6.24}$$

The safety factor of the wall in tipping can now be estimated as the ultimate bearing capacity of the base divided by the actual average bearing pressure as determined by the equilibrium of moments above.

$$S.F. = \frac{q_{ult}}{q} = \frac{\tfrac{1}{2}\gamma 3XN\gamma + cN_c}{N/(3X)} \tag{6.25}$$

Problem 6.4. Fig. 6.14 shows a concrete gravity wall having a height of 4 m, retaining dry compact sand with the properties noted. What is the safety factor of this wall in sliding and tipping?

The active earthpressure coefficient for this case can be found from Eqn. 6.12 or Appendix 3 to be K_a=0.366. Thus;

$$P_a = \gamma H^2 K_a/2 = 43.0 \text{ kN/m}$$

$$H = P\sin(\alpha - \delta) = 32.5 \text{ kN/m}$$
$$V = P\cos(\alpha - \delta) = 28.2 \text{ kN/m}$$

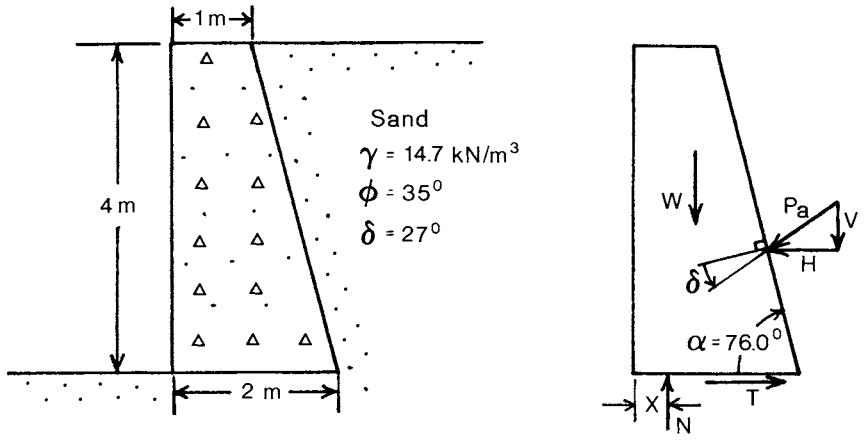

Fig. 6.14. Gravity retaining wall of Problem 6.4.

Taking the specific gravity of concrete as 2.4, the wall weight is;

$$W = 4m \times 1.5\ m \times 2.4 \times 9.8\ kN/m^3 = 141.1\ kN/m$$

$$N = W + V = 169.3\ kN/m$$

and the safety factor in sliding;

$$S.F. = \frac{N\tan\delta}{H} = \frac{169.3\ \tan 27^0\ kN/m}{32.5\ kN/m} = \underline{2.66}$$

For the safety factor in tipping, first the position of force N is determined using Eqn. 6.23, which simplifies in this example to;

$$X = (Vx_p - Hz_p + Wx_{cg})/N$$

$$= (28.2x1.67 - 32.5x1.33 + 141.1x0.78)kN/169.3\ kN/m = 0.673m$$

The frictional bearing capacity factor for this soil strength is found in Appendix 1 as $N_\gamma = 39$, and the ultimate bearing capacity over wall base width, 3X, is;

$$q_{ult} = \frac{1}{2}\gamma 3XN_\gamma = \frac{1}{2}14.7x3x0.673x39\ kPa = 579\ kPa$$

Thus the safety factor of bearing, with the moments in equilibrium, is;

$$S.F. = q_{ult}/q = 579\ kPa/(N/3X) = 579\ kPa/83.9\ kPa = \underline{6.9}$$

In this example, there appears to be no problem with the bearing capacity under the wall. Primarily, this is due to the relatively large internal friction angle of the soil, and high bearing capacity. If ϕ were reduced by just 5^{0}, the bearing safety factor would be diminished to about one third of the value obtained above.

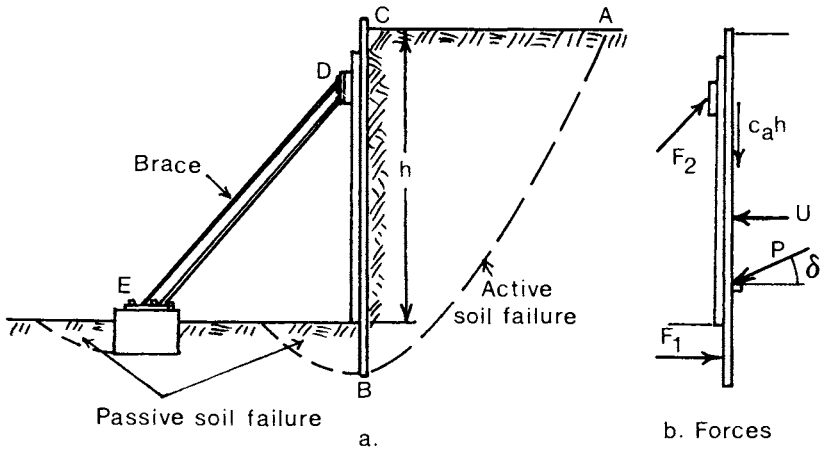

Fig. 6.15. Forces acting on a braced sheet metal retaining wall.

Another type of retaining wall does not depend on wall weight for stability, but uses braces for support as shown in Fig. 6.15(a). There are many different configurations of braced walls, and Fig. 6.15 depicts only one example. Nonetheless a similar analysis procedure is used in all cases, namely to find the active soil and water forces, P, U and $c_a h$, and then to design the supporting members, such as brace DE and the soil in front of the wall at B in Fig. 6.15. The forces F_1 and F_2 are found from the equilibrium of moments taken about a chosen point in Fig. 6.15(b), and the strength of the wall and bracing members verified accordingly. The strength of the soil in passive soil failure at B and E must be checked also, as is described in the next section. The safety factor for the design of wall and bracing member strength need not be as high as 3.0 because soil deformation is not involved in these elements. However, the safety factor should be about 3.0 for the passive soil resistance at points like B and E in the case shown, in order that soil movement at these locations be kept to a reasonable level.

6.3. PASSIVE SOIL RESISTANCE

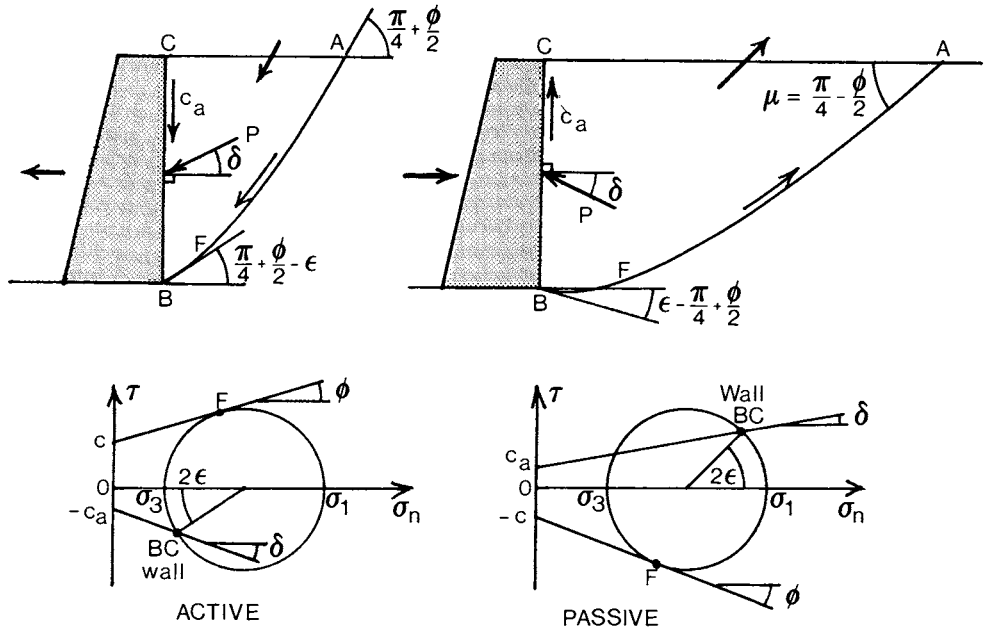

Fig. 6.16. The active and passive soil failure conditions behind a retaining wall, and the Mohr's circles of stresses at soil points beside the wall.

The definition of passive soil failure is the movement of soil partly in an upwards direction, opposite to gravity. Fig. 6.16 shows some of the differences between the active and passive soil failure cases. Some of these differences are:

- The shear stress on the internal soil rupture surface, F, is positive in active failure and negative (i.e. clockwise) in passive failure.
- The frictional and adhesive shear forces acting on the wall surface, BC, are downwards in the active case, and upwards in the passive.
- The inclination from the horizontal of the soil rupture plane at the surface, A, is $(\pi/4)+(\phi/2)$ and $(\pi/4)-(\phi/2)$ in the active and passive cases, respectively.
- The normal stress on the wall, BC, is on the minor half of Mohr's circle of stresses (nearer σ_3) while it is on the major side in the passive case. This means, of course, that the passive wall force is much greater than the active one, as will be demonstrated below.

In both cases shown in Fig. 6.16, the soil failure line is generally curved. This happens because of the roughness of the wall surface which rotates the wall normal and shear stress combination on Mohr's circle away from σ_3 in the active case, and σ_1 in the passive case, counterclockwise by an angle 2ϵ. Thus, in the case of a vertical wall, the soil failure plane is rotated clockwise by the angle ϵ from its inclination at the surface, (point A).

The smooth vertical wall case of Coulomb (1776) is not really more representative of real conditions in the passive failure case shown in Fig. 6.17 than it was in the active situation, Fig. 6.4. However, the model is simple and serves to illustrate the difference between active and passive failure conditions in a simple manner. Using the knowledge contained in Mohr's circle (which was not available to Coulomb in 1776), and assuming that the soil is in the failure condition along plane AB, the following expressions can be obtained for the relationship between vertical and horizontal stresses at the wall surface, BC, and for the passive wall force P.

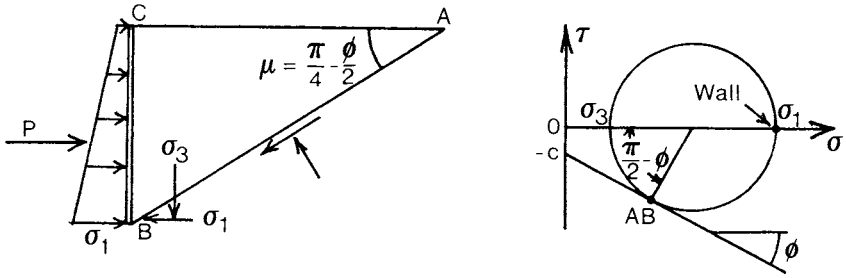

Fig. 6.17. The smooth wall passive soil failure case.

$$\sigma_1 = \sigma_3\left[\frac{1 + \sin\phi}{1 - \sin\phi}\right] + 2c\sqrt{\frac{1 + \sin\phi}{1 - \sin\phi}} = \sigma_3 K_p + 2c\sqrt{K_p} \qquad (6.26)$$

$$P = \frac{1}{2}\gamma h^2 K_p + 2ch\sqrt{K_p} \qquad (6.27)$$

Comparing Eqn. 6.27 with 6.6 for the active case, it can be seen that the passive earthpressure coefficient is the inverse of the active one. For an example soil angle of internal friction of 30^0, the active wall pressure is one third of the vertical stress at a point, while the passive wall stress is three times the vertical pressure, or nine times the active pressure for the same vertical stress.

For the general case of an inclined rough wall, the relatively straightforward passive stress analysis above cannot be used due to the curved soil failure line. Hettiaratchi (1969) and Hettiaratchi and Reece (1974) have demonstrated how the shapes of soil failure surfaces can be determined, and the wall stresses calculated using the characteristic equations described by

Sokolovski (1956) and shown previously in Section 2.4. They presented charts of passive earthpressure coefficients, for soil movement in two dimensions, which are substituted into the expression below. This formula which is very similar to that of the active case.

$$P = \frac{1}{2}\gamma h^2 K_p + chK_c + c_a hK_{ca} + qhK_q \tag{6.28}$$

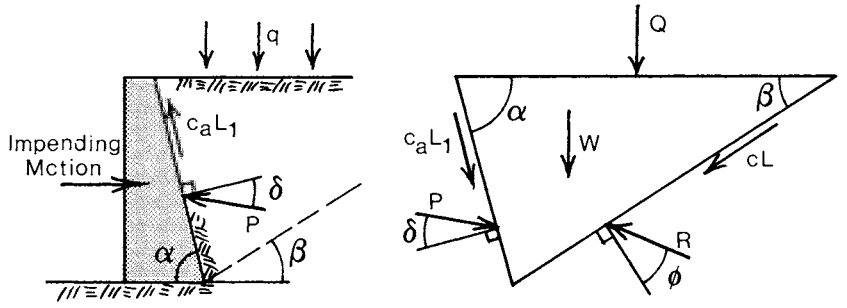

Fig. 6.18. The general passive soil failure wedge model.

Coulomb's (1776) notion that a straight line adequately represents the internal soil failure surface in the active case can be tested also for the passive case by means of the force model shown in Fig. 6.18. The angles of P and R, and the presence of cohesive and adhesive shear strength on surfaces AB and BC meet the requirement of passive soil failure. The equilibrium condition yields the following expressions for the passive earthpressure coefficients in Eqn. 6.28.

$$K_p = \frac{(\cot\alpha + \cot\beta)\,\sin(\beta+\phi)}{2\sin(\alpha+\beta+\delta+\phi)} \tag{6.29}$$

$$K_c = \frac{\cos\phi}{\sin\beta\,\sin(\alpha+\beta+\delta+\phi)} \tag{6.30}$$

$$K_{ca} = \frac{-\cos(\alpha+\beta+\phi)}{\sin\alpha\,\sin(\alpha+\beta+\delta+\phi)} \tag{6.31}$$

$$K_q = 2K_p \tag{6.32}$$

In order to determine the best approximation for the failure plane inclination, β, the K_p term is minimized (rather than maximized as in the active case) with respect to that angle, with the following result.

$$\cot\beta = \frac{\sqrt{\frac{\sin(\alpha+\delta)\,\sin(\delta+\phi)}{\sin\alpha\,\sin}} - \cos(\alpha+\delta+\phi)}{\sin(\alpha+\delta+\phi)} \qquad (6.33)$$

TABLE 6.2. Example values of passive soil wedge failure angle, β, and earthpressure coefficients, compared to more exact results from Hettiaratchi and Reece (1974):*

ϕ^0	δ^0	α^0	β^0	K_p	K_c	K_{ca}	$*K_p^1$	$*K_p^2$
30	20	90	18.1	3.05	7.47	2.00	2.70	2.90
		70	26.0	1.79	3.53	1.12	1.77	1.87
		50	32.5	1.45	2.19	0.68	1.40	1.45
		30	36.9	1.58	1.64	0.23	1.49	1.52
		10	28.4	3.20	1.82	-2.12	3.23	3.38
35	23.3	90	14.6	6.00	11.1	2.59	4.05	4.62
		70	22.7	2.40	4.38	1.34	2.39	2.62
		50	29.5	1.75	2.48	0.81	1.74	1.87
		30	33.4	1.78	1.75	0.35	1.71	1.77
		10	27.3	3.38	1.79	-1.76	3.53	3.58

[1]Extrapolated by the power law: $K_p = K_o(K_\phi/K_o)^{\delta/\phi}$ (6.34)

[2]Extrapolated by linear proportion: $K_p = K_o + (K_\phi - K_o)(\delta/\phi)$ (6.35)

where K_o and K_ϕ apply to the cases $\delta=0$ and $\delta=\phi$, respectively.

The angle β determined by Eqn. 6.33 for a particular wall geometry and set of soil strength parameters is substituted into the expressions for earthpressure coefficients in Eqn. 6.29 to 6.32. Table 6.2 gives some examples of the coefficients calculated by the above method for a range of wall inclination angles, and compares them to the more exact results of Hettiaratchi and Reece (1974). Surprisingly enough, the values are quite close together in most cases.

As in the active case, the wedge method allows one to include many complications such as layered soils, water tables, irregular shapes of wall and soil surface, surface loads and even curved wall or soil cutting tool shapes, by using appropriate average and approximate quantities.

Problem 6.5. In Fig. 6.19 an example is shown of a sand layer above a clay soil behind an inclined wall. The force diagram for a soil wedge is shown also for the passive failure case, using the average angle of internal friction, $\bar{\phi}$, of the two layers and the average angle of soil to wall friction, $\bar{\delta}$. The

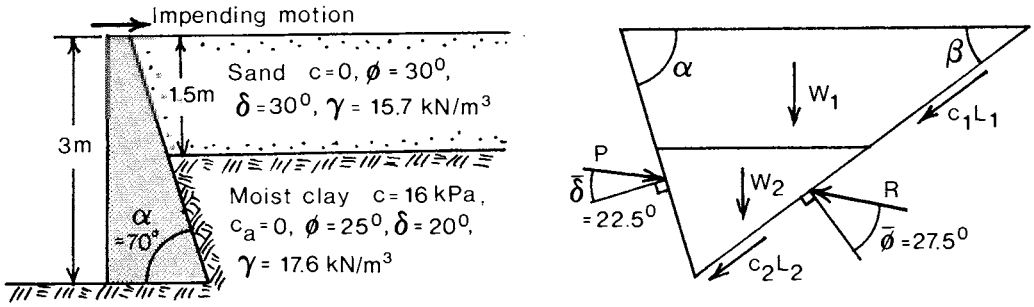

Fig. 6.19. Layered soil in passive failure (Problem 6.5).

densities and cohesive strengths of the layers can be included separately in their respective volumes or lengths of action, to give weights W_1 and W_2, as well as cohesive resistance forces c_1L_1 and c_2L_2. Equilibrium gives the following expression for passive wall force, P.

$$P = \frac{(W_1 + W_2) + (c_1L_1 + c_2L_2)(\sin\beta + \cos\beta \cot[\beta + \phi])}{\cos(\alpha + \delta) + \sin(\alpha + \delta)\cot(\beta + \phi)} = P_p + P_c$$

$$= \frac{72.77(\cot\alpha + \cot\beta) + 24(1 + \cot\beta \cot[\beta + \phi])}{\cos(\alpha + \delta) + \sin(\alpha + \delta)\cot(\beta + \phi)} \text{ kN/m}$$

Two parts, P_p and P_c, of wall force P are apparent, arising from the mass and frictional strength of the soil, and the cohesion, respectively. Following Coulomb's (1776) principle, and that of Hettiaratchi and Reece (1974), only the soil and wall frictional strengths govern the shape of the soil failure surface. Therefore, in order to estimate the failure angle, β, just P_p should be minimized with respect to variations in that angle. Table 6.3 indicates the variations in both P_p and total force P with β. The minimum value of P_p occurs at a different failure angle (25^0) than does P (27^0), because of the influence of soil cohesion in the latter case. It can be concluded in this example that the likely passive wall force is 340.3 kN/m, acting at the angle shown in Fig. 6.19.

TABLE 6.3. Trial and error solution for wall force P_p as a function of soil failure plane inclination, β.

β^0	P_p, kN/m	$P = P_p + P_c$, kN/m
24	252.9	341.9
25	252.5	340.3
26	252.6	339.4
27	253.1	339.2
28	254.0	339.6

6.4. PRESSURES ON BIN AND SILO WALLS

Bins and silos are used universally to store agricultural products such as grains, silages, vegetables and fruits. Most of these materials can be treated as continuous media with mechanical properties very similar to those of soils, including internal angle of friction strength, angle of friction strength between material and walls and even pore pressures for substances which are nearly saturated with water or juices. Table 6.4 gives guideline examples of these properties for several agricultural materials.

TABLE 6.4. Average mechanical properties of some agricultural materials (A.S.A.E., 1985, Mohsenin, 1970).

Material	γ, kN/m^3	ϕ^0	δ^0		
			Metal[2]	Wood[3]	Concrete[4]
Silage, 10% m.c.[1]	2.9	20	20	20	20
50% m.c.	3.9	33	33	31	33
Corn, 10% m.c.	6.9	--	14	17	22
14% m.c.	7.8	--	19	19	33
Oats, 10% m.c.	4.9	--	12	14	22
16% m.c.	4.9	--	22	19	25
Rice, 14% m.c.	5.9	--	23	27	27
Soybeans, 7% m.c.	12.7	--	12	17	21
12% m.c.	13.7	--	12	24	29
Wheat, 10-15% m.c.	7.8	27	11	22	27
16-20% m.c.	6.9	27	22	27	27

[1]m.c. = moisture content on a percent wet basis.
[2]Galvanized sheet steel.
[3]Douglas fir or oak, averaged.
[4]Steel trowel finish.

A review of the theories available for calculating lateral pressures on the walls of bins or silos was provided by Singh and Moysey (1985). One of the early theories was given by Janssen (1895), and it is still used widely for the case of filling a bin owing to its relative simplicity. The assumption for his model was that a horizontal thin slice at each depth in a bin or silo has a uniform vertical pressure acting on it, and the following formula resulted for the pressure perpendicular to the wall.

$$P_h = \frac{\gamma R}{\tan\delta}\left[1 - e^{-K h \tan\delta / R}\right] \tag{6.36}$$

where P_h = lateral bin wall pressure,
γ = material bulk density,
K = ratio of lateral to vertical pressure,
h = depth from the top surface of the material.

R is the hydraulic radius of the bin or silo, defined as the cross sectional area of the structure divided by the perimeter length. For different cross sectional shapes of bins or silos, R can be found as follows.

$$R = \pi r^2/(2\pi r) = r/2 \quad \text{for a circle of radius r,} \tag{6.37}$$

$$R = B^2/(4B) = B/4 \quad \text{for a square of side B,} \tag{6.38}$$

$$R = BL/(2B+2L) \quad \text{for a rectangle of sides B and L.} \tag{6.39}$$

One of the difficult constants to determine for use in Eqn. 6.36 is the ratio, K, of lateral to vertical pressures. It was suggested by Ketchum (1919) that K_a be used (Eqn. 6.7) as in an active failure case. This assumption, however, is based on a smooth wall model, which is not the case in a real bin or silo. Jaky (1948) suggested that $K = 1 - \sin\phi$ could be used. This term has sometimes been called K_0 in soil mechanics, the coefficient of earthpressure at rest, and is larger than K_a. Everts et al. (1977) and Moysey (1979) proposed a form of K which depends upon both the angles of internal and interface friction of the material in a bin, such as Eqn. 6.12 for walls. This relation is shown below for the active material failure case.

$$K = \frac{1 - \sin\phi\cos 2\epsilon}{1 + \sin\phi\cos 2\epsilon} \tag{640}$$

where $2\epsilon = \sin^{-1}(\sin\delta/\sin\phi) - \delta$

For a material such as wheat, which often has an internal friction angle of near 27^0 and an angle of material to steel wall friction of 17^0, Ketchum's value of K would be 0.376, while Jaky's would be computed as 0.546 and Everts et al. or Moysey's is 0.411. Some experimantal investigations have been

made also on lateral pressures in bins involving different materials. Ketchum (1919), for example, reported K to be measured as 0.6 for wheat, while Caughy et al. (1951) also found K = 0.6 for wheat and corn. Pieper (1969) found K = 0.5 when filling a plywood bin with barley, and Mohsenin (1970) suggested that K be 0.42 for barley, 0.4 to 0.5 for grain corn, 0.23 to 0.38 for rice and 0.33 to 0.44 in the case of wheat.

Another mechanical model was developed by Lvin (1970) for cylindrical bins. It employed concentric rings of stored material as mechanical elements, rather than Janssen's slices. This model predicts that wall pressure will increase to a certain depth below the material surface, and then remain constant at greater depths, as follows.

$$P_h = \gamma K h(1 - K h \tan\delta/D) \qquad \text{for } h/D < 1/(2K\tan\delta) \tag{6.41}$$

$$P_h = \gamma D/(4\tan\delta) \qquad \text{for } h/D \geq 1/(2K\tan\delta) \tag{6.42}$$

Experimental results reported by Turitzin (1963), Pieper (1969) and Moysey (1983) have shown that Lvin's model generally predicts higher lateral pressures than that of Janssen, and usually comes very close to estimating actual experimental wall pressures in cylindrical wood and concrete bins (Singh and Moysey, 1985).

Problem 6.6. Given a 4 m inside diameter grain bin of height 20 m filled with wheat having an average bulk density of 7.8 kN/m^3, angle of internal friction 27^0 and angle of wall friction 17^0, find the distribution of wall pressure with depth according to the theories of (a) Janssen (1895) and (b) Lvin (1970).

As mentioned previously, the ratio of lateral to vertical pressure, K, for these friction angles calculated by Eqn. 6.40 is 0.411. The depth at which lateral pressure ceases to increase in Lvin's model is;

$$h = D/(2K\tan\delta) = 4\ \text{m}/(2\text{x}0.411\tan 17^0) = 15.9\ \text{m}$$

The formulae of (a) Janssen and (b) Lvin can then be evaluated as;

$$\text{(a) } P_h = \frac{7.8\text{x}1\ \text{kPa}}{\tan 17^0}\left[1 - e^{-\tan 17^0 \text{x} 0.411 h/1\text{m}}\right] = 25.5\left[1 - e^{-h/8\text{m}}\right]\ \text{kPa}$$

$$\text{(b) } P_h = 3.22h/(1 - h/31.83\text{m})\quad \text{kN/m}$$

and the values of lateral pressure predicted by the two methods at various depths are shown in Table 6.5 below as well as in Fig. 6.20.

Lvin's predicted lateral silo pressures are consistently higher than those of Janssen, as is usually the case, by 59 to 330% in this example.

TABLE 6.5. Values of lateral pressures on a silo wall from Problem 6.6.

h, m	P_h,kPa (Janssen)	P_h, kPa (Lvin)
5	11.9	19.1
10	18.2	47.0
15	21.6	91.3
20	23.4	102.3

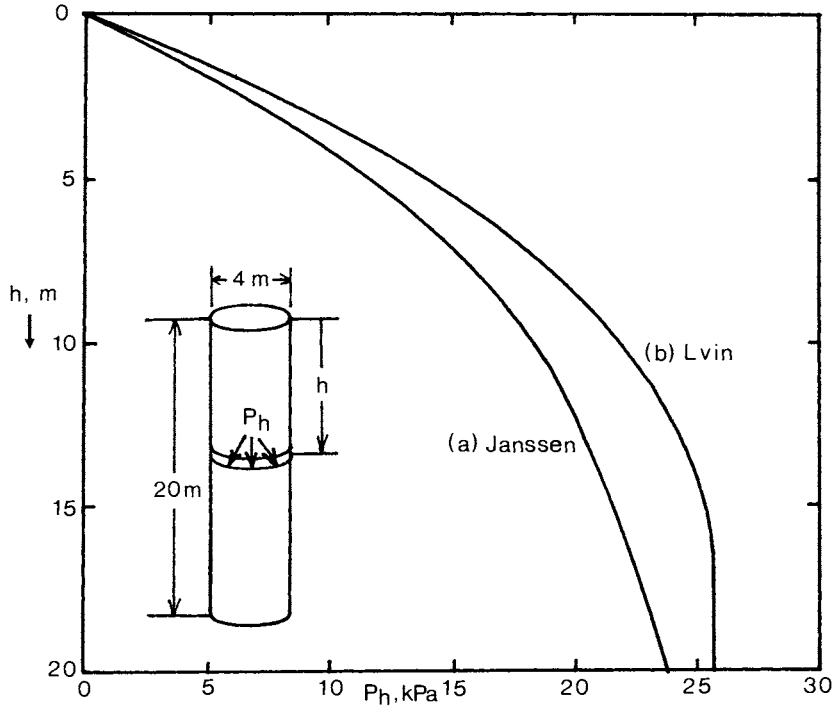

Fig. 6.20. Curves of normal wall pressure versus depth in the tower silo of Problem 6.6 by the theories of (a) Janssen and (b) Lvin.

6.5. PRESSURES ON BURIED PIPES AND CONDUITS

The theory of vertical pressure which must be withstood by buried pipes, culverts, conduits and the like has been developed by Marston and Anderson (1913) and is well explained by Spangler and Handy (1982). As Fig. 6.21 shows,

the theory begins with the assumption that a trench of width B has been excavated and then refilled for the installation of the pipe or conduit. The weight of soil in this trench, and a possible surcharge load Q, force per unit length of trench, are being counteracted by friction at the trench sides. The theory assumes that the normal pressure on the trench sides is the vertical pressure in the trench soil times the coefficient of active earthpressure, called K in this instance, where;

$$K = \frac{1 - \sin\phi}{1 + \sin\phi} \qquad (643)$$

and ϕ is the angle of internal friction of soil filled in the trench.

Thus the horizontal forces per unit length on the sides of an elemental slice of height dh in the trench soil are the average side pressure, KV/B,

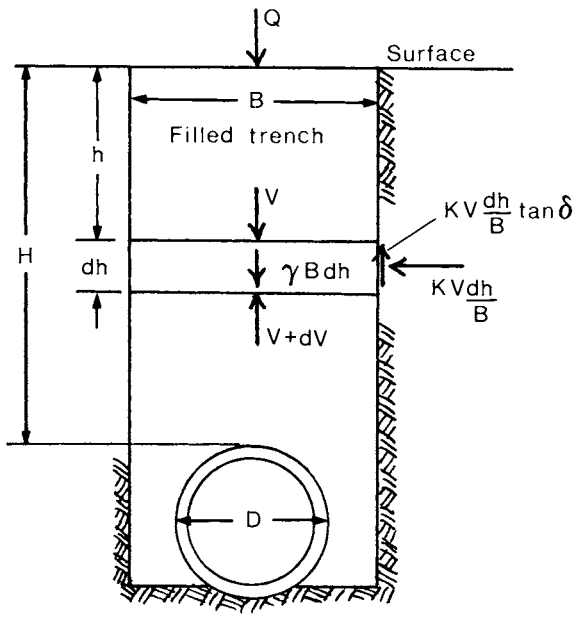

Fig. 6.21. Theoretical model for buried pipes (Spangler and Handy, 1982).

times the slice height, dh. And the shear forces on the slice sides are the horizontal forces times the coefficient of friction, tanδ, between the materials inside and outisde the trench. The weight of soil in the slice dh is γBdh, per unit length of trench. Thus the sum of vertical forces acting on a slice is equated to zero for equilibrium as follows.

$$V + dV + 2KV(\tan\delta)dh/B - V - \gamma Bdh = 0 \qquad (6.44)$$

$$dV + 2KV(\tan\delta)dh/B - \gamma Bdh = 0 \qquad (6.45)$$

This differential equation has a solution of the form;

$$V = A_1 + A_2 e^{Ch} \qquad (6.46)$$

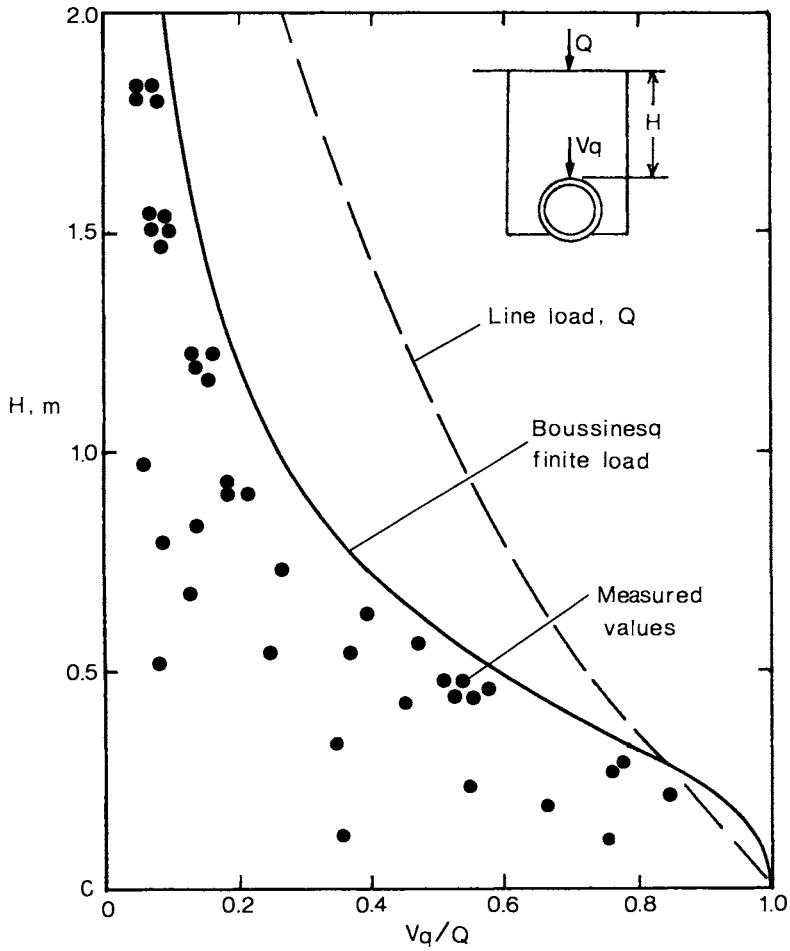

Fig. 6.22. Theoretical and experimental pipe loads transmitted from static surface wheel loads (Spangler and Handy, 1982).

Substituting this form into Eqn. 6.45, and evaluating vertical force V as Q, force per unit length at the surface where h = 0 gives the general result below.

$$V = \frac{\gamma B^2}{2K\tan\delta}\left[1 - e^{-2K(\tan\delta)h/B}\right] + Qe^{-2K(\tan\delta)h/B} \qquad (647)$$

Marston and Anderson (1913) found that Eqn. 6.47 works quite reliably to predict vertical loads on pipes of diameters 457 and 914 mm buried in trenches of widths 683 and 1266 mm, respectively, at depths of about 5 m without a surcharge load, Q.

When a surcharge load is of finite length, such as a vehicle wheel, Spangler (1973) suggested that a Boussinesq type of pressure distribution can be used to design conservatively for the load carried by a certain length of pipe or conduit, and he recommended that a length of 1 m be considered. Fig. 6.22 shows his theoretical calculation, which is consistently equal to or higher than experimental measurements of pipe loads from static wheels on the soil surface. Also in Fig. 6.22 is drawn the predicted curve from the second term of Eqn. 6.47 above which involves a line load, Q, using typical soil strength quantities. That part, V_Q, of the vertical load due to a line load is larger than the Boussinesq rectangular load on a pipe, because the latter spreads out in two dimensions in the soil (ref. Fig. 4.7). Thus the Boussinesq curve appears to be the logical design tool for this situation.

6.6. PROBLEMS

6.7. A concrete wall (γ = 23.5 kN/m^3) supports dry sand as shown in Fig. 6.23. (a) What should be the width, B, of the top of the wall in order that it should have a safety factor of 3.0 in sliding? (b) What then is the safety factor in bearing at the bottom left hand edge of the wall?

Answer: (a) B = 2.36 m, (b) S.F. = 5.0.

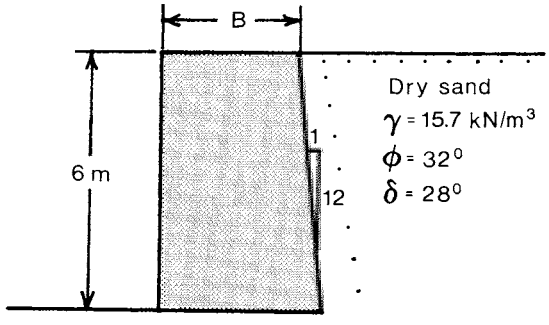

Fig. 6.23. Gravity retaining wall in Problem 6.7.

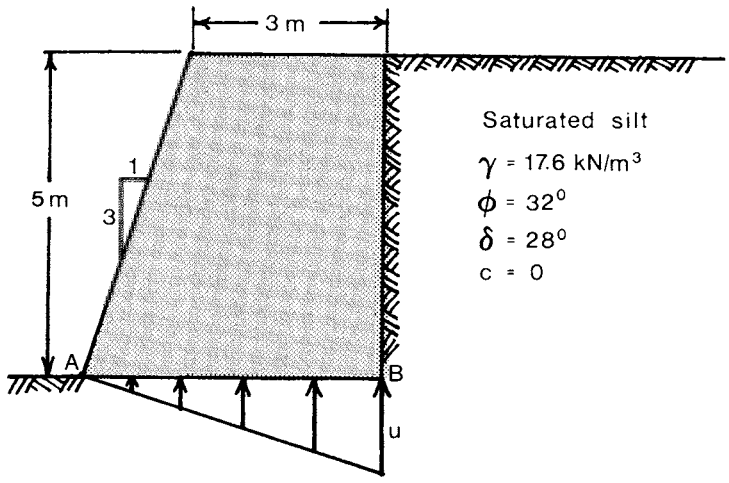

Fig. 6.24. Wall retaining saturated soil, Problem 6.8.

6.8. In Fig. 6.24, a concrete gravity wall is illustrated supporting saturated silt. If it is assumed that the water pressure, u, on the bottom wall has a linear decrease between the maximum value at point B and zero at corner A, find the safety factor of this wall in sliding. Is this safety factor adequate?

Answer: S.F. = 1.27. Not adequate.

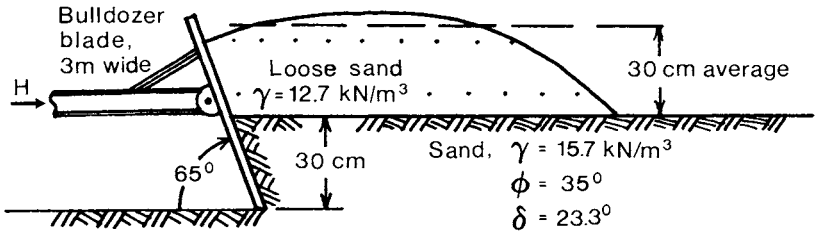

Fig. 6.25. Passive soil failure by a wide blade, Problem 6.9.

6.9. Fig. 6.25 shows a 3 m wide bulldozer blade cutting 30 cm deep in a compact sand. There is a surcharge of loose sand on the surface which has an average depth of 30 cm. Using a two dimensional passive soil failure analysis, estimate (a) the horizontal component, H, of the force needed to push the blade in the configuration shown, and (b) the percentage of the total horizontal force which arises because of the surcharge load. (Assume that the surcharge is semi-infinite in extent).

Answer: (a) H = 14.5 kN, (b) Surcharge component = 36%.

6.10. A steel silo has an inside diameter of 7.3 m and height 24 m. It is filled with corn silage having a moisture content of 50%, average density 4.9 kN/m^3 and internal and wall friction angles of 33^0. Using the formulae of Lvin (1970), estimate the maximum lateral pressure level expected on the inside of the silo, and at what depth it occurs?

Answer: P_h = 13.8 kPa, between 10.4 m depth and the bottom.

6.11. In Problem 6.10 above, if the vertical shear stress on the silo wall is always P tanδ at every point, what proportion of the total silage weight is carried by wall friction?

Answer: About 80% of the silage weight.

6.12. In Fig. 6.26, find F.

Answer: F = 479 kN.

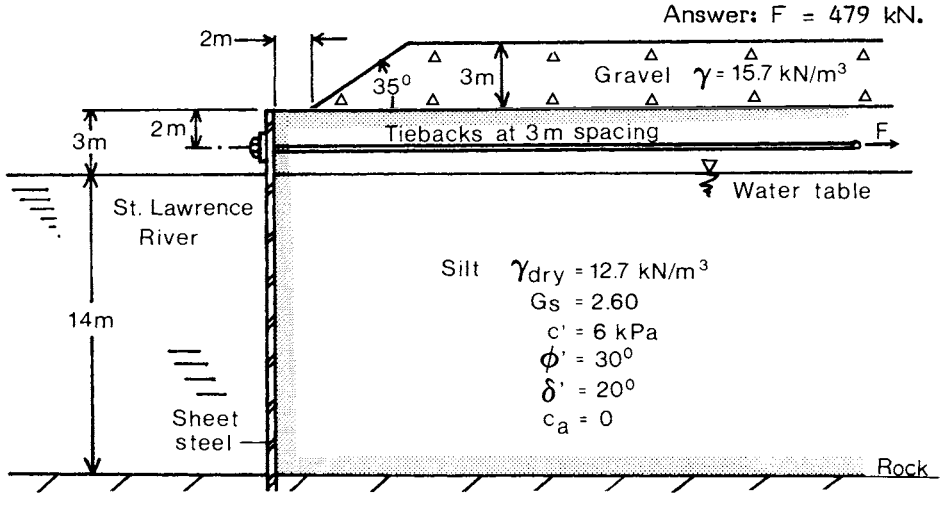

Fig. 6.26. Sheet steel wall for Problem 6.12.

6.13. Fig. 6.27 depicts a vertical retaining wall holding a soil of low cohesion, and a strip load having 60 kPa average pressure on the soil surface. Find the maximum horizontal pressure on the wall and the depth at which it acts.

Answer: Maximum p_h = 19.8 kPa at the wall bottom.

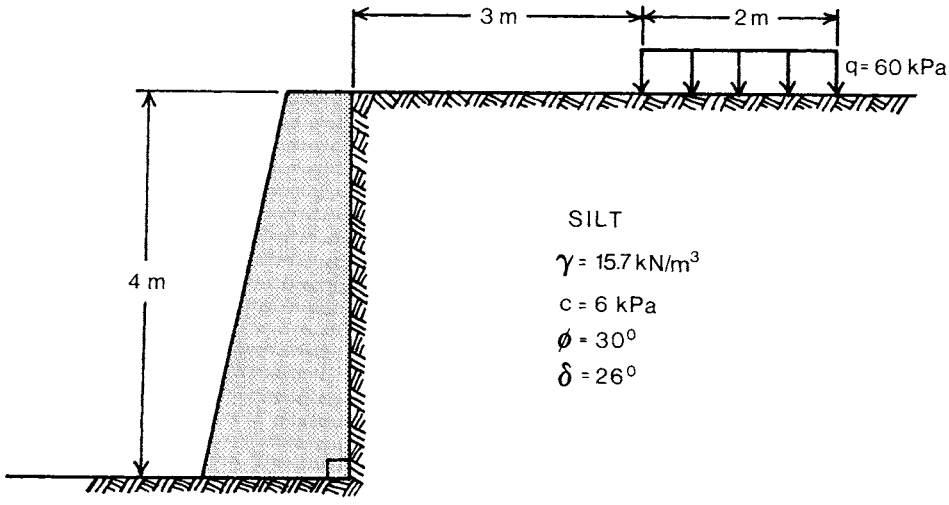

Fig. 6.27. Gravity wall with surcharge load, Problem 6.27.

Chapter 7. Soil erosion and protection

Erosion is regarded as the detachment, movement and deposition of soil particles due to environmental factors. It is considered one of the more serious forms of soil degradation in all regions of the world. The principal agents responsible for soil erosion are wind and water.

7.1. WATER EROSION

Water erosion of soil occurs because of the progressive concentration of surface water runoff. The kinetic energy of falling raindrops causes the detachment of soil particles which are subsequently transported by water moving on the surface. As the velocity of overland flow, the slope of a field and the travel length increase, water flow concentrates into small rivulets which carry soil mass. This phenomenon is known as rill erosion. The combined action of soil detachment by raindrops and the soil movement in thin layers is denoted as interrill erosion, while the deterioration and collapse of stream banks due to streamflow is called streambank erosion.

The movement of soil particles from a field leads not only to a breakup of the soil structure and a loss of topsoil resources, but it also contributes to downstream pollution of watercourses and revenue losses in the form of agricultural chemicals, including fertlizers, pesticides and the like.

7.2. THE UNIVERSAL SOIL LOSS EQUATION (USLE)

The universal soil loss equation as developed by Wischmeier (1976) is designed to be used to estimate the quantity of soil eroded from land by rainfall runoff. It is used primarily for planning purposes as a first estimate of soil losses on a particular field. Then, based on what is judged as an allowable annual soil loss rate, different cropping systems or conservation practices could be recommended. The equation and its components are;

$$A = 2.24\ \text{(t/ha)/(ton/ac)}\ RKLSCP \qquad (7.1)$$

where A = the average annual soil loss in t/(ha year),
R = the rainfall and runoff erosivity index (Fig. 7.1)
K = soil erodibility factor, tons/(acre year) (Table 7.1)
L = length factor of the field (Eqn. 7.2)
S = the slope factor (Eqn. 7.3)
C = crop management factor (Table 7.2)
P = conservation practice factor (Table 7.3).

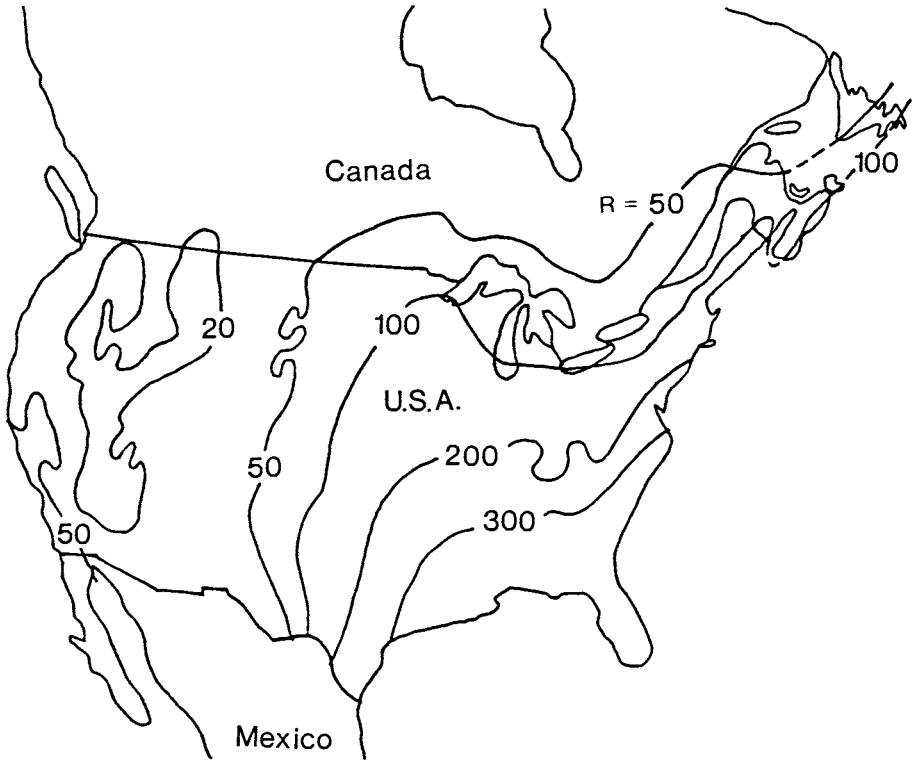

Fig. 7.1. The rainfall and runoff erosivity indices for North America (data from USDA-EPA, 1975, and Wall et al., 1983).

The length and slope factors in the universal soil loss equation are determined from Eqn. 7.2 and 7.3 below.

$$L = (l/22m)^x \tag{7.2}$$

where l = the length of a slope, m,
x = an exponent = 0.5 for slopes less than 4%, = 0.4 for a 4% slope, = 0.3 for slopes less than 4%.

$$S = (0.43 + 0.30s + 0.043s^2)/6.574 \tag{7.3}$$

where s = the field slope expressed in percent.

TABLE 7.1. Soil erodibility factors, K, by soil texture in tons/(acre year) for use in Eqn. 7.1 (USDA-EPA 1975).

Soil textural class	Soil organic matter content %		
	0.5	2	4
Fine sand	0.16	0.14	0.10
Very fine sand	0.42	0.36	0.28
Loamy sand	0.12	0.10	0.08
Loamy very fine sand	0.44	0.38	0.30
Sandy loam	0.27	0.24	0.19
Very fine sandy loam	0.47	0.41	0.33
Silt loam	0.48	0.42	0.33
Clay loam	0.28	0.25	0.21
Silty clay loam	0.37	0.32	0.26
Silty clay	0.25	0.23	0.19

TABLE 7.2. Crop management factors, C, for the universal soil loss equation (Smith and Weischmeier, 1962).

Crop practice	Crop stage period				
	0	1	2	3	4
First year corn after grass	0.15	0.30	0.27	0.15	0.22
Second year corn with residues	0.32	0.51	0.41	0.22	0.26
Second year corn without residues	0.60	0.65	0.51	0.24	0.65
Third or later year corn with residues	0.36	0.63	0.50	0.26	0.30
Small grains after two years corn	-	0.30	0.18	0.03	0.02
Small grains on disked corn stubble	-	0.80	0.50	0.07	0.03
Established grass and legume meadow	-	-	.004	-	-

0 - moldboard plowing to seedbed preparation; 1 - first month after seeding; 2 - second month; 3 - between second month and harvest; 4 - stubble or residue after harvest before plowing.

TABLE 7.3. Soil conservation practice factors, P, (Wischmeier and Smith, 1965).

Percent slope	Contouring (l_{max},m)	Strip cropping	Terracing and contouring
Up and down	1.0	-	-
Parallel (12%)	0.8	-	-
1.1 - 2	0.6 (150)	0.30	-
2.1 - 7	0.5 (100)	0.25	0.10
7.1 - 12	0.6 (60)	0.30	0.12
12.1 - 18	0.8 (20)	0.40	0.16
18.1 - 24	0.9 (18)	0.45	-

Problem 7.1: An example of the use of the universal soil loss equation for the prediction of an approximate rate of soil erosion is as follows. Consider a silage corn field near Detroit, Michigan or Windsor, Ontario, on a sandy loam field having a slope of 2% and a slope length of 100 m. The cultivation practice has been plowing up and down the slope of the field. The relevant parameters in this case are;

R = 100 (Fig. 7.1)
K = 0.24 tons/(acre year) (Table 7.1)

$L = (100/22)^{0.3} = 1.57$ (Eqn. 7.2)

S = (0.43 + 0.3x2 + 0.043x4)/6.574 = 0.18 (Eqn. 7.3)
C = 0.51 averaged over the year without residue (Table 7.2)
P = 1.0 (Table 7.3)

The estimated annual soil loss due to water erosion would then be

A = 2.24 x 100 x 0.24 x 1.57 x 0.18 x 0.51 x 1.0 = 7.75 t/(ha y)

Problem 7.2: The universal soil loss equation can be used to assess the suitability of different cropping and conservation systems to reduce soil losses, and to permit a certain loss tolerance, (allowable rate). Assume, for example, a soil loss tolerance of 1.5 t/(ha y) for the same region. The values of R, K, L and S would remain constant, but the following new practices could be introduced in the prediction.

Winter wheat planted after two years of corn (C = 0.13), and crops are planted along field contour lines (P = 0.6).

The estimated annual soil losses would then be changed to;

$$A = 2.24 \times 100 \times 0.24 \times 1.57 \times 0.18 \times 0.13 \times 0.6 = \underline{1.19 \text{ t/(ha y)}}$$

Theoretically, the above practices meet the recommended soil loss tolerance of 1.5 t/(ha y), and a considerable saving of topsoil, approximately 6.56 t/(ha y), could be realized by the introduction of these cropping and conservation practices. Examples of soil loss tolerances have been given by the American Society of Agronomy (1982).

7.3. MODIFIED UNIVERSAL SOIL LOSS EQUATION

A disadvantage of the standard Eqn. 7.1 is that it does not take into account the runoff volume during an individual storm. The R factor is based on long term rainfall characteristics, and does not reflect rainfall intensity accurately during specific storms. Williams and Berndt (1977) modified Eqn. 7.1 by replacing the R factor with a runoff factor. The application of Eqn. 7.1 on a watershed basis requires information on delivery ratios. Topographic variations within a watershed area result in soil losses from some areas, and soil deposition in others. The R factor represents the energy used only in the detachment of soil particles, whereas the runoff factor in the modified equation takes account of the energies used in both detachment and sediment transport, as follows.

$$Y = 11.8(Q \times q_p)^{0.56} K L S C P \qquad (7.4)$$

where

Y = the sediment yield from an individual storm, in metric tonnes,

Q = storm runoff volume, m^3

q_p = peak runoff rate, m^3/sec, and

K, L, S, C, P are as previously defined

Several methods are available for evaluating Q and q_p, the most common of which is the Soil Conservation Service triangular hydrograph (Schwab et al., 1981).

7.4. THE SOIL LOSS ESTIMATOR FOR SOUTHERN AFRICA (SLEMSA)

The application of the universal soil loss equation has proved to be very difficult in some areas of the world. Where the annual variations in climate and cropping practices are quite different from those in North America, some of the factors in the USLE are not appropriate, or would be enormously costly and time consuming to determine accurately. For example, the rainfall and

runoff erosivity factor, R, is based on the kinetic energy of an individual rainstorm multiplied by its maximum 30 minute intensity, and summed over many years of observation. In many tropical regions, erosion producing storms are often shorter than 30 minutes and their intensity would be artificially diminished if spread out over this time span. Furthermore, the permeability, structure and shallow depth of many tropical soil types are virtually impossible to fit into the USLE soil textural classes (Table 7.1 above), and differentiate properly according to their structure and erodibility (Wendelaar, 1978).

In addition to these difficulties, many tropical area rotations and cropping practices are not listed in Table 7.2 of crop management factors, C. Such regions usually have a well defined wet season lasting from three to six months. Land plowing can take place at any time near the end of the rainy season or during the dry period. Also, crops needing the maximum of precipitation are planted at the beginning of the wet season, but irrigated crops can be planted a month or more beforehand, and dryland crops towards the end. Thus it is difficult to categorize such practices into the five American crop stage periods (Table 7.2), and tropical crop stages occur at widely varying times within the rainfall season, when soil properties differ greatly. It could be possible to evaluate the USLE factors experimentally for individual tropical regions, and be able to make use of the equation as a result. However, taking into account the variety and combinations of tillage, cropping, rotation and soil management practices which are found, the financial and time resources which would be necessary are prohibitive.

In view of the above difficulties encountered in attempting to apply the USLE in a tropical area, a modelling approach has been taken by researchers in southern Africa with the result being the soil loss estimator for southern Africa, SLEMSA, (Elwell, 1978, 1984). The model is designed for arable lands in regions of high intensity rainfall, and for a wide variety of cropping conditions. However, interpretations of the factors in the model must be made from relatively few field plots. For this purpose, the soil sheet erosion model has been divided into five principal control variables as follows.

1. Seasonal rainfall energy, E (J/m^2),
2. Soil erodibility index, F_b,
3. Rainfall energy interception by crops, i (%),
4. Field slope length, L (m), and
5. Slope steepness, S (%).

The above control variables are related to soil losses at the submodel level. The principal submodel, quantity K, combines the effects of the rainfall energy, E, and the soil erodibility index, F_b, in such a way as to yield the estimated mean annual specific soil loss from a conventionally tilled bare field having a slope of 4.5% and length 30 m. A factor C, derived from the proportion of rainfall energy intercepted by crops, corrects the above soil loss estimate for cropped land, and a topography ratio, X, accounts for different field slopes and lengths. The resulting estimate of mean annual soil loss, Z in

t/(ha y), is then;

$$Z = KCX \tag{7.5}$$

The three main factors are given below, K in Fig. 7.4, C in Fig. 7.5 and X in Fig. 7.6 and 7.7, or Eqn. 7.6 and 7.7.

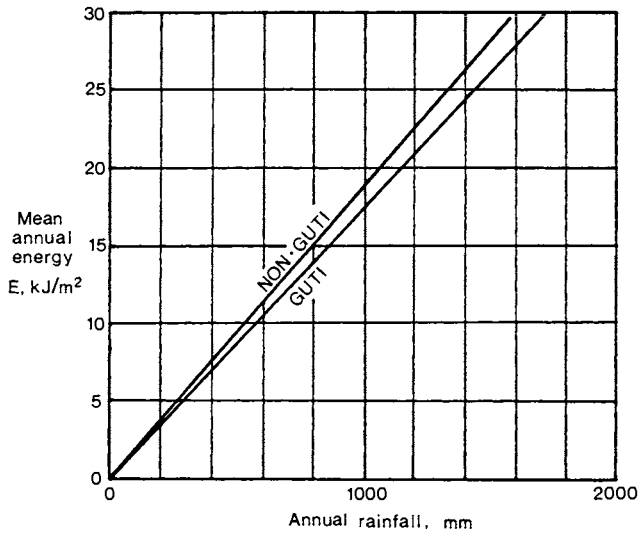

Fig. 7.2 Mean annual rainfall energy versus annual rainfall depth for guti and non-guti regions (more or less than 20 days of early morning drizzle, respectively) from Elwell (1980).

7.4.1. Soil loss rate, K

In order to begin the estimation of the bare soil erosion rate K, the average annual incident rainfall energy can be estimated directly for southern Africa from the mean annual precipitation, as shown in Fig. 7.2. There is a difference between guti and non-guti regions, guti inferring that there are at least 20 days per year on the average with early morning drizzle. The rainfall energy versus precipitation line is lower in the guti case since the morning drizzles are of relatively lower energy intensity. The mean annual rainfall map for Zimbabwe is shown as an example of a tropical precipitation pattern in Fig. 7.3.

The combination of mean annual rainfall energy, E, and soil erodibility, F_b, is conducted in Fig. 7.4 in order to estimate the bare soil erosion quantity, K. Table 7.4 gives estimates of the basic values, F_b, for several types of

Fig. 7.3. Mean annual rainfall in Zimbabwe (Elwell, 1980), mm/y.

tropical soil, while Table 7.5 provides correction factors, taking into account soil management practices. These correction factors are added algebraically to F_b in order to arrive at the total soil erodibility index, F_m. F_m has been designed to be a reduction factor for soil losses. It can be noted in Fig. 7.4 that as F_m increases, the rate of soil loss is smaller. Also, the more conservation practices which are present, including ridging, planting on contours, rough plowing and installing pasture as shown in Table 7.5, the larger are the correction factors which reduce the bare soil loss estimate, K.

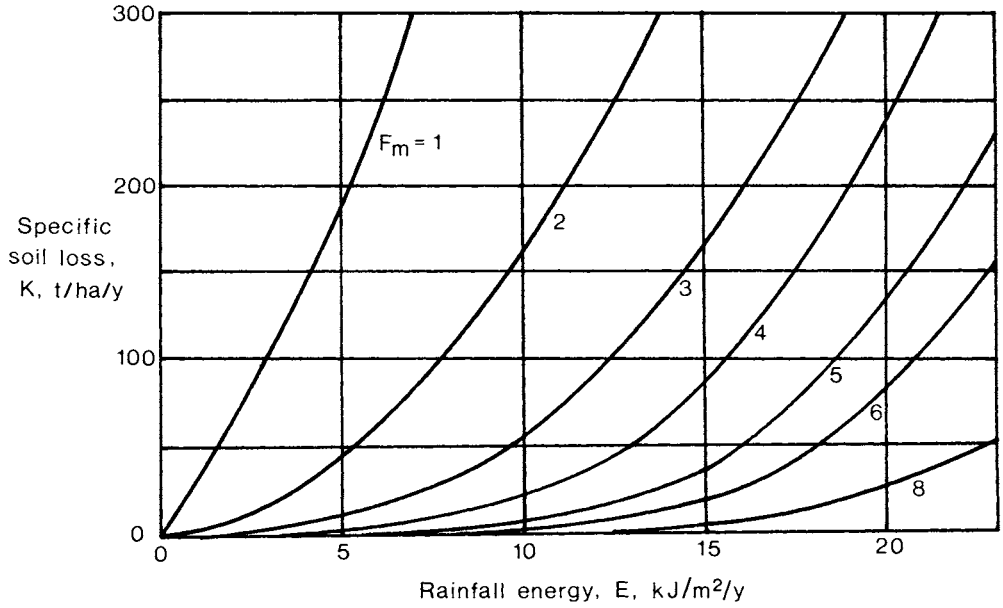

Fig. 7.4. Specific soil loss rate, K, versus rainfall energy, E, for different degrees of soil erodibility, F (Elwell, 1980).

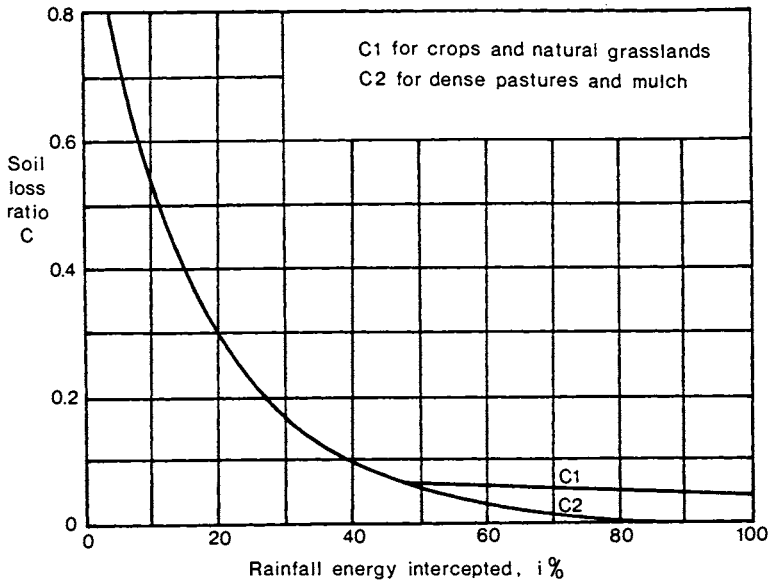

Fig. 7.5. Soil loss ratio, C, versus i (Elwell, 1980).

TABLE 7.4. Basic soil erodibility factors, F_b, for various tropical soils, from Elwell (1980).

Soil group	Soil family	Texture of topsoil		
		Sands	Loams	Clays
Regosol	Kalahari sand	4.0		
Lithosol	Lithosol	2.0	2.5	4.0
Vertisol	Basic rocks			5.0
	Sediments			4.5
Siallitic	Basic rocks		3.5	4.0
	Ultra basic			4.0
	Sediments			3.5
	Sandstones	3.5	4.0	
	Granites			
Fersiallitic	Basic rocks		5.5	6.0
	Ultra basic			6.0
	Sediments		4.5	4.5
	Granites	4.0	4.5	
	Arenaceous	3.5	4.0	
Paraferrallitic	Granites	4.5	5.0	
Orthoferrallitic	Basic rocks			7.0
	Sediments			5.5
	Granites	5.5	6.5	6.5
	Sandstones	5.0	6.0	
Sodic	Strongly sodic	1.0	1.5	1.5
	Weakly sodic/saline	1.0	1.5	2.0

7.4.2. Cropping factor, C

The next step in estimating soil losses is to evaluate the crop cover effect. As mentioned above, the SLEMSA model approach is to obtain a single number for the proportion of rainfall energy which is intercepted by any crop and at any stage of growth. Tables 7.6 and 7.7 give estimations of the proportion of rainfall energy, i%, which is intercepted by various crops, depending on their date of emergence relative to the beginning of the rainy season, or age of plantation. From this energy interception index, the crop soil loss ratio C, to use in Eqn. 7.5 is read from Fig. 7.5.

7.4.3. Topography factor, X

The estimation of the topography factor, X, combines the effects of field length, L, and slope, S, much in the same manner as does the universal soil loss equation (Eqn. 7.2 and 7.3 in Section 7.2). The equation coefficients are different, however, due to the different standard field length and slope used in the SLEMSA model (30m versus 22m and 4.5% rather than 9%). Eqn. 7.6

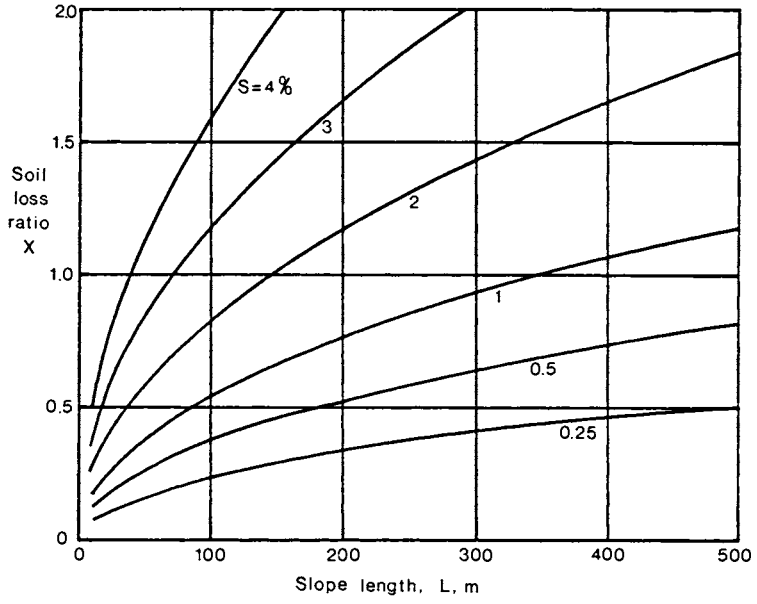

Fig. 7.6. Soil loss ratio, X, versus slope length, L (Elwell, 1980).

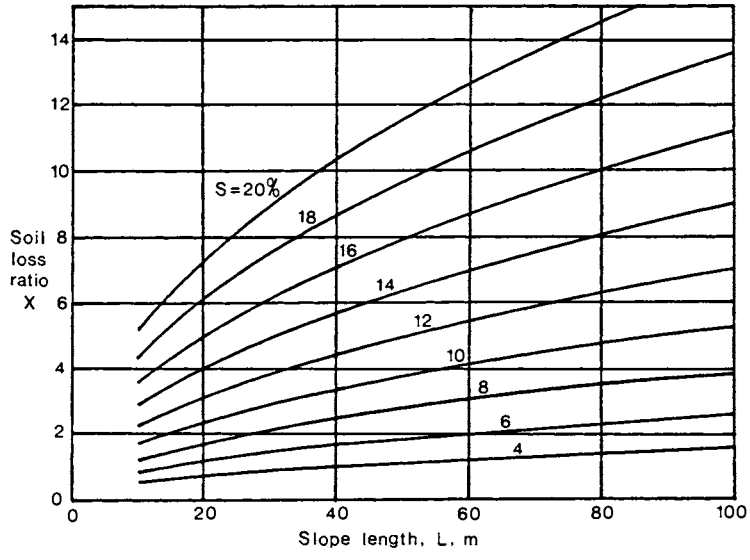

Fig. 7.7. Soil loss ratio X for higher slopes, S (Elwell, 1980).

and 7.7 below give the appropriate topography factors, X, for slopes less or greater than 1%. In these equations, L is in metres and S is in percent.

For $S < 1\%$ $$X = S\sqrt{L}/(10.74S + 8.04) \quad (7.6)$$

For $S > 1\%$ $$X = \sqrt{L}\,(0.76 + 0.53S + 0.076S^2)/25.65 \quad (7.7)$$

TABLE 7.5. Correction factors to be added algebraically to the soil erodibility factor, F, for soil management techniques (Elwell, 1980). $F_m = F_b$ + correction factors.

Practice		Factor
A. Soil loss in previous year	<10 t/ha	0
	10 to 20 t/ha	-0.5
	>20 t/ha	-1.0
B. Ridging practices	Normal tilth	0
	Fine powdery	-0.25
B1. Crops on large ridges (>200 mm)	Slope < 1%	1.5
Ridges without tie-ridges	Slope < 1%	1.0
	Slope 1 to 2%	0
	Slope > 2%	-1.0
B2. Crops on small ridges (<200 mm)	Slope < 1%	-1.0
	Slope 1 to 2%	0
	Slope > 2%	-1.0
C1. Annual crops planting direction	On contours	0
	Angle to contours	-0.25
	At right angle	-0.5
C2. Tillage techniques	Fine powdery tilth	-0.5
	Zero tillage	-0.5
	Disced fine tilth	0
	Ripped and disced	0
	Plowed and rolled	0.5
	Plowed only	1.0
D. Fallows and leys	First year	0
	Second year	1.0
	Third year and more	2.0
	Good pasture	2.0
E. Perennial crops and orchards	Mechanical cultivation	-0.5
	Herbicide weed control	0
	Mulch soil cover	2.0
F. Irrigated lands	Sands and loams	-0.5
	Good pastures	3.0

TABLE 7.6. Values of rainfall energy interception proportion, i%, for various crops and emergence times before (-) or after the start of the rainy season (Elwell, 1980).

Crop	Yield (t/ha)	Emergence time after start of rainy season				
		-1 mo.	0	1 mo.	2 mo.	3 mo.
Cotton	1.0	62	55	41	24	9
	2.5	84	75	56	32	13
	4.5	95	84	63	36	14
Cowpeas hay	1.5	54	62	67	55	35
	2.5	65	76	81	67	43
" silage	2.0	26	29	32	29	20
	6.0	43	50	54	49	34
	10.0	61	70	83	69	48
" green crop	6.0	5	17	26	30	22
	10.0	7	24	35	41	36
Groundnuts	0.8	50	57	49	32	16
	1.5	64	73	62	41	20
	3.0	71	80	69	45	22
Maize	2.0	24	29	28	21	12
	6.0	43	52	51	37	21
	10.0	55	68	66	48	27
Rice	1.5	54	56	53	40	24
	2.5	69	72	67	51	31
	4.5	84	88	82	62	37
Sorghum	1.0	39	40	35	25	12
	2.0	47	49	43	30	15
	6.0	81	84	73	52	26
Soybeans	0.8	34	38	36	27	14
	1.5	51	57	54	39	20
	2.5	69	77	73	53	28
	4.0	80	90	85	62	32
Sunflowers	0.1	5	8	11	9	5
	0.4	11	19	24	21	12
	1.3	28	50	62	55	30
Tobacco	1.0	3	6	8	6	3
	2.0	11	21	26	22	11
	3.0	19	36	46	38	20
	4.0	27	52	66	54	28
Grass ley			97	89	68	42
Poor ley			65	55	33	14
Weed fallow			0	2	10	32
Poor fallow			0	1	5	14

In addition, the topography factor X is shown graphically in Fig. 7.6 and 7.7 for different ranges of field slopes.

Once the variables K, C and X have been estimated for a particular case, they are simply inserted into Eqn. 7.5 (Z = KCX) in order to estimate the mean annual soil loss from a field.

TABLE 7.7. Values of rainfall energy interception proportion, i%, for evergreen orchard trees (except apples) and coffee plantations (Elwell, 1980).

Year	Evergreen tree spacing, m				Coffee tree spacing, m		
	7.25x7.25	6.75x6.75	4.5x6.0	3.0x4.5	2x3	2.5x2.5	2.5x3
1st	1	1	2	3	0.6	0.5	0.4
2nd	3	4	6	13	8	7	5
3rd	9	10	17	34	23	22	18
4th	17	20	32	51	43	41	34
5th	27	31	51	57	57	58	48
6th	45	52	68	59	60	70	58
7th	52	60	72	63	60	71	60

Problem 7.3: A farm field 20 km northeast of Harare, Zimbabwe is 100 m long and has a uniform 3% slope. The soil is a fersiallitic clay loam with normal tilth. Maize was planted for the third year on November 1 (the beginning of the rainy season) with the rows along contour lines and no special ridging techniques. The expected yield of the crop is 6 t/ha. If the rainfall is 850 mm that year, estimate the annual water erosion soil loss.

From Fig. 7.2, rainfall energy E is 12,000 J/m^2.

From Table 7.4, soil erodibility factor F_b = 6.0.

From Table 7.5, correction factors are essentially zero.

Fig. 7.4 gives the bare soil erosion estimate K as 7 t/ha.

From Table 7.6, for a 6 t/ha crop planted at the beginning of the rainy season, i = 52%. This gives a cropping factor C of 0.06 in Fig. 7.5.

Fig. 7.6 combines the 100 m field length and 3% slope to yield a topography factor X of 1.2.

Eqn. 7.5 is now used to estimate the annual soil loss.

$$Z = KCX = (7 \text{ t/ha}) \times 0.06 \times 1.2 = \underline{0.50 \text{ t/ha}}$$

Problem 7.4: The next year on the field of Problem 7.3, for one reason or another, the maize was planted one month late and yielded only 2 t/ha. What difference does this make to the estimate of annual soil loss?

Only the crop energy interception factor, i, varies in this case. Table 7.6 gives i = 28% which yields a cropping factor C = 0.19 from Fig. 7.5. The estimate of soil loss is thus three times higher than for the previous year, or;

$$Z = (7 \text{ t/ha}) \times 0.19 \times 1.2 = \underline{1.60 \text{ t/ha}}$$

Problem 7.5: What would be the effect of constructing high ridges (200 mm) with tie-ridges on a relatively flat field (0.5%) composed of fersiallitic sand topsoil, with a cropping factor C = 50% and a topography factor, X, of 1.0? Assume that the annual rainfall energy is 10 kJ/m^2.

From Table 7.4, the erodibility index for the soil type is found to be 4.0. From Fig. 7.4, the bare soil erosion is estimated to be about 21 t/(ha y). Thus, including the cropping and topography factors, C and X, the soil loss estimate without ridges would be:

$$Z = KCX = (21 \text{ t/ha/y}) \times 0.50 \times 1.0 = \underline{10.5 \text{ t/(ha y)}}$$

With 200 mm ridges and tie-ridges, Table 7.5 indicates that a correction factor of 1.5 should be added to F_b to calculate a value of F_m of 4.0 + 1.5 = 5.5. Then the annual bare soil loss estimate from Fig. 7.4 is reduced to approximately 6 t/ha, and the net estimate is;

$$Z = 6 \text{ t/(ha y)} \times 0.50 \times 1.0 = \underline{3 \text{ t/(ha y)}}, \text{ (29\% of the previous value)}$$

7.5. DESIGN OF SOIL CONSERVATION PRACTICES AND STRUCTURES

The conservation practices listed in Table 7.3 are illustrated schematically in Fig. 7.8 to 7.10. Contouring is the practice of executing plowing, planting and cultivation as closely as possible along elevation contours. The plow furrows and later rows which result can store some of the rainfall runoff and decrease the downhill velocity of water. Stored water in the rows infiltrates into the soil and is an added benefit in dry areas where water conservation is also important (Schwab et al., 1981). Table 7.3 indicates that on slopes up to 12%, contour plowing reduces water erosion soil losses by 40 to 50% compared to plowing up and down the slope.

Strip cropping, as shown in Fig. 7.9, consists of planting strips of a buffer crop, such as grass or legumes, between uniformly wide strips of row crops planted along contours. In areas where wind erosion is a more serious problem than that due to water, the buffer strips and crop rows are installed perpendicular to the direction of the prevailing winds (Schwab et al., 1981). The buffer strips trap much of the water flowing downhill, and retain soil washed from the row crop areas. Table 7.3 indicates that strip cropping,

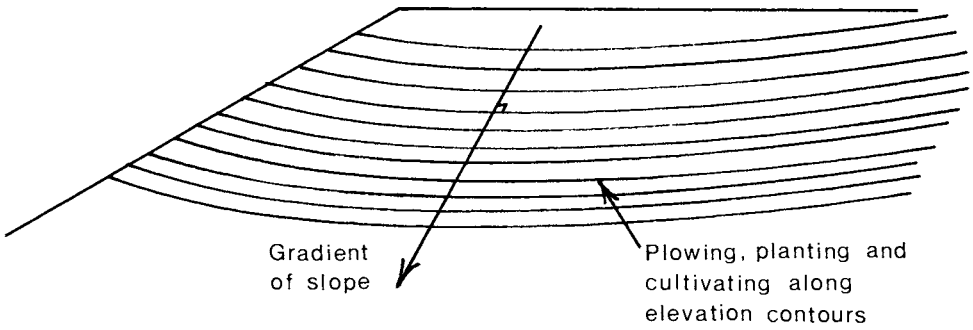

Fig. 7.8. Contouring a slope as an erosion control practice.

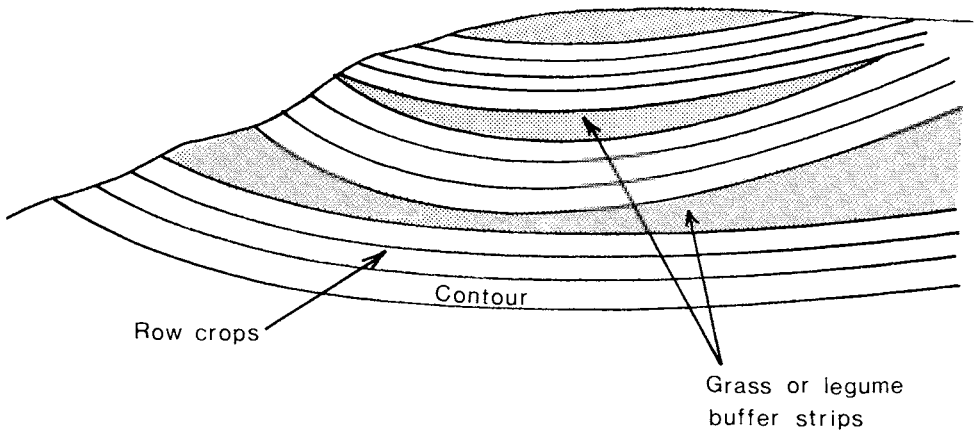

Fig.7.9. Contouring and buffer strips to reduce runoff and erosion.

including rotation in the row crop areas, can reduce soil losses by about 70% for slopes up to 12%.

Terracing (Fig. 7.10) is a method of altering the landform to provide cutoffs to downhill waterflow, and lower slopes over much of the land area. Broadbase terraces include shallow channels cut along contours and spaced at 30 m or so. The cuts and fills are not steep, and so practically all of the field area can be used for cultivation. In addition, not a great deal of earthmoving is required for this type of terrace, and thus landforming costs are low (Fig. 7.10a).

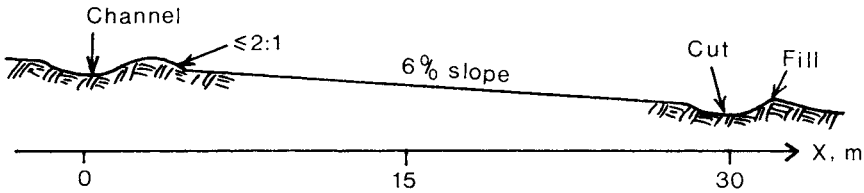

(a) Broadbase

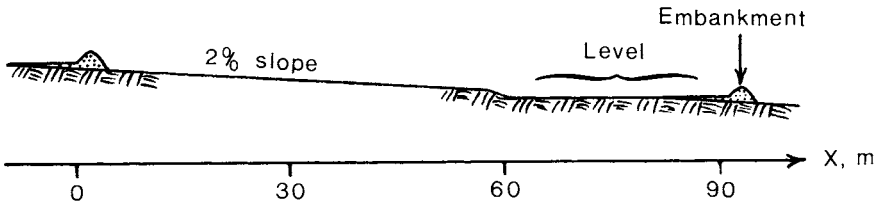

(b) Conservation bench

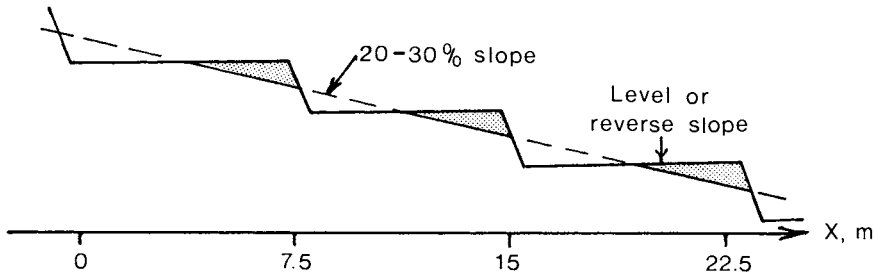

(c) Bench

Fig. 7.10. Soil conservation benches, (a) broadbase bench, (b) conservation bench with embankments and (c) level or reverse slope benches.

Conservation benches (Fig. 7.10b), on the other hand, involve the movement of more soil than broadbase terracing, in order to construct level strips of land of about 30 m width every 90 m. These level areas hold water trapped by the embankments, and allow the infiltration and storage of more water than the former terrace configuration. This is important in drier areas of the world in which water conservation is desirable.

Bench terraces (Fig. 7.10c) comprise flattened shelves cut into steep slopes of 20% or more. They are used to control the distribution of irrigation water (especially in wet crops such as rice), or to stabilize steeper slopes which would be subjected to severe water erosion when cleared of grass or trees for cultivation. The back of each terrace can have a small slope to the horizontal (0.2 - 2%) in order to channel excess runoff to grassed waterways or surface inlets which will allow it to move downhill safely.

The recommended horizontal interval (HI) between terraces can be calculated as follows.

$$HI = \left[\frac{100\ LS}{0.75 + 0.53\ S_1 + 0.076\ S_1^2} \right]^2 \qquad (7.8)$$

where S_1 = the land slope in %

and LS is calculated from Eqn. 7.1, based on a predetermined or tolerable rate of soil erosion.

The use of vertical pipe inlets to control surface water runoff is another useful practice. The distance of overland flow should be minimized to prevent excessive removal of topsoil during rainfall events. Vertical inlets also reduce the danger of soil slumping in embankment structures due to water seepage at the downstream side. Structures such as silt traps or sedimentation basins could also be constructed in order to prevent downstream siltation in watercourses, or further gully erosion.

7.6. WIND EROSION

Erosion due to wind occurs in localized areas, and can often be as severe a problem as water erosion is in others. Wind erosion is more pronounced in dry locations or periods and where sandy or silty soils predominate, or where light organic soils are found. These soils have a low resistance to movement by the wind due to their low cohesion and unit weight. The amount of soil liable to be moved by wind is dependent primarily on two factors, namely wind velocity and the roughness of the soil surface. Soil particles of less than 2 mm diameter are the most susceptible to movement by air. Hudson (1981) has reported soil deposition rates due to wind erosion as high as 35 g/(m^2day).

Methods for controlling wind erosion are aimed mainly at keeping the ground surface under vegetal cover. Tillage methods which can be incorporated

with crop stubble management are therefore advantageous. The use of natural and artificial windbreaks is also recommended. Natural windbreaks, or vegetative barriers, can be created by planting trees or by strip cropping with alternate bands of tall and shorter crops. Artificial windbreaks include fences and vertical geotextile walls, and are also effective in reducing the velocity of the wind over the ground surface.

Soil mulching can also be effected, and has two main effects. It leaves less soil particles exposed to the wind, and retains more moisture in the soil, thereby increasing internal soil cohesion.

7.7. PROBLEMS

7.6. A sandy loam field near Montreal, Canada (R = 75) is 100 m long with a 2% slope. The organic matter in the topsoil averages 2%, and silage corn has been grown the year previous leaving no residues. Plowing and planting have been done on contours, but no strip cropping or terracing have been effected. What is the estimated rate of soil loss during the first month after seeding the second year of silage corn?

Answer: 9.4 t/(ha y).

7.7. Is it possible to incorporate a conservation practice on the above field in order to reduce the soil loss in this period to below 1.5 t/(ha y)?

Answer: Yes, by terracing and contouring, $A < 1.5$ t/(ha y).

7.8. A rainstorm occurs in a 4 km^2 agricultural area of New York State resulting in a total runoff volume of 10,000 m^3 and a peak runoff rate of 0.25 m^3/s. The average soil erodibility factor of the soil in the area is 0.20 tons/acre, the average length and slope factors are 8 and 0.2, respectively, and the practice factor is 0.6. How much soil per hectare can be expected to be carried from the area?

Answer: Y = 8 t/ha.

7.9. A cotton field near Lusaka, Zambia receives 600 mm of annual rainfall. The field has a siallitic sandy loam topsoil, length 150 m and average slope 4%. The crop was planted at the beginning of the rainy season on field contours with a very fine powdery soil tilth and no ridges or terraces, and the expected yield is 2.5 t/ha. What is the estimated annual rate of soil loss?

Answer: Z = 4.4 t/(ha y).

7.10 To what level could the estimated annual soil loss be reduced on the field of Problem 7.9 if the soil were plowed and disced in a more conventional manner?

Answer: $Z = 2.4$ t/(ha y).

7.11 A corn field in southern Ontario receives an annual rainfall of 1000 mm and has an erosivity index of 100. The field is 100 m long up a 3% slope across which grain corn is planted for the second year after conventional tillage and no residues remaining. The field topsoil is a siallitic sandy loam derived from sandstone and has about 2% organic matter content. The corn was planted at the beginning of the growing season and is expected to yield approximately 10 t/ha after 5 months. Estimate the annual water erosion soil loss rate by (a) the universal soil loss equation, and (b) the soil loss estimator for southern Africa.

Answer: (a) 8.3 t/(ha y), (b) 9.9 t/(ha y).

Chapter 8. Soil cutting and tillage

8.1. CUTTING FORCES

8.1.1. Two dimensional cases

In Chapters 2 and 6 the basic notions of soil failure mechanics and lateral pressures were discussed. These same principles apply to walls, anchors or soil cutting tools which move soil in passive failure. The two dimensional approach can be valid for cases in which the structure or tool in question is considerably wider than it is deep (a ratio of about ten to one). Mechanically speaking, there is actually no difference between, say, a bulldozer blade and a retaining wall which fails the soil passively, as shown in Fig. 8.1. The slope of the soil internal failure plane at the bottom of the wall or blade is governed by the interface angle and angles of internal friction and soil to wall or blade friction (ref. Fig. 6.11). The slope of the failure line at the surface is also the same in both cases as shown.

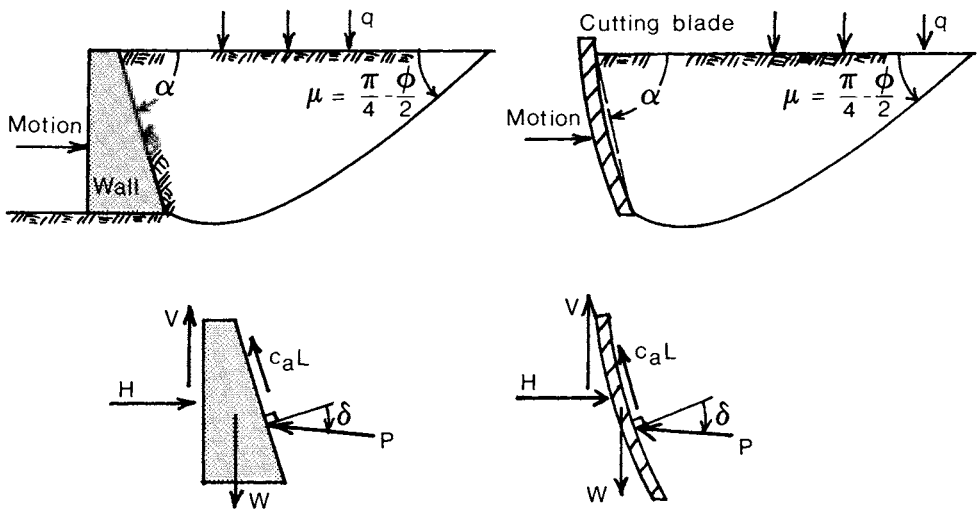

Fig. 8.1. A comparison between a retaining wall and a cutting blade failing soil in the passive case.

The forces which are required to move the wall or blade and soil can be composed in the horizontal and vertical directions and labelled H and V as illustrated. If the weight of the wall or the blade and its carriage, W, is

significant compared to the vertical component of the required soil force, then it should be included as well in the calculation of V. Also, a wall or blade of finite width should have this width, w, included in the calculation of soil force P and the adhesion force, as shown below.

$$P = (\gamma h^2 K_p + chK_c + c_a hK_{ca} + qhK_q)w \tag{8.1}$$

$$H = P\sin(\alpha + \delta) + c_a dw\cot\alpha \tag{8.2}$$

$$V = P\cos(\alpha + \delta) - c_a dw + W \tag{8.3}$$

The soil force, P, to be determined in each case, can be found using the coefficients of passive earthpressure calculated by Eqn. 6.27 to 6.32 in Chapter 6, or by using the soil cutting factors located in Appendix 5 and putting them into Eqn. 8.1. In the case of passive soil failure in two dimensions, the straight wedge model represented by Eqn. 6.27 to 6.32 can be used, or the more accurate log spiral failure shape employed by Hettiaratchi (1969), (Hettiaratchi and Reece, 1974).

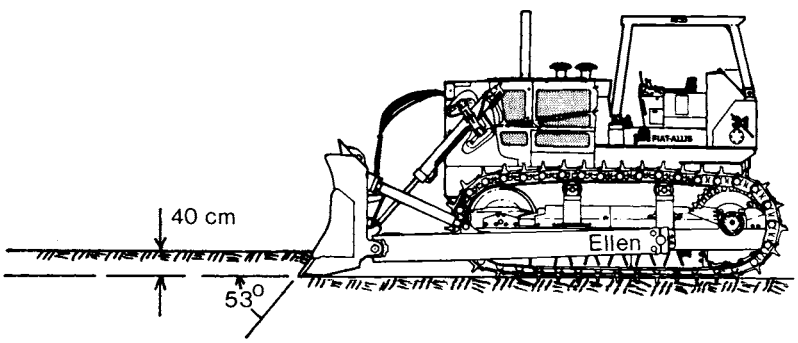

Fig. 8.2. A bulldozer soil cutting blade in Problem 8.1.

Problem 8.1. An example application of the technique is illustrated in Fig. 8.2. A 317 kW tracked tractor with a mass of 41.8 t is shown with a flat bulldozer blade having a total width of 4.80 m. The tractor is beginning to cut soil at a depth of 40 cm as indicated, the soil properties being γ=17.6 kN/m^3, ϕ=30^0, δ=20^0, c=10 kPa and c_a=4 kPa. The blade itself, not including the arms which support it, has a mass of 4 t. Find the horizontal (draft) and vertical uplift forces required to move the blade through the soil.

The coefficients of passive earthpressure must be determined by referring to Hettiaratchi and Reece (1974), (Appendix 5), or by following the procedure outlined in Section 6.3 which will be done as follows.

$$\beta = \cot^{-1}\left[\frac{\sqrt{\frac{\sin(\alpha+\delta)\sin(\delta+\phi)}{\sin\alpha\sin\phi}} - \cos(\alpha+\delta+\phi)}{\sin(\alpha+\delta+\phi)}\right] = 31.67^{o}$$

$$K_p = \frac{(\cot\alpha + \cot\beta)\sin(\beta+\phi)}{2\sin(\alpha+\beta+\delta+\phi)} = 1.47$$

$$K_c = \frac{\cos\phi}{\sin\beta\sin(\alpha+\beta+\delta+\phi)} = 2.32$$

$$K_{ca} = \frac{-\cos(\alpha+\beta+\phi)}{\sin\alpha\sin(\alpha+\beta+\delta+\phi)} = 0.73$$

Then the soil force P can be determined from Eqn. 8.1, multiplying the force per unit blade width by the width, w=4.8 m.

$$P = (\gamma h^2 K_p + chK_c + c_a hK_{ca})w = 70.1 \text{ kN}$$

Now Eqn. 8.2 and 8.3 are applied to find the horizontal and vertical forces required to move the blade in the manner shown.

$$H = P\sin(\alpha+\delta) + c_a hw\cot\alpha = 72.8 \text{ kN}$$

$$V = P\cos(\alpha+\delta) - c_a hw + W = 52.0 \text{ kN}$$

It is interesting to note in the above case that the gravity coefficients of passive earthpressure, K_p, given by Hettiaratchi and Reece (1974) for the relevant blade and soil parameters are 0.92 and 1.75 for $\delta=0$ and $\delta=\phi$, respectively. A linear extrapolation (McKyes, 1985) for $\delta=20^{o}$ gives $K_p=1.47$, exactly the same answer as was determined above using the straight line wedge failure model. The power extrapolation suggested by Hettiaratchi and Reece (1974) gives K_p of 1.41. The coefficients do not always equal each other using the two approaches, but the difference is usually less than 10%.

Problem 8.2.

Another example is shown in Fig. 8.3 involving a structure. An anchor made of concrete (specific gravity 2.4) is designed with the dimensions shown to hold down a cable with a design tension of 450 kN. The soil has been compacted around the anchor to have properties γ=19.6 kN/m^3, $\phi=35^{o}$, $\delta=27^{o}$, c=15 kPa and c_a=5 kPa. In order to determine the safety factor of this overall design, the maximum strength of the anchor-soil combination must be estimated for horizontal movement and vertical uplift.

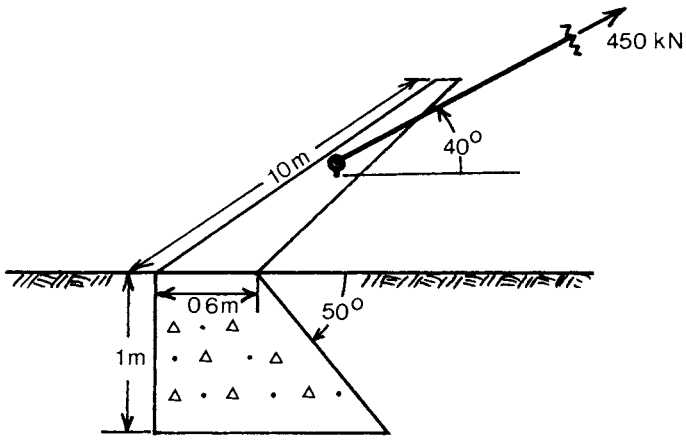

Fig. 8.3. A buried anchor, Problem 8.2.

Eqn. 6.28 to 6.32 and 8.1 are used to calculate the following constants and forces.

$$\beta = 27.6^{0},\ K_p = 1.88,\ K_c = 2.73,\ K_{ca} = 0.77.$$

$$P = (\gamma h^2 K_p + chK_c + c_a hK_{ca})w = 817 \text{ kN}$$

and Eqn. 8.2 and 8.3 give the estimated maximum horizontal and vertical forces which the anchor can resist before movement.

$$H_m = P\sin(\alpha + \delta) + c_a dw\cot\alpha = 838 \text{ kN}$$

$$V_m = P\cos(\alpha + \delta) - c_a dw + W = 369 \text{ kN}$$

The safety factor of this structure can then be calculated either as the horizontal load capacity of the anchor divided by the horizontal component of the design cable tension, or similarly in the vertical direction, whichever is less. The design load components in these two directions are;

$H = 450\cos 40^{0}$ kN = 345 kN, and $V = 450\sin 40^{0}$ kN = 294 kN

In the horizontal direction, S.F. = H_m/H = 838/345 = 2.43

In the vertical direction, S.F. = V_m/V = 369/294 = <u>1.26</u>

The vertical safety factor is the critical one in this example and can be used as the safety factor for the particular structure. Again comparing the wedge method for estimating K_p with the log spiral of Hettiaratchi and Reece (1974), the straight line model predicts K_p=1.88, while the latter method gives values of 1.96 or 1.87 using a linear and power extrapolation, respectively, between the quantities for δ=0 and δ=ϕ.

8.1.2. Three dimensional cases

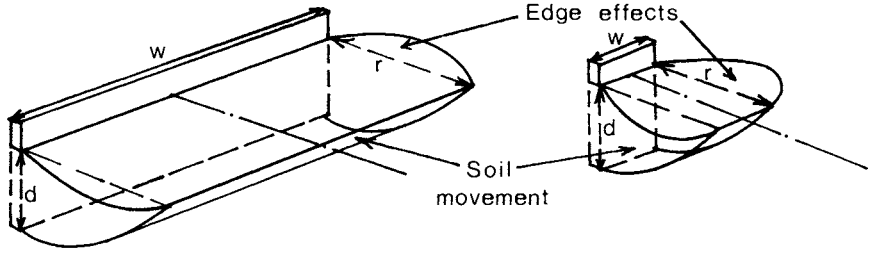

(a) Wide blade (b) Narrow blade

Fig. 8.4. The difference in soil movement pattern between a wide and narrow cutting blade (after Payne, 1956).

When a structure or tool moving soil passively is less than ten times as wide as it is deep, the accuracy of the two dimensional approach described above can be poor. This occurs principally because a considerable amount of soil moves sideways near the edges of the moving soil zone, rather than simply forward and vertically. Payne (1956) illustrated this phenomenon by conducting field tests with flat steel blades having different depths and widths in several soil types. His observations with respect to edge effects in passive soil failure are illustrated in Fig. 8.4.

Evidently, the edge effects, comprising soil moving outside the edges of a blade, are larger in comparison to the central soil zone, directly ahead of the blade, for narrower tools. This fact manifested itself in Payne's measurements of horizontal draft force by the higher forces per unit width of blade in the case of narrower tools in the same soil. The two dimensional passive earth pressure theory discussed earlier would dictate that the soil force per unit width should remain constant. But the two dimensional treatment does not take into account the effects of soil movement outside the width of the blade itself.

Not only did Payne find unit draft force to be affected by tool width, but even the pattern of soil failure at the center of tools was altered by blade width. One of the measurements of the soil rupture surface geometry is the

surface distance from the blade to the forward failure plane, labelled r in Fig. 8.4. Payne observed in field tests that this distance was affected by the width of a blade at constant operating depth. The ratio r/d changed from about 1.6 for a wide vertical blade (w/d=5) to nearly 1.0 for a narrower blade having w/d=0.2 in sandy soil, and similar effects were seen in loam and clay soils. It would appear that the edge effects on narrow blades, and the requirement of the blade to move soil sideways as well as only forward, alters the whole pattern of soil failure ahead of the tool.

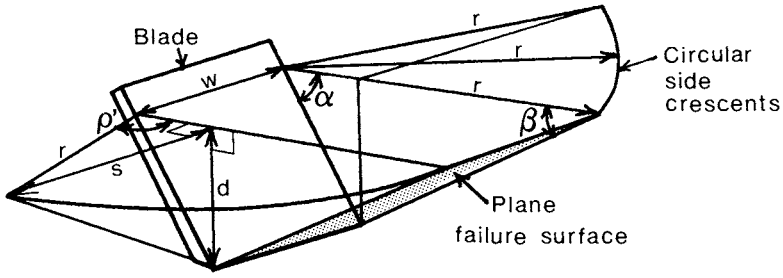

Fig. 8.5. Three dimensional wedge soil failure model (McKyes and Ali, 1977).

There is a mechanical model which can approximate such behavior, and estimate draft forces in different soils for varying widths of cutting tool (McKyes and Ali, 1977). As illustrated in Fig. 8.5, the model uses a plane soil failure surface ahead of the blade, just like the two dimensional wedge approximation for active or passive soil failure seen in Sections 6.1 and 6.3. The failure plane has a slope, β, to the horizontal and the rake angle of the blade is called α. Directly ahead of the tool is a prismatic moving soil section of constant width, w. To each side of this center zone is a circular crescent edge section having the same surface radius, r, as the length of the center zone. This shape of edge zone was suggested by Godwin in 1974 (Godwin and Spoor, 1977), and it was presumed that the maximum width, s, of the side crescents occurred beside the lower tip of the blade, as shown in Fig. 8.4. This assumption forces the width, s, of the side zones to be a function of the blade rake angle and soil failure plane angle for a certain blade depth, as follows.

$$s = r\sin\rho' = d\sqrt{\cot^2\beta + 2\cot\alpha\cot\beta} \qquad (8.4)$$

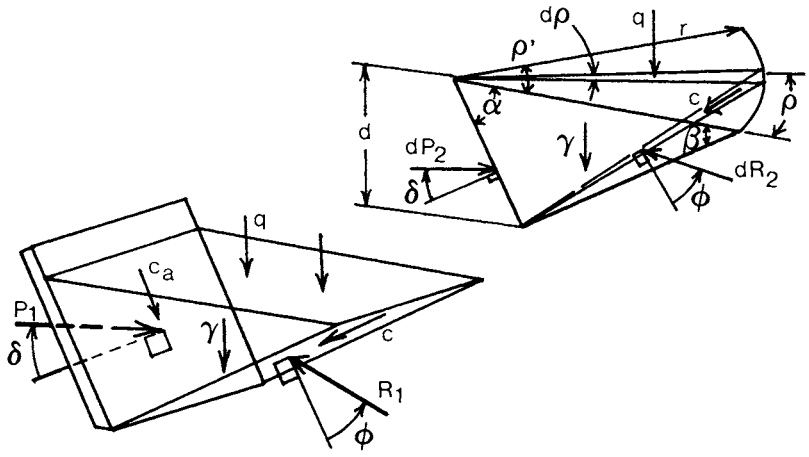

Fig. 8.6. Separation of forces acting on centre and side soil elements (McKyes and Ali, 1977).

Fig. 8.6 shows the pressures and forces acting on the surfaces of the separated sections, in front and to the sides of the blade. The resultant forces on the center section are identical to those formulated for the two dimensional passive soil failure case seen in Section 6.3. For the side crescents, a differential approach must be taken because the forces are distributed around the circular arcs which bound these zones. Godwin (1974) showed how a differential element of these side crescents can be defined by taking an arc having horizontal included angle $d\rho$, as shown in Fig. 8.6. The top area of this section is $r^2 d\rho/2$, the soil internal failure plane area is $rd\ d\rho/(2\sin\beta)$ and the volume is $r^2 d\ d\rho/6$.

Having the surface areas and volumes of the center and side sections allows the computation of forces on these surfaces. The requirement of equilibrium can then be used to eliminate soil reaction forces, R_1 and dR_2 and formulate the blade forces P_1 and dP_2.

For the center section, the result for P_1 is as in Section 6.3, for a blade of width, w.

$$P_1 = \frac{\left[\left(\frac{1}{2}\gamma d^2 + qd\right)(\cot\alpha + \cot\beta)\sin(\alpha+\delta) + cd\frac{\cos\phi}{\sin\beta} - c_a d\frac{\cos(\alpha+\beta+\phi)}{\sin\alpha}\right] w}{\sin(\alpha+\beta+\delta+\phi)} \qquad (8.5)$$

For a differential section of the side crescents, the blade force dP_2 is;

$$dP_2 = \frac{\left[(\frac{1}{6}\gamma d r^2 + \frac{1}{2}qr^2)\sin(\alpha+\delta) + \frac{1}{2}crd\frac{\cos\phi}{\sin\beta}\right]d\rho}{\sin(\alpha+\beta+\delta+\phi)} \tag{8.6}$$

Each of these elemental forces is at an angle ρ from the forward travel direction. The component of each in the forward direction is $dP_2\cos\rho$, and the total force from each side crescent can be found by integrating the forward components of the elemental forces over the included angle, ρ'.

$$P_2 = \int_0^{\rho'} dP_2\cos\rho$$

$$= \frac{\left[(\frac{1}{6}\gamma d r^2 + \frac{1}{2}qr^2)\sin(\alpha+\delta) + \frac{1}{2}crd\frac{\cos\phi}{\sin\beta}\right]\sin\rho'}{\sin(\alpha+\beta+\delta+\phi)} \tag{8.7}$$

The components of the elemental forces perpendicular to the direction of travel are equal and opposite to the corresponding forces from the crescent on the other side, and thus they cancel each other out. At this point, the total force, P, required by the blade can be found by adding together the forces from the center section and those of the two side crescents.

$$P = \frac{\left[\left[\frac{1}{2}\gamma d^2\frac{r}{d}(1+\frac{2s}{3w}) + qd\frac{r}{d}(1+\frac{s}{w})\right]\sin(\alpha+\delta) + cd\frac{\cos\phi}{\sin\beta}(1+\frac{s}{w}) + c_a d\frac{\cos(\alpha+\beta+\phi)}{\sin\alpha}\right]w}{\sin(\alpha+\beta+\delta+\phi)}$$

$$= (\gamma d^2 N_\gamma + cdN_c + qdN_q + c_a dN_{ca})w \tag{8.8}$$

Eqn. 8.8 resolves intself into dimensional components similar to the K factors of lateral earthpressure seen in Chapter 6, and in fact is in the same form as the universal earthmoving equation proposed by Reece (1965). In its form of Eqn. 8.8, the equation for soil moving does not have the slope angle, β, of the soil failure plane determined. When the geometrical details are included in the first coefficient, $N\gamma$, it looks like this.

$$N\gamma = \frac{\frac{1}{2}(\cot\alpha + \cot\beta)\left[1 + \frac{2d}{3w}\sqrt{\cot^2\beta + 2\cot\alpha\cot\beta}\right]\sin(\alpha+\delta)}{\sin(\alpha+\beta+\delta+\phi)} \tag{8.9}$$

It can be seen in Eqn. 8.9 that the slenderness ratio, d/w, is an implicit component of the $N\gamma$ factor, and will thus affect the force per unit width on a cutting blade. Also, if the principle used in Chapter 6 is employed, to find the most likely failure plane by minimizing the $N\gamma$ term, then the failure angle, β, will be influenced also by the blade depth to width ratio. These effects are in agreement with the physical observations of Payne (1956).

The use of Coulomb's (1776) principle of minimization of Eqn. 8.9, with respect to $\cot\beta$ by calculus, is a bit formidable since such a procedure results in some 25 terms in $\cot\beta$, its square and combinations of square roots. In this instance, it is simpler to formulate Eqn. 8.9 in a computer or a programmable calculator, and determine the values of failure angle, β_{cr}, which yield the minimum quantities of $N\gamma$ by a trial and error procedure. The same value of β_{cr} in each case is then substituted into the other factors, N_c, N_q and N_{ca} to give the complete solution for any combination of soil and interface friction angles, blade rake angle and slenderness ratio. Table 8.1 gives examples of this procedure, and further values of the four N factors are provided in Appendix 5 for different values of these variables.

TABLE 8.1. Example values of the critical failure plane slope angle, β_{cr}, and N factors for particular quantities of soil friction angle, interface friction angle and tool depth to width ratio.

ϕ^0	δ^0	α^0	d/w	β_{cr}^0	$N\gamma$	N_c	N_q	N_{ca}
30	20	70	0	26.0	1.79	3.53	1.48	1.12
			0.1	28.6	2.06	4.23	1.99	1.27
			0.2	30.2	2.31	4.88	2.46	1.38
			0.5	33.0	3.03	6.78	3.80	1.60
			1.0	35.3	4.17	9.82	5.95	1.81
			2.0	37.2	6.38	15.83	10.19	2.01
			5.0	38.9	12.89	33.7	22.8	2.23
			10.0	39.7	23.7	63.5	43.9	2.34
			20.0	40.1	45.2	123.1	86.1	2.40
30	20	40	0	34.8	1.45	1.85	1.10	0.48
			0.1	39.4	1.66	2.14	1.46	0.67
			0.2	42.4	1.86	2.42	1.79	0.80
			0.5	48.2	2.41	3.23	2.73	1.10
			1.0	53.2	3.25	4.57	4.19	1.42
			2.0	58.0	4.84	7.21	7.06	1.81
			5.0	62.9	9.44	15.13	15.54	2.32
			10.0	65.4	16.97	28.4	29.7	2.66
			20.0	66.9	31.9	54.9	57.9	2.90

The first line of Table 8.1, for d/w=0 or a very wide blade, is the same as would be predicted by the two dimensional passive wedge theory of Section 6.3, and $N\gamma$ was shown to be close to the value predicted by Hettiaratchi and Reece (1974) using characteristic equations. Upon the introduction of the side effects, however, all of the N factors increase with d/w, the slenderness ratio, and the soil failure plane angle, β_{cr}, increases also.

Thus the trend of this model matches the observations of Payne (1956), namely that the failure pattern on the soil surface becomes shorter, and the draft per unit tool width increases with blade slenderness.

In fact, Payne had made measurements in the field of draft forces (horizontal component of P) for flat, vertical steel blades in different soil types. In addition, he employed a torsional shear box to measure field values of soil cohesion and friction angle, independently of the blade trials. Therefore, his measurements can be used to check the model for the three

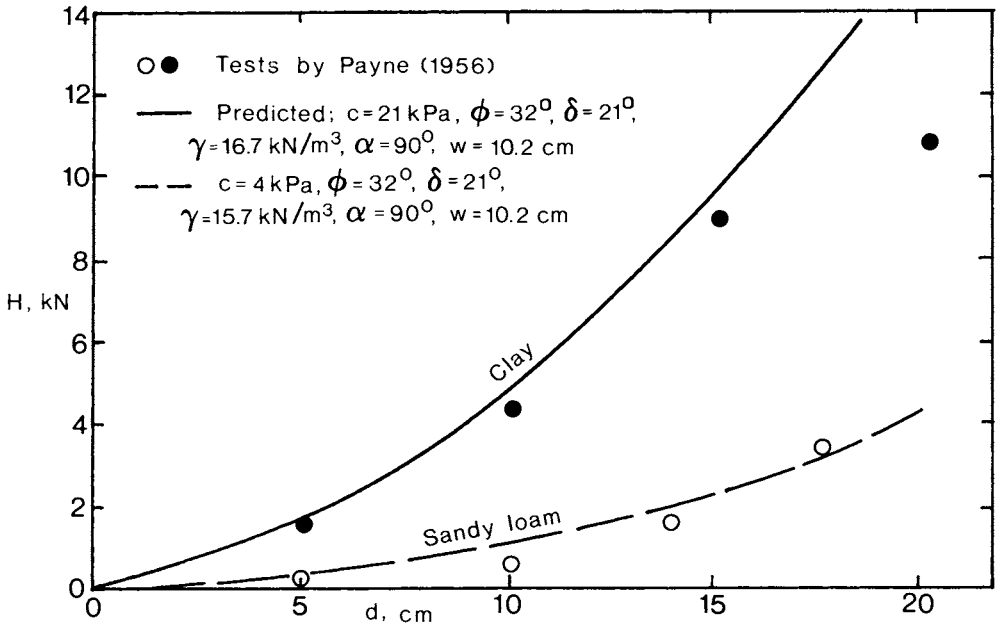

Fig. 8.7. Experimental measurements of passive soil cutting draft forces for narrow vertical steel blades in a clay and sandly loam by Payne (1956) compared to theoretical predictions.

dimensional passive soil failure condition presented above. In Fig. 8.7, Payne's observations of draft force, H, are shown for a 10.2 cm wide vertical blade at various depths in both a clay and sandy loam.

Using Payne's values of measured cohesion, friction angle and soil density, averaged over the depths of 0-20 cm, the N factors can be calculated (or taken from Appendix 5) for every blade depth to width ratio, and placed into Reece's earthmoving Eqn. 8.8 to predict the force, P, on the blade for each depth of the field tests. Then, Eqn. 8.2 is used to estimate the theoretical values of draft, H. Adhesion between soil and blade was not measured by

Payne (1956), and so it was assumed to be zero. The solid and dashed line curves in Fig. 8.7 represent the predictions of draft for the two soils, and they are seen to be reasonable approximations of the experimentally measured values.

Later, Luth and Wismer (1971) conducted laboratory tests on a dry sand in a soil bin using flat steel blades moving horizontally at constant speed. They also measured soil cohesion and internal friction angle of the sand by triaxial shear tests, as well as the soil density and the coefficient of soil to steel friction with an annular shear device. Their measurements for a 12.7 cm wide blade at a rake angle of 30^0 are shown for different depths of operation in Fig. 8.8. Using the same procedure as above with the soil properties which Luth and Wismer reported, a predicted curve of draft force versus depth has been prepared also in Fig. 8.8. Here again, the model appears to hold up well in the light of experimental measurements.

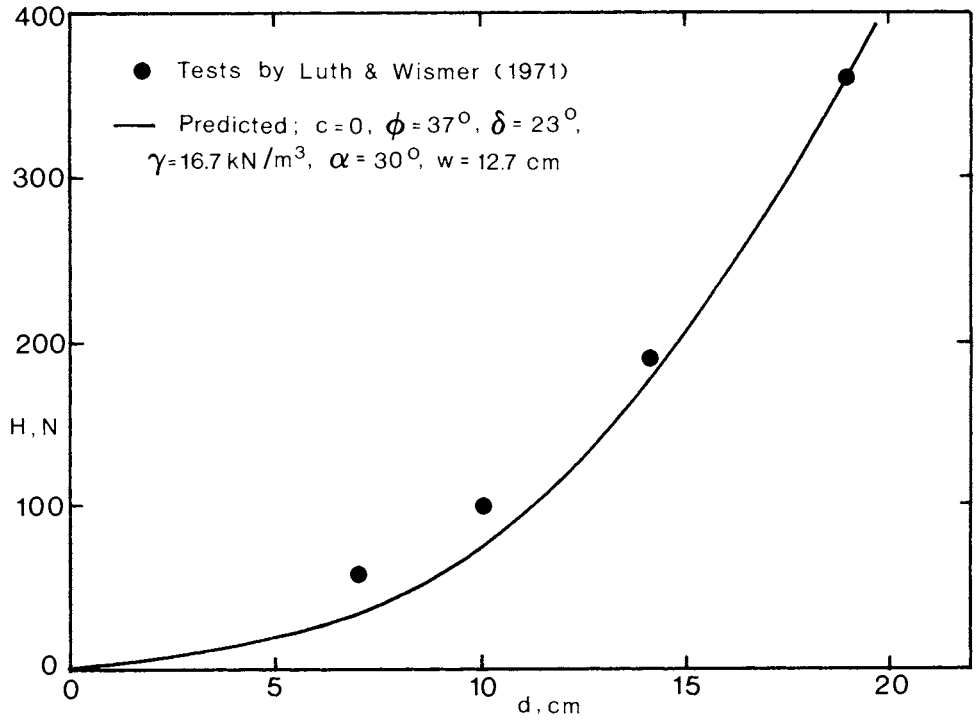

Fig. 8.8. Laboratory tests of narrow cutting blade draft forces in dry sand by by Luth and Wismer (1971) compared to model predicitions.

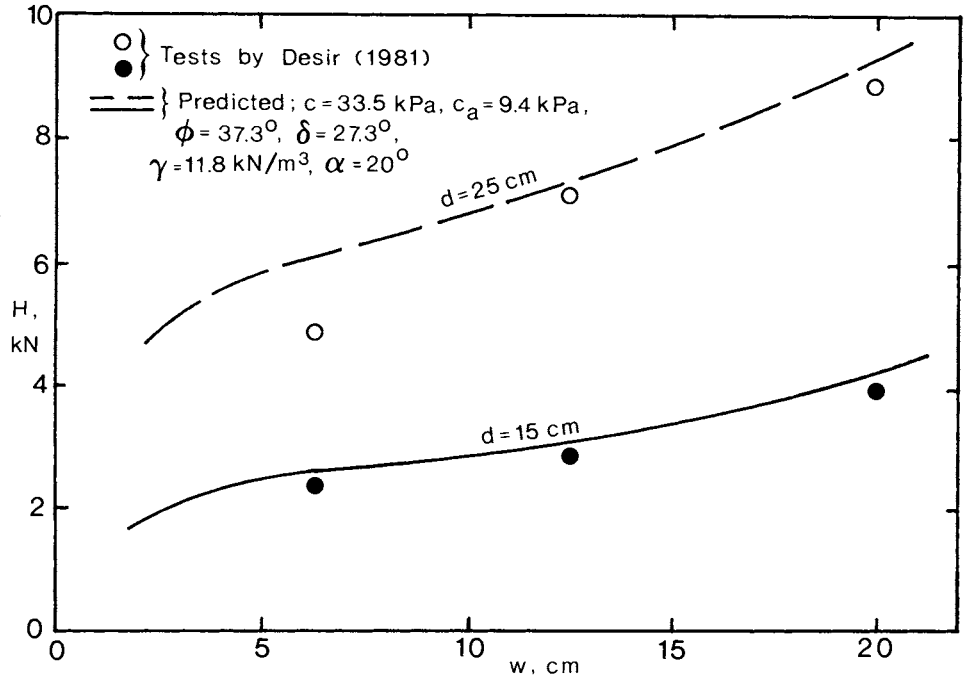

Fig. 8.9. Field test results of narrow cutting tools in clay loam by Desir (1981) compared to theoretical calculations.

In 1981, Desir reported the results of a series of field tests on a clay loam field, using flat mild steel blades having a rake angle of 20^0 and various values of width and depth. He had measured the soil strength properties with a Cohron sheargraph (Section 2.7), including internal soil, and soil to metal angles of friction, as well as blade adhesion, soil cohesion and density. The results of his observations of draft force are reproduced graphically in Fig. 8.9, along with the predictions of the above model, using his reported soil properties. The predictions of draft, H, are slightly high in this case, but usually by not more than 10%, which is acceptable considering the absolute accuracy of the shear strength testing device used by Desir (1981).

While these comparisons of the three dimensional soil cutting model do not comprise an exhaustive proof of its validity, they do show that the model can perform an acceptable task of explaining the measurements of soil cutting forces, which have been given in the literature together with independently measured soil strength properties.

The three dimensional soil cutting model can be used to predict the forces and energy requirements of various earthmoving and tillage tools, or to determine theoretically the best design of a tool for a given purpose, before

prototype trials are conducted. In addition, the model can be employed to analyze different soil cutting procedures, such as the example portrayed in Problem 8.3 below.

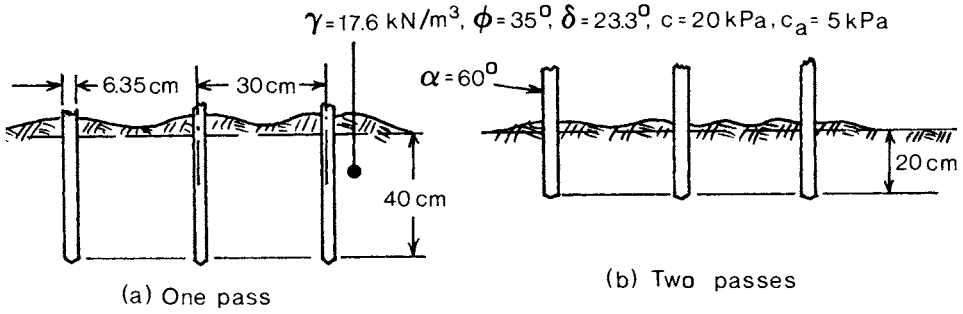

Fig. 8.10. Cross-section of (a) one deep pass and (b) the first of two passes of a set of chisel plows, Problem 8.3.

Problem 8.3. In Fig. 8.10, two possible methods for deep chiselling a soil to a 40 cm depth are shown. Firstly, the three shank chisel plow can be operated directly at 40 cm depth in one pass as illustrated in Fig. 8.10(a). Alternatively, the chisels can be run at 20 cm depth (Fig. 8.10b), and then a second pass performed at a total of 40 cm deep.

The reason for the two pass method is that the first pass at a 20 cm depth will loosen most of the soil in that layer, and make it easier for the tractor to manage the second pass at a depth of 40 cm. With respect to the mathematical cutting model, the second pass would have an effective depth, d, of 20 cm in undisturbed soil with the original soil strength. The original top 20 cm layer would be a surcharge pressure, q, assuming that it is much weaker than the undisturbed lower 20 cm stratum.

The calculations proceed as follows.

(a) For the first pass at 40 cm deep,

$d/w = 40/6.35 = 6.30$

$\beta_{cr} = 39.5^0$, $N_\gamma = 18.53$, $N_c = 39.8$, $N_{ca} = 2.14$

$$P = 3(17.6 \times 0.4^2 \times 18.53 + 20 \times 0.4 \times 39.8 + 5 \times 0.4 \times 2.14)0.0635 = 71.4 \text{ kN}$$

$$H = P\sin(\alpha + \delta) + c_a dw\cot\alpha = 71.1 \text{ kN}$$

(b) For the first pass at 20 cm;

$d/w = 20/6.35 = 3.15$

$\beta_{cr} = 38.5^0$, $N_\gamma = 10.40$, $N_c = 21.66$, $N_q = 15.78$, $N_{ca} = 2.02$

$$P = 3(17.6 \times 0.2^2 \times 10.4 + 20 \times 0.2 \times 21.66 + 5 \times 0.2 \times 2.02)0.0635 = 18.30 \text{ kN}$$

$$H_1 = P\sin(\alpha + \delta) + c_a dw\cot\alpha = 18.27 \text{ kN}$$

For the second pass at 40 cm total depth,

$$P = 3(\gamma d^2 N_\gamma + cdN_c + qdN_q + c_a dN_{ca})w$$

where $d = 0.20$ m

and $q = 0.20$ m $\times$ 17.6 kN/m^3 = 3.52 kPa

$P = 20.43$ kN

$$H_2 = P\sin(\alpha + \delta) + c_a dw\cot\alpha = 20.40 \text{ kN}$$

Therefore, the soil cutting model theory tells us that each of the passes in the two-pass system will require much less traction force than the single pass directly at 40 cm depth (about 29%), thus allowing a smaller tractor to be used for this task. Even adding the combined energy consumption quantities of the two passes together gives less work required than in the single pass method.

$$H_1 + H_2 = \underline{38.7 \text{ kN} = 54\% \text{ of the one pass draft}}$$

Another example of the theoretical work which can be accomplished with the mechanical model of passive soil failure by narrow blades is the optimization of tool design for particular purposes, as illustrated by the problem solved below.

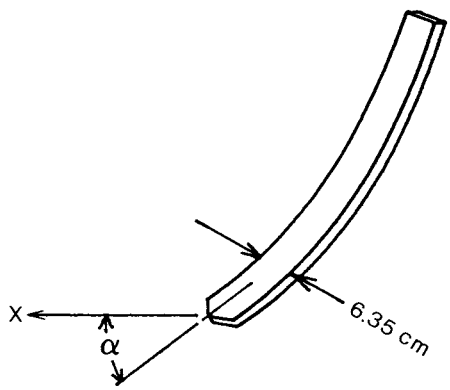

Fig. 8.11. Chisel plow example in Problem 8.4.

Problem 8.4. Fig. 8.11 shows a typical chisel shank with an overall width of 6.35 cm. The chisel can be mounted on a frame at a variety of rake angles, α. Estimate which rake angle would yield the smallest draft force for a single chisel such as this.

The soil forces are calculated for different rake angles, as shown in Table 8.2, using Eqn. 8.8.

TABLE 8.2. Calculations of draft force for a 6.35 cm wide chisel having varying rake angle, in a soil having γ=17.6 kN/m^3, ϕ=35^0, δ=23.3^0, c=20 kPa, c_a=5 kPa, and operating at a 20 cm depth.

α^0	$N\gamma$	N_c	N_{ca}	H, N
15	17.0	9.6	10.0	932
20	12.0	9.7	5.0	892
25	10.5	9.8	2.6	903
30	9.1	10.2	2.1	970

In this instance, the theoretical model has predicted that a rake angle between 20 and 25 degrees will provide the least draft force in the type of soil represented.

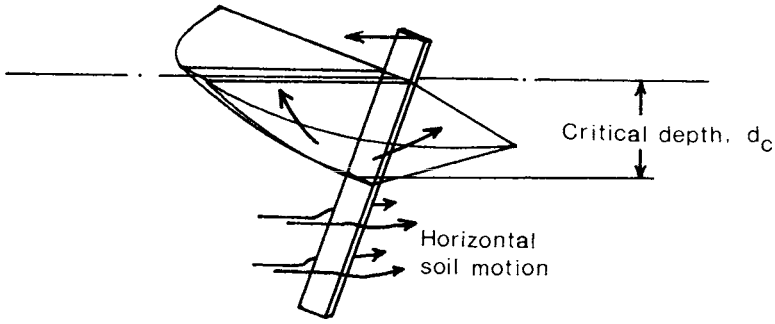

Fig. 8.12. The occurrence of a critical depth in soil cutting. Below the critical depth, soil is not lifted upwards but moves horizontally around the tool.

8.1.3. Critical depth

The models of soil cutting, whether they be in two or three dimensions, have all assumed that soil is moved upwards over the entire depth range of the cutting tool (e.g. Fig. 8.1, 8.4 and 8.5). It has been observed that this is not always the case, especially in instances where a narrow cutting implement is operating at depth in a plastic soil. Zelenin (1950) and Kostritsyn (1956) both reported observations of this phenomenon which has come to be called 'critical depth', and Kostritsyn suggested from his experience that this depth is usually seven to eight times the tool width.

Fig. 8.12 illustrates schematically what occurs in the soil when a critical depth is present. The critical depth, d_c, can be defined approximately at the point below which soil is moved by a tool principally along horizontal lines. Above the critical depth, soil moves horizontally and upwards as in the previous models. Reports of the value of the critical depth have varied considerably depending on the type of soil in question. O'Callaghan and Farrelly (1964) observed critical depths of the same order of magnitude as the blade width when testing vertical steel blades in plastic sandy and clay loam soils. Using similar tools, however, Miller (1971) found critical depths up to 14 times the blade width dimension in stiff sand, and Godwin (1974) observed critical depth to blade width ratios to vary from 10 to 16, depending on the blade rake angle in a friable sandy loam.

In 1974, Godwin also postulated a model with which the regime of forces in the soil can be analyzed when a critical depth is present. As depicted in Fig. 8.13, soil is moved to the sides of the tool at depths geater than the critical one, along logarthmic spiral paths, similar to the deep foundation failure model postulated by Meyerhof (1951). The effective end of the spirals along which soil is moved is located at an angle ϕ behind the blade face. At the back of the tool, a horizontal pressure is assumed to act on the soil, and is calculated as 'at rest' earthpressure, $p_0=\gamma K_0 = \gamma z(1-\sin\phi)$. The Meyerhof (1951) formula is then used to calculate the horizontal pressure, q', acting on the tool face below the critical depth.

$$q' = cN'_c + p_o N'_q = cN'_c + \gamma z K_o N'_q \tag{8.10}$$

$$N'_q = \left[\frac{1 + \sin\phi}{1 - \sin\phi}\right] e^{2(\pi/2 + \phi)\tan\phi} \tag{8.11}$$

$$N'_c = \cot\phi \left[\left[\frac{1 + \sin\phi}{1 - \sin\phi}\right] e^{2(\pi/2 + \phi)\tan\phi} - 1\right] \tag{8.12}$$

The integration of this horizontal pressure from the critical depth down to the bottom of the blade yields the total force Q acting over this portion of the tool.

$$Q = \left[cN'_c(d - d_c) + \frac{\gamma}{2} K_o N'_q (d^2 - d_c^2)\right] w \tag{8.13}$$

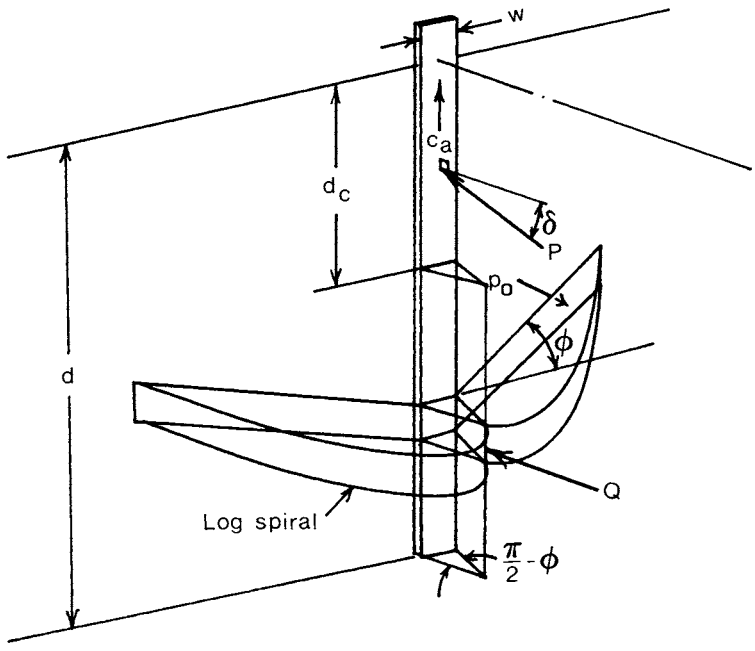

Fig. 8.13. The force model for critical depth failure of Godwin (1974).

For the force P on that part of a blade above the critical depth, the three dimensional model of Section 8.1.2 is used. Thus the total horizontal draft required to move the implement is the sum of Q below the critical depth, and H_1 above it as shown below.

$$H = Q + H_1 = Q + P\sin(\alpha + \delta) + c_a d_c w \cot\alpha \qquad (8.14)$$

In addition, Godwin (1974) noted that the location of a critical depth could be predicted theoretically using the above model. If trial values of critical depth are chosen, the forces P and Q acting above and below this depth can be found. Combining the terms as in Eqn. 8.14 gives the total estimated draft force of the tool. Following the principle of soil failing on the path of least resistance, it is logical that the critical depth is that which results in the smallest overall draft for the tool. Thus, the trial critical depth which gives the lowest total draft, H, is the likely one.

Problem 8.5.

Suppose that a steel flat blade with a width of 5 cm operates at 100 cm depth in a loam soil with properties γ=19.6kN/m^3, c=30 kPa, c_a=5 kPa, ϕ=35^0 and δ=23.3^0. Find if a critical depth occurs at tool rake angles of 90, 60 and 30^0.

Table 8.3 shows the calculations for H using different trial critical depths, and at the three different rake angles of the flat blade. Eqn. 8.8 is used to calculate H_1 for the draft arising above the critical depth, and Eqn. 8.13 for Q below the critical depth. In Table 8.3, a critical depth is found for each of the three rake angles in the case of this example cutting blade.

As Godwin (1974) noted, the critical depth changes with rake angle. Fig. 8.14 shows this change graphically for the preceding examples with the curve which is labelled ϕ=35^0. Example curves have been drawn also in Fig. 8.11 for friction angles of 30^0 and 40^0, with the soil to metal angle of friction being two thirds of ϕ in each case. These theoretical results match the aspects of experimental observations, insofar as the critical depth decreases with α from the horizontal, and increases also with ϕ.

TABLE 8.3. Example trial critical depths in the calculation of draft forces on a flat steel blade operating at 100 cm depth.

K_o = 0.426, N'_q = 78.33, N'_c = 110.44

α^0	d_c,cm	Q,kN	d_c/w	N_γ	N_c	N_{ca}	H_1,kN	$H = H_1+Q$,kN
90	5	173.7	2	15.7	45.5	3.5	3.2	176.5
	7	170.3	1.4	19.0	54	3.6	5.4	175.7
	10	165.3	2	26.5	79	3.8	11.2	176.5
	15	156.8	3	36	109	3.9	23.4	180.2
60	30	130.8	6	27.5	38	2.1	19.6	150.4
	40	113.1	8	23	51	2.2	34.2	147.3
	45	102.5	9	25	57	2.2	43.5	146.0
	50	95.1	10	28	61	2.2	52.6	147.7
30	60	76.7	12	27	34	2.8	32.6	109.3
	70	58.0	14	33	41	2.8	40.0	98.0
	80	39.0	16	36	46	2.9	62.9	101.9

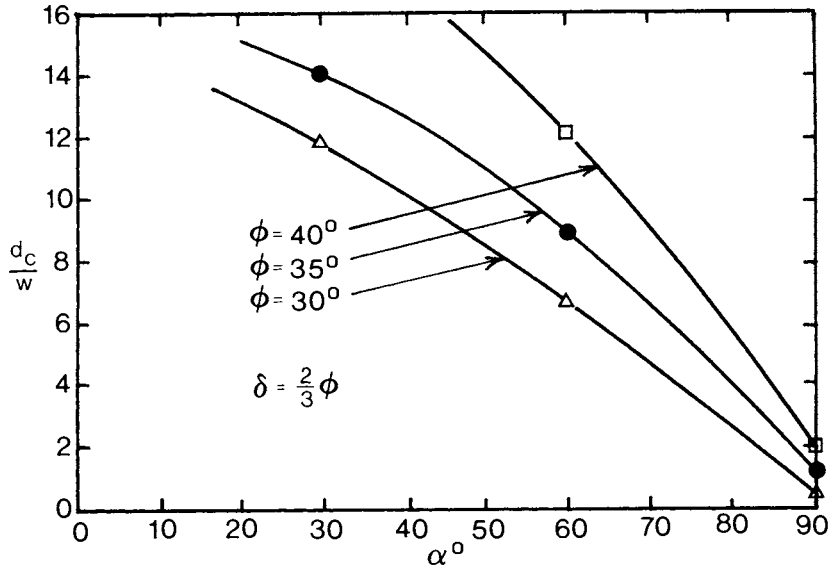

Fig. 8.14. Critical depth ratios for various rake and friction angles.

As Table 8.3 demonstrates, the draft force does not change a great deal because of the existence of a critical depth. However, the volume of soil which is lifted by a cutting tool (rather than compressed to the sides) changes considerably as indicated in Fig. 8.12. This is an important consideration for the loosening of soils in the tillage of agricultural land or other purposes.

When a narrow high rake angle soil cutting tool does exhibit the critical depth behavior, modifications can be made to the implement design in order to reduce or eliminate the effect in the same soil. The following problem gives an example of how this can be accomplished.

Problem 8.6. A narrow vertical tool operating at 100 cm depth is shown in Fig. 8.15(a). If the soil strength properties are taken the same as in Problem 8.5, Table 8.3 indicates that the illustrated tool will have a critical depth of about 7 cm. Fig. 8.15(b) shows an attachment which can be made to the original tool design. A flat blade has been fixed to the base of the vertical leg like a wing, with a rake angle of 30^0 to the horizontal, and a width of 10 cm.

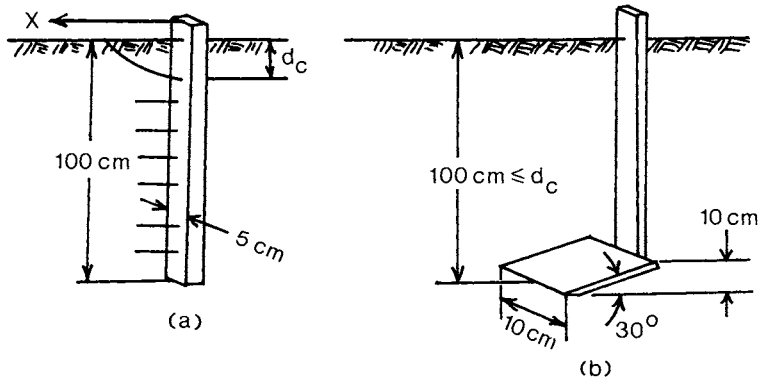

Fig. 8.15. A narrow leg with and without a wing, Problem 8.6.

The 'lift' or height of the wing should be at least 10 cm for a 100 cm operating depth in order to ensure full failing of the soil by the wing to the surface (McKyes, 1985). How much will the critical depth be increased by this attachment?

To check for a critical depth with this new design, the calculations are repeated as in Table 8.3.

Trial d_c = 80 cm, Q = 78.0 kN, H_1 + Q = 142.4 kN

Trial d_c = 90 cm, Q = 39.4 kN, H_1 + Q = 123.7 kN

Trial d_c = 100 cm, Q = 0, H_1 + Q = 107.5 kN

In Table 8.3, the draft of the unmodified vertical tool of Fig. 8.15(a) was estimated as 175.7 kN with a critical depth at approximately 7 cm. The calculations above indicate that there is no critical depth likely with the new design, since the minimum draft is calculated with the critical depth at least equal to the tool depth. In addition, theoretically, the required draft force of the tool has been reduced by some 39%.

The elimination of critical depth illustrated in Problem 8.6 occurred in the theoretical analysis because, firstly, the new design is wider, thus doubling a critical depth for the same critical depth to width ratio. Secondly, the effective rake angle of the cutting tool has been altered to 30^0 rather than 90^0. Fig. 8.14 shows that theoretically this can increase the critical depth to width ratio by up to ten times. One must conclude that the design shown in

Fig. 8.15(b) is superior in theory from the points of view of cutting efficiency and depth of soil lifting. Some experimental work performed on soil loosening by cutting tools of different geometries is given further in this Chapter.

8.2. VOLUME OF SOIL CUT

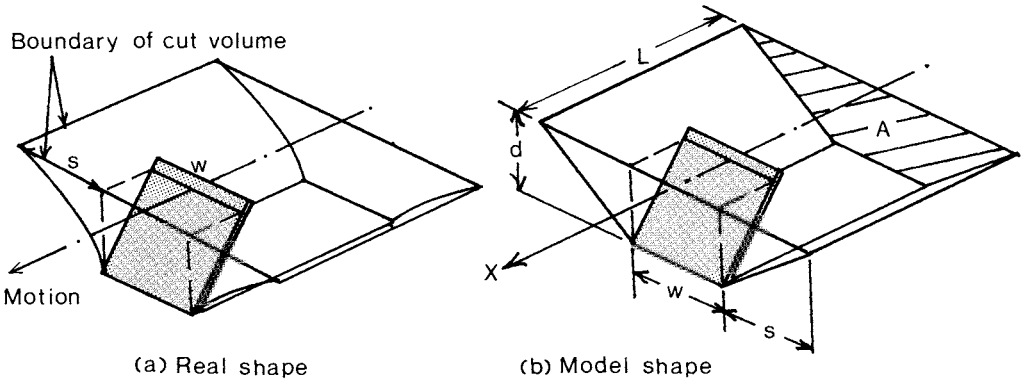

Fig. 8.16. (a) Observed cross sectional area of soil disturbed by a narrow tool and (b) the shape predicted by the three dimensional wedge model.

The volume of soil cut by an earthmoving or tillage tool is defined as the volume per unit tool travel distance of soil which is moved appreciably from its original position, and changed in density or structure. Fig. 8.16(a) illustrates the shape of soil volume typically moved or disturbed by a symmetrical cutting tool, and Fig. 8.16(b) shows how such a volume is estimated by the mechanical models of Godwin (1974) (Godwin and Spoor, 1977) or McKyes and Ali (1977). The assumption in Fig. 8.16(b) is that negligible disturbance is imparted to the soil outside of the range of soil failure, and that the cut volume boundaries are straight lines. Noting that the volume cut per unit travel distance is the same as the cross sectional area of soil cut, the mechanical models would predict the following cross sectional areas, A, of soil disturbed by a typical implement having width, w, and depth, d.

$$A = (w + s)d \tag{8.15}$$

If a cutting tool is narrow, and a critical depth, d_c, occurs below which soil is not lifted appreciably, then d_c should be used in Eqn. 8.15 rather than

the total tool depth, d.

Because real cross sectional boundaries of soil cut are curved, as shown in Fig. 8.16(a), the model shape with straight sides is bound to overestimate the volume for the same side distance, s, by a small amount. Nonetheless, the models are useful for predicting the trends of cut volume and loosening efficiency as blade design parameters are altered. For example, the volume of soil cut per unit input energy could be estimated as a function of varying geometrical parameters of cutting tools. These quantities can evaluate the relative efficiency of different implement designs for the purpose of moving soil. It can be noted that volume of soil cut per unit input energy is the same as the inverse of the of the average normal pressure applied by a tool to the vertical cross sectional area, A/H, as shown in the equation below, in which X is the distance travelled.

$$\frac{\text{Volume cut}}{\text{Energy input}} = \frac{AX}{HX} = \frac{A}{H} \qquad (8.16)$$

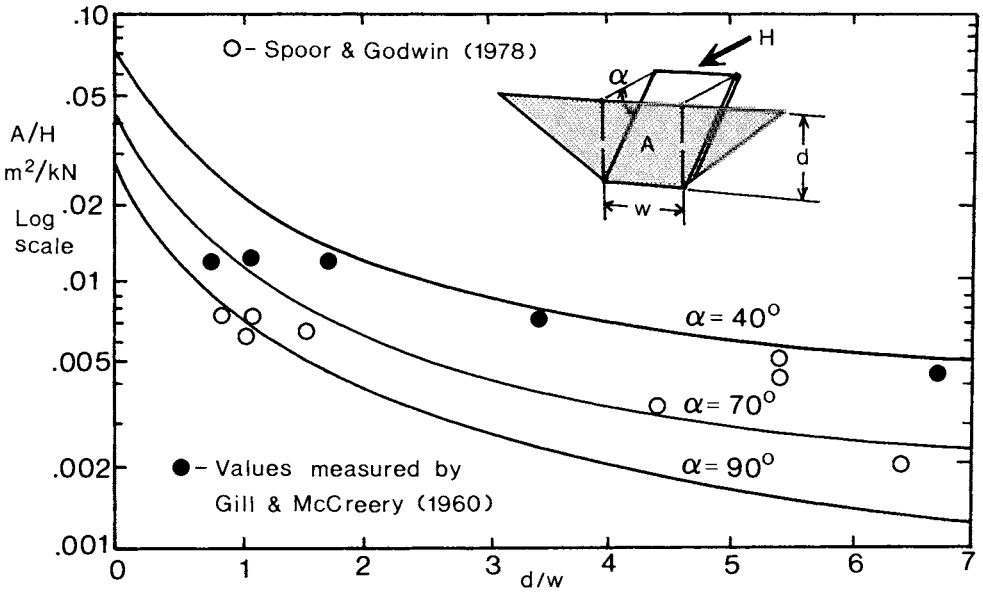

Fig. 8.17. Wedge model theoretical curves of area of soil disturbed per draft force unit, compared to measurements by Spoor and Godwin (1978) and Gill and McCreery (1960).

As an example, the soil volume cut per unit energy input, or A/H, has been calculated and plotted in Fig. 8.17 for a flat blade having a depth of operation of 30 cm and three different rake angles, working in a loam soil with γ=19.6 kN/m^3, c=20 kPa, c_a=0, ϕ=30^0 and δ=20^0 using the above theories. The design parameters are the depth to width of the blade on the graph abscissa, and the three rake angles. Two trends are evident in the figure. Firstly, the tool is much less efficient in terms of specific energy input as the depth to width, or slenderness of the blade increases. In addition, higher rake angles are less efficient than lower ones (at least down to 20^0 or so). These theoretical results do not indicate differences in the quality of soil loosening performed in terms of changes in soil structure. Nonetheless, they demonstrate that wider tools of lower rake angle are more efficient in moving a volume of soil for a specific energy expenditure.

Also in Fig. 8.17 are plotted some experimental measurements conducted by Gill and McCreery (1960) using moldboard plows cut to different widths in a Decatur silty clay loam at an average 14% moisture content by weight.

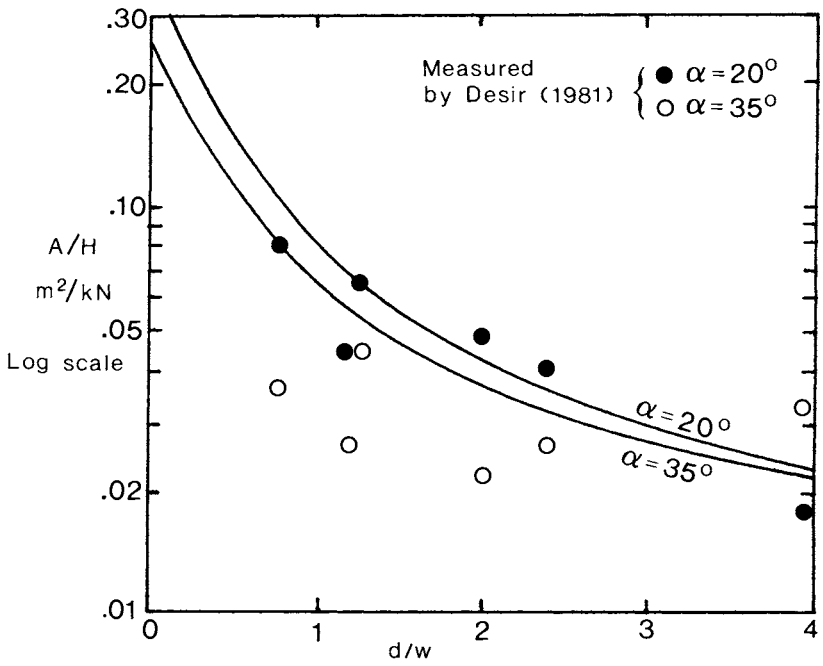

Fig. 8.18. Field test results of soil area cut by narrow blades per draft force, compared to theoretical predictions.

They did not provide the strength properties of that soil, nor the effective rake angle of the plows employed. Nevertheless, their measured results of area of soil cut per unit draft force generally lie close to the 40^0 rake angle theoretical curve of Fig. 8.17.

In Fig. 8.17 experimental results of Spoor and Godwin (1978) are shown too, measured on conventional subsoilers, winged subsoilers and a chisel shank in clay soils. The values of area of soil disturbed per unit draft force lie within the range of predicted quantities, but generally lower than those of Gill and McCreery, possibly due to a stronger soil in the former case.

Other measurements were performed in a field of clay loam by Desir (1981), (McKyes and Desir, 1984) at depths of 15 to 25 cm, and the soil strength properties were measured independently with a sheargraph (ref. Section 2.7). Flat steel blades of varying width and rake angles were operated at a horizontal speed of 1.4 m/s, and the draft measured by a hydraulic cylinder dynamometer connected to a pressure gauge. After each run, soil was excavated by hand and the area of soil disturbed by the tools measured. The average soil properties at the time of the field tests were m.c.=22%, γ=14.5 kN/m^3, c=6.3 kPa, c_a=2.2 kPa, $\phi=36^0$ and $\delta=23.3^0$. Theoretical model curves for cutting efficiency (A/H) have been constructed in Fig. 8.18 for these soil properties, and the two rake angles and varying depth to width ratios tested.

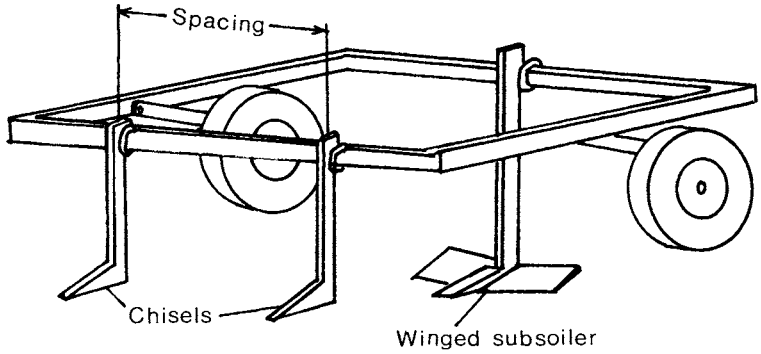

Fig. 8.19. A winged subsoiler preceeded by two chisels (Spoor and Godwin, 1978).

The measured results are quite close to the theoretical predictions for the 20 blade rake angle, but are generally lower than predictions for the 35^0 tool. The trends of changes in volume cutting efficiency with varying rake angle and slenderness ratio predicted by the mechanical model are confirmed by these experimental field results in any event.

Another possibility for improving soil cutting efficiency is to arrange implements to follow one another at different depths. Spoor and Godwin (1978) tested such a system in a friable clay soil. As pictured in Fig. 8.19, the combination comprised two chisel plow shanks followed by a deeper winged subsoiler. The subsoiler had a total width of 30 cm, wings at a rake angle of 22^0 and a depth of operation of 40 cm. The chisels were 8 cm wide with a tip rake angle of 20^0 and were varied in both depth and spacing as indicated in Table 8.4 below. There was no great difference in the draft requirement of the system no matter what the chisel depths or spacing. However, the area disturbed by the tool combination increased markedly with both chisel depth and spacing. The best configuration from the point of view of efficiency was that having the widest chisel spacing and depth, and was about 77% more efficient in the volume of soil cut per unit draft than the subsoiler shank operated alone.

TABLE 8.4. Draft forces and disturbed soil areas for the combination of two chisels followed by a deeper subsoiler shank in a friable clay (Spoor and Godwin, 1978).

Chisel spacing cm	Chisel depth cm	Total draft kN	Subsoiler draft kN	Draft of chisels kN	Area of soil disturbed m^2	Specific resistance kN/m^2
Subsoiler alone		23.94	23.94	0	0.242	99
50	16	21.41	16.18	5.23	0.238	90
50	24	20.86	12.25	8.61	0.283	74
100	16	20.80	15.23	5.57	0.360	58
100	24	23.48	14.84	8.64	0.418	56

Problem 8.7. A flat chisel blade is 63.5 mm wide and operates 200 mm deep in a clay loam field having $\gamma = 15.7$ kN/m^3, $\phi = 30^0$, $\delta = 23.3^0$, cohesion 20 kPa and adhesion 6 kPa. If there is an option to operate the chisel at rake angles of 30 or 60^0, which would provide the best cutting efficiency in terms of least draft force per unit area of soil cut?

Using Eqn. 8.9 for the $N\gamma$ passive earthpressure term, the minimization of this term gives the soil wedge angle β as follows, with a depth to width ratio of 200/63.5. The area of soil cut and the draft force are calculated using Eqn. 8.15, 8.8 and 8.2.

$$N\gamma = \frac{\frac{1}{2}(\cot\alpha + \cot\beta)\left[1 + \frac{2d}{3w}\sqrt{\cot^2\beta + 2\cot\alpha\cot\beta}\right]\sin(\alpha+\delta)}{\sin(\alpha+\beta+\delta+\phi)}$$

$$s = d\sqrt{\cot^2\beta + 2\cot\alpha\cot\beta}$$

$$H = P\sin(\alpha+\delta) + c_a dw\cot\alpha = (\gamma d^2 N\gamma + cdN_c + c_a dN_{ca})w\sin(\alpha+\delta) + c_a dw\cot\alpha$$

α^0	β^0	$N\gamma$	N_c	N_{ca}	A=(w+s)d, m^2	H, kN	H/A, kPa
30	61	9.21	10.46	2.25	0.0724	2.69	37.2
60	38.5	10.40	21.66	1.95	0.0824	3.34	40.6

The smaller rake angle yields less draft force per unit area of soil cut, and therefore the higher cutting efficiency by about 10%.

8.3. SOIL LOOSENING

The cutting efficiency of soils, as defined above, involves only the volume of soil cut per unit energy input, but not the considerations of change in soil density or structure. In agricultural applications, the change in soil volume and structure are important aspects of the physical fertility of soil for crop growth. Even in earthmoving operations, the change in soil density during excavation is of interest because of the resulting volume of soil to be transported. The experience of the earthmoving industry in this regard is reflected by Table 8.5 below. This table gives the average in situ, or 'bank' densities of some typical soils, together with their new unit masses after they have been excavated completely and redeposited into a truck or trailer. The swell factor is defined as the percent increase in soil volume above the original.

$$\text{Swell factor} = (V_f/V_o - 1) \times 100\% = \left(\frac{\gamma_o - \gamma_f}{\gamma_f}\right) \times 100\% \qquad (8.16)$$

where V_f = the volume of soil after cutting,
V_0 = the original soil volume,
γ_f = the soil density after cutting,
γ_0 = the original in situ soil density.

Table 8.5 serves only as a rough guideline to expected degrees of soil loosening during soil cutting. The change in soil density during the cutting process depends not only on the original soil condition, but also on the geometry of the cutting implement and its speed of operation. Desir (1981),

TABLE 8.5. Guideline values of in situ and excavated densities for different soils from industry experience (Caterpillar Co., 1981).

Material	γ_0 , kN/m^3	γ_f , kN/m^3	Swell factor %
Dry clay	18.0	14.5	24
Wet clay	20.4	16.3	25
Wet 'earth'	19.8	15.7	26
Dry loose sand	15.7	13.9	13
Wet sand	20.4	18.0	13
Topsoil	13.4	9.3	44

(McKyes and Desir, 1984), conducted field tests on clay and loam soils at different moisture contents using flat blades having varying widths and rake angles. He observed that the degree of soil loosening in both soil types was increased with;

- increasing blade rake angle from 20^0 to 35^0,
- decreasing blade width from 1.33 to 0.25 times the depth, and
- decreasing moisture content from 44 to 40% in the clay, and from 30 to 22% in the loam.

The observed values of soil swell factor varied from 30 to 100% for the clay, and from 25 to 70% for the loam, within the ranges of tool geometry and soil moisture contents indicated above. These swell factors attain larger values than those of Table 8.5, but in the field tests performed for these measurements, the soil was left untouched after the passage of the cutting blades. The earthmoving guidelines in the Table imply that excavated soil has been dropped into a truck or trailer body from a height of two to three metres, and to a load depth of 2 m or so, which presumably entails some soil recompaction from the excavated volume.

Nonetheless, these field results demonstrate that the particular state of the soil, especially humidity, and the geometry of the cutting tool have a profound effect on the final soil density. When it is desired to simply lift soil as efficiently as possible, then the designer should aim for a wide cutting implement ($d/w<1$) with a low rake angle of 20 to 30^0. If it is important to produce a loose structure in the excavated soil, then a narrower tool ($d/w>2$) should be utilized with a rake angle greater than 45^0.

Another aspect of the quality of soil structure produced by the mechanical action of cutting tools is the clod sizes. Gill and McCreery (1960) have shown here again that a narrower implement breaks up the soil structure more than a wider one. In tests using 17 cm deep moldboard plow shapes varying from 2.5 to 20 cm in width, the clod mean weight diameter of the plowed soil increased from 3.7 to 21.9 cm, that is in the same order of magnitude as the width of the tools. And, although the widest plow they used required about

3.5 times the draft force of the narrowest, and cut eight times as much soil volume, the increase in volume cutting efficiency in the latter case was offset by the equivalent larger energy input in terms of soil structural breakup. In fact, comparing the clod mean weight diameters to those developed in drop-shatter tests, it was estimated that the narrower plow was more than five times as efficient in applying specific clod breakup energy to the soil structure than the wider tool. This observation complements that mentioned above concerning the superior loosening of soils by narrower tools.

8.4. PROBLEMS

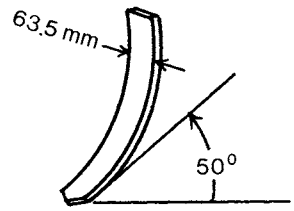

Fig. 8.20. Chisel plow in Problem 8.8.

8.8. Fig. 8.20 shows a steel chisel plow with an effective rake angle of 50 degrees to the horizontal. The chisel has a width of 63.5 mm and operates in a clay loam soil having $c = 20$ kPa, $c_a = 6$ kPa, $\phi = 30^0$, $\delta = 20^0$ on steel and $\gamma = 14.7$ kN/m^3. What will be the draft force of this implement at operating depths of (a) 15 cm, and (b) 30 cm?

Answer: (a) $H = 1.9$ kN, (b) $H = 7.2$ kN.

8.9. For the same chisel plow and soil as in Problem 8.8, how deep can the implement be operated before the critical depth phenomenon will be encountered?

Answer: $d = 0.55$ m.

8.10. A flat road grader blade is 3 m long and to be operated in soil at a depth of 10 cm. What would be the rake angles of this blade to provide the minimum horizontal draft forces in (a) a sand having $\gamma = 14.7$ kN/m^3, $c = 0$, $\phi = 35^0$ and $\delta = 23^0$, and (b) a clay with $\gamma = 14.7$ kN/m^3, $c = 30$ kPa, $c_a = 5$ kPa, $\phi = 30^0$ and $\delta = 20^0$?

Answer: (a) $\alpha = 27^0$, (b) $\alpha = 9^0$.

8.11. Fig. 8.21 depicts an excavating bucket with a width of 1.5 m and an effective attack angle of 30^0 to the horizontal. The maximum horizontal thrust or 'breakout force' of the machine, H, is 50 kN. In a soil with γ = 15.7 kN/m^3, c = 30 kPa, c_a = 9 kPa, ϕ = 30^0 and δ = 20^0, find the maximum depth, d, which this bucket can cut. (Note that the soil moves inside the bucket in essentially a two dimensional fashion.)

Answer: d = 0.65 m.

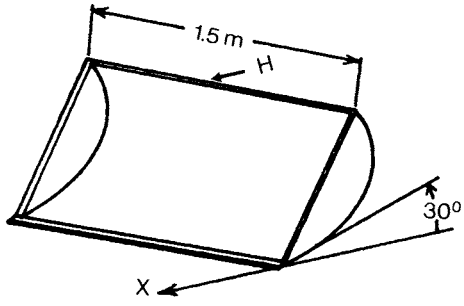

Fig. 8.21. Excavating bucket in Problem 8.11.

8.12. A 100 kW tractor has a maximum draft force of 50 kN on a particular field. The soil has properties γ = 15.7 kN/m^3, c = 25 kPa, c_a = 5 kPa on steel, ϕ = 30^0 and δ = 20^0. How many chisels of width 63.5 mm, rake angle 60 degrees and operating depth 150 mm can the tractor pull?

Answer: 15 chisels.

8.13. A flat steel soil cutting tool is 30 cm wide and operates at a 30 cm depth in a loam soil with γ= 16.7 kN/m^3, c = 15 kPa, c_a = 4 kPa, ϕ = 35^0 and δ = 23^0. At rake angles of (a) 30^0 and (b) 60^0, how much cross sectional area of soil will be cut by this tool, and what is the energy input for both per unit volume of soil cut?

Answer: (a) A=0.19 m^2, H/A=36.6 kPa, (b) A=0.21 m^2, H/A=71.6 kPa.

8.14 The tractor back blade illustrated in Fig. 8.22 weighs 1500 N, is 210 cm wide and is used to scrape soil on a clay field with soil properties γ = 15.7 kN/m^3, c = 25 kPa, c_a = 0, ϕ = 35^0 and δ = 23^0. With an effective rake angle of 80^0, how deep can the blade cut this soil with the weight which it has? What would the draft force be at this depth?

Answer: d = 2 cm; H = 6.5 kN.

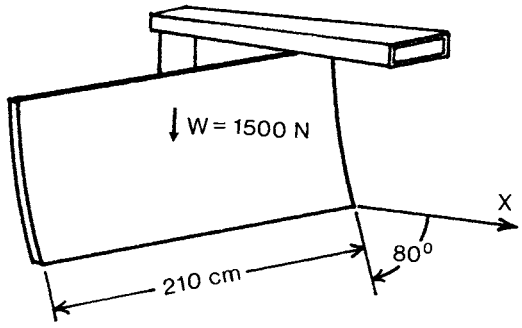

Fig. 8.22. Tractor back blade of Problem 8.14.

Chapter 9. Soil compaction

9.1. COMPACTION FOR EARTHWORK CONSTRUCTION

When soil is excavated and replaced in a new location for the construction of foundation subbases, roads, dams or backfills as examples, it is usually necessary to compact the material in order to improve its mechanical properties. The soil strength and impermeability to water flow both increase considerably with applied compactive effort, and these enhanced qualities are most often desirable in earthwork designs. The extent to which compaction and dry mass density can alter soil physical properties is indicated in Table 9.1.

TABLE 9.1. The effect of soil dry density on some mechanical properties.

Property	Soil type	Density range t/m^3	Property range	Source
c	Clay	0.84-1.89	0-282 kPa	1
ϕ	Clay	0.84-1.89	$0-37^0$	1
ϕ	Sand	1.74-2.11	$18-55^0$	1
ϕ	Sand	1.60-1.72	$27-32^0$	2
Penetration resistance	Clay	0.84-1.89	0-8250 kPa	1
Undrained C	Clay	1.02-1.25	5-40 kPa	3
k_c	Yolo loam	1.26-1.55	980-5200 kPa/m^{n-1}	4
k_ϕ	Sandy loam	1.48-1.73	2470-4800 kPa/m^n	4
Hydraulic	Beach sand	1.40-1.66	0.05-0.02 cm/s	2
conductivity	Clay	1.15-1.55	$2700-100x10^{-6}$ cm/s	5
"	Silt	1.43-1.66	$60-0.6x10^{-6}$ cm/s	2
"	Boston silt	1.27-1.51	$1-0.002x10^{-6}$ cm/s	6

1. Proctor (1948)
2. Taylor (1948)
3. Graecan (1960)
4. Chancellor and Schmidt (1962)
5. Rowles (1948)
6. Lambe and Whitman (1979)

The compaction test, which was described in Section 2.6.4, is usually employed to characterize the compaction behavior of a particular soil, and the design specifications for construction are based on the results of this test. For example, the water content at which field compaction is to be conducted can be specified within a certain range around the 'optimum' which was found

in the appropriate compaction test, and the final soil dry density specification can be a certain percentage of the experimental maximum density, typically 95% or more.

Problem 9.1. Laboratory results from a modified Proctor compaction test performed on a clay soil are shown below.

Soil water content, %	10	12.5	15	17.5	20	22.5
Dry mass density, t/m^3	1.60	1.68	1.74	1.72	1.65	1.60

At what range of moisture content should this soil be compacted to ensure that the resulting density will be 98% of the maximum, assuming that the compactive effort is the same as that in the test?

The compaction test results are plotted as dry density versus molding water content in Fig. 9.1. The range of moisture contents is that for which the compaction curve lies above the required dry mass density level, which is 98% x 1.75 = 1.715 t/m^3, and is 14 to 17.5%.

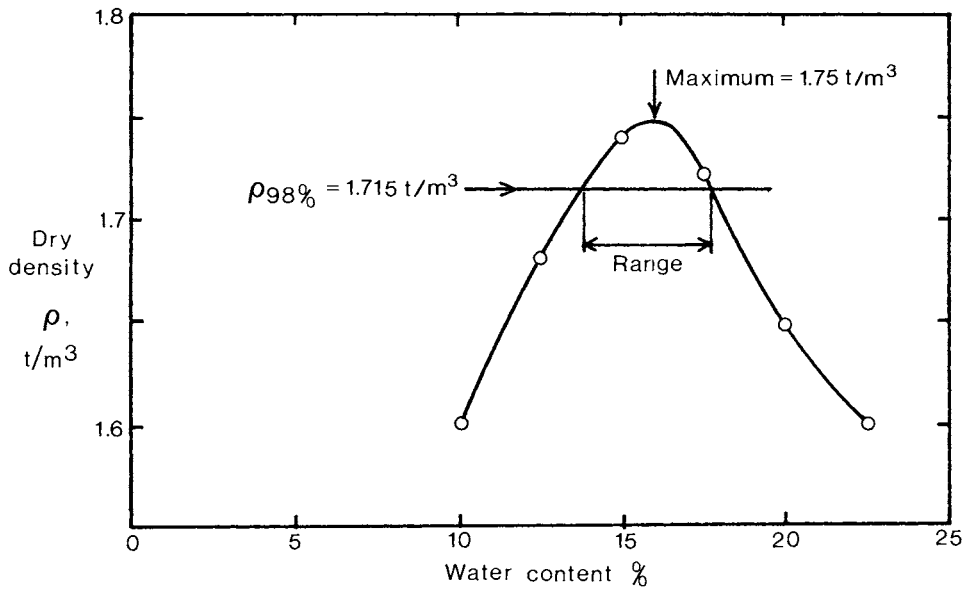

Fig. 9.1. Compaction curve results for Problem 9.1.

It has been found that the compaction of unsaturated fine grained soils, as measured by the change in dry density, increases proportionally with the logarithm of applied pressure (Vanden Berg, 1966; Raghavan et al., 1977a). Other factors include the amount of shear strain suffered by the soil during compression, and the number of repetitions of applied pressure. The equation below summarizes these effects, and that of soil moisture content as well.

$$\rho_{dry} = \rho_0 + A \log[Np(1 + S\%)/p_0] + B \log(w\%) \qquad (9.1)$$

where ρ_{dry} = compacted dry mass density
ρ_0 = initial dry density before compaction
A, B = soil constants
N = number of repeated applications of pressure
p = applied compaction pressure
S = wheelslip = slip speed divided by wheel or track speed
p_0 = soil precompaction pressure
w = soil water content by mass (less than the optimum).

The constant B is a measure of the sensitivity of the compactibility of a soil to increases in moisture content up to the optimum water content. Beyond the optimum moisture content, B will have a negative value. Examples of some of the constants in Eqn. 9.1 are given in Table 9.2 below.

TABLE 9.2. Example values of constants in the compaction prediction Eqn. 9.1.

Soil	ρ_0, t/m^3	p_0, kPa	A, t/m^3	B, t/m^3	Source
Ste. Rosalie clay	0.7	3	0.13	0.4	1
Loamy sand	1.0	7	0.17	0.3	1
Sandy loam	0.8	7	0.17	0.5	1
Yolo silt loam	1.0	7	0.13	1.1	2
Heavy loamy clay	1.1	7	0.17	0.5	2
Clay	1.2	7	0.14	0.3-0.7	3
Sandy loam	1.3	7	0.17	0.5	3

1. Raghavan et al., (1977a, b)
2. Soehne (1958)
3. Hovanesian (1958)

Problem 9.2. A clay loam soil has an average dry density of 1.1 t/m^3 from 0 to 30 cm depth, and a moisture content of 25% by weight. If the constants A and B in Eqn. 9.1 are 0.15 and 0.3 t/m3, and the 'precompaction pressure' is 7 kPa, what will be the changes in soil density under the wheels of a two wheel drive tractor with a ground pressure of 60 kPa when it passes (a) once

and (b) twice over the same track with negligible slip?

$$\rho_{dry} - \rho_o = [0.15 \log(Nx60/7) + 0.3 \log(25)]\,t/m^3$$

$$= \left[\begin{Bmatrix}0.14\\0.19\end{Bmatrix} + 0.42\right] t/m^3 = \underline{\begin{Bmatrix}0.56\\0.80\end{Bmatrix}\ t/m^3}$$

In the case of granular soils, including gravels and coarse sands, it has been found that the shape of the grain size distribution curve affects compaction stability. This stability refers to the degree of compactness under a given input energy, and the strength of the compacted granular soil. For example, a soil with very low compaction stability is almost impossible to compact into a material suitable for high bearing capacity applications, such as a road surface. Fig. 9.2 shows the range of grain size distributions which are likely to produce stable compacted soils. The maximum size of particle of the stable range in the figure is 25 mm (1 inch). If a particular soil has a maximum grain size different from this size, the shaded area can be slid left or right in the diagram to begin at the appropriate largest diameter.

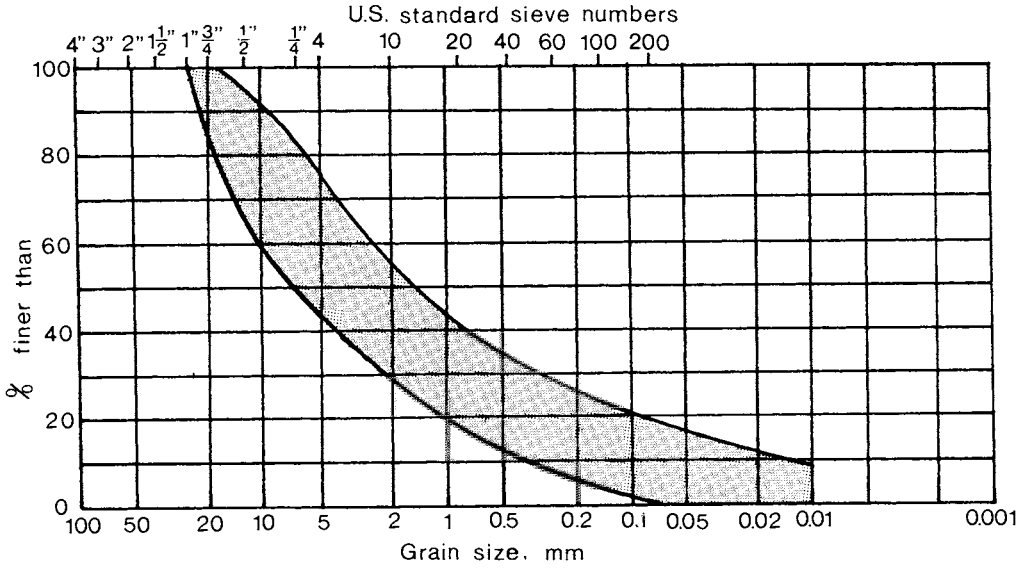

Fig. 9.2. The envelope of grain size distribution for soils which are stable when compacted. The envelope should be shifted horizontally in order that the top left corner corresponds to the maximum soil grain size, if it is different from one inch (25.4 mm).

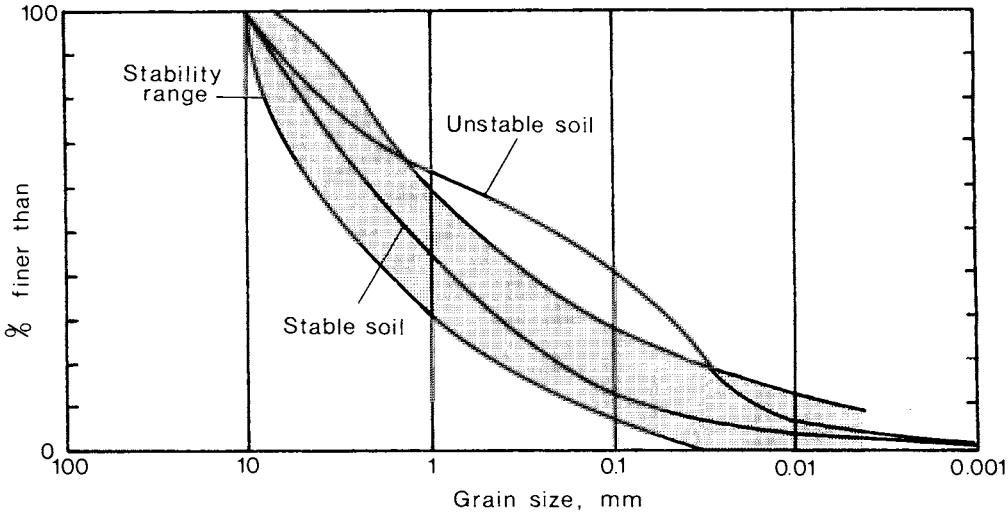

Fig. 9.3. Examples of stable and unstable grain size distributions for two soils having a maximum grain size of 10 mm.

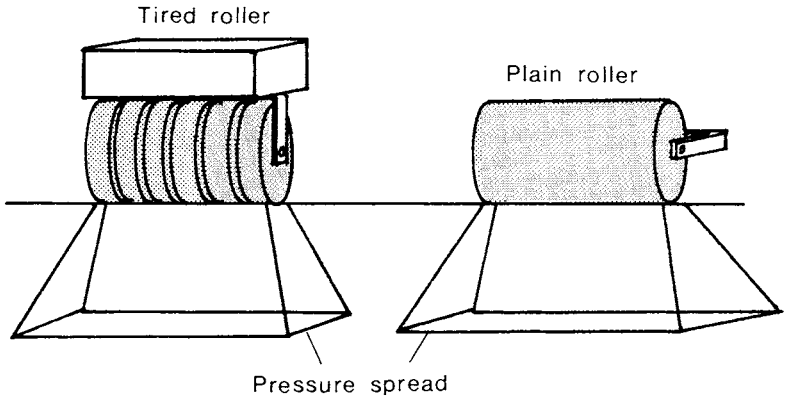

Fig. 9.4. The concept of decrease in vertical pressure with depth below a rubber tired or plain compaction roller.

An example of this procedure is shown in Fig. 9.3 for a soil having 10 mm as the largest grain size, and examples of stable and unstable soil grain size distributions are provided also.

When compaction is conducted in the field, only a limited depth of soil, either in situ or transported, can be compressed effectively at a time. This is because the pressure applied by compaction rollers spreads out with depth, as shown in Fig. 9.4. This limits the depth of soil which receives adequate compaction pressure to between 0.3 and 0.6 m, depending on the size and weight of the compaction device. The rubber tired and plain rollers which are represented in Fig. 9.4 are manufactured in masses up to 180 t. The rubber tired machine is the more effective in compacting sandy and clayey soils, because of the shear action which takes place between individual tires. Rollers with vibrating mechanisms are also available, and are effective on cohesionless soils, but not as useful on clays. Another variation is called the sheeps-foot roller and it has foot shaped knobs protruding from a plain roller to promote shear strains and increased soil compaction.

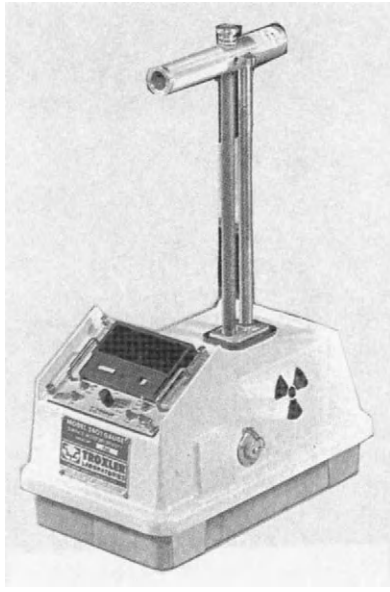

Fig. 9.5. A gamma ray soil density measuring probe (Troxler Inc.).

Whichever compaction device is employed, the soil to be compressed must be within the appropriate range of moisture content, as noted above. This may require the wetting or drying of the material before compaction is conducted. With some soil types, such as a poorly drained silt, and in cool, humid climates, the drying process can be very time consuming, with up to a week or more required to dry a one metre thickness of soil. On some large projects, heating ovens have even been employed to speed up the soil drying process. When the soil is dryer than the optimum range of moisture content specified, water can be added to soil layers by a sprinkler tank, and the soil layer mixed before compaction.

In order to verify that the compaction process has been carried out to the predetermined specifications, nuclear density meters are manufactured to measure the unit wet mass of the final product. An example of such a gauge is shown in Fig. 9.5 with a variable range of measuring depth up to 30 cm. The gamma rays produced by a radioactive source in the probe are attenuated quite proportionally with the total soil density, and the intensity of rays passing through the soil are monitored by a geiger counter in the meter base. Individual readings are averaged over 30 seconds to two minutes, and the new meters available are calibrated to give a direct electronic reading of the total unit mass of the soil over each measuring depth. The moisture content of the soil must also be measured in order to calculate soil dry density using Eqn. 2.36. This can be accomplished either by a neutron moisture gauge, or by drying soil samples in an oven and measuring the weight loss.

9.2. COMPACTION OF AGRICULTURAL SOILS

Table 9.1 indicated increases in soil strength and stiffness, as well as a decrease in hydraulic conductivity with increased compaction. For construction purposes, these effects are desirable for they provide stronger and more impermeable earth structures. To some extent, however, the same effects in soils are the opposite of desirable for agricultural purposes. Increased soil strength prevents the proper growth of crop roots and increases the energy input requirement for soil tillage. In addition, severely reduced hydraulic conductivity can impede proper soil drainage and the flow of water to plant roots. One of the main purposes of soil tillage is the reduction of soil density and the production of a loose soil tilth for water flow and plant growth.

It is difficult to specify what exactly is the optimum dry density for a particular soil and crop combination, because the best density for crop performance depends somewhat on annual climate. In a relatively dry location or year, the best soil density is somewhat higher than for more humid conditions, since water must be conserved better in the dry periods. When there is sufficient or excess precipitation, a looser soil structure aids in the adequate drainage of water from the root zone and prevents the occurrence of waterlogged conditions. Also, water retention is not required to the same degree because of the more frequent advent of rainfall to the soil.

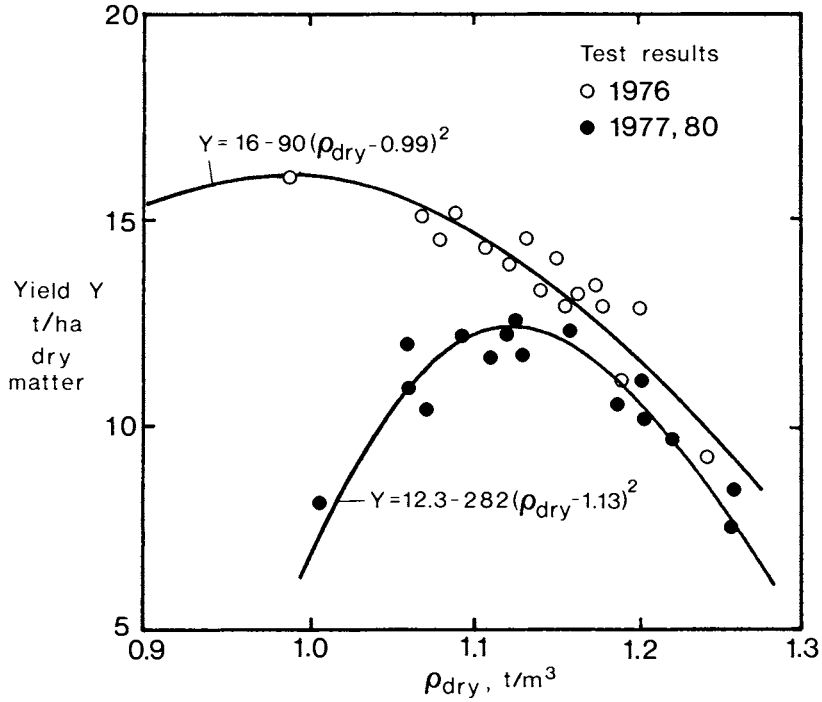

Fig. 9.6. Experimental results of silage corn yields in different years on plots of clay soil having different degrees of compaction (McKyes, 1985).

This effect is shown in Fig. 9.6 where silage corn is the example crop grown on a clay field in seasons of differing rainfall. In the wet year of 1976 (330 mm of rain in June, July and August combined), the optimum soil dry density appears to have been 0.99 t/m^3. However, in the relatively dry years 1977 and 1980 (215 to 220 mm of rain in the same months), a larger density of about 1.13 t/m^3 resulted in higher crop yields than lower or higher densities. At dry densities between 1.15 and 1.25 in this soil, the yield results were of comparable magnitude for all of the years, but were lower than the optimum yields. It can be noted also that the constant of sensitivity to compaction, C, was considerably larger in the drier years 1977 and 1980, 282 (t/ha)/(t/m^3)^2, as compared to 90 in 1976. The optimum yield constant, on the other hand, was higher in 1976 (16 t/ha as opposed to 12.3). In the wetter year, it is apparent that the crop was able to take advantage of the more

plentiful precipitation, and a tighter soil fabric was not required since there were fewer and shorter periods of dryness in that season.

For both dry and wet conditions, the crop yield versus soil density relation of Vomicil (1955) can be applied, but with different constants in each case.

$$Y^* - Y = C\,(\rho_{dry} - \rho^*_{dry})^2 \tag{9.2}$$

where Y^* = the maximum obtainable crop yield
Y = the actual expected crop yield
C = a soil-crop-climate constant
ρ_{dry} = actual soil dry density (10 - 40 cm depth average)
ρ^*_{dry} = optimum dry density for a particular crop and climate.

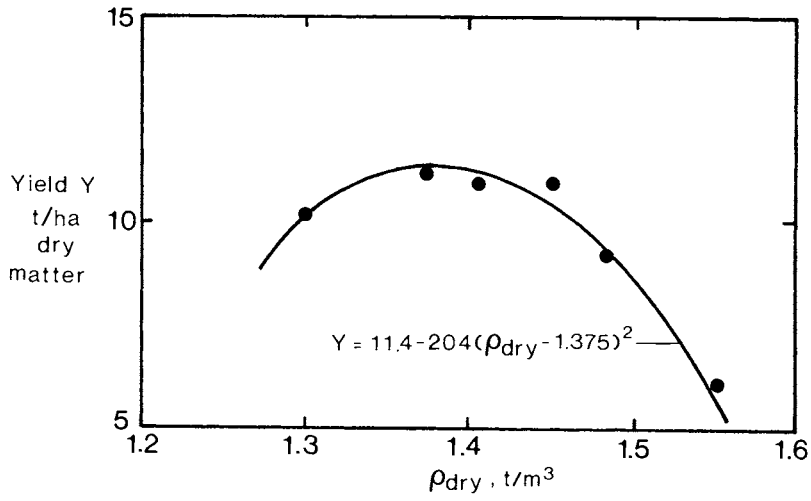

Fig. 9.7. Experimental results of silage corn yield on plots of sandy loam soil having different degrees of compaction (Negi et al., 1981).

Fig. 9.7 shows another case where Vomicil's equation applies well, this time in a sandy loam soil. The shape of the crop yield versus soil dry density curve is the same as that for the clay soil, but the density values are larger due to the higher natural density of the loam soil.

Problem 9.3. The clay field on which the results of Fig. 9.6 were measured is in a location where one of each four years is relatively wet like 1976, and the other three are dry like 1977. What would be the best soil dry density to use each year in order to maximize the yields over the four year period?

The four year yield can be summed as;

$$Y = \left[16 - 90(\rho_{dry}-0.99)^2 + 3\left[12.3 - 282(\rho_{dry}-1.13)^2\right]\right] \text{ t/ha}$$

To find the dry density for the best average yield, Y can be maximized with respect to the density using calculus.

$$\frac{dY}{d\rho_{dry}} = -180\,\rho_{dry} + 178 - 1692\,\rho_{dry} + 1912 = -1872\,\rho_{dry} + 2090 = 0$$

$$\rho_{dry} = \underline{1.12 \text{ t/m}^3}$$

9.3. PROBLEMS

9.4. A standard Proctor compaction test series is performed on a silty clay soil. The compaction mold has an empty mass of 3.50 kg and trimmed volume 1/1060 m^3. After compaction in three layers and weighing of the mold plus soil, samples have been extracted from the top, center and bottom of the mold and combined in one drying can per test. The measurements are as follows.

Mass of mold plus soil, kg	5.27	5.41	5.51	5.53	5.49	5.46
Can plus wet soil, g	74.58	70.95	81.12	76.42	78.38	82.96
Can plus dry soil, g	71.61	66.73	75.13	69.42	70.03	73.27
Mass of drying can, g	20.32	20.40	20.65	20.13	20.38	20.05

What is the optimum moisture content for compaction in this test series, and what is the range of moisture content for 98% compaction?

Answer: w_{opt} = 11%. Range = 10 to 14%.

9.5. A Ste. Rosalie clay soil has the following constants for compaction Eqn. 9.1. ρ_0= 0.7 t/m^3, p_0 = 3 kPa, A = 0.13 t/m^3 and B = 0.4 t/m^3. If the soil is at an average water content of 20% by mass, what will be the resultant dry densities under the wheel tracks of a tractor with 70 kPa ground pressure after (a) one pass, and (b) five passes, with no wheelslip?

Answer: (a) ρ_{dry} = 1.40 t/m^3, (b) ρ_{dry} = 1.49 t/m^3.

9.6 A sandy loam field has the following constants in the compaction Eqn. 9.1; ρ_0= 0.8 t/m^3, p_0 = 7 kPa, A = 0.17 t/m^3 and B = 0.5 t/m^3. Also it has been found in a year of average precipitation to have the following constants in Vomicil's crop yield Eqn. 9.2 for silage corn; ρ^* = 1.375 t/m^3, Y* = 11.4 t/ha and C = 204 (t/ha)/(t/m^3)^2. If the post-tillage machinery activities are estimated to have an average ground pressure effect over the entire field equivalent to 30 kPa, what would be the silage corn yields of the field if these machinery operations were performed with no wheelslip at average topsoil moisture contents of (a) 10% and (b) 20%?

Answer: (a) Y = 11.2 t/ha; (b) Y = 4.4 t/ha.

9.7 A clay field has compaction constants ρ_0 = 0.7 t/m^3, p_0 = 3 kPa, A = 0.15 t/m^3 and B = 0.3 t/m^3. For the production of grain corn in an average year, the constants are ρ^* = 1.2 t/m^3, Y* = 8 t/ha dry matter and C = 200 (t/ha)/(t/m^3)^2. The farm's 80 kW tractor has a mass of 5 t resting on the two rear wheels together, and each rear tire has a field contact area of 0.45 m^2. If the average topsoil moisture content is 20% by weight, and there is little wheelslip, would there be more crop loss in the rear wheel tracks if (a) single rear wheels were used, or (b) dual rear wheels which effectively halve the ground pressure but cover twice the field area per pass?

Answer: Single wheels loss in tracks = 1.3 t/ha; duals loss in tracks = 0.2 t/ha x twice the area = 0.4 t/ha total. Dual wheels cause less loss.

9.8 A sandy gravel from La Grande near James Bay, Quebec is analyzed for grain size distribution using sieves, with the results given below. Is this a suitable material for constructing a road surface? If not, what could be done to improve it?

d, mm:	10	4.7	2.3	1.2	0.4	0.2
% finer:	100	75	65	52	14	2

Answer: Not suitable. Add about 20% by weight of fine sand.

Chapter 10. Geotextiles

10.1. USES OF GEOTEXTILES

Geotextiles are cloth materials, either woven or bonded and non-woven, usually manufactured from polymers and used in geotechnical applications. There are five principal uses of geotextiles in earthworks, namely;

1. Separation of soil materials,
2. Lateral retention of material layers,
3. Spreading of loads in the subsoil,
4. Drainage envelopes and
5. Erosion protection.

The property of geotextiles which allows them to perform the above functions is their tensile strength in two dimensions, a property which is not shared by granular soil materials. When, for example, large particles rest on a layer of a finer grained soil, especially a wet soil with large pore pressures, individual gravel or sand grains can sink into the finer soil thus destroying the original configuration and function of the earthwork design. Fig. 10.1, for instance, shows the installation of a sheet of geotextile between layers of gravel and wet fine grained soil. The geotextile allows water to be transmitted through the boundary, thus permitting drainage and the relief of soil pore pressure. However, by virtue of its tensile strength and size of openings, the geotextile does not permit the entrance of gravel particles down into the subsoil, or pumping of wet fines upwards into the gravel layer. Therefore, the gravel layer remains intact as a roadbase, foundation subbase or whatever function desired. In this manner, a geotextile can replace soil filter materials.

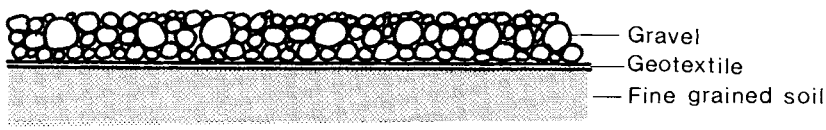

Fig. 10.1. Separation of gravel from a fine grained soil by a geotextile.

In much the same application, geotextiles can assist in the prevention of deformation of a layer of granular soil. Fig. 10.2 illustrates schematically how the tensile strength and friction of the geotextile at the interface with a

granular layer can help to hold the gravel in place, preventing its lateral movement and change in thickness. Furthermore, geotextile sheets aid in the distribution of pressure in a subbase, again because of their tensile strength. The distribution of a load over a greater area reduces the pressure in the subsoil and its concurrent deformations, providing a superior load bearing surface as shown schematically in Fig. 10.3.

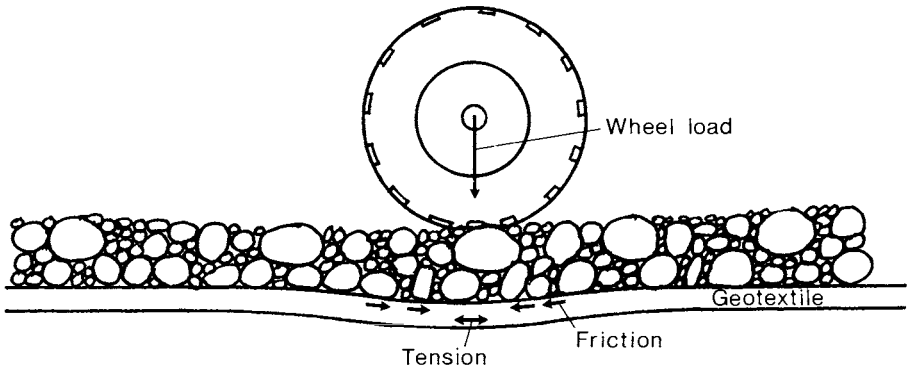

Fig. 10.2. The stabilizing effect of a geotextile on road material arising from friction and tension in the material.

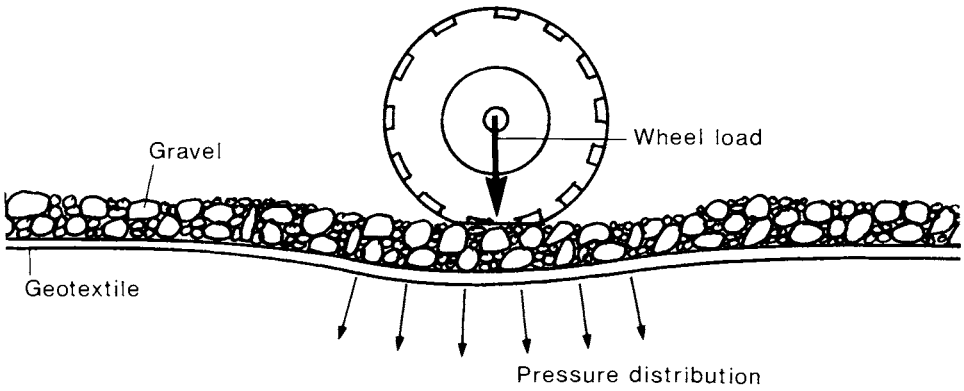

Fig. 10.3. The distribution of loads by a geotextile under a road.

Another important application of geotextiles is in the drainage of earthworks, especially roads. Rather than using open ditches if space is at a premium, subsurface drains can be used to maintain road bases at low water contents throughout the year, and hence at higher strength levels. Excavations are made to the sides of a road at the desired depth and longitudinal slope, between 30 and 60 cm in width depending on the expected volume of water flow. A geotextile is then used to line the excavated ditch, and permeable granular fill is placed to the desired depth on the geotextile. If faster water flow is needed in a particular application, then a perforated drain tile can also be installed in the excavation and surrounded by granular material. The granular material serves to improve hydraulic conductivity and the performance of the drain, thus enhancing the net drainage effect. Fig. 10.4 shows both of these options. The geotextile is then wrapped around the top of the granular fill material and the surface topped up with existing soil.

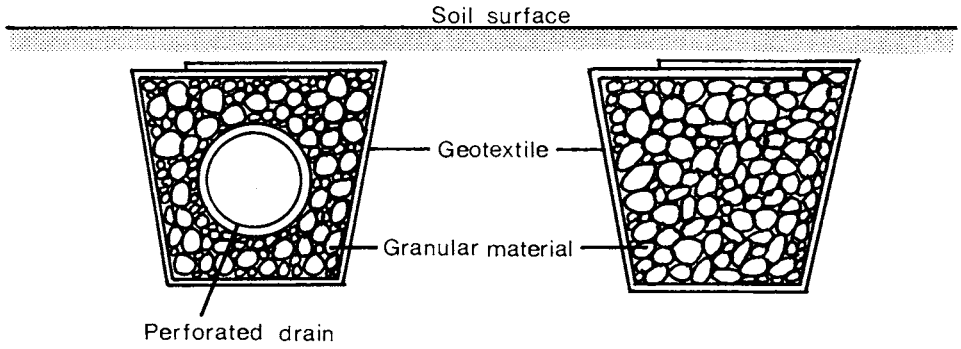

Fig. 10.4. Geotextiles used to wrap rock drains with or without a drain pipe.

The use of a geotextile in this drainage application is primarily as a filtering material which prevents fine particles of the surrounding soil from entering and blocking the granular drain fill. Again its tensile strength allows the geotextile continuity to be maintained, yet a high permeability to water flow has a minimal detrimental effect on the rate of water inflow to drains. Some geotextiles are used directly on drain tiles, especially in cases where a large quantity of tile is placed. This is particularly true in the case of subsurface drainage of agricultural fields where up to 1000 m of subsurface drains may be installed per hectare of surface area. In these applications, the addition of gravel envelopes around drains is economically prohibitive. However, the lack of gravel renders the entry area for water to drains considerably smaller, and the flow of water longitudinally through geotextiles to entry holes in drain tiles more critical. Research projects on these problems are ongoing today, and the reader is referred to recent articles in agricultural engineering research journals for the latest developments.

In the drain tube envelope application, it should be noted that non-woven geotextiles allow the fabrication of filters with much smaller openings than woven fabrics. Thus the former material exhibits a superior performance in fine soils, whereas woven materials do not function as well in preventing soil particles from penetrating subsurface drain tubes. In addition, if a woven geotextile, such as a nylon woven sock, is stretched, then the pore size openings increase in size even further.

Some recent findings have been reported by McKyes and Broughton (1974), Broughton et al. (1976, 1982) and Bonnell et al. (1986). It has been found that synthetic fabrics, of specific masses ranging from 20 to 250 g/m^2 of area, do provide adequate water flow into drain tubes in the short term. However, in many cases of fine sandy and silty soils, the fabrics tend to be blocked by fine soil particles and the rate of water entry is reduced substantially. Spun bonded polyethylene and knitted nylon geotextile materials have proved to be the best at maintaining reasonably high water flows into drains, while preventing soil particles from being transmitted. In the same fine sandy soils in which these materials were tested, drain tubes with openings as small as 0.7 mm were often filled with fine sand after several months of field operation. Gravel envelopes are still superior to thin geotextiles for preventing soil entry into drains and allowing high water flow rates, but as mentioned previously, their cost is many times larger.

Two other problems which have been observed in the abovementioned thin geotextile tests were the formation of iron ochre on the material in soils of substantial iron content (Gameda et al., 1983) and the need for sufficient strength of the geotextiles in order to withstand handling during transport and installation. Lightweight materials of less than 50 g/m^2 or so were seen to suffer considerable abrasive and tearing damage, and thus a reduction in their filtering effectiveness.

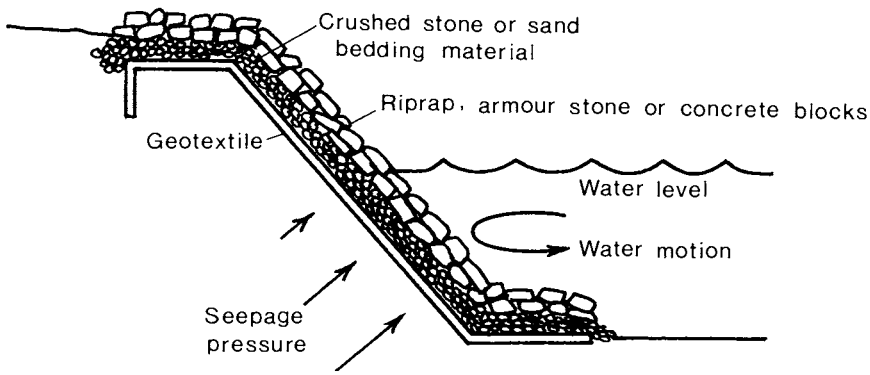

Fig. 10.5. The use of a geotextile to separate riprap and crushed stone from a shoreline, while allowing the dissipation of wave energy and exit of soil seepage pressures.

A further use of geotextiles is in soil erosion control on coastal shorelines and waterways, in conjunction with coarse rock or concrete block armor. A multilayered aggregate filter can also be used for this purpose, but it is usually more time consuming and expensive to install, and has less erosion resistance. As shown in Fig. 10.5, a geotextile sheet allows bank seepage pressures to exit, but resists the movement of soil from within the bank. A certain reverberation action is allowed to be transmitted from water wave action, which results in less energy being expended in bank erosion. Yet, the geotextile material also resists the action of the moving water, which would tend to wash material from beneath the coarse bank armor, and it provides a relatively permanent installation.

10.2. DESIGN OF GEOTEXTILE APPLICATIONS

10.2.1. Bearing capacity of fills.

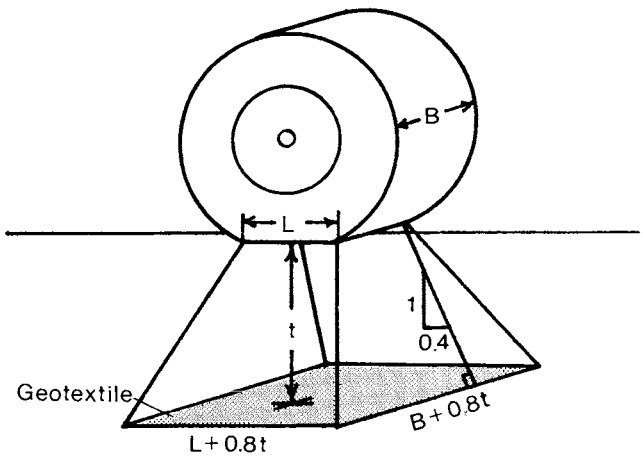

Fig. 10.6. The assumed spread of pressure beneath a rectangular loaded area.

When gravel or sand fill is placed on a softer soil, such as in the case of road construction, geotextiles can be used to prevent the fill from entering the soft subbase as mentioned earlier. In order to calculate the safe load which can be carried by the fill surface, the tensile strength of the geotextile is not taken into account in a conservative approach. However, the spreading of the surface contact load to a larger area at the bottom of the fill is considered as shown in Fig. 10.6 (Gourc, 1983). For a load, Q, such as from a vehicle wheel, the width, B, and length, L, of the horizontal loaded area

can be taken to increase with depth at a slope of about 0.4 to 1, as indicated in Fig. 10.6. The average pressure, q_o, at the base of the fill with a thickness t is thus;

$$q_o = \frac{Q}{(B + 0.8t)(L + 0.8t)} \qquad (10.1)$$

The design load which can be carried safely by the fill surface depends on the ultimate bearing capacity of the softer soil below, and it can be calculated as follows for a cohesive subsoil. Here S.F. is the desired safety factor (usually 3.0 in order to limit vertical deflections of the subsoil).

$$Q_{design} = \frac{cN_c(B+0.8t)(L+0.8t)}{S.F.} = \frac{6.28c(B+0.8t)(L+0.8t)}{S.F.} \qquad (10.2)$$

The weight of the fill itself does not need to be considered in Eqn. 10.2. It is true that the depth of fill also applies a vertical pressure, $q=\gamma t$, onto the interface between fill and subsoil, but this portion of the pressure is cancelled exactly by the additional bearing capacity arising from the fill pressure to the sides of the area loaded by a wheel (qN_q in Eqn. 3.3, where $N_q=1$ for $\phi=0$).

Problem 10.1: A clay soil has an undrained strength of 15 kPa. How thick must compacted gravel be placed to make a road base capable of carrying a 50 kN wheel load on a tire of 30 cm width and 30 cm contact length, with a safety factor of 3 on the clay?

Using Eqn. 7.2;

$$50 \text{ kN} = 6.28 \times 15 \text{ kPa } (0.3 \text{ m} + 0.8t)^2/3$$

$$t = \underline{1.2 \text{ m}}$$

The conservative approach used above does not take into account the tensile strength of the geotextile, and the additional bearing capacity which it can contribute. Experimental work by Gourc (1983) has demonstrated considerable increases in allowable bearing pressure on the base of a plate at different depths of penetration, depending on the strength of the geotextile material used, and the undrained shear strength, C, of the subsoil, as shown in Fig. 10.7. Theoretically, using the strip footing cohesive bearing capacity factor of 5.14 (Appendix 1), the ultimate bearing pressure at the base of the 15 cm wide plate would be;

$$q_{ult} = cN_c(B + 0.8t)/B = 9 \text{ kPa} \times 5.14 \times (0.15 + 0.08)/0.15$$

$$= \underline{70.9 \text{ kPa}}$$

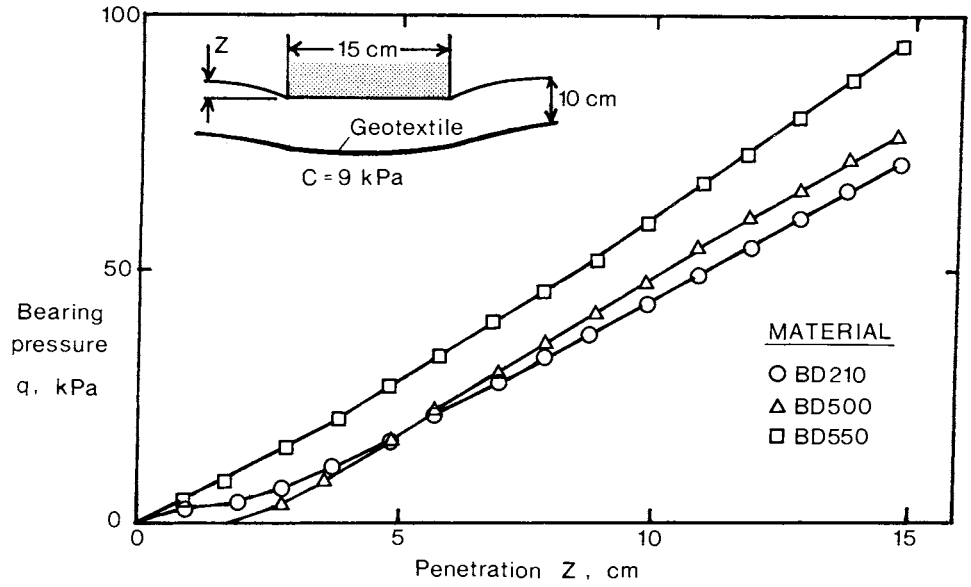

Fig. 10.7. The reduction in penetration of a load in the presence of increasingly heavier geotextiles (Gourc, 1983).

However, Fig. 10.7 shows that the BD 550 geotextile has increased the maximum possible bearing pressure to about 90 kPa, whereas the weaker BD 210 material yields a bearing capacity of only 70 kPa, which is essentially the same as the unreinforced estimate above in which geotextile strength was ignored.

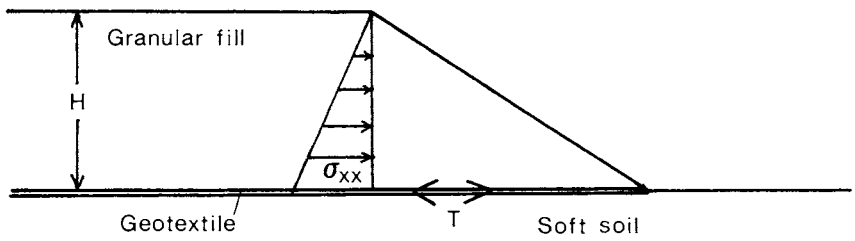

Fig. 10.8. Simplified representation of lateral pressure within a slope, and the tensile force in a reinforcing geotextile.

10.2.2. Slopes on soft strata.

In situations wherein fills are placed with slopes on soft soil strata, such as illustrated in Fig. 10.8, a layer of geotextile material can be used to separate the two soil types, and also to reinforce the stability of the slope. Two criteria can be used to estimate the suitability of the geotextile strength in relation to the relative soil strength parameters. If it is considered that there is negligible or very small shear strength on a horizontal plane at the base of the slope, then the geotextile material can be considered to provide all of the necessary shear force. As Fig. 10.8 indicates, the lateral pressure on a plane under the top of the slope, σ_{xx}, can be calculated as follows as a function of depth z measured from the top for a granular fill.

$$\sigma_{xx} = K_a \gamma z \tag{10.3}$$

The total shear force per unit length of slope is the integral of the above expression over the height H of the slope.

$$T = \tfrac{1}{2} K_a \gamma H^2 \tag{10.4}$$

This is the force per unit width of footing which the geotextile is expected to support in tension if the above assumptions are accepted.

Problem 10.2: A gravel fill is placed three metres high on a soft clay soil such as pictured in Fig. 10.8. The gravel has a unit weight of 17.6 kN/m^3 and an angle of internal friction 35^0. Find the required geotextile tensile strength to prevent sliding of the fill slope.

The coefficient of active earthpressure, K_a, is found from Eqn. 6.7 as:

$$K_a = \frac{1 - \sin\phi}{1 + \sin\phi} = \frac{1 - \sin 35^0}{1 + \sin 35^0} = 0.271$$

The tensile stress, in force per unit width of geotextile material, required is then found from Eqn. 10.4.

$$T = K_a \gamma H^2/2 = 0.271 \times 17.6 \text{ kN/m}^3 \times (3 \text{ m})^2/\ 2 = 21.5 \text{ kN/m}$$

Another approach to the analysis of geotextile reinforced slopes was taken by Gourc (1983). It is assumed that a base circular soil slip circle forms at the slope failure condition, as shown in Fig. 10.9. The geotextile sheet at the slope base is placed under tension as the failure circle forms, and thus adds to the slope strength. Fig. 10.10 indicates the additional height, H, which the slope can attain for a safety factor of 1.0 under different conditions of subsoil undrained shear strength (C) and geotextile tension per unit width (T). The unreinforced maximum slope height, H_c, is also shown for various subsoil

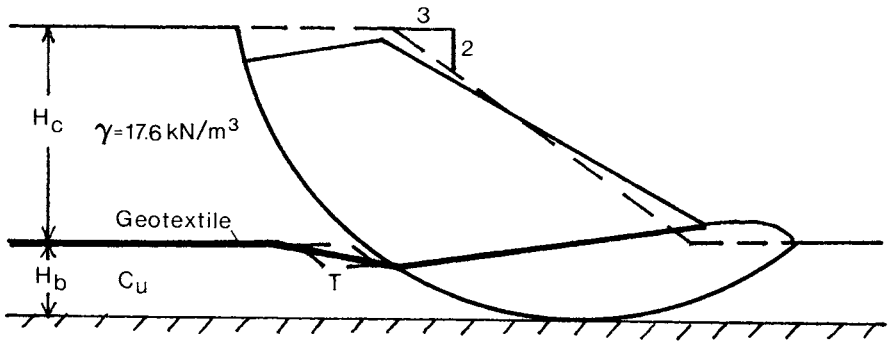

Fig. 10.9. The tensile reinforcing effect of a geotextile in a slope tending to fail along a circular slip line, (after Gourc, 1983)|

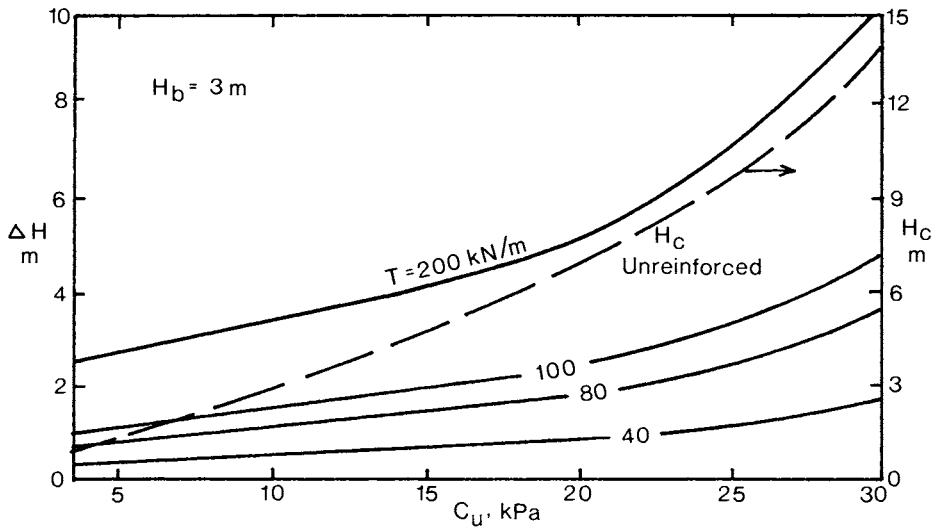

Fig. 10.10. The additional height, ΔH, possible in a slope for different geotextile tensile strengths, T, as a function of soil undrained shear strength, C_u, (after Gourc, 1983).

strength values in Fig. 10.10 for the example base depth, H_b, of 3 m, a 2/3 slope and soil density 17.6 kN/m^3. At low values of subsoil shear strength (5 kPa) and a high geotextile tensile strength (200 kN/m), the increase in permissible slope height can reach 80%.

Problem 10.3: A slope begins at 3 m above a strong base at a slope of 2/3 as shown in Fig. 10.9. The undrained shear strength of the subsoil is 22 kPa. What tensile strength per metre width would a base reinforcing geotextile material require in order to allow the slope to reach a height of 11 m?

Extrapolating from Fig. 10.10, the unreinforced slope height for an undrained shear strength of 22 kPa is about 8.0 m. The additional reinforced height, ΔH = 11 - 8 = 3 m. Again from Fig. 10.10, the geotextile unit strength is extrapolated to be approximately 120 kN/m.

There are many more applications for geotextiles in the construction of drains, roads, filters, watercourse banks, dams and the like, and the reader is referred to Koerner (1986) for a more exhaustive treatment.

10.3. PROBLEMS

10.4. A gravel roadbed of thickness 0.8 m and density 17.6 kN/m^3 is separated by a thin geotextile sheet from a clay subsoil having an undrained shear strength of 20 kPa. If a truck tire is 25 cm wide and has a 50 cm contact length on the gravel, what is the safe wheel load in this situation.

Answer: Q = 42.5 kN.

10.5. If in the situation of Problem 10.4 above the geotextile sheet between the gravel roadbed and clay subsoil were not thin, but a stronger BD 550 geotextile such as in Fig. 10.7, what might the expected allowable wheel load be on the truck tire?

Answer: Q = 54.6 kN.

10.6. A 4 m high slope composed of sand requires construction on the surface of a layer of soft clay, as in Fig. 10.8. If the sand has a density of 16.7 kN/m^3 and an angle of internal friction strength of 30^0, what tensile strength, T, per unit width of geotextile is required at the interface between sand and clay to just prevent the clay from failing in the horizontal direction?

Answer: T = 44.4 kN/m.

10.7. A clay slope such as shown in Fig. 10.10 has a rise over run of 2/3, a soil density of 17.6 kN/m^3 and an undrained shear strength of 20 kPa. (a) What would be the unreinforced maximum possible height of the slope, and (b) what would be the maximum height with a base reinforcing geotextile with a strength per unit width of 100 kN/m?

Answer: (a) H_c = 7.0 m, (b) H_c = 9.2 m.

Chapter 11. Soil Freezing

11.1. FROST PENETRATION

At locations in the world where soil temperatures are caused to descend below 0°C, by either natural or artificial agents, the free water in the soil will freeze with time. This phenomenon causes the soil strength to increase, depending on the temperature and the fraction of soil water frozen. In the case of coarse sands and gravels, it is usually considered that practically all of the soil water freezes into a normal ice structure. However, in finer grained soils containing appreciable amounts of silt and clay, both pore water solutes and the interactions between water and soil particles cause much of

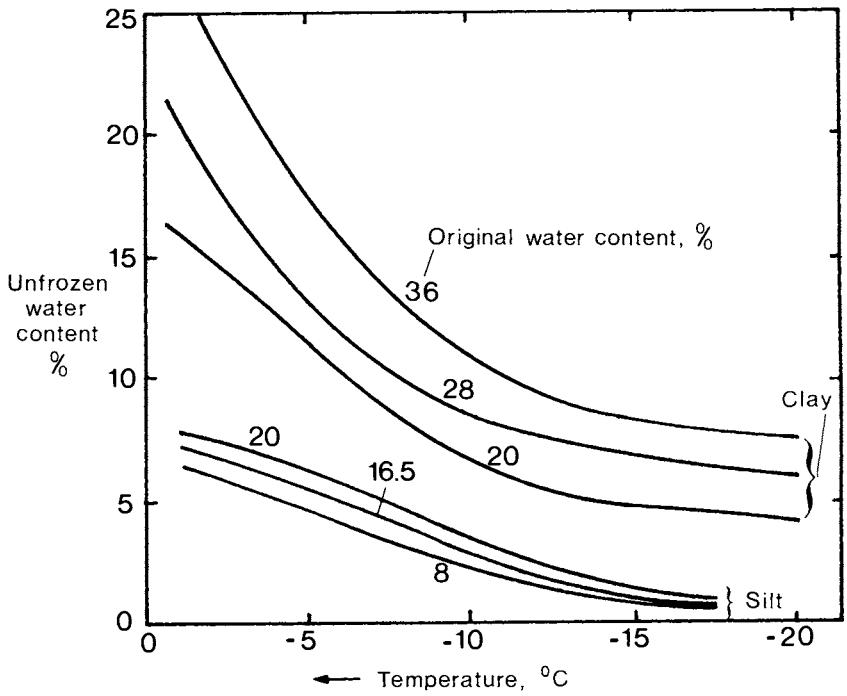

Fig. 11.1. The unfrozen water content in silts and clays are a function of both original moisture content and temperature (Yong, 1965).

the water to remain unfrozen at temperatures a few degrees below the normal freezing point, with less water being unfrozen as the temperature is progressively lowered, (Yong and Warkentin, 1975). Fig. 11.1 gives examples of such soil water behavior for two soils.

In coarser grained soils, it is possible to estimate theoretically the depth to which frost will penetrate from the surface in sub-zero air temperature conditions with the assumption that all of the pore water freezes. The heat flow in soil follows a behavior pattern similar to that of water flow (Chapter 4) as follows.

$$q = -k \frac{\partial T}{\partial z} \tag{11.1}$$

where q = heat flow rate per unit cross sectional area,
k = thermal conductivity,
T = temperature,
z = depth.

By the rule of energy conservation, the change in heat flow rate with position equals the rate of change of heat content at a particular point in the soil, and the heat content is related to the point temperature by the specific volumetric heat content, C. Thus;

$$- \frac{\partial q}{\partial z} = C \frac{\partial T}{\partial t} = k \frac{\partial^2 T}{\partial z^2} \tag{11.2}$$

$$\frac{\partial T}{\partial t} = a \frac{\partial^2 T}{\partial z^2} \tag{11.3}$$

where $a = k/C$ is the thermal diffusivity constant for the soil material.

Eqn. 11.2 and 11.3 can be used to calculate transient heat flows in soil under changing temperature conditions. However, a simplification can be made if it is assumed that temperatures remain essentially constant with time if they change only very slowly. Both sides of Eqn. 11.3 then go to zero, and the temperature distribution with soil depth must be a straight line since the first derivative, or slope of temperature change with depth will be a constant. This constant will depend on the boundary temperatures of the soil profile, as shown in Fig. 11.2 for a subzero air temperature case. In this instance T_f is the subzero surface temperature, and z_f is the depth to the zero Celsius isotherm. Then the temperature at any depth can be found as;

$$T = -T_f + (T_f/z_f)z \tag{11.4}$$

Using the above simplification, the Stefan model for estimating the depth of frost penetration over time can be developed, if it is assumed that the

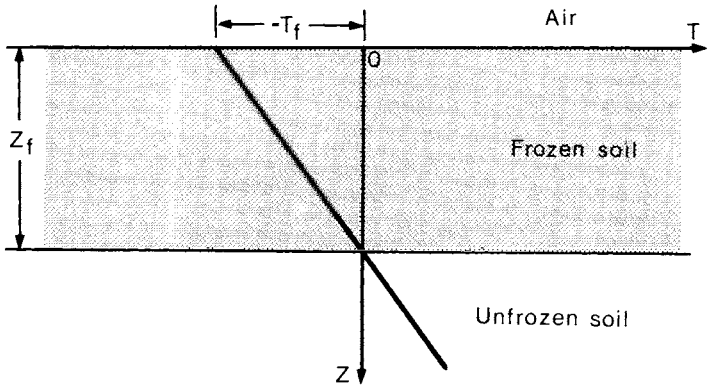

Fig. 11.2. The assumption of a straight line temperature distribution with depth in a soil layer.

frost line of 0°C moves downwards very slowly in subzero air conditions. Eqn. 11.1 gives the rate at which heat is transferred through soil for a given temperature gradient. The quantity of heat which must be moved to advance the frost front in depth is primarily the latent heat of fusion, L_s, of the pore water per unit volume of soil as it freezes. In the expression of this equality below, k_f is the thermal conductivity of the soil when it is frozen. Fig. 11.3 gives typical values of this parameter for two soils at various moisture contents.

$$- k_f \frac{T_f}{z_f} = L_s \frac{dz_f}{dt} \tag{11.5}$$

The latent heat of fusion of pore water per unit volume of soil can be calculated as a function of w, the water content fraction on a dry solids basis, and ρ_{dry}, the dry mass density of soil, as follows.

$$L_s = 334.8 \; w \; \rho_{dry} \text{ (kJ/kg or MJ/t)} \tag{11.6}$$

Integrating Eqn. 11.5 with the convention that the frost depth is zero when time t = 0;

$$\frac{z_f^2}{2} = \frac{k_f}{L_s} \int_0^t -T_f dt \tag{11.7}$$

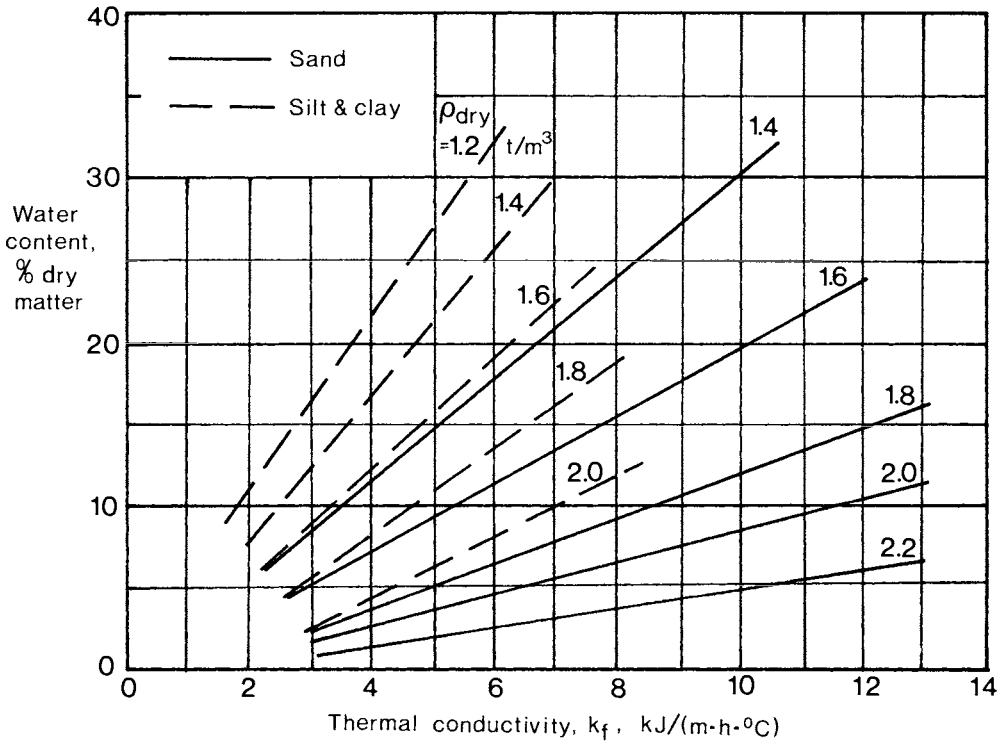

Fig. 11.3. Thermal conductivity, k_f, of frozen sand or silt and clay as a function of dry density and water content (converted from Aldrich, 1956).

The integral of subzero temperature with time is commonly called the freezing index, F, and is usually expressed in degree-days. Maps of average annual freezing indices are available for many parts of the world, and the freezing index for a particular location can be used in the expression below which solves for frost depth z_f.

$$z_f = \sqrt{\frac{2k_f F}{L_s}} \tag{11.8}$$

When using Eqn. 11.8, it must be remembered to match the units of time in the parameters k_f and F. If one is expressed in terms of hours and the other in days, then a conversion of one or the other will be necessary. Similarly, if one term is in imperial units and the other SI, conversions will

be needed to obtain the required depth unit for z_f.

It has been noted by Yong and Warkentin (1975) that the Stefan Eqn. 11.8 tends to predict a larger frost penetration depth than is actually measured. This is due probably to the facts that additional heat content of the soil and water must also be transferred to increase the frost depth, and that the straight line temperature distribution is not a rigorous analysis of the real situation.

Problem 11.1: A silty soil has a dry mass density of 1.7 t/m^3 and a water content of 20%. If it has also a bare surface which has been subjected to 900 degree (C) days freezing index, estimate the depth of frost penetration.

From Fig. 11.3, the frozen thermal conductivity, k_f, can be estimated as about 7.25 $kJ/(mh^oC)$.

Eqn. 11.6 is used to find the pore water latent heat of fusion.

$$L_s = 334.8 \text{ MJ/t} \times 0.20 \times 1.7 \text{ t/m}^3 = 113.8 \text{ MJ/m}^3 = 113{,}800 \text{ kJ/m}^3$$

The estimated depth of frost penetration, z_f, is obtained from Eqn. 11.8.

$$z_f = \sqrt{\frac{2 \times 7.25 \times 900 \text{ kJ}(^oC)\text{m}^3\text{days}}{113{,}800 \text{ kJ}(^oC)\text{mh}} \times \frac{24 \text{ h}}{\text{day}}} = \sqrt{2.75 \text{ m}^2} = \underline{1.66 \text{ m}}$$

11.2. FROST HEAVE PRESSURE

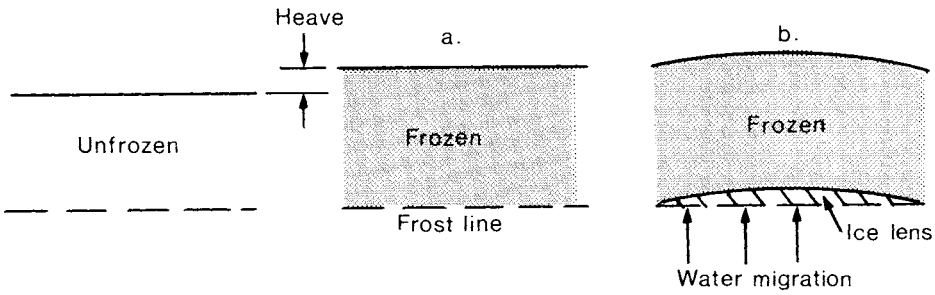

Fig. 11.4. Heave of the soil surface upon freezing due to (a) water expansion alone and (b) migration of water to an ice lens.

When soil water freezes it can cause expansion of the soil. This can arise either from the normal increase in volume of water when it solidifies (about 9% near 0^oC), or the migration of water towards the frost line and the buildup of ice 'lenses' within the soil as shown schematically in Fig. 11.4.

11.2.1. Water expansion.

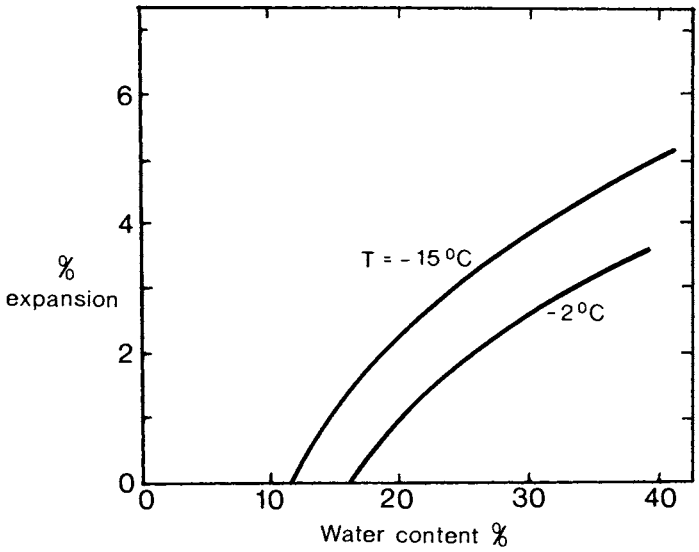

Fig. 11.5. The expansion of soil water in situ is a function of both soil water content and temperature. The example shown is typical for silt.

If water migration does not occur, then only the soil water which was originally in the frozen zone contributes to the expansion in soil volume. The increase in specific volume of soil will not be as large as that of pure water since water does not occupy all of the soil volume. At low degrees of saturation, there is sufficient air in a soil to allow freezing water to expand into air spaces and not require an overall soil volume increase. As the water content increases, some soil expansion will occur as it becomes more difficult for frozen water to enter the remaining void space. And as the soil approaches 100% saturation, the soil expansion on freezing will be a considerable fraction of that of pure water. Some typical results for a silt soil are shown in Fig. 11.5. As the soil temperature decreases below $0^{o}C$, the expansion of fine grained soils increases as more water freezes. This increase depends on the fineness of soil grains, the nature of the soil minerals and the pore water solutes which are present.

Also, as the soil temperature drops below $0^{o}C$ it becomes increasingly difficult to prevent a wet soil from expanding. The pressure that would be required from a rigid structure to stop a soil at subzero temperatures from expanding can become very large. The Clapeyron relation gives the pressure, p, required to produce a certain freezing point depression, ΔT_f, on a flat ice

surface (Penner, 1959).

$$p = \frac{L_s \Delta T_f}{T(v_w - v_i)} \tag{11.9}$$

where L_S = the latent heat of fusion of water,
T = ambient absolute temperature,
v_w = the specific volume of water and
v_i = the specific volume of ice per unit mass.

Near 0^0C the specific volume of water is 1 m^3/t, that of ice is 1.090 m^3/t and the heat of fusion of water is 334.8 kJ/kg or MJ/t. Thus the pressure required for a certain freezing point depression (i.e. in order to prevent freezing and expansion at a certain temperature below 0^0C) is;

$$p = - \frac{334.8 \text{ MJ/t } \Delta T_f}{273^0 \times 0.09 \text{ m}^3/\text{t}} = - 13.6 \Delta T_f \text{ MPa/}^0 \tag{11.10}$$

Thus one is talking of over 13 MPa applied to the soil water for each degree Celsius of freezing point depression in order to prevent expansion, and it is obvious that a rigid restraint to soil volume increase would be subjected to very high pressures from wet soil at just a few degrees below 0^0C.

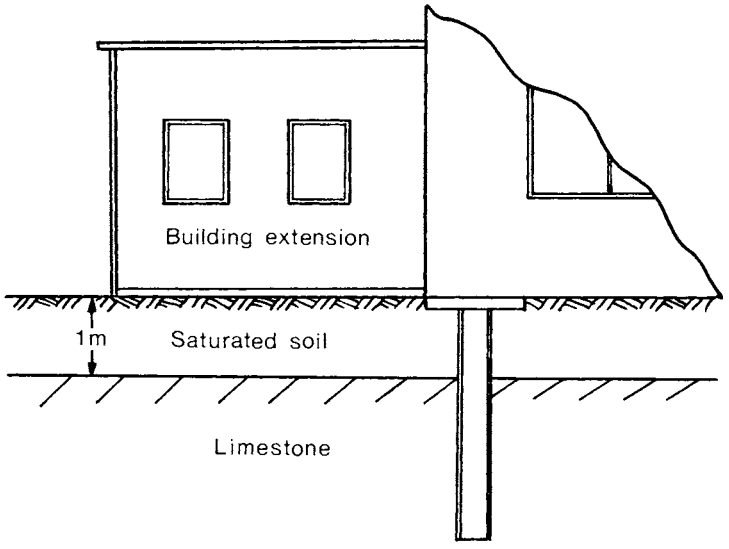

Fig. 11.6. Building extension of Problem 11.2.

Problem 11.2: A building in northern latitudes has a very large mass and is founded on piles at 3 m below the soil surface in limestone. An extension is connected rigidly to this building, but its floor rests directly on the soil surface (Fig. 11.6). The soil layer is 1 m deep to the rock surface, and is saturated at 35% water content. In February the soil freezes to the 1 m depth at an average temperature in the profile of $-5^{o}C$. (a) What pressure could result as an uplift stress on the building extension floor? (b) If the extension connection to the main building cannot resist such a floor pressure, how much could the extension be expected to rise?

(a) From Eqn. 11.10, $p = -13.6\ MPa/^{o} \times (-5^{o}) =$ 68 MPa

(b) Assuming that the soil is similar to that of Fig. 11.5, the percent expansion would be an average of approximately 3.5%. The heave, Δh, is then the percent expansion times the frozen depth:

$\Delta h = 3.5\% \times 1\ m =$ 3.5 cm

11.2.2. Ice lensing.

Fig. 11.4(b) shows schematically a case of an ice lens separating itself from the soil. This phenomenon occurs essentially at the frost front in situations where there is a plentiful water supply within the soil, and sufficient time for the water to move to the ice lens. When a soil is nearly saturated, water does tend to move naturally from warmer depths to colder places, because of the higher free energy in warmer water. Pore water will move faster, of course, in a coarse grained soil with a high permeability, and if there is an upwards hydraulic gradient (artesian conditions).

When the frost front is stationary for some time, the ice lens will continue to grow upwards from the freezing depth and lift the soil above, provided that the water supply remains in existence. The reason for which the ice lens grows is that portions of the lower surface of the ice are at a higher freezing point than the local temperature itself. These areas are those of negative curvature, shown as points A in Fig. 11.7, because the ice-water surface tension gives rise to a reduction in pressure on the curved ice surface.

On the other hand, ice locations with a positive curvature (B in Fig. 11.7) have a relative pressure increase on them due to ice-water surface tension, and their freezing point is lower than the existing temperature. Therefore, freezing will not occur at these latter places, and the ice front does not advance in the soil. However, the freezing of water continues at points A as water is supplied from below, and the ice lens grows. Given sufficient time and a high soil hydraulic conductivity, the growth of the ice lens can be considerable, even at rates up to several mm/h.

The potential heaving pressure is not as great as that of water at several degrees below freezing, however, since the freezing point depression required to stop growth of the ice lens is small at points A in Fig. 11.7. In fact the effective negative pressure, p, acting on points A can be calculated as:

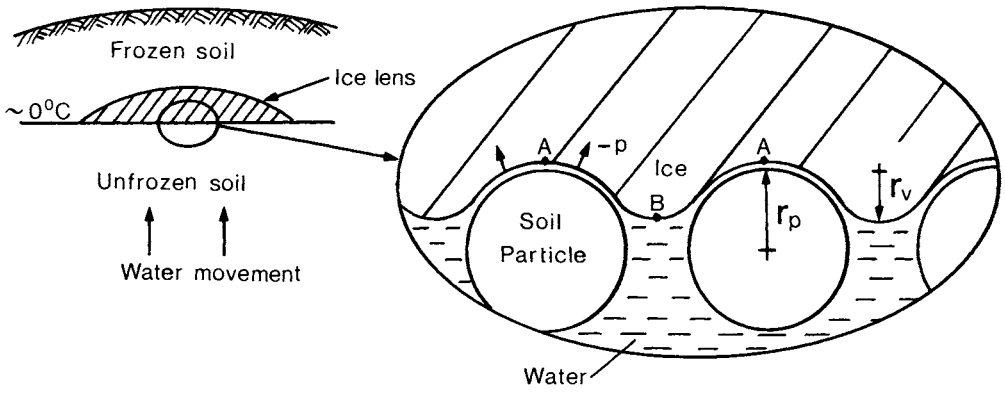

Fig. 11.7. The geometry of the ice-water interface at the frost front during the ice lens growth process.

$$p = -\frac{2\sigma_{iw}}{r_p} \tag{11.11}$$

where σ_{iw} = the ice-water surface tension (energy per unit area), and
r_p = the radius of curvature of the ice surface indentation.

Sill and Skapski (1956) showed that Maxwell's thermodynamic relations can be used for a curved ice to water interface in order to predict the rate of positive normal pressure required per degree of freezing point depression as follows:

$$\frac{dp}{dT_f} = -\frac{L_s}{v_i T} \tag{11.12}$$

Putting Eqn. 11.12 into an incremental form allows its combination with Eqn. 11.11 to find the freezing point elevation for location A on the ice front having a radius of curvature r_p.

$$\Delta T_f = \frac{2\sigma_{iw} T v_i}{r_p L_s} \tag{11.13}$$

Likewise, the freezing point depression for positively curved sections B in Fig. 11.7 is;

$$\Delta T_f = -\frac{2\sigma_{iw} T v_i}{r_v L_s} \tag{11.14}$$

The temperature of the frost front will be $0^{o}C$ minus this latter freezing point depression, because that is where ice ceases to advance in the soil pores at points B. Thus the relative freezing point elevation of negatively curved locations A on the ice front will be the sum of the two freezing point differences, or;

$$\Delta T_f = \frac{2\sigma_{iw} T v_i}{L_s}\left[\frac{1}{r_p} + \frac{1}{r_v}\right] \tag{11.15}$$

Knowing that σ_{iw}= 0.020 J/m^2 (Yong, 1967), absolute temperature T is 273^{o}, v_i = 0.00109 m^3/kg and L_s = 334,800 J/kg;

$$\Delta T_f = 3.56 \times 10^{-8}\left[\frac{1}{r_p} + \frac{1}{r_v}\right]{}^{o}m \tag{11.16}$$

As the above expression shows, the freezing point elevation of portions of the ice-water interface increases with the inverse of effective particle plus void radii. The Clapeyron Eqn. 11.9 indicates that the pressure required to lower the freezing point, and thus halt the freezing process, is proportional to the freezing point difference. Therefore, finer grained soils such as silts and clays are expected to have proportionally higher frost heave pressures than coarser materials including sands and gravels. This can be shown explicitly by substituting Eqn. 11.16 into 11.10 with the following result.

$$p = 4.84 \times 10^{-4}\left[\frac{1}{r_p} + \frac{1}{r_v}\right] \text{ kPa m} \tag{11.17}$$

This is the pressure which would need to be applied to the concave sections of the ice lens lower surface (around points A in Fig. 11.7) The average observed pressure across the soil projected area would be less than this amount. A simplified geometric model assuming uniform spherical soil particles in a cubic pattern can produce an estimate of the ratio between the soil cross sectional area, A_c, which contacts the bottom of the ice lens, divided by the total area, A, as follows (McKyes, 1966; Yong, 1967).

$$A_c/A = (1 - \eta)^{2/3} \tag{11.18}$$

where η = the soil void ratio (volume of voids over total volume).

In addition, the model can give a relationship between the effective void space radius, r_v, and the uniform particle radius, r_p, as follows.

$$r_v = r_p\left[\frac{\eta}{1 - \eta}\right]^{1/3} \tag{11.19}$$

Combining the last three equations gives an expression for the average soil cross sectional frost heave pressure, p_f, which could be expected from an ice

lens in a uniform soil.

$$p_f = \frac{4.84 \times 10^{-4}}{r_p}\left[1 + \left(\frac{1-\eta}{\eta}\right)^{1/3}\right]\left[1-\eta\right]^{2/3} \text{ kPa m} \qquad (11.20)$$

In the case, for example, that the void ratio of a soil is 0.5;

$$p_f = \left[\frac{4.84 \times 10^{-4}}{r_p}\right](2)(0.63) \text{ kPa m} \qquad (11.21)$$

The number 2 in the bracket above shows that the particle and void radii are essentially equal in this case, and 0.63 is the ratio of soil area contacting the ice lens to the total cross sectional area for this void ratio.

Problem 11.3: A uniform silt has an effective grain size diameter of 0.010 mm and a void ratio of 0.5. What frost heave pressure could be expected from an ice lens formation?

The particle radius of the soil is $(10/2) \times 10^{-6}$ m.

Using Eqn. 11.21: $$p_f = \frac{6.10 \times 10^{-4} \text{ kPa m}}{(10/2) \times 10^{-6} \text{ m}} = \underline{122 \text{ kPa}}$$

When soils do not have a uniform grain size, an effective particle radius must be found. Casagrande (1931) suggested that the particle diameter at 10% passing (10% particles smaller by mass) can represent a characteristic particle size for both frost heaving as well as hydraulic conductivity purposes in fairly uniform soils. 10% of the soil mass appears to be just enough to represent the smallest particles which completely cover a cross sectional area in a soil mass. If a grain size represents more mass, numerous smaller particles fill the voids between particles of that size. Any less mass appears to be insufficient to represent the controlling diameter of particles and voids which can completely cover a sectional area in the soil.

It was further noted (Terzaghi and Peck, 1967) that frost heaving does not normally occur in soils having less than 1% of the grains smaller than 0.02 mm. Assuming a well graded soil, such as the examples shown in Fig. 1.8 or 9.2, one could estimate roughly that the 10% passing diameter of such soils would be in the order of 0.1 mm. If 0.05 mm is substituted into Eqn. 11.21 for the effective particle radius, the potential ice lens frost heave pressure of such a non-frost susceptible soil is calculated as approximately 12 kPa. Such a pressure would be developed by the self weight of a 0.6 m depth of soil having a density of 20 kN/m^3. Thus there is logical support for the above criterion for a soil which is not frost susceptible, since at a frost depth of 0.6 m or so, a typical wet soil has sufficient vertical pressure from its own weight to prevent frost heaving.

Another way of characterizing the void size distribution in a soil is by

measuring the pore water tension required to extract different amounts of liquid. The advance of air through soil voids, on the microscopic scale (Fig. 11.8), appears very similar to the advance of ice (Fig. 11.7). In fact, the same formula as Eqn. 11.11 can be used to find the required air pressure, p, or pore water tension, -u, for this advance with the substitution of the air-water surface tension quantity, σ_{aw}, for the ice-water tension as follows.

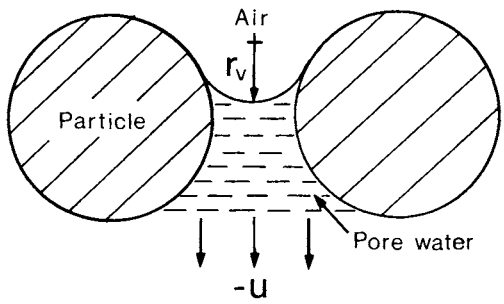

Fig. 11.8. The curvature of an air-water interface within a soil is similar to that of water and ice.

$$p = -u = \frac{2\sigma_{aw}}{r_v} \tag{11.22}$$

Using the above equation, an approximation of the effective average void radius can be made from the measurement of pore water tension when air enters the soil in considerable quantity, (the "air-entry" tension value). Yong and Osler (1971) showed that a good correlation can be drawn between the water tension at air entry in a soil, expressed in m of water head, and the ice lens frost heaving pressure measured, as shown in Fig. 11.9.

It must be remembered that the frost susceptibility of soil is subject to two principal criteria, namely the pressure which an ice lens can exert, and the speed at which the ice lens can grow. If either of these factors is very small, then a soil does not present a practical danger for frost heaving. For large grained soils such as coarse sand and gravel, the potential frost heave pressure is so small that even a thin layer of the soil itself will provide the pressure necessary to arrest frost heaving (see Fig. 11.10). On the other hand, very fine grained clay soils have such low permeability (Fig. 11.10) that it takes longer than a few days for any appreciable water movement and ice lens growth to occur, and by then the soil may be unfrozen or the frost front has changed location. Fig. 11.10 shows that the most dangerous of frost susceptible soils lie in the grain size range of fine sands and silts. This has been borne out by experience as well.

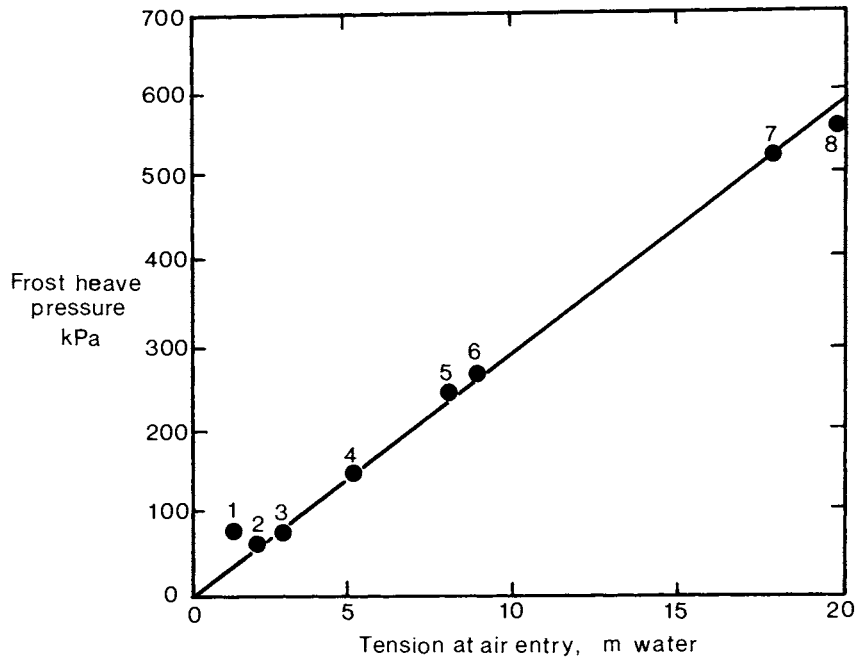

Fig. 11.9. Correlation of frost heave pressures in various soils with the soil water tension at air entry (Yong and Warkentin, 1975). The soils and sources of data are shown below.

1. Silty sand (Hammamji, 1969).
2. Augrey sand (Hoekstra et al., 1965).
3. Seaway silt (McKyes, 1966).
4. Potter's flint (Penner, 1959).
5. Sandy silt (Janiga, 1970).
6. New Hampshire silt (Hoekstra et al., 1965).
7. Richfield silt (Hoekstra et al., 1965).
8. Seaway till (Janiga, 1970).

When a soil is frost susceptible, Fig. 11.10 indicates that it is capable of developing heave pressures of 10 to 100 kPa. Such uplift pressure can pose very serious problems for structures placed on such a soil. There are two solutions to the dilemma. Firstly, the foundations of structures can be placed

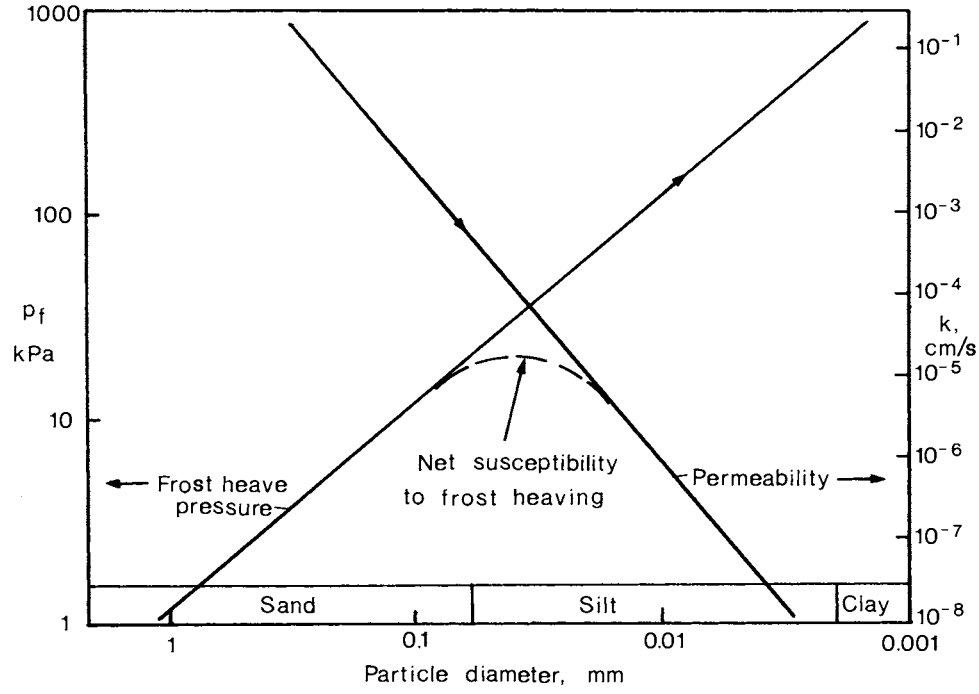

Fig. 11.10. The net susceptibility or danger of frost heaving of a soil is a combination of both the potential heave pressure and the saturated permeability. If one or the other is too small, the soil presents little frost heave danger. The maximum susceptibility comes in the grain size range of silts and fine sands.

below the frost level, that is the maximum depth of frost penetration for a particular climatic region. Regional building codes and other manuals, such as the Midwest Plan Service Structures and Environment Handbook (1983), give the local average and extreme depths of frost penetration for a certain area.

When deep foundations are not feasible, such as in the cases of roads, retaining walls, raft foundations and the like, the solution to preventing frost heaving is thorough drainage of the subsoil. If there is little water in the soil, it will not cause soil expansion upon freezing (see Fig. 11.5). Surface drainage is important in these situations also for the periods of daytime thawing and night freezing in the spring. During these events only the surface layer of soil thaws during the day, and the frozen soil beneath can form a barrier to water drainage if excess water enters by the soil surface. This is one of the principal causes of the deterioration of paved roads during the springtime in cold regions.

11.3. PROBLEMS

11.4. A railway is situated on a saturated silty soil having an average water content of 35%, and the extreme depth of frost penetration is 3 m. How much can the railway be expected to heave if the average temperature in the frost zone is -5^0C, and little water movement occurs?

Answer: Heave = 11 cm.

11.5. In the situation of Problem 11.4, to what water content should the silt subsoil be drained in order to prevent frost expansion problems?

Answer: w = 15%.

11.6. A refrigeration plant in the State of Florida features an underground liquid ammonia tank which has an average internal temperature of -40^0C. If the soil surrounding the tank is a saturated silt with an effective grain size of 0.04 mm and a void ratio of 0.5, what frost heave pressure might be expected to act on the tank due to ice lensing?

Answer: p_f = 32 kPa.

11.7. A fine silt soil has a 10% passing grain size of 0.008 mm and a void ratio of 0.5. (a) What maximum ice lens heave pressure could this soil exert, and (b) at what speed could an ice lens grow if the water pressure dynamic gradient below the ice lens is 0.2 m head per metre length and the frost front remains stationary for several days?

Answer: (a) p_f = 160 kPa, (b) Speed = 0.055 mm/day.

11.8. (a) What would the effective grain size diameter have to be in a soil where an ice lens is observed to grow at a rate of 1 mm per hour with a hydraulic pressure gradient in the soil water of 0.4 m/m towards the ice lens? (b) What heave pressure could this soil exert?

Answer: (a) d = 0.03 mm, (b) p_f = 45 kPa.

References

ALDRICH, H.P. (1956). Frost penetration below highway and airfield pavements. Highway Res. Board Bull., Vol. 135, pp. 124-144.

A.S.A.E. (1985). ASAE standards 1985. Amer. Soc. Agric. Engrs., St. Joseph, MI.

A.S.T.M. (1985). Annual A.S.T.M. standards. Part 11, Bituminous materials, soils, skid resistance. Amer. Soc. for Testing and Materials, Philadelphia, PA.

AMERICAN SOCIETY OF AGRONOMY (1982). Determinants of soil loss tolerance. Amer. Soc. Agron. Publ. No. 45, Madison, WI, 153 pp.

ATTERBERG, A. (1911). Über die physikalishe Bodenuntersuchung und über die Plastizität der Tone. Int. Mitt. für Bodenkunde, Vol. 1, pp. 10-43.

BEKKER, M.G. (1956). Theory of land locomotion - the mechanics of vehicle mobility. Univ. Mich. Press, Ann Arbor, MI, 210 pp.

BEKKER, M.G. (1960). Off the road locomotion: research and development in terramechanics. Univ. Mich. Press, Ann Arbor, MI, 220 pp.

BERNSTEIN, R. (1913). Probleme zur experimentellen Motorpflugmechanik. Der Motorwagen, Vol. 16, pp. 199-227.

BJERRUM, L. (1954). Geotechnical properties of Norwegian marine clays. Géotechnique, Vol. 4, pp. 49-69.

BJERRUM, L. and EGGESTAD, A. (1963). Interpretation of loading tests on sand. Proc. Eur. Conf. Soil Mech. and Found. Eng., Wiesbaden, Vol. 1, pp. 199-203.

BONNELL, R.B., BROUGHTON, R.S. and BOLDUC, G. (1986). Hydraulic failure of the soil - drain envelope interface of subsurface drains. Can. Water Res. J., Vol. 11, No. 3, pp. 24-34.

BROUGHTON, R.S., ENGLISH, B., DAMANT, C., AMI, S., McKYES, E. and BRASSEUR, J. (1976). Tests of filter materials for plastic tubes. Proc. 3rd Nat. Drainage Symp., Amer. Soc. Agric. Engrs., St. Joseph, MI.

BROUGHTON, R.S., GAMEDA, S. and GIBSON, W. (1982). Field tests of some drain tube enevelope materials. Advances in Drainage, Proc. 4th Nat. Drainage Symp., Amer. Soc. Agric. Engrs., St. Joseph, MI, pp. 69-78.

BUTTON, S.J. (1953). The bearing capacity of footings on a two-layer cohesive subsoil. Proc. 3rd Int. Conf. Soil Mech. and Found. Eng., Zurich, Vol. 1, p. 332.

CANADA PLAN SERVICE (1977). Reinforced extended ring foundations for top-unloading concrete tower silos. Bulletin No. 7411, Canada Plan Service, Agriculture Canada Research Branch, Ottawa, ON.

CASAGRANDE, A. (1936). The determination of the pre-consolidation load and its practical significance. Proc. 1st Int. Conf. on Soil Mechanics, Cambridge, MA, Vol. 3, pp. 60-64.

CASAGRANDE, A. (1948). Classification and identification of soils. Trans. Amer. Soc. Civil Eng., Vol. 113, pp. 901-992.

CATERPILLAR CO. (1981). Handbook of earthmoving. Caterpillar Tractor Co., Peoria, IL, 24 pp.

CAUGHY, R.A., TOOLES, C.W. and SCHEER, A.C. (1951). Lateral and vertical pressures of granular material in deep bins. Bull. 172, Iowa Engineering Experiment Station, Ames IA.

CHANCELLOR, W.J. and SCHMIDT, R.H. (1962). A study of soil deformation beneath surface loads. Trans. Amer. Soc. Agric. Engrs., Vol. 5, pp. 240-246, 249.

CORPS OF ENGINEERS. (1944). Construction and routes of communication. War Department Field Manual No. FM 5-10, U.S. Gov't. Printing Off., Washington DC, 596 pp.

COULOMB, C.A. (1776). Essai sur une application des règles des maximis et minimis à quelques problèmes de statique relatifs à l'architecture. Academie royale des Sciences: Mémoires de Mathématique et de Physique, presentés à l'Academie royale des Sciences, par divers savants, et lus dans les Assemblées, Paris, Vol. 7, pp. 343-382 + 2 plates.

DARCY, H. (1856). Les fontaines publiques de la ville de Dijon. Dalmont, Paris, 674 pp.

DESIR, F.L. (1981). A field evaluation of the wedge approach to the analysis of soil cutting by narrow blades. M.Sc. Thesis, McGill Univ., Dept. Agric. Eng., Montreal, QC. 245 pp.

ELWELL, H.A. (1978). Modelling soil losses in southern Africa. J. Agric. Eng. Res., Vol. 23, pp. 117-127.

ELWELL, H.A. (1980). Design of safe rotational systems. Dept. Cons. and Ext. Report, Min. Agr., Harare, Zimbabwe, 50 pp.

ELWELL, H.A. (1984). Sheet erosion from arable lands in Zimbabwe: prediction and control. Proc. Symp. Challenges in African Hydrology and Water Resources, Harare, IAHS Publ. No. 144, pp. 429-438.

EVERTS, R., VAN ZANTEN, D.C. and RICHARDS, P.C. (1977). Bunker design. Part 4: Recommendations. Trans. Amer. Soc. Mech. Engrs. J. Eng. Industry, Vol. 99, pp. 824-827.

FAN, Tai-Lin (1985). Multi-plate penetration tests to determine soil stiffness moduli. M.Sc. Thesis, McGill Univ., Dept. Agric. Eng., Montreal, QC. 99 pp.

FORTIER, S. and SCOBEY, F.C. (1926). Permissible canal velocities. Trans. Am. Soc. of Civil Eng., Vol. 89, pp. 940-984.

GAMEDA, S. JUTRAS, P.J. and BROUGHTON, R.S. (1983). Ochre in subsurface drains in a Quebec fine sandy loam. Can. Agric. Eng., Vol. 25, No. 2, pp. 209-213.

GILL, W.R. and McCREERY, W.F. (1960). Relation of size of cut to tillage tool efficiency. Agric. Eng., Vol. 41, pp. 372-374, 381.

GODWIN, R.J. (1974). An investigation into the mechanics of narrow tines in frictional soils. Ph.D. Thesis, Univ. of Reading, 248 pp.

GODWIN, R.J. and SPOOR, G. (1977). Soil failure with narrow tines. J. Agric. Eng. Res., Vol. 22, pp. 213-228.

GORIATCHKIN, V.P. (1937). Kolesa zhatvennih mashin. Sobranie sochinenii, Selkhozgiz, Vol. 2 and 4, Moscow.
GOURC, J.P. (1983) Études de cas; chaussées provisoires, remblais, soutenements. Dans Cours intensifs - les Géotextiles. École polytechnique, Centre de Cours intensifs, Montréal, QC.
GRAECEN, E.L. (1960). Water content and soil strength. J. Soil Sci., Vol. 11, pp. 313-333.
HAMMAMJI, Y. (1969). Some factors affecting heave pressures of frozen soils. M.Sc. Thesis, McGill University, Montreal, QC.
HANSEN, J. BRINCH (1957). Foundation of structures - general report. Proc. 4th Int. Conf. Soil Mech. and Found. Eng., London, Vol. II, pp. 441-447.
HARR, M.E. (1966). Foundations of theoretical soil mechanics. McGraw-Hill, New York, NY. 381 pp.
HETTIARATCHI, D.R.P. (1969). The calculation of passive earthpressure. Ph.D. Thesis, Univ. of Newcastle-upon-Tyne.
HETTIARATCHI, D.R.P. and REECE, A.R. (1974). The calculation of passive soil resistance. Géotechnique, Vol. 24, No. 3, pp. 289-310.
HOEKSTRA, P., CHAMBERLAIN, E. and FRATE, T. (1965). Frost heaving pressures. Cold Regions Res. Eng. Lab. Res. Report 176, Hannover, NH.
HOOGHOUDT, S.B. (1940). Bijdrage tot de kennis van enige natuurkundige grootheden van de grond. Verslagen van Landbouwkundige Onderzoekingen, Vol. 46, No. 7, pp. 515-707.
HOVANESIAN, J.D. (1958). Development and use of a volumetric transducer for studying effects of soil parameters on compaction. Ph.D. thesis, Michingan State Univ., East Lansing, MI.
HUDSON, N. (1981). Soil conservation. Cornell Univ. Press, Ithica, NY, 324 pp.
HVORSLEV, M.J. (1937). Über die Festigkeitseigenschaften gestörter bindinger Böden. Danmarks Naturvidenkabelige Samfund, Ingeniorvidenskabelige Skrifter, Series A, No. 45, Copenhagen, 159 pp.
ILRI (1964). Code of practice for the design of open watercourses and ancillary structures. Int. Inst. for Land Reclamation and Improvement, Wageningen, The Netherlands, Bull. No. 7.
IRELAND, H.O. (1957). Pulling tests on piles in sand. Proc. 4th Int. Conf. on Soil Mech. and Found. Eng., London, Vol. II, pp. 43-45.
JAKY, J. (1948). Pressures in silos. Proc. 2nd Int. Conf. Soil Mech., Rotterdam, Vol. I, pp. 103-108.
JANIGA, P.V. (1970). Some considerations in in-situ frost heaving. M.Sc. Thesis, McGill University, Montreal, QC.
JANSSEN, H.A. (1895). Versuche über Getreidedruck in Silozellen. Z. Vereines Deutscher Ingenieure, Vol. 39, pp. 1045-1049.
KETCHUM, M.S. (1919). Design of bins, walls and grain elevators. McGraw Hill, New York, NY.
KOERNER, R.M. (1986). Designing with geosynthetics. Prentice-Hall, Englewood Cliffs, NJ. 424 pp.

KOSTRITSYN, A.K. (1956). (Cutting of a cohesive soil medium with knives and cones). Vsesoiuzz Akad. Sel'skokhoziaistvennykh Nauk. Zeml. Mekh. Sborn. Trudov, Leningrad, Vol. 3, pp. 247-290, (NIAE Translation No. 58).

LAMBE, T.W. (1951). Soil testing for engineers. Wiley, New York, NY. 165 pp.

LAMBE, T.W. and WHITMAN, R.V. (1979). Soil mechanics, SI version. Wiley, New York, NY. 553 pp.

LUNDGREN, H. and MORTENSEN, K. (1953). Determination by the theory of plasticity of the bearing capacity of continuous footings on sand. Proc. 3rd Int. Conf. Soil Mech. and Found. Eng., Zurich, Vol. 1, pp. 409-412.

LUTH, H.J. and WISMER, R.D. (1971). Performance of plane soil cutting blades in sand. Trans. Amer. Soc. Agric. Engrs., Vol. 14, No. 2, pp. 255-259, 262.

LUTHIN, J.N. (1957). Editor. Drainage of agricultural lands. Amer. Soc. Agron., Madison, WI. 620 pp.

LUTHIN, J.N. (1973). Drainage engineering. Krieger, Huntington, NY, 250 pp.

LVIN, J.B. (1970). Analytical evaluation of pressures of granular materials on silo walls. Powder Technol., Vol. 4, pp. 280-285.

MARSTON, A. and ANDERSON, A.O. (1913). The theory of loads on pipes in ditches and tests of cement and clay tile and sewer pipe. Bull. 31, Iowa Engineering Experiment Station, Ames IA.

MAVIS, F.T. (1935). The transportation of detritus by flowing water. Bull. No. 5. Studies in Engineering. State University of Iowa, Ames, IA.

McKYES, E. (1966). Theoretical and experimental determination of frost heaving pressures in a partially frozen silt. B. Eng. Thesis, McGill University, Montreal QC, 44 pp.

McKYES, E. and BROUGHTON, R.S. (1974). A laboratory study of some drain tube filter materials. Can. Agric. Eng., Vol. 16, No. 2, pp. 60-62.

McKYES, E. and ALI, O.S. (1977). The cutting of soil by narrow blades. J. Terramechanics, Vol. 14, No. 2, pp. 43-58.

McKYES, E., NEGI, S.C., DOUGLAS, E., TAYLOR, F. and RAGHAVAN, V. (1979). The effect of machinery traffic and tillage operations on the physical properties of a clay and on yield of silage corn. J. Agric. Eng. Res., Vol. 24, pp. 143-148.

McKYES, E. and DESIR, F.L. (1984). Prediction and field measurements of tillage tool draft forces and efficiency in cohesive soils. Soil Tillage Res., Vol. 4, No. 4, pp. 459-470.

McKYES, E. (1985). Soil cutting and tillage. Elsevier, Amsterdam, 217 pp.

McKYES, E. and FAN, Tai-Lin (1985). Multiplate penetration tests to determine soil stiffness moduli. J. Terramechanics, Vol. 22, No. 3, pp. 157-162.

MEYERHOF, G.G. (1951). The ultimate bearing capacity of foundations. Géotechnique, Vol. 2, No. 4, pp. 301-332.

MEYERHOF, G.G. (1953). The bearing capacity of foundations under eccentric and inclined loads. Proc. 3rd Int. Conf. Soil Mech. and Found. Eng., Zurich, Vol. 1, pp. 440-445.

MEYERHOF, G.G. (1955). Influence of roughness of base and ground-water conditions on the ultimate bearing capacity of foundations. Geotechnique, Vol. 5, pp. 227-242.

MIDWEST PLAN SERVICE (1983). Structures and environment handbook. 11th Ed. Midwest Plan Service, Iowa State University, Ames IA 50011.

MILLER, P.C.H. (1971). Soil failure and the nature of the force system with very narrow tines. B.Sc. Thesis, Nat. Col. Agric. Eng., Silsoe, Bedford, U.K.

MOHR, O. (1914). Die Elastizitätsgrenze und Bruch eines Materials. Z. Ver. Dtsch. Ing., Vol. 44, P. 1524.

MOHSENIN, N.N. (1970). Physical properties of plant and animal materials. Gordon and Breach, New York, 734 pp.

MORIN, J.P. and BOZOZUK, M. (1983). Performance of concrete tower silos on clays in Quebec. Can. Agric. Eng., Vol. 25, No. 1, pp. 81-88.

MOYSEY, E.B. (1979). Active and passive pressures in deep bins. Trans. Amer. Soc. Agric. Engrs., Vol. 22, No. 6, pp. 1409-1413.

MOYSEY, E.B. (1983). Static and dynamic pressures in grain storage phase III. Eng. and Stat. Res. Inst., Agr. Canada, Ottawa, ON.

NEGI, S.C., McKYES, E., RAGHAVAN, G.S.V. and TAYLOR, F. (1981). Relationships of field traffic and tillage to corn yields and soil properties. J. Terramechanics, Vol. 18, No. 2, pp. 81-90.

NEGI, S.C., OGILVIE, J.R. and NORRIS, E.R. (1977). Silage pressures in tower silos. Part 3. Experimental model studies and comparison with some silo theories. Can. Agric. Eng., Vol. 19, No. 2, pp. 107-110.

O'CALLAGHAN, J.R. and FARRELLY, K.M. (1964). Cleavage of soil by tined implements. J. Agric. Eng. Res., Vol. 9, No. 3, pp. 259-270.

ONTARIO SILO ASSOCIATION (1980). Standards for conventional open-top concrete tower silo construction. Ontario Silo Association, Box 8125, Kitchener, ON, N2K 3B6, Canada.

PAYNE, P.C.J. (1956). The relationship between the mechanical properties of soils and the performance of simple cultivation implements. J. Agric. Eng. Res., Vol. 1, No. 1, pp. 23-50.

PENNER, E. (1959). The mechanism of frost heaving in soils. Highway Res. Board Bull., Vol. 225, pp. 1-13.

PIEPER, K. (1969). Investigation of silo loads in measuring models. Trans. Amer. Soc. Mech. Engrs. J. Eng. Industry, Vol. 91, pp. 365-372.

PRANDTL, L. (1921). Über die Eindringungsfestigkeit (Härte) platischer Baustoffe und die Festigkeit von Schneiden. Zeit. angew. Math. Mech., Vol. 1, No. 1, pp. 15-20.

PROCTOR, R.R. (1933). Fundamental principles of soil compaction. Eng. News-Record, Vol. 111, Aug. 31, pp. 245-248; Sept. 7, pp. 286-289; Sept. 21, pp. 348-351; Sept. 28, pp. 372-376.

PROCTOR, R.R. (1948). The relationship between foot pounds per cubic foot of compactive effort and shear strength of compacted soils. Proc. 2nd Int. Conf. Soil Mech., Rotterdam, Vol. 5, p. 219.

RAGHAVAN, G.S.V., McKYES, E. and BEAULIEU, B. (1977a). Prediction of clay soil compaction. J. Terramechanics, Vol. 14, No. 1, pp. 31-38.

RAGHAVAN, G.S.V., McKYES, E. and CHASSÉ, M. (1977b). Effect of wheel slip on soil compaction. J. Agric. Eng. Res., Vol. 22, pp. 79-83.
REECE, A.R. (1965). The fundamental equation of earth-moving mechanics. Proc. Inst. Mech. Engrs., Vol. 179, Part 3F, pp. 16-22.
ROWLES, W. (1948). Physical properties related to structure of Sainte-Rosalie clay and their seasonal variation. Scientific Agr., Vol. 28, pp. 558-573.
SCHWAB, G.O., FREVERT, R.K., EDMINSTER, T.W. and BARNES, K.K. (1981). Soil and water conservation engineering. 3rd Ed., Wiley, New york, 525 pp.
SCOTT, R.F. (1963). Principles of soil mechanics. Addison-Wesley, Reading, MA, 422 pp.
SILL, R.C. and SKAPSKI, A.S. (1956). Method for determination of surface tension of solids from their melting points in thin wedges. J. Chem. Phys., Vol. 24, pp. 644-651.
SINGH, D. and MOYSEY, E.B. (1985). Grain bin wall pressures: theoretical and experimental. Can. Agric. Eng., Vol. 27, No. 1, pp. 43-48.
SKEMPTON, A.W. (1948). The ϕ=0 analysis of stability and its theoretical basis. Proc. 2nd Int. Conf. Soil Mech., Rotterdam, Vol 1, pp. 72-78.
SMEDEMA, L.K. and RYCROFT, D.W. (1983). Land drainage. Batsford, London, U.K. 376 pp.
SMITH, D.D. and WISCHMEIER, W.H. (1962). Rainfall erosion. Advances in Agronomy, Vol. 14, pp. 109-148.
SOEHNE, W. (1958). Fundamentals of pressure distribution and soil compaction under tractor tires. Agric. Eng., Vol. 39, pp. 276-281, 290.
SOILTEST, INC. (1976). Soil testing equipment. Soiltest, Inc., Evanston IL, 160 pp.
SOKOLOVSKI, V.V. (1956). Statics of soil media. Butterworth, London, 237 pp.
SPANGLER, M.G. (1973). Long time measurement of loads on three pipe culverts. Highway Res. Board Rec., Vol. 443.
SPANGLER, M.G. and HANDY, R.L. (1982). Soil Engineering. 4th ed., Harper and Row, New York, NY. 819 pp.
SPOOR, G. and GODWIN, R.J. (1978). An experimental investigation into the deep loosening of soil by rigid tines. J. Agric. Eng. Res., Vol. 23, pp. 243-258.
TAYLOR, D.W. (1937). Stability of earth slopes. J. Boston Soc. Civil Engrs., Vol. 24, pp. 197-246.
TAYLOR, D.W. (1948). Fundamentals of soil mechanics. Wiley, New York, NY. 700 pp.
TENG, W.C. (1962). Foundation design. Prentice-Hall, Englewood Cliffs, NJ, 466 pp.
TERZAGHI, K. (1936). The shearing resistance of saturated soils. Proc. 1st Int. Conf. Soil Mech., Cambridge, MA, Vol. 1, pp. 54-56.
TERZAGHI, K. (1943). Theoretical soil mechanics. Wiley, New York, NY. 510 pp.
TERZAGHI, K. (1954). Anchored bulkheads. Trans. Amer. Soc. Civil Eng., Vol. 114, p. 1243.

TERZAGHI, K. and PECK, R. B. (1967). Soil mechanics in engineering practice. 2nd ed., Wiley, NY. 729 pp.

TURITZIN, A.M. (1963). Dynamic pressures of granular material in deep bins. Proc. Amer. Soc. Civ. Engrs., Vol. 89, No. ST2, pp. 49-73.

TURNBULL, J.E., JACKSON, H.A. and LOWE, D. (1979). Reinforced extended ring foundations for top-unloading concrete tower silos. Can. Agric. Eng., Vol. 21, No. 2, pp. 111-116.

USDA-EPA (1975). Control of water pollution from cropland. U.S. Gov't. Printing Off., Washington DC, Vol. I.

VANDEN BERG, G.E. (1966). Triaxial measurements of shear strain and compaction in unsaturated soil. Trans. Amer. Soc. Agric. Engrs., Vol. 9, No. 4, pp. 460-463, 467.

VAN SCHILFGAARDE, J. (1957). Approximate solutions to drainage flow problems. Drainage of agricultural lands, J.N. Luthin Editor, Amer. Soc. Agron., Madison, WI. pp. 79-112.

VOMICIL, J.A. (1955). Ph.D. thesis, Rutgers Univ., New Brunswick, NJ.

WAGNER, A.A. (1957). The use of a unified soil classification system by the Bureau of Reclamation. Proc. 4th Int. Conf. Soil. Mech. and Found. Eng., London, Vol. 1, p. 125.

WALL, G., DICKINSON, W.T. and GREVEL, J. (1983). Rainfall erosion indices for Canada east of the Rocky Mountains. Can. J. Soil. Sci., Vol. 63, pp. 271-280.

WENDELAAR, F.E. (1978). Applying the universal soil loss equation in Rhodesia. Inst. Agric. Eng. Rep., Min. Agr., Zimbabwe, 23 pp.

WILLIAMS, J.R. and BERNDT, H.D. (1977). Sediment yield prediction based on watershed hydrology. Trans. Amer. Soc. Agric. Engrs., Vol. 20, No. 6, pp. 1100-1104.

WISCHMEIER, W.H. (1976). Cropland erosion and sedimentation. USDA-EPA Control of Water Pollution. U.S. Gov't. Printing Off., Washington DC, Vol. II, Chapter 3.

WISCHMEIER, W.H. and SMITH, D.D. (1965). Predicting rainfall-erosion losses from cropland east of the Rocky Mountains. USDA-ARS Agric. Handbook No. 282.

YONG, R.N. (1965). Soil suction effects on partial soil freezing. Highway Res. Board Res. Record, Vol. 68, pp. 31-42.

YONG, R.N. (1967). On the relationship between partial soil freezing and surface forces. Physics of snow and ice. H. Oura Editor, Inst. Low Temp. Sci., Hokkaido Univ., Vol. 1, pp. 1375-1385.

YONG, R.N. and OSLER, J.C. (1971). Heave and heaving pressures in frozen soils. Can. Geotech. J., Vol. 8, pp. 272-282.

YONG, R.N. and WARKENTIN, B.P. (1975). Soil properties and behaviour. Elsevier, Amsterdam. 449 pp.

ZELENIN, A.N. (1950). Fizicheski osnovy teorii rezaniya gruntov. Akad. Nawk, Moscow-Leningrad, 353 pp., (NIAE Translation).

APPENDIX 1. BEARING CAPACITY FACTORS FOR SHALLOW FOUNDATIONS

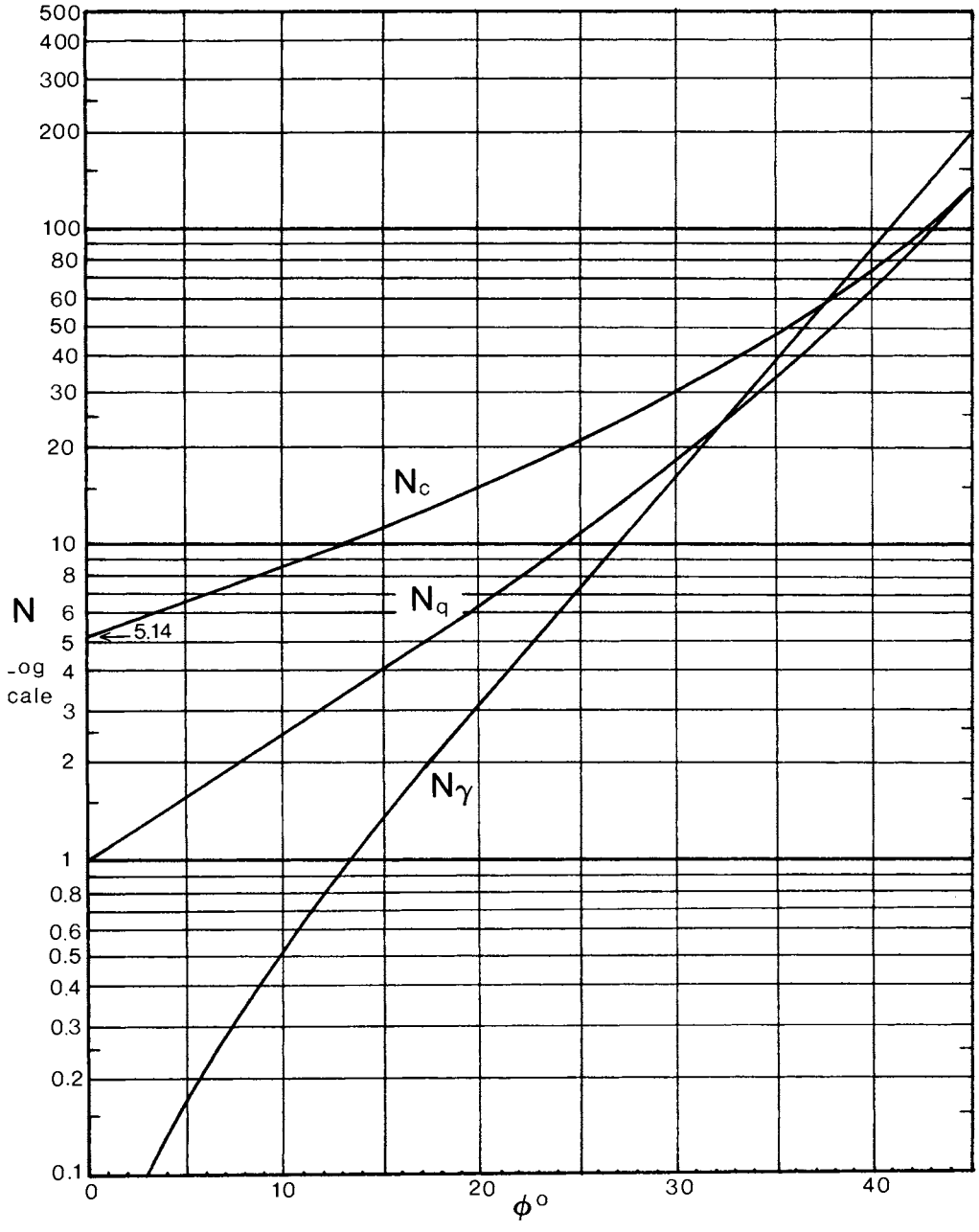
500
400
300
200
100
80
60
50
40
30
20
10
8
6
5
4
3
2
1
0.8
0.6
0.5
0.4
0.3
0.2
0.1
N
-og
cale
5.14
N_c
N_q
N_γ
0
10
20
30
40
ϕ^o

APPENDIX 2. DESIGN REQUIREMENTS FOR EXTENDED SILO RING FOUNDATIONS

(Turnbull et al., 1979)

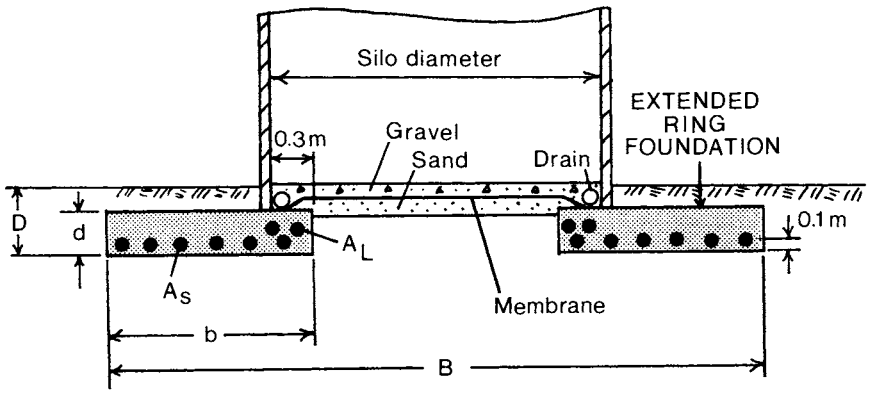
Silo diameter
EXTENDED
RING
FOUNDATION
0.3m
Gravel
Sand
Drain
D
d
A_L
A_S
0.1 m
Membrane
b
B

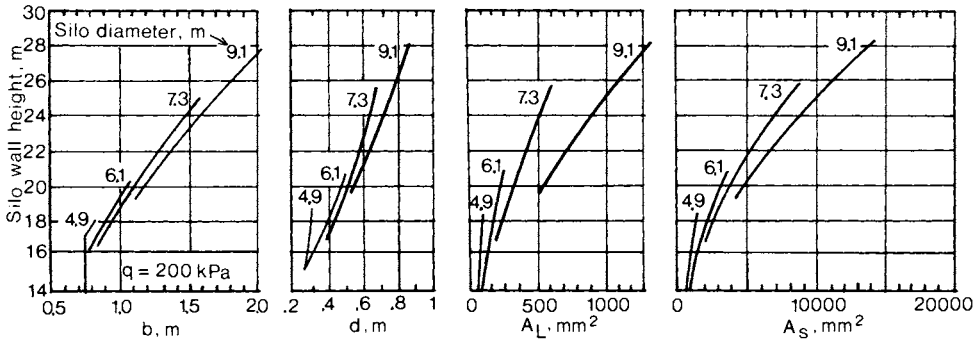
Silo wall height, m
Silo diameter, m
9.1
7.3
6.1
4.9
q = 200 kPa
b, m
d, m
A_L, mm²
A_S, mm²

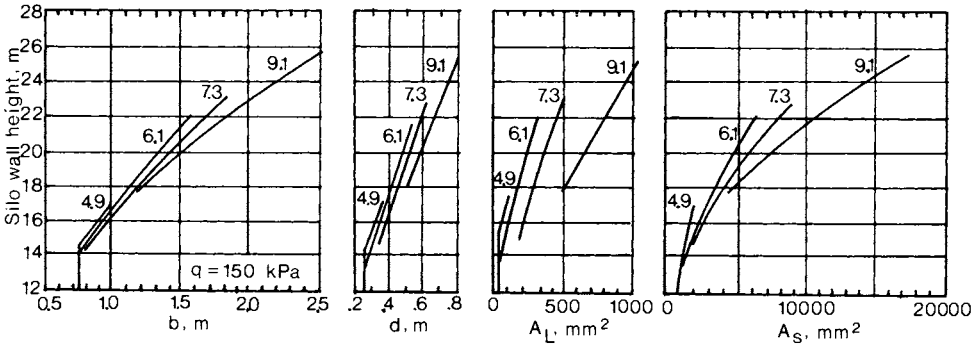
Silo wall height, m
9.1
7.3
6.1
4.9
q = 150 kPa
b, m
d, m
A_L, mm²
A_S, mm²

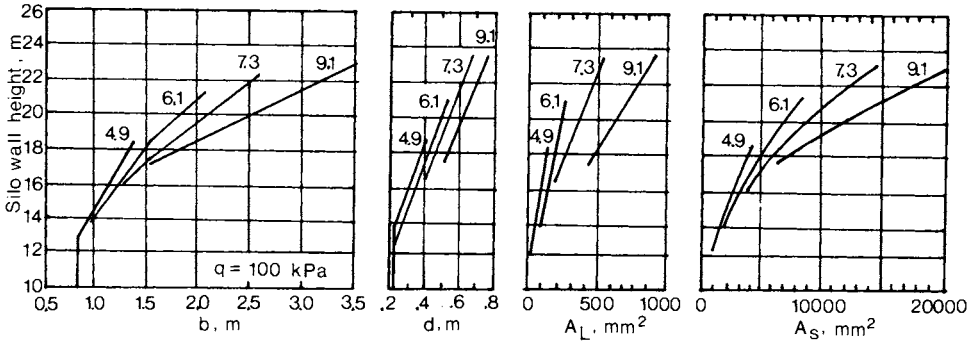
Silo wall height, m
9.1
7.3
6.1
4.9
q = 100 kPa
b, m
d, m
A_L, mm²
A_S, mm²

APPENDIX 3. WALL PRESSURE FACTORS IN FRICTIONAL SOILS

K_{ah} = horizontal component, K_{av} = vertical component.

ϕ^0	δ^0	α^0	K_{ah}	K_{av}	ϕ^0	δ^0	α^0	K_{ah}	K_{av}	ϕ^0	δ^0	α^0	K_{ah}	K_{av}
36	32	90	0.202	0.126	34	30	90	0.221	0.128	32	28	90	0.243	0.129
		85	.222	.167			85	.242	.169			85	.264	.171
		80	.240	.216			80	.261	.219			80	.283	.221
		75	.256	.275			75	.278	.278			75	.301	.280
		70	.269	.345			70	.292	.348			70	.315	.350
		65	.279	.430			65	.302	.431			65	.326	.433
		60	.283	.533			60	.307	.533			60	.333	.533
30	26	90	0.266	0.130	28	25	90	0.289	0.135	26	23	90	0.316	0.134
		85	.287	.173			85	.310	.179			85	.337	.179
		80	.307	.223			80	.330	.231			80	.357	.232
		75	.325	.283			75	.347	.291			75	.375	.293
		70	.340	.352			70	.362	.362			70	.390	.364
		65	.352	.435			65	.374	.445			65	.403	.447
		60	.360	.533			60	.381	.545			60	.411	.545
24	21	90	0.345	0.132	22	19	90	0.377	0.130	20	17	90	0.412	0.126
		85	.367	.179			85	.399	.178			85	.434	.175
		80	.387	.233			80	.419	.232			80	.454	.231
		75	.405	.294			75	.437	.295			75	.472	.295
		70	.421	.366			70	.453	.367			70	.488	.368
		65	.433	.449			65	.466	.450			65	.501	.451
		60	.442	.546			60	.476	.547			60	.511	.548
36	24	90	0.215	0.096	34	23	90	0.234	0.099	32	21	90	0.257	0.099
		85	.238	.132			85	.257	.137			85	.281	.137
		80	.260	.175			80	.280	.182			80	.304	.183
		75	.281	.228			75	.301	.235			75	.325	.236
		70	.300	.290			70	.320	.298			70	.345	.300
		65	.316	.364			65	.336	.373			65	.362	.375
		60	.330	.454			60	.349	.464			60	.376	.465

ϕ^0	δ^0	α^0	K_{ah}	K_{av}	ϕ^0	δ^0	α^0	K_{ah}	K_{av}	ϕ^0	δ^0	α^0	K_{ah}	K_{av}
30	20	90	0.279	0.102	28	19	90	0.304	0.105	26	17	90	0.332	0.102
		85	.304	.142			85	.328	.146			85	.357	.144
		80	.326	.188			80	.350	.194			80	.380	.194
		75	.348	.244			75	.372	.251			75	.401	.251
		70	.367	.308			70	.391	.316			70	.421	.317
		65	.384	.384			65	.408	.394			65	.438	.395
		60	.398	.475			60	.422	.485			60	.453	.486
24	16	90	0.361	0.103	22	15	90	0.391	0.105	20	13	90	0.427	0.099
		85	.385	.148			85	.415	.151			85	.451	.147
		80	.407	.199			80	.437	.204			80	.473	.201
		75	.429	.258			75	.458	.264			75	.494	.263
		70	.448	.325			70	.476	.333			70	.513	.333
		65	.465	.404			65	.493	.413			65	.529	.414
		60	.479	.496			60	.506	.506			60	.544	.507

APPENDIX 4. CONSOLIDATION TIME FACTORS

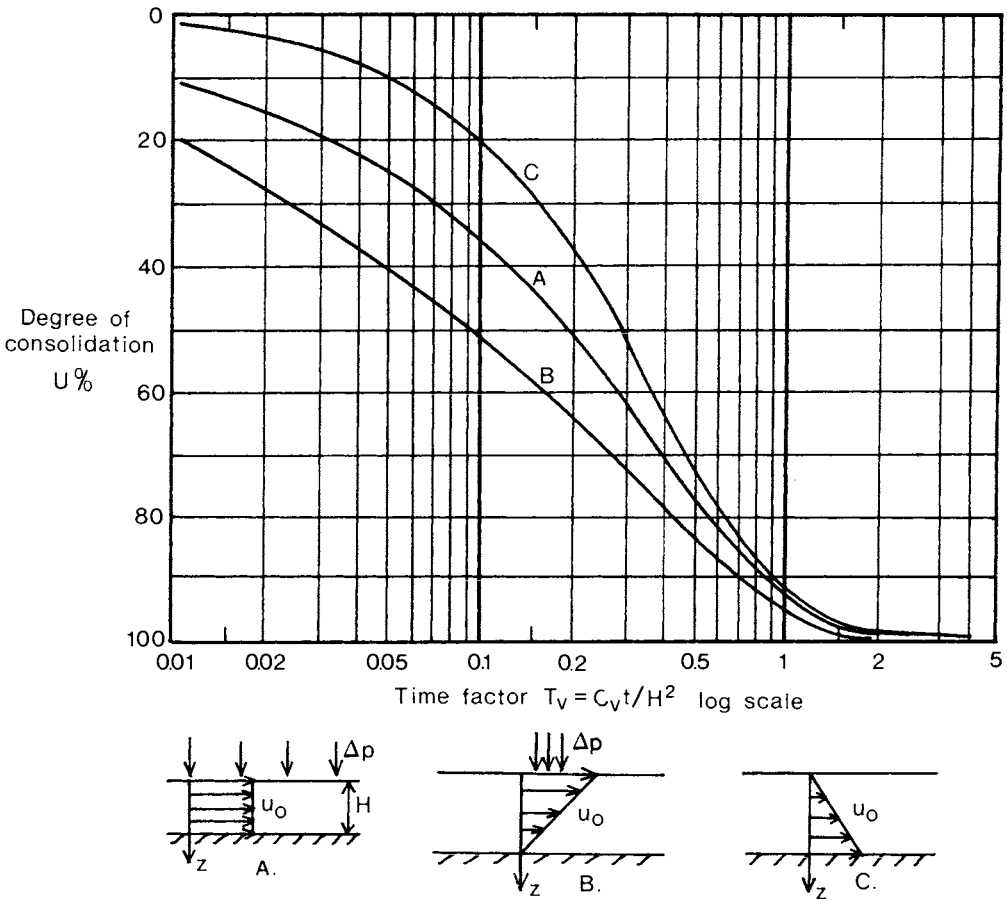
0
20
40
60
80
100
Degree of consolidation U %
C
A
B
0.01
0.02
0.05
0.1
0.2
0.5
1
2
5
Time factor $T_V = C_V t/H^2$ log scale
Δp
u_o
H
z
A.
Δp
u_o
z
B.
u_o
z
C.

APPENDIX 5. PASSIVE SOIL CUTTING FACTORS

$$P = (\gamma d^2 N_\gamma + cdN_c + qdN_q + c_a dN_{ca})\, w$$

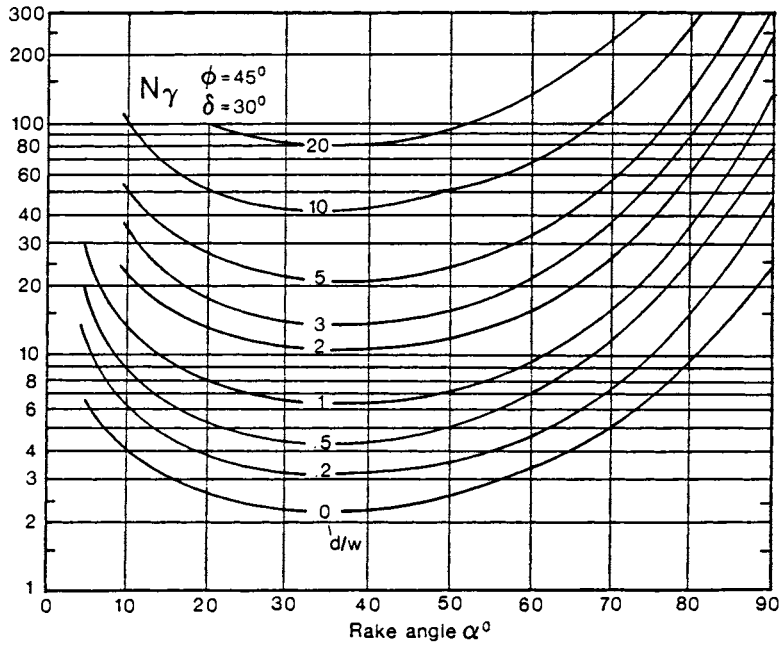
N_γ $\phi = 45^0$ $\delta = 30^0$
20
10
5
3
2
1
.5
.2
0
d/w
300
200
100
80
60
40
30
20
10
8
6
4
3
2
1
0 10 20 30 40 50 60 70 80 90
Rake angle α^0

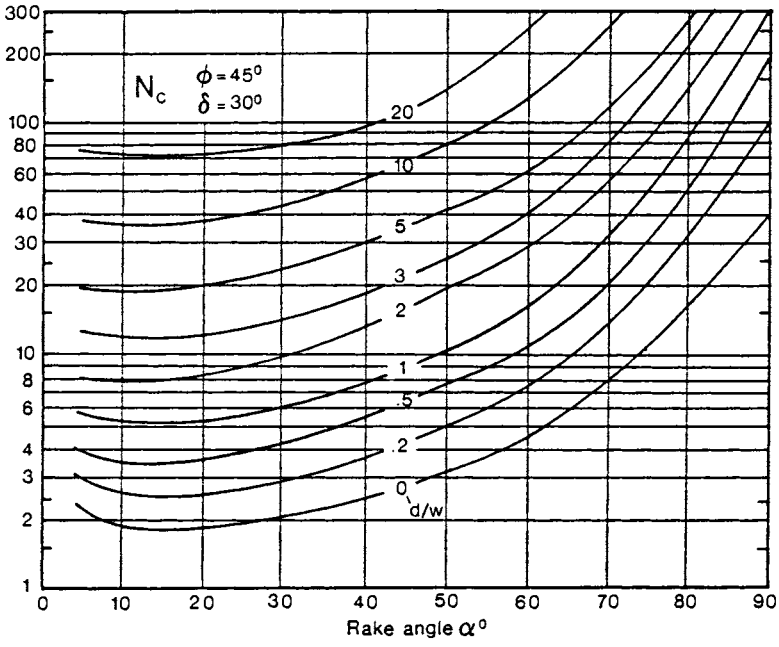
N_c $\phi = 45^0$ $\delta = 30^0$
20
10
5
3
2
1
.5
.2
0
d/w
300
200
100
80
60
40
30
20
10
8
6
4
3
2
1
0 10 20 30 40 50 60 70 80 90
Rake angle α^0

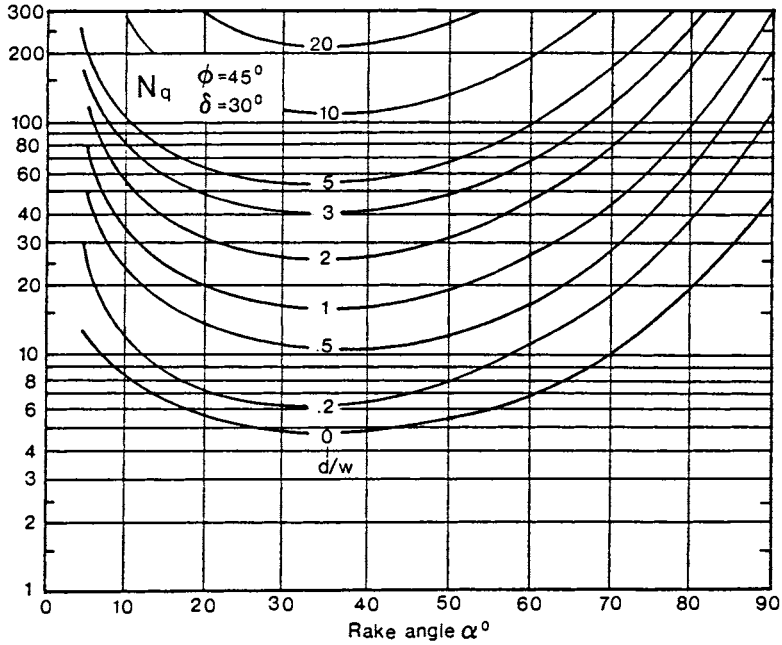
N_q $\phi=45^\circ$ $\delta=30^\circ$
20
10
5
3
2
1
.5
.2
0
d/w
300
200
100
80
60
40
30
20
10
8
6
4
3
2
1
0 10 20 30 40 50 60 70 80 90
Rake angle α°

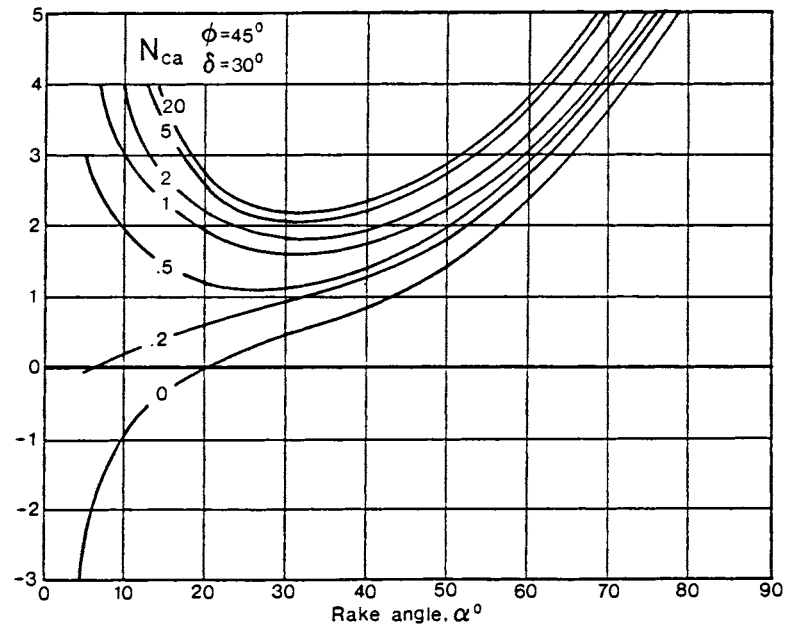
N_{ca} $\phi=45^\circ$ $\delta=30^\circ$
20
5
2
1
.5
.2
0
5
4
3
2
1
0
-1
-2
-3
0 10 20 30 40 50 60 70 80 90
Rake angle, α°

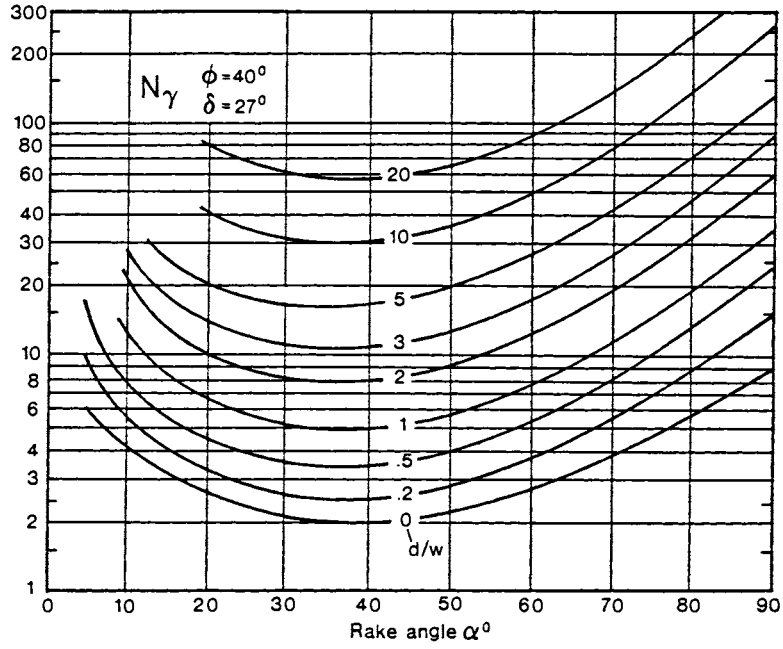
N_γ $\phi = 40^0$ $\delta = 27^0$
20
10
5
3
2
1
.5
.2
0
d/w
300
200
100
80
60
40
30
20
10
8
6
4
3
2
1
0 10 20 30 40 50 60 70 80 90
Rake angle α^0

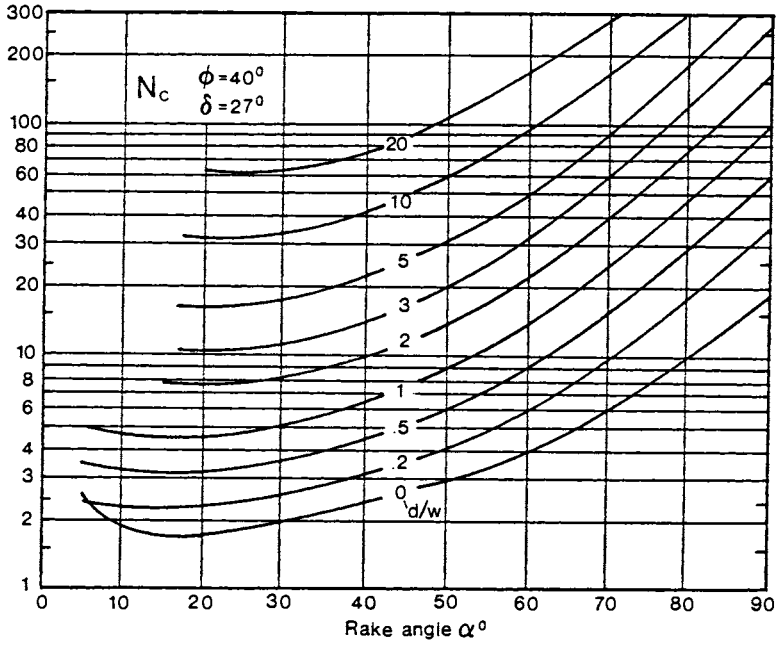
N_c $\phi = 40^0$ $\delta = 27^0$
20
10
5
3
2
1
.5
.2
0
d/w
300
200
100
80
60
40
30
20
10
8
6
4
3
2
1
0 10 20 30 40 50 60 70 80 90
Rake angle α^0

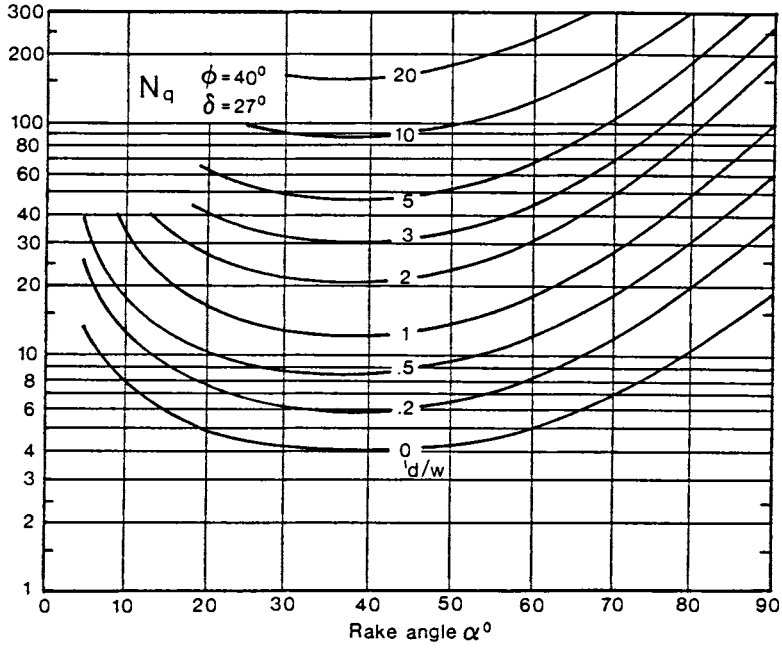
N_q $\phi = 40^0$ $\delta = 27^0$
20
10
5
3
2
1
.5
.2
0
d/w
300
200
100
80
60
40
30
20
10
8
6
4
3
2
1
0 10 20 30 40 50 60 70 80 90
Rake angle α^0

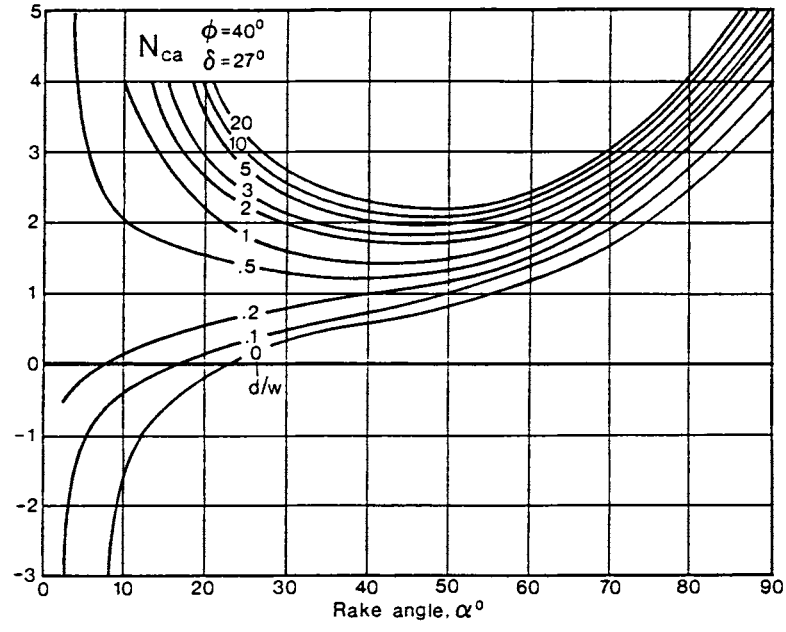
N_{ca} $\phi = 40^0$ $\delta = 27^0$
20
10
5
3
2
1
.5
.2
.1
0
d/w
5
4
3
2
1
0
-1
-2
-3
0 10 20 30 40 50 60 70 80 90
Rake angle, α^0

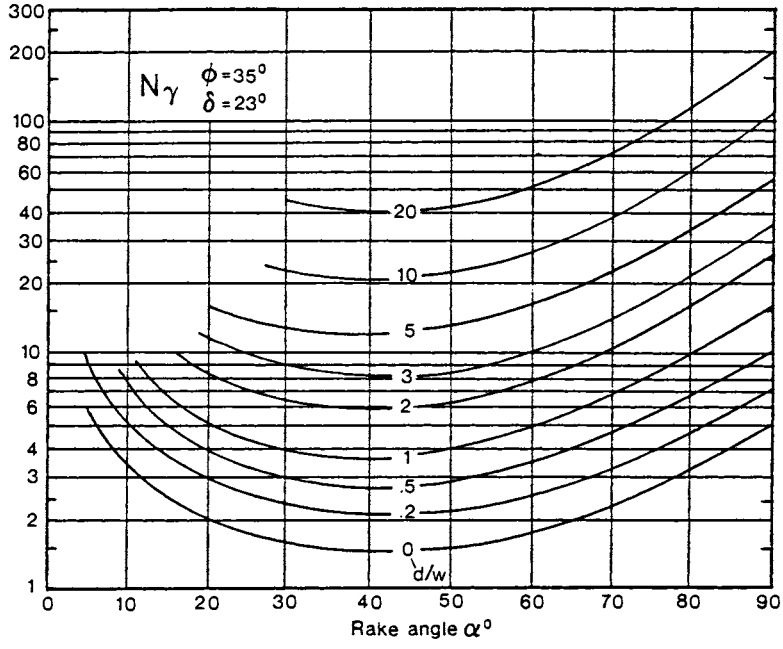
N_γ $\phi = 35^0$ $\delta = 23^0$
300
200
100
80
60
40
30
20
10
8
6
4
3
2
1
20
10
5
3
2
1
.5
.2
0
d/w
0 10 20 30 40 50 60 70 80 90
Rake angle α^0

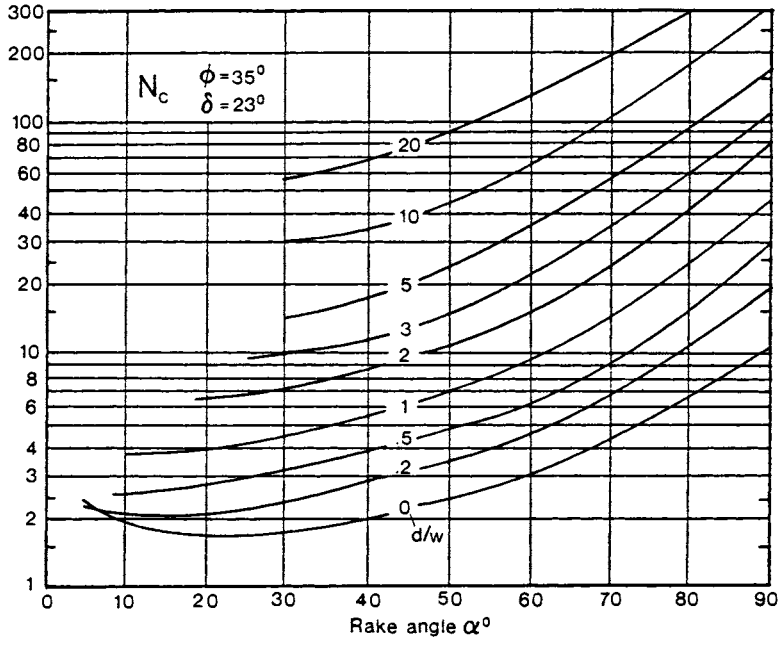
N_c $\phi = 35^0$ $\delta = 23^0$
300
200
100
80
60
40
30
20
10
8
6
4
3
2
1
20
10
5
3
2
1
.5
.2
0
d/w
0 10 20 30 40 50 60 70 80 90
Rake angle α^0

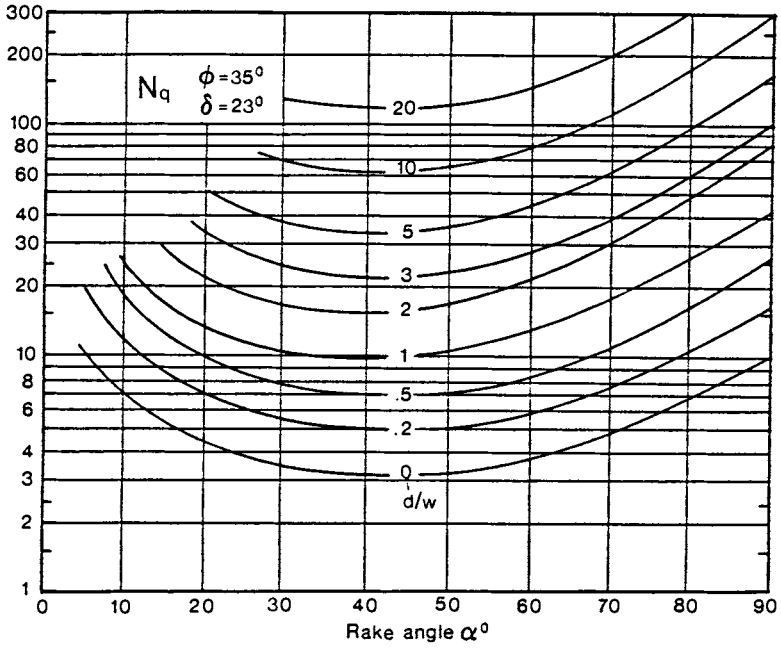
N_q $\phi=35^0$ $\delta=23^0$
20
10
5
3
2
1
.5
.2
0
d/w
300
200
100
80
60
40
30
20
10
8
6
4
3
2
1
0 10 20 30 40 50 60 70 80 90
Rake angle α^0

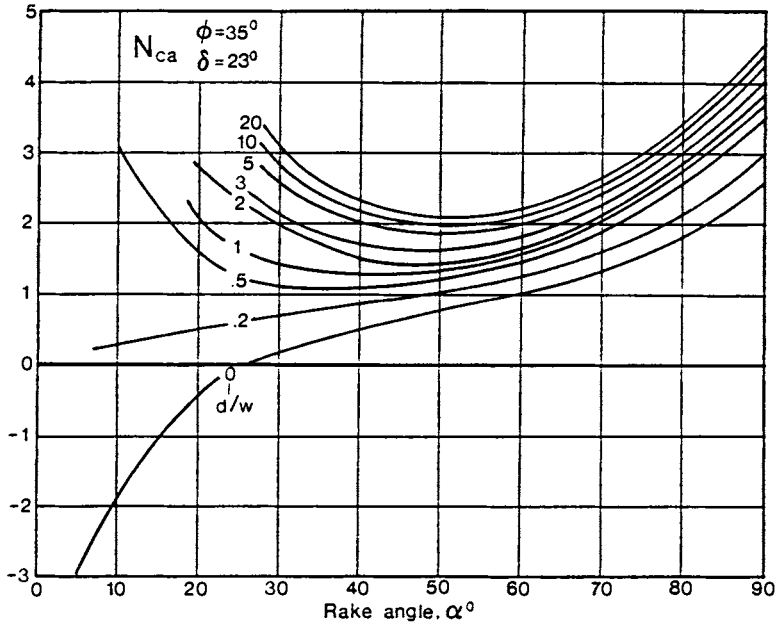
N_{ca} $\phi=35^0$ $\delta=23^0$
20
10
5
3
2
1
.5
.2
0
d/w
5
4
3
2
1
0
-1
-2
-3
0 10 20 30 40 50 60 70 80 90
Rake angle, α^0

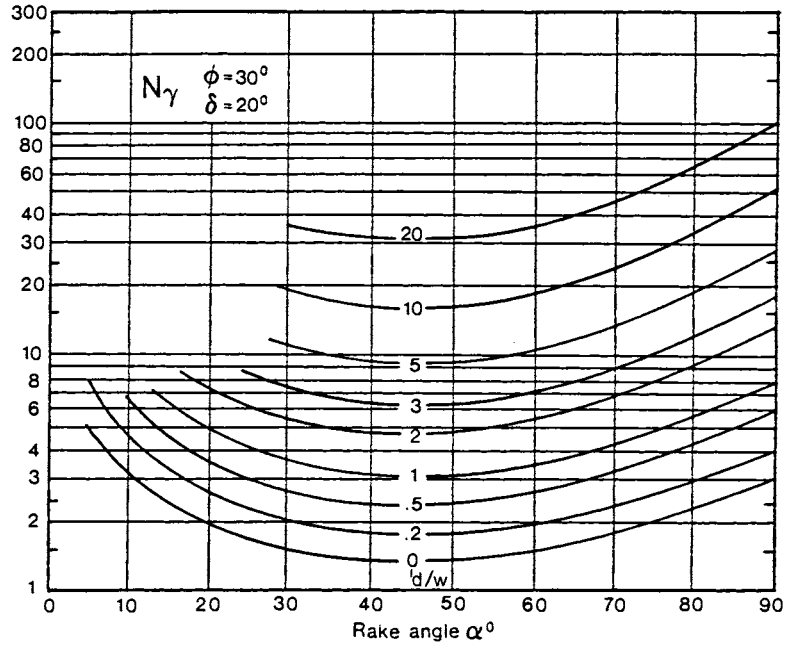
N_γ $\phi = 30^0$ $\delta = 20^0$
300
200
100
80
60
40
30
20
10
8
6
4
3
2
1
20
10
5
3
2
1
.5
.2
0
d/w
0
10
20
30
40
50
60
70
80
90
Rake angle α^0

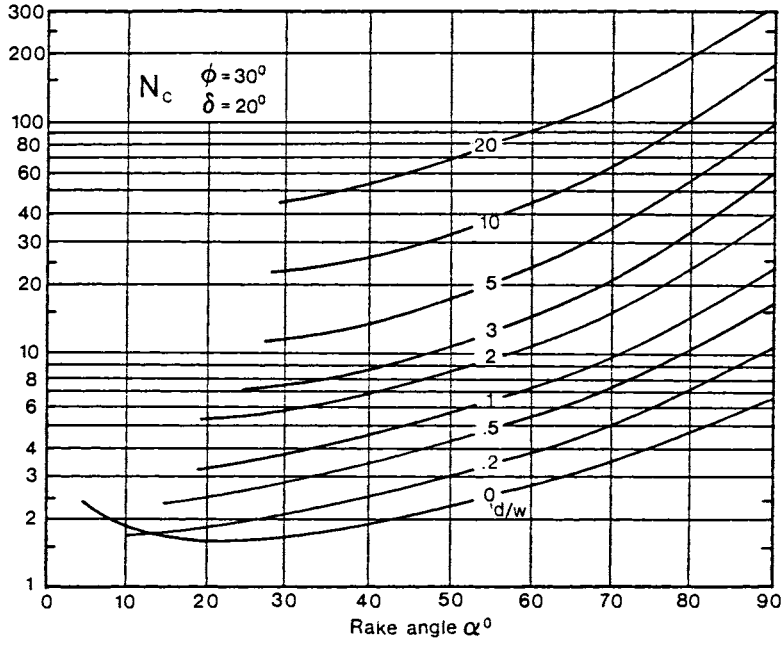
N_c $\phi = 30^0$ $\delta = 20^0$
300
200
100
80
60
40
30
20
10
8
6
4
3
2
1
20
10
5
3
2
1
.5
.2
0
d/w
0
10
20
30
40
50
60
70
80
90
Rake angle α^0

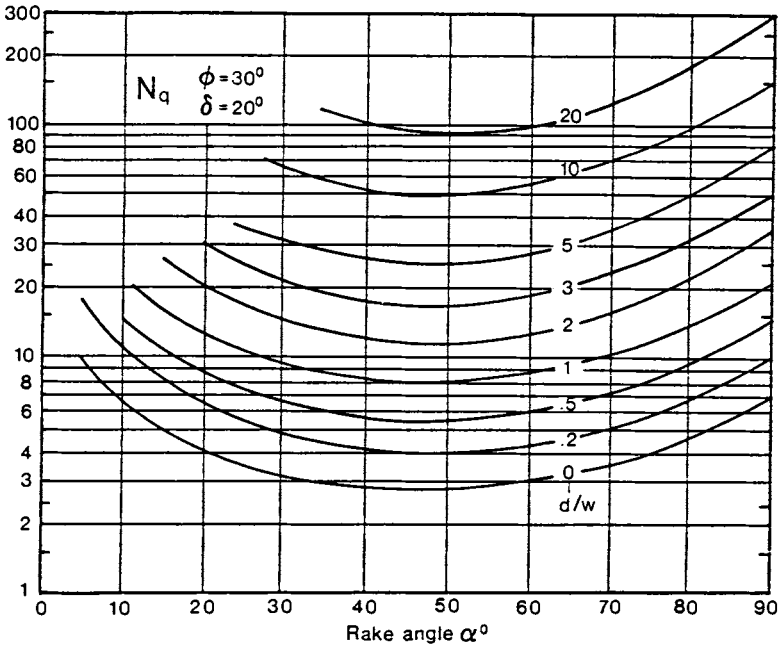
N_q $\phi=30^0$ $\delta=20^0$
20
10
5
3
2
1
.5
.2
0
d/w
Rake angle α^0

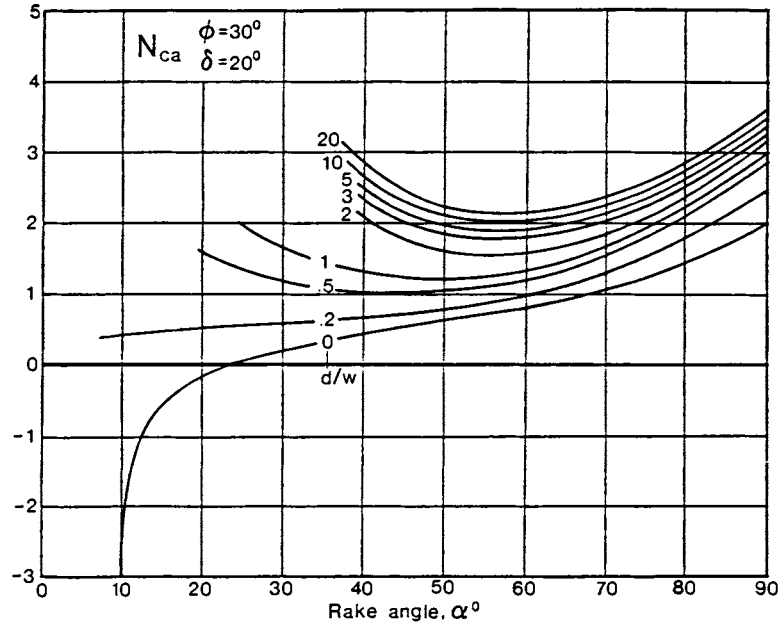
N_{ca} $\phi=30^0$ $\delta=20^0$
20
10
5
3
2
1
.5
.2
0
d/w
Rake angle, α^0

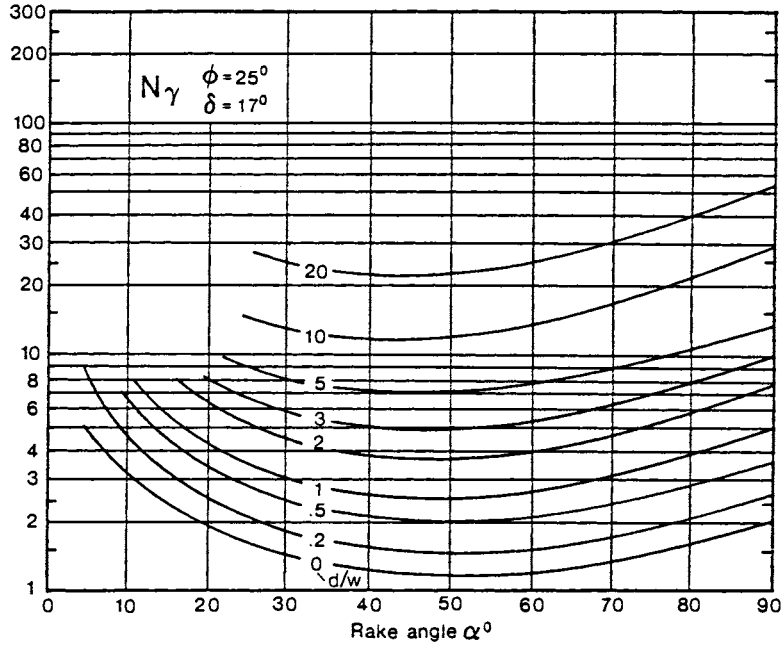
N_γ $\phi = 25^0$ $\delta = 17^0$
300
200
100
80
60
40
30
20
10
8
6
4
3
2
1
20
10
5
3
2
1
.5
.2
0
d/w
0 10 20 30 40 50 60 70 80 90
Rake angle α^0

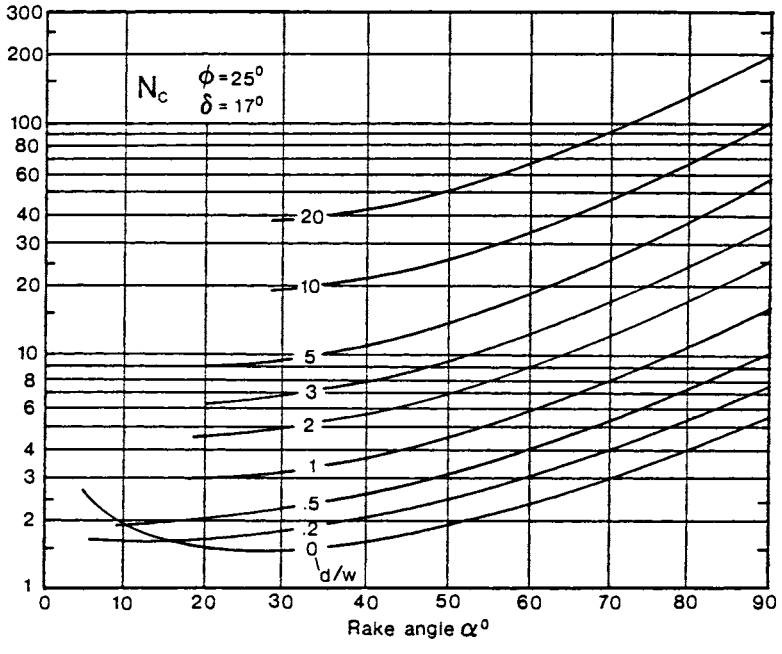
N_c $\phi = 25^0$ $\delta = 17^0$
300
200
100
80
60
40
30
20
10
8
6
4
3
2
1
20
10
5
3
2
1
.5
.2
0
d/w
0 10 20 30 40 50 60 70 80 90
Rake angle α^0

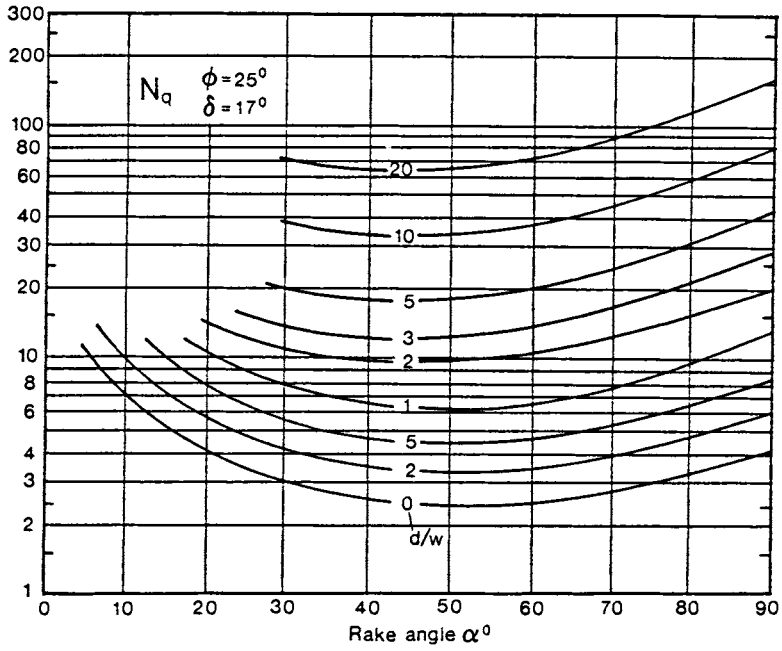
N_q $\phi = 25^0$ $\delta = 17^0$
20
10
5
3
2
1
5
2
0
d/w
300
200
100
80
60
40
30
20
10
8
6
4
3
2
1
0 10 20 30 40 50 60 70 80 90
Rake angle α^0

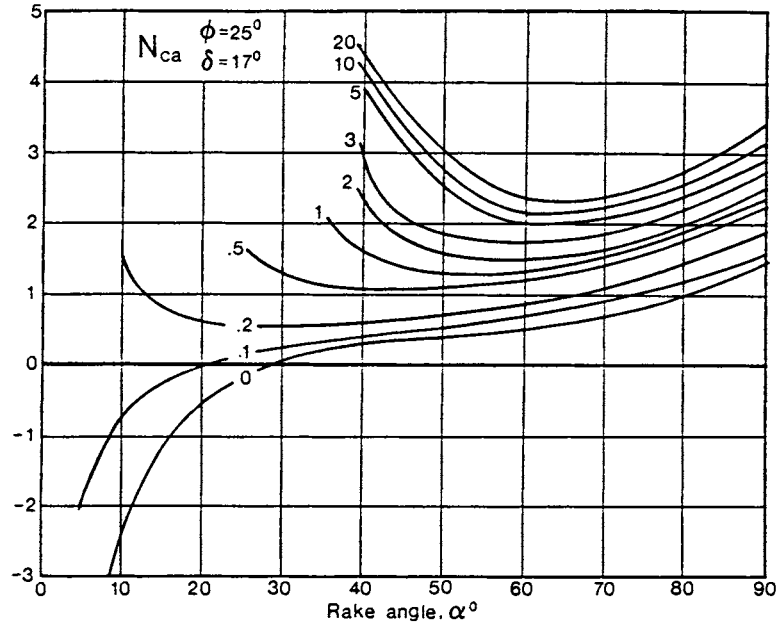
N_{ca} $\phi = 25^0$ $\delta = 17^0$
20
10
5
3
2
1
.5
.2
.1
0
5
4
3
2
1
0
-1
-2
-3
0 10 20 30 40 50 60 70 80 90
Rake angle, α^0

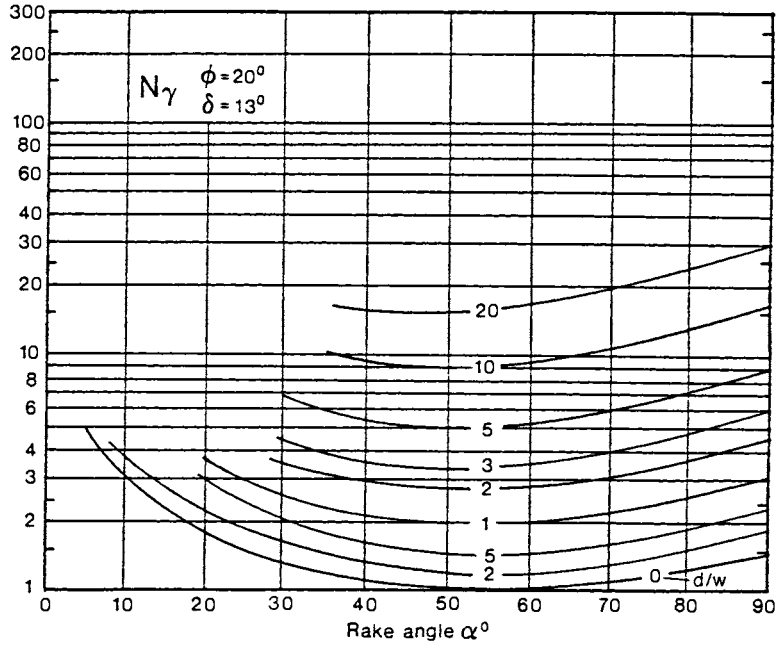
N_γ $\phi = 20^0$ $\delta = 13^0$
300
200
100
80
60
40
30
20
10
8
6
4
3
2
1
20
10
5
3
2
1
5
2
0
d/w
0
10
20
30
40
50
60
70
80
90
Rake angle α^0

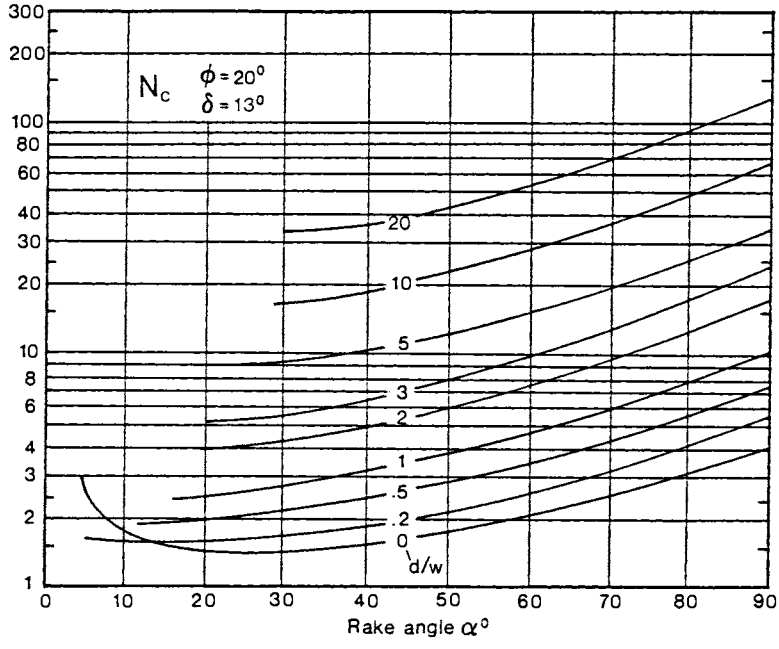
N_c $\phi = 20^0$ $\delta = 13^0$
300
200
100
80
60
40
30
20
10
8
6
4
3
2
1
20
10
5
3
2
1
.5
.2
0
d/w
0
10
20
30
40
50
60
70
80
90
Rake angle α^0

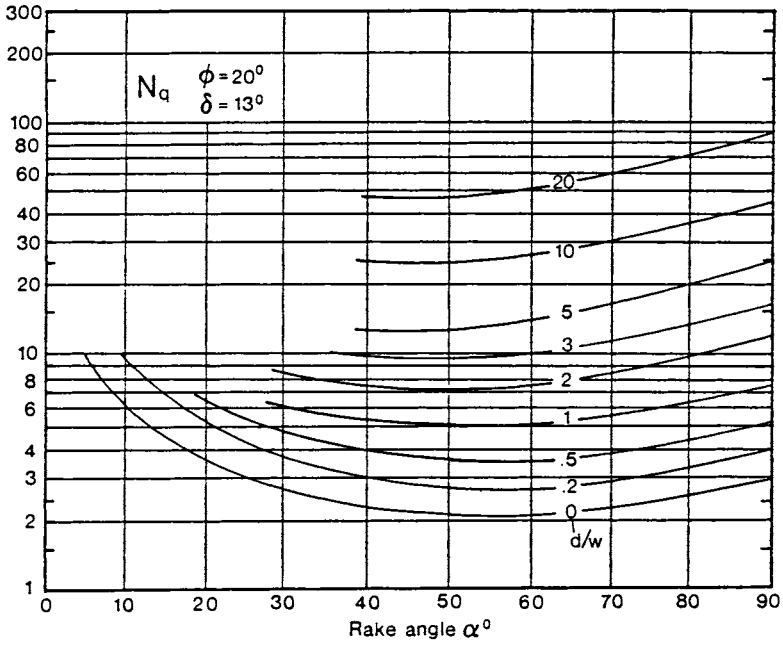
N_q $\phi = 20^0$ $\delta = 13^0$
300
200
100
80
60
40
30
20
10
8
6
4
3
2
1
20
10
5
3
2
1
.5
.2
0
d/w
0
10
20
30
40
50
60
70
80
90
Rake angle α^0

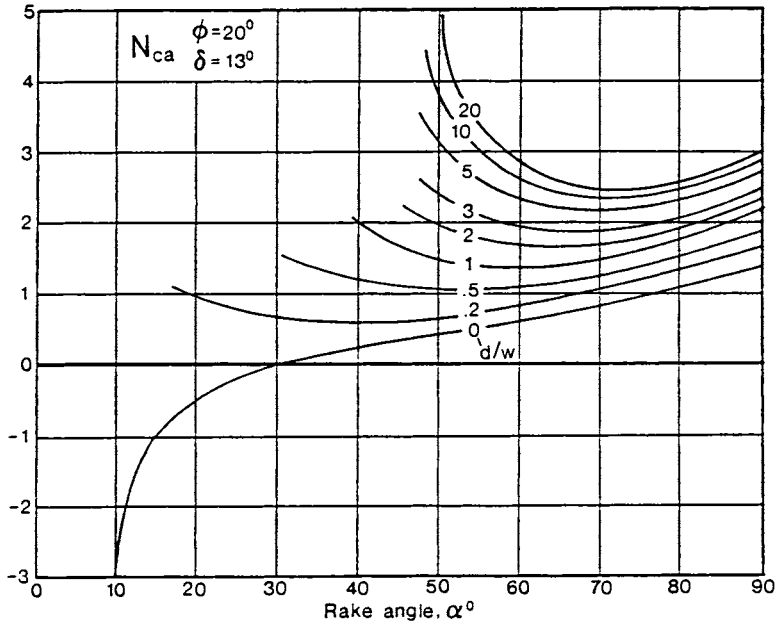
N_{ca} $\phi = 20^0$ $\delta = 13^0$
5
4
3
2
1
0
-1
-2
-3
20
10
5
3
2
1
.5
.2
0
d/w
0
10
20
30
40
50
60
70
80
90
Rake angle, α^0

APPENDIX 6. SELECTED VALUES OF SOIL MECHANICAL PROPERTIES (from Bekker, 1969).

Soil	m.c. %	k_c kPa/m^{n-1}	k_ϕ kPa/m^n	n	c kPa	ϕ^0
Sandy loam, Michigan	11	52	1127	0.9	4.8	20
	13	17	911	0.8	6.9	29
	21	11	1138	0.4	17.2	22
	23	11	1802	0.7	11.0	25
	23	11	808	0.4	9.6	35
Sandy loam, Maryland	26	3	141	0.3	13.8	22
	29	3	169	0.6	13.8	26
	30	6	3	0.4	6.2	23
	31	1	36	0.4	5.5	15
	32	1	52	0.5	5.2	11
Dry sand[a]	0	1	1527	1.1	1.0	28
Sandy loam[a]	15	5	1514	0.7	1.7	29
	22	3	43	0.2	1.4	38
Unplowed soil, MI		17	2322	0.6	11.0	38
Plowed soil, MI		5	169	0.8	6.9	20
Clay, Thailand	38	13	692	0.5	4.1	13
	43	105	752	0.9	1.8	10
	45	7	297	0.3	5.5	17
	47	38	500	0.6	7.6	14
	55	48	1356	1.0	0	11
	55	16	1262	0.7	2.1	10
	185	21	814	1.0	3.4	11
Heavy clay[b]	25	13	1555	0.13	68.9	34
	30	7	696	0.12	48.2	22
	35	4	153	0.125	34.5	14
	40	2	103	0.11	20.7	6
Lean clay[b]	22	16	1723	0.20	68.9	20
	24	10	1030	0.17	48.2	18
	26	7	580	0.17	34.5	15
	28	3	372	0.16	27.6	12
	30	3	248	0.16	17.2	11
	32	2	120	0.15	13.8	11

[a] Land Locomotion Laboratory, Detroit MI.

[b] Waterways Experimentation Station, Vicksburg MS.

AUTHOR INDEX

SUBJECT INDEX